UNIVERSITY OF OKLAHOMA

GRADUATE COLLEGE

A PSEUDO-DUAL-DOPPLER ANALYSIS OF CYCLIC TORNADOGENESIS

A Dissertation

SUBMITTED TO THE GRADUATE FACULTY

in partial fulfillment of the requirements for the

degree of

Doctor of Philosophy

By

DAVID C. DOWELL

Norman, Oklahoma

2000

UMI Number: 9956999

UMI®

UMI Microform 9956999

Bell & Howell Information and Learning Company
300 North Zeeb Road
P.O. Box 1346
Ann Arbor, MI 48106-1346

A PSEUDO-DUAL-DOPPLER ANALYSIS OF CYCLIC TORNADOGENESIS

A Dissertation APPROVED FOR THE

SCHOOL OF METEOROLOGY

BY

Howard B. Bluestein

John P. Albert

David Jorgensen

[illegible]

[illegible]

Morris L. Weisman

ACKNOWLEDGMENTS

Many helpful comments on this research were provided by my doctoral committee: John Albert, Howie Bluestein, David Jorgensen, Doug Lilly, Alan Shapiro, and Morris Weisman. Most of all, I would like to thank Howie for his input and support throughout my graduate program. This research was funded by National Science Foundation grant ATM-9612674.

Contributions from many others also made this study possible. I am grateful to the following individuals: Wen-Chau Lee for providing the ELDORA data and answering many questions about airborne radar, Susan Stringer (and Wen-Chau Lee) for providing the GRID2PS graphics software, Michelle Case and Dick Oye for answering questions about the REORDER objective analysis software, Erik Rasmussen for leading the VORTEX field program and motivating careful analysis of the data that were collected, Roger Wakimoto for directing the aircraft operations, Josh Wurman for leading the Doppler on Wheels project, Jerry Straka and Erik Rasmussen for designing and coordinating the mobile mesonets, all other VORTEX participants for their efforts during the project, Mike Magsig for providing WSR-88D data and adding insightful comments on the 8 June 1995 case, Frank Gallagher for scanning images, John Mewes for providing comments on dual-Doppler analysis methods, Ed Adlerman for offering helpful comments on cyclic tornadogenesis, Bruce Haynie for contributing video and photographic documentation of the McLean storm, and Herb Stein, Cristina Kaufman, Tim Marshall, Dave Ewoldt, and Scott Richardson for providing other documentation of the storm. This work would not have been possible without the computer assistance of Tom Condo and Mark Laufersweiler at OU. For the test-case numerical simulations, the National Center for Atmospheric Research (NCAR) provided computer time on a Cray. NCAR is sponsored by the National Science Foundation.

Last but not least, I want to thank Mom, Dad, Don, and Darren for their support throughout my days as a graduate student.

TABLE OF CONTENTS

ABSTRACT

Several tornadic storms formed in the Texas Panhandle on 8 June 1995, the date of the last mission of VORTEX (Verification of the Origins of Rotation in Tornadoes EXperiment). The southernmost storm in this severe weather outbreak produced a family of at least five tornadoes near the town of McLean. Airborne Doppler radar scans of this storm by the ELDORA (ELectra DOppler RAdar) offer the most detailed look to date at a storm producing a family of tornadoes.

The goals of this study were twofold. The first was to determine a pseudo-dual-Doppler wind synthesis method in Cartesian coordinates appropriate for the analysis of the ELDORA data. Unique aspects of this part of the study include a comparison of wind synthesis methods based on variational formulations and the use of a non-uniform moving reference frame for the syntheses. A dual-Doppler formulation in which the radial velocity and continuity equations are all satisfied as weak constraints (Gamache 1997, Shapiro and Mewes 1999) yields a more accurate wind field than traditional (and variational) methods in which the radial velocity equations are satisfied exactly.

The second goal of this study was to diagnose both the cyclic process and the formation of individual tornadoes. The McLean storm produced three large tornadoes at 18 min intervals. The last of these then lasted much longer (over one hour) and was stronger than the previous tornadoes. New pre-tornadic vortices formed on the east side of the updraft by tilting of strong environmental low-level horizontal vorticity into the vertical and then stretching of the vertical vorticity within the updraft. The vortices did not mature at low levels until they migrated to the west side of the updraft. Indirect evidence indicates that both baroclinic generation of horizontal vorticity and the rear downdraft may have played roles in tornado formation at this stage.

The tornadic potential of a storm appears to be related to the relative strength of low-level storm outflow and inflow beneath the west side of updraft. Cyclic tornadogenesis modes may be possible both when the inflow slightly dominates and when the outflow slightly dominates. The description of an inflow-dominated cyclic mode like that observed in the McLean storm is original. Internal cell interactions within

the McLean storm appear to have helped the transition from the cyclic phase to a more steady phase.

1. INTRODUCTION

An individual supercell thunderstorm that is capable of producing a tornado is often capable of producing a series of tornadoes. This is especially true during tornado outbreaks, in which the tornadoes tend to be organized into famililes of many tornadoes produced by individual storms (Fujita et al. 1970, Fujita 1974) (Figure 1.1). Doswell and Burgess (1988) argue that some of the very long swaths of tornado damage thought originally to have been produced by single long-track tornadoes were more likely the result of tornado families. Individual tornadoes within a family often overlap in lifetime with the previous tornado (e.g., Fig. 1.2) such that damage may be continuous in time and nearly continuous in space along the surface.

Previous documentation of cyclic tornadogenesis (that is, the formation of a succession of tornadoes in a single storm) is mostly in the form of single-Doppler observations (Burgess et al. 1982) and visual observations (photographs, videos, and surveys of tornado tracks) (e.g., Fujita et al. 1970, Rasmussen et al. 1982, Jensen et al. 1983, Davies et al. 1994). Multiple-Doppler observations capable of resolving the 3D wind field in cyclic storms have been very limited. Perhaps the best case was the Fort Cobb, Oklahoma storm of 20 May 1977 (Johnson et al. 1987). In this case, however, the tornadoes were ~60 km from one of the two radars, and there was a gap of 20 min between dual-Doppler volumes during the most critical stage (Ray et al. 1981, Johnson et al. 1987). The quality of Doppler observations of cyclic tornadogenesis improved dramatically in 1995 with the use of airborne Doppler radar in a tornado field program.

One of the primary motivations for the development of airborne Doppler radar was the study of hurricanes (Marks and Houze 1984, 1987; Jorgensen and Marks 1984). Since hurricanes and other tropical precipitating systems are often far away from land-based radars along coastlines, the advantage of the moving airborne platform is obvious. Airborne radar was employed extensively in a recent field program in the tropics (Webster and Lukas 1992).

Airborne radar has also been used to probe individual thunderstorms over land (Hildebrand and Mueller 1985, Ray et al. 1985, Ray and Jorgensen 1988, Ray and Stephenson 1990), including some supercells during COPS-91 (Cooperative Oklahoma

Profiler Studies 1991) (Dowell et al. 1997). The most extensive use of the airborne platform specifically for tornado research was during a 1994-5 field program known as VORTEX (Verification of the Origins of Rotation in Tornadoes EXperiment) (Rasmussen et al. 1994). Although tornadoes sometimes occur close to ground-based radars in the operational network, the mobility of airborne radar offers the potential of collecting close-up observations of tornadoes much more frequently.

VORTEX was a collaboration of university and government scientists aimed at understanding tornadogenesis and tornado dynamics (Rasmussen et al. 1994). Measurements with a suite of mobile ground-based instruments such as mesonets, Doppler radars, and sounding equipment complemented observations by the NOAA P-3 airborne radar (Jorgensen et al. 1983) and the NCAR Electra' s ELDORA system (Table 1.1) (Hildebrand et al. 1994, Wakimoto et al. 1996).

The last mission of the project turned out to be one of the most productive. On the morning of 8 June 1995, the southern High Plains were beneath moderate southwesterly flow aloft (with stronger flow upstream) to the east of a trough in the Southwest (Fig. 1.3). By evening, high CAPE (approximately 5000 J kg^{-1}) and strong vertical shear of the horizontal wind (30 m s^{-1} over the lowest 6 km) were in place in the eastern Texas Panhandle east of a north-south oriented dryline (Fig. 1.4, 1.5).

VORTEX teams initially targeted a storm in the eastern Oklahoma Panhandle (Fig. 1.6.a). However, when it became clear that the initial target storm was becoming less intense at 2200 UTC, the teams focused their attention on storms that had formed along the dryline farther south in the Texas Panhandle (Fig. 1.6.b). By the end of the day, these storms in the Texas Panhandle had produced at least 18 tornadoes (D. Crowley, National Weather Service, Amarillo, Texas, 1996, personal communication).

Early echoes (Fig. 1.6.b) of the eventual target storm (the "McLean, Texas storm") appeared on the Amarillo WSR-88D display at 2050 UTC. The early cells formed approximately 12 km east of Silverton, Texas above one of the steepest terrain slopes along the Caprock Escarpment. The storm grew in size and intensity as it moved to the northeast (Fig. 1.6.c).

The P-3 and Electra arrived at the McLean storm just before it started to produce a family of at least five tornadoes (Fig. 1.7, Table 1.2). A summary of these tornadoes is given below.

tornado (time UTC)	damage rating	location
1 (~2252 to 2315)	F2	15 km south of Alanreed to 4 km south of Alanreed
2 (2310 to 2322)	F2	8 km east-southeast of Alanreed to 6 km northeast of Alanreed
3 (2321 to 2323)	F0	2 km southwest of McLean
4 (2328 to >0030)	F4	northwest side of McLean to 10 km northeast of Mobeetie
5 (0005)	F0	8 km northeast of Kellerville

The times of the tornadoes are based on a video tape provided by Bruce Haynie. The tornado damage ratings (Fujita 1981) are from the Amarillo National Weather Service (D. Crowley 1996, personal communication). At least one of the ratings is controversial; Wakimoto et al. (1996) describe tornado #4 as reaching F5 intensity.

Tornadoes #1, #2, and #4 were all large (Fig. 1.8), but tornado #4 was by far the longest lived. The ending time of tornado #4 is unknown, as it had become enshrouded in rain by 0030. It is possible that the McLean storm was still producing a tornado as late as 0100 (P. Robinson and J. Straka 1995, personal communication). It is clear, though, that tornado #4 lasted at least one hour.

In contrast, tornadoes #3 and #5 were small and brief (Fig. 1.8 and 1.9). Tornado #5 initially had a ropelike appearance (Fig. 1.9); later, it had a wider but shallower condensation funnel hanging down from the cloud base (not shown). Tornado #5 eventually appeared to be absorbed into the circulation of tornado #4 to its south (D. Ewoldt and C. Kaufman 1995, personal communication).

There is a description in *Storm Data* (U. S. Dept. of Commerce 1995) of another brief F0 tornado that occurred earlier (2219 UTC) to the southwest of Clarendon, Texas. However, I can not confirm its existence from a second source; an experienced storm chaser was observing a wall cloud with occasional very small funnels extending down from it around this time (B. Haynie 1995, personal communication).

Other tornadoes near McLean include a weak tornado in a companion storm that formed to the west of the McLean storm (Fig. 1.6.d) and a violent tornado near Allison, Texas in a storm that formed later to the east of the McLean storm (not shown). In this study, I will focus on the McLean storm only and not on the neighboring storms.

The Electra flew 17 approximately east-west oriented legs just south of the McLean storm at ~500 m AGL for over 1.5 hours (Table 1.2). The ELDORA dataset ends abruptly at 0015 UTC 9 June, while tornado #4 was still in progress. At this time, the Electra encountered extreme turbulence southwest of the tornado. A few of the occupants of the aircraft were injured; therefore, the pilots aborted the mission and returned to the airport in Oklahoma City. Since VORTEX ground crews were out of position after following the original target storm, they did not arrive to the McLean storm until very late (0010 UTC). The mobile mesonet and ELDORA data overlap only during the last (incomplete) aircraft pass.

The ELDORA transmits pulses at two different pulse repetition frequencies so that the effective unambiguous velocity (Table 1.1) has a magnitude suitable for the study of severe convective storms (Wakimoto et al. 1996). In addition, the radar transmits at multiple frequencies, which allows for a relatively rapid antenna rotation rate owing to the decreased time required to obtain independent samples (Hildebrand et al. 1994). For typical Electra flight speeds (120 m s^{-1}) and antenna rotation rates during convective mode scanning (complete 360° sweep every 2.7 seconds), the along-flight-track spacing between consecutive sweeps is ~300 m. This is comparable to the beamwidth, which was 160-600 m at ranges of 5-19 km to the McLean storm tornadoes (Table 1.3). With this spatial resolution and with the ~6 min time resolution, the ELDORA scans of the McLean storm are the best set of observations to date of the wind field within a storm producing a series of strong tornadoes.

Chapter 2 is a summary of the methodology for the pseudo-dual-Doppler analysis of the ELDORA data. Data collected by the airborne research radars during VORTEX include observations at high elevation angles. Traditional dual-Doppler wind syntheses in Cartesian coordinates fail to converge for this geometry. Variational formulations instead provide a basis for synthesizing the 3D wind field in Cartesian coordinates, and they can be used to obtain coherent solutions even in the presence of noisy observations. A separate issue for airborne pseudo-dual-Doppler radar is the temporal distribution of data, which necessitates special attention to the reference frame of the wind synthesis.

Chapter 3 begins with a brief introduction to supercell dynamics and continues with a description of tornadogenesis in the McLean storm. The observational study of cyclic tornadogenesis is currently limited by the availability of only one detailed dual-Doppler case. However, the comparison of the behavior of the McLean storm to that in previous observations and numerical simulations motivated the formulation of a new hypothesis for explaining two types of cyclic storm evolutions and transitions from a cyclic phase to a steady phase in a storm. The hypothesis centers on the relative strength of low-level storm inflow and outflow beneath the west (upshear) side of the updraft, and on the importance of small-scale influences that come from outside the main storm updraft and downdraft. Tornado families tend to occur on the storm days that have the highest potential to produce loss of life (Fujita et al. 1970, Fujita 1974). Therefore, if the hypothesis is correct, then severe storm forecasting and nowcasting could potentially benefit from increased attention to detecting inflow-outflow balance and to detecting storm interactions.

Chapter 4 is a summary of the work in the previous chapters and contains a list of proposed avenues for future work.

2. PSEUDO-DUAL-DOPPLER ANALYSIS METHODOLOGY

2.1 Background

Three critical issues in the formulation of a dual-Doppler wind synthesis method are the spatial distribution of the data relative to the radars, the time distribution of the data, and the impact of errors in the data. The following review of dual-Doppler methods for airborne radar will emphasize these three issues in particular for VORTEX (Rasmussen et al. 1994) data.

During VORTEX, the pilots of the NCAR Electra and NOAA P-3 often flew east-west legs at low levels (~500 m AGL) close to the south sides of supercells. Figure 2.1.1, which shows a slice through the McLean storm including one of the tornadoes, demonstrates the geometry of the problem for VORTEX airborne Doppler data. Most of the data of interest (the storm updraft and tornado) are on one side of the aircraft. However, potentially useful data are also found on the opposite side of the aircraft (e.g., in the clear air data at low levels) and overhead (e.g., in the storm anvil). For much of the airborne Doppler data from VORTEX, the radar scanned the storms with a wide range of incidence angles. Scans of the tornado at low levels were approximately horizontal, while scans of the storm top were closer to vertical (Fig. 2.1.1).

The ELDORA is essentially two radar systems (Hildebrand et al. 1994). Back-to-back flat plate antennas transmit pulses in opposite directions as they rotate about the aircraft axis. One beam sweeps out a cone in a slightly forward direction, while the other beam sweeps out a cone in a slightly aft direction (Fig. 2.1.2). This scanning pattern for airborne radar is commonly known as FAST (Fore/Aft Scanning Technique) (Jorgensen and DuGranrut 1991). Given the motion of the aircraft, the radar sweeps out a helical pattern in a ground-relative sense. Since the radar beams do not point perpendicular to the flight track, the motion of the aircraft contributes to the observed Doppler velocity; this component is removed before the 3D wind synthesis (Lee et al. 1994).

The advantage of FAST is that pseudo-dual-Doppler data can be collected from a single straight flight leg (Fig. 2.1.3) (Jorgensen and DuGranrut 1991). "Pseudo-dual-Doppler" refers to the Doppler sampling of a feature with a single radar platform but from two different viewing angles at two different times. As the aircraft flies along, it first samples a point within the domain with the fore radar and then later with the aft radar (Fig. 2.1.3). This is in contrast to early studies with airborne Doppler radar, in which the radar beams scanned vertical planes normal to the flight track, and pseudo-dual-Doppler data were collected from two perpendicular (L-shaped) flight legs (Jorgensen et al. 1983, Ray et al. 1985).

An ideal dual-Doppler analysis would be based on simultaneous, instantaneous scans of a storm from two angles. However, this is not practical for current radar systems. The tradeoff between the original airborne scanning method and the present one (Jorgensen and DuGranrut 1991) involves the time distribution of the observations and the pseudo-dual-Doppler angle between beams. For carefully designed L-shaped flight legs, the between-beam angle (~90°) is optimal for dual-Doppler wind synthesis. However, the total time to complete the flight legs around a storm is large (up to 10-12 minutes). The total scan time is not the only issue; in addition, for particular points within the domain, the pseudo-dual-Doppler analysis would be based on two observations separated in time by as much as 10-12 minutes.

In contrast, for a plane flying a straight leg and employing FAST, both the total time required to scan a storm (~5 min) and the time lag between observations are less. The magnitude of the time lag is given by

$$\Delta t = \frac{2r \tan \tau}{V_a} \tag{2.1.1}$$

where r is the range to the target, τ is the radar tilt angle (20°) (Fig. 2.1.2, 2.1.3), and V_a is the ground-relative speed of the aircraft (Hildebrand et al. 1994). For typical flight speeds (~120 m s^{-1}) and ranges to storms (~20 km) during VORTEX, the time lag between observations (~120 s) was much less than what it would have been for a plane flying L-shaped patterns. However, the between-beam angle, which is twice the radar tilt angle, was only 40°. This results in a doubling of expected error in the synthesized along-track wind component (but only a 25% decrease in error in the cross-track wind component) relative to what would have been the case for an optimal (90°) between-angle (Hildebrand et al. 1994).

Attempts to determine the complete 3-D wind field from observations from two radars ("dual-Doppler analysis") began in the late 1960's (Armijo 1969). The fundamental equations for a dual-Doppler wind synthesis are (Lhermitte 1968, Armijo 1969):

$$c_1^{(1)}u + c_2^{(1)}v + c_3^{(1)}w = v_r^{(1)} - c_3^{(1)}w_t \equiv V_1 \tag{2.1.2}$$

$$c_1^{(2)}u + c_2^{(2)}v + c_3^{(2)}w = v_r^{(2)} - c_3^{(2)}w_t \equiv V_2 \tag{2.1.3}$$

$$\frac{\partial u}{\partial x} + \frac{\partial v}{\partial y} + \frac{\partial w}{\partial z} + \kappa w = 0 \tag{2.1.4}$$

where u, v, and w are the Cartesian wind components, v_r is the Doppler radial velocity (positive values away from radar), w_t (a negative quantity) is the terminal fall speed of the scatterers, and κ is a function of the base state density $\rho(z)$, given by

$$\kappa = \frac{1}{\rho}\frac{d\rho}{dz}. \tag{2.1.5}$$

In the case of ground-based dual-Doppler radar, the superscripts in (2.1.2) and (2.1.3) refer to observations from each of the two radars; in the case of airborne pseudo-dual-Doppler radar, the superscripts "1" and "2" refer to the fore and aft radar measurements, respectively.

Equation (2.1.4) is the anelastic form of the mass continuity equation, appropriate for the analysis of deep convection (Ogura and Phillips 1962). Equations (2.1.2) and (2.1.3) are purely based on geometry, relating the observed radial velocities to the Cartesian wind components. The coefficients are:

$$c_1 = \sin a \cos e \tag{2.1.6}$$

$$c_2 = \cos a \cos e \tag{2.1.7}$$

$$c_3 = \sin e \tag{2.1.8}$$

where a is the azimuth angle of the beam (measured clockwise from due north), and e is the elevation angle (measured upward from horizontal). Many papers on dual-Doppler analysis (e.g., Armijo 1969, Shapiro and Mewes 1999) express the geometric coefficients in terms of Cartesian distances from the radars. This is appropriate for radars at fixed sites. However, for moving platforms such as airborne radar, it is necessary to work in terms of angles. Expressing a and e in earth-relative, rather than aircraft-relative, coordinates simplifies the analysis of airborne data (Lee et al. 1994).

An inherent assumption in the dual-Doppler analysis is that velocities are functions of space but not of time. However, since it takes a finite amount of time to collect Doppler observations, and since the observed phenomenon can both move and evolve during this time, the stationarity assumption is not necessarily valid. The total time to scan a storm (~5 min) is similar for both ground-based and airborne radar; however, the time lag between observations for an airborne radar employing FAST is unavoidable. Methods to minimize errors associated with this time lag will be considered in Sections 2.5 and 2.6.

Other error sources particular to airborne radar include antenna pointing errors and increased statistical uncertainty of the Doppler velocities resulting from movement of the radar platform (Jorgensen et al. 1983, Hildebrand et al. 1994). Standard deviations of the radial velocity measurements are ~1.5 m s^{-1}.

One troublesome unknown quantity in the dual-Doppler equations is w_t, the terminal fall velocity of scatterers (usually assumed to be rain or hail). Since precipitation fall speed is not usually an observed quantity, dual-Doppler studies of thunderstorms (e.g., Brandes 1977a, Ray et al. 1981) have historically employed empirical estimates of w_t based on reflectivity. That is the option I have chosen as well, although I have attempted to fine tune the empirical relationship for the McLean storm dataset (Appendix C).

The observed Doppler velocities, less the correction for precipitation fall speed, are defined as V_1 and V_2 in Equations (2.1.2) and (2.1.3); these variables represent the estimated radial velocity of the air corresponding to the measurements for the scatterers ($v_r^{(1)}$ and $v_r^{(2)}$). The difference between *horizontal* air velocity and scatterer velocity is generally considered negligible, although for scans of a strong tornado, that might not be appropriate (Appendix E).

Uncertainty in the vertical density profile for Equation (2.1.4) also introduces error into a dual-Doppler analysis. For simple upward or downward integration of the continuity equation, the error can be significant. However, the wind synthesis methods I will introduce later in this chapter employ two boundary conditions for vertical velocity. In this case, the dual-Doppler analysis is insensitive to the choice of ρ (Ray et al. 1980).

Given estimates of both ρ and w_t, one can solve Equations (2.1.2)-(2.1.4) as a system of three equations with three unknowns (u, v, and w). Two of the equations are algebraic, and the third (continuity) is a first order differential equation. Therefore, the use of one boundary condition yields a unique solution to the equation set. Armijo (1969) was the first to describe a rigorous procedure for solving the dual-Doppler equations. He simplified the procedure by expressing the system of equations in cylindrical coordinates, with the axis of the cylinder oriented along the baseline of the two radars. With this coordinate system, two of the wind components (the components along and perpendicular to the baseline) can be calculated directly from observations. The third component is obtained by integration of the continuity equation along arcs of constant radius from the baseline (Figure B.1).

Given the intersections of fore and aft scans (Figs. 2.1.2, 2.1.3) in circles perpendicular to the flight track, the cylindrical geometry appears to be natural for solving the dual-Doppler equations for airborne radar data (Chong and Testud 1996). However, I prefer to work in Cartesian coordinates instead for several reasons. The first of these is that the Cartesian system is more physical. For example, vertical motions (and vertical gradients) are inherently different from horizontal motions (and horizontal gradients) owing to the vertical density stratification. Cartesian velocities are physically meaningful quantities, and the Cartesian grid structure allows for easy finite-difference estimation of vertical and horizontal derivatives. When velocities are calculated on a cylindrical grid instead, one must generally interpolate the velocities in order to compute vertical and horizontal derivatives.

Another reason why I prefer Cartesian coordinates is that boundary conditions for the solution of the dual-Doppler equations are more easily expressed in Cartesian coordinates (e.g., w=0 at the ground and at the storm top). A third reason is that there are fewer constraints on the scanning geometry. The cylindrical method instead requires a straight radar baseline. This condition is not always satisfied for airborne radar (i.e., when the flight track curved).

Although I choose to work in Cartesian coordinates, I understand the arguments in favor of cylindrical coordinates. Use of the cylindrical geometry simplifies the continuity equation to a partial differential equation of only one unknown variable (Armijo 1969). It also leads to a precise condition for solution uniqueness in the case of over-determined methods (Shapiro and Mewes 1999).

Schneider (1991) applied a quasi-cylindrical technique to dual-Doppler observations of a convective boundary layer. This technique yielded more realistic vertical velocity variances near the top of the boundary layer than Cartesian methods. Several years later, Chong and Testud (1996) argued that the cylindrical coordinate system is preferable because it yields velocities with less small-scale noise than those computed in a Cartesian framework. However, this argument is questionable since their cylindrical coordinate synthesis includes a smoothing constraint that the Cartesian synthesis does not.

In practice, for most dual-Doppler studies of tornadic thunderstorms, the dual-Doppler equations have been solved by iterative procedures in Cartesian coordinates (e.g., Brandes 1977a, 1981, 1984b; Ray et al. 1980; Dowell and Bluestein 1997; Wakimoto et al. 1998). In the "traditional" iterative method (Brandes 1977a, Ray et al. 1980), the radial velocity equations are solved for u and v in terms of the observed quantities and the estimate of w:

$$u = \frac{c_2^{(2)} V_1 - c_2^{(1)} V_2 + \left(c_2^{(1)} c_3^{(2)} - c_3^{(1)} c_2^{(2)}\right) w}{c_1^{(1)} c_2^{(2)} - c_2^{(1)} c_1^{(2)}} \tag{2.1.9}$$

$$v = \frac{c_1^{(1)} V_2 - c_1^{(2)} V_1 + \left(c_3^{(1)} c_1^{(2)} - c_1^{(1)} c_3^{(2)}\right) w}{c_1^{(1)} c_2^{(2)} - c_2^{(1)} c_1^{(2)}}. \tag{2.1.10}$$

The solution in the first iteration is based on a first guess value of w; in the following iterations, vertical velocity is computed from vertical integration of the continuity equation (2.1.4). The velocity estimates at a particular level are successively refined by repeated applications of (2.1.9), (2.1.10), and (2.1.4) until the solution converges; then, the process continues at the next grid level. The solution proceeds either upward or downward from a boundary at which w is specified (e.g., w=0 at the surface or at storm top).

The traditional iterative method converges on a solution if the elevation angles of the data are small and if the horizontal projections of the two beams are not parallel. However, these conditions are not always met for airborne pseudo-dual-Doppler data (including those for the McLean storm). First of all, for dual-Doppler observations directly above and below the flight track, the orientation of the common plane of the fore and aft beams (Fig. 2.1.3) is vertical. In this situation, the denominator in (2.1.9) and (2.1.10) is zero because the earth-relative azimuth angles of the fore and aft beams differ by 180°. Therefore, the solution of Equations (2.1.9) and (2.1.10) is undefined (Chong and Campos 1996). Secondly, the iterative procedure is mathematically unstable for dual-Doppler scans at high incidence angles (Appendix B). The instability arises when $|\theta| > \tan^{-1}\left(\frac{\Delta x}{\Delta z}\right)$, where Δx and Δz are the horizontal and vertical grid spacings, respectively, and θ is the elevation angle of the grid point with respect to the radar baseline (Fig. 2.1.3).

When collecting airborne radar data, one could avoid these geometrical problems by flying the plane far enough away from the storm so that all of the observations are at low elevation angles. However, this solution is not optimal because it sacrifices spatial resolution in the observations. Sperow et al. (1995) describe another method of vertical integration of the continuity equation. In their two-step Lax-Wendroff scheme (Richtmyer and Morton 1967), staggering the w estimates vertically with respect to the grid levels for u and v simplifies the integration process. Their scheme can be used to compute vertical velocities at higher elevation angles than for the traditional iterative method because iteration is not involved. However, repeated applications of the Sperow et al. (1995) method still result in the same instability as for the traditional iterative method.

Even when the traditional iterative method is stable, upward or downward integration is not usually practical since errors in the vertical velocity estimates accumulate significantly (Ray et al. 1980). Relatively small errors in horizontal velocity estimates result in large errors in divergence estimates (and thus vertical velocity estimates). For example, in the McLean storm ELDORA data, computation of vertical velocity by simple upward integration of the continuity equation yields physically implausible values of w (over 200 m s^{-1}) in the upper half of the troposphere (not shown).

Although one can filter the deduced wind fields until the vertical velocities are of a desired magnitude, Ray et al. (1980) suggest that the introduction of new physical constraints into the dual-Doppler analysis is a more attractive approach for obtaining realistic vertical velocity estimates. Many published dual-Doppler analyses of thunderstorms or thunderstorm complexes (e.g., Ray et al. 1980, Brandes et al. 1988, Jorgensen and Smull 1993, Dowell and Bluestein 1997) incorporate two physical constraints on vertical velocity, typically boundary conditions of w=0 at *both* the surface and the top of the storm. The use of boundary conditions at both the bottom and top of the storm requires data through the entire depth of a storm; the ELDORA scanning method (Fig. 2.1.2) naturally produces such data.

The simplest approach for including two boundary conditions on vertical velocity is commonly known as an O'Brien (1970) correction but was originally employed by Lateef (1967). In this method, a linear (in terms of height or pressure) correction is applied to the values of vertical velocity computed from continuity, so that the corrected vertical velocities satisfy both boundary conditions (Lateef 1967, O'Brien 1970).

The introduction of additional physical constraints into a dual-Doppler analysis (such as two boundary conditions on w) makes the problem over-determined; in other words, Equations (2.1.2)-(2.1.4) can no longer all be satisfied exactly. In the case of the O'Brien correction, the synthesized winds still satisfy the radial velocity equations exactly; however, the adjusted vertical velocities satisfy a modified continuity equation (O'Brien 1970):

$$\frac{\partial w}{\partial z} + \kappa w = -\left(\frac{\partial u}{\partial x} + \frac{\partial v}{\partial y} + D\right). \tag{2.1.11}$$

$D(x, y)$ is a correction added to the divergence estimates in each column such that the vertical integral of (2.1.11) satisfies the two boundary conditions for w. In practice, it is simpler to find the solution for w by differentiating Equation (2.1.11) with respect to height, which eliminates D from the equation:

$$\frac{\partial^2 w}{\partial z^2} = -\frac{\partial}{\partial z}\left(\frac{\partial u}{\partial x} + \frac{\partial v}{\partial y} + \kappa w\right). \tag{2.1.12}$$

To obtain a converged solution of Equations (2.1.2), (2.1.3), and (2.1.12) in Cartesian coordinates, one may iteratively adjust the estimates of u, v, and w as in the traditional iterative technique. The use of this scheme (with two boundary conditions for w) minimizes the impact of errors in the observations if the error distribution is constant with height. However, this method still suffers from the geometrical limitations of the traditional formulation. An iterative solution of Equations (2.1.2), (2.1.3), and (2.1.12) will not converge unless the elevation angles are low enough to satisfy the same stability constraint (Appendix B) as in iterative upward or downward integration.

A desire to find solutions of the dual-Doppler equations that satisfy prescribed boundary conditions and that converge even for high elevation angles has fueled recent interest in application of 3D variational methods to the problem. Variational methods will be considered in Sections 2.3 and 2.4, but a brief summary is given here. Variational techniques (Sasaki 1970) are useful when enough constraints (e.g., w=0 at both the top and bottom of the domain) are included in the dual-Doppler analysis so that the problem is overdetermined.

Scialom and Lemaitre (1990) tackled the dual-Doppler synthesis problem by expressing the wind components in terms of pre-determined analytic functions. Their variational problem consists of finding coefficients which, in a least squares sense over the whole domain, cause the analytic functions to best satisfy the radial velocity observations, continuity, and the boundary condition at the ground. In this scheme, all constraints are satisfied approximately.

Gamache (1997) also formulated the dual-Doppler wind synthesis as a variational problem. The goal of his method, like that of Scialom and Lemaitre (1990), is to find velocities that best satisfy the radial velocity equations and continuity over the whole domain. However, Gamache's (1997) technique, like the traditional dual-Doppler methods, imposes no restriction on the functional form of the velocities. The variational dual-Doppler method of Bousquet and Chong (1998) has a similar formulation to that of Gamache (1997) but differs in solution technique.

Shapiro and Mewes (1999) describe a general set of variational schemes for dual-Doppler wind synthesis. In the first of these, the radial velocity equations are satisfied exactly ("strong constraints") while mass continuity is satisfied approximately ("weak constraint"). The opposite is the case in the second method, in which continuity is a strong constraint and the radial wind observations are weak constraints. In their third method, all constraints are satisfied weakly, in the same manner as for Scialom and Lemaitre (1990) and Gamache (1997). Shapiro and Mewes (1999) derived algorithms for solving the three variational problems in cylindrical coordinates. In contrast, the discussion in Sections 2.3 and 2.4 will focus on methods in Cartesian coordinates.

The goal of the work described in the rest of this chapter is to answer the following questions:

- How may one find a solution of the dual-Doppler equations in Cartesian coordinates that, like the traditional method, satisfies the radial velocity equations exactly but that is not restricted by the scanning geometry?
- How does a dual-Doppler analysis with all weak constraints (Gamache 1997, Shapiro and Mewes 1999) compare to such a method, with and without errors in the observations?
- How may one minimize the impact of movement and evolution of the observed features between the times of the fore and aft radar observations?

The wide range of incidence angles of the beams presents a challenge in the analysis of ELDORA data from VORTEX. In contrast, previous ground-based dual-Doppler studies of tornadic storms (e.g., Brandes 1977b, 1981, 1984b; Dowell and Bluestein 1997) have relied on data at relatively low elevation angles only. After introducing test cases used to evaluate the dual-Doppler methods (Section 2.2), I address the first question above

(Section 2.3). The 3D variational formulation with the radial velocity equations satisfied exactly and continuity satisfied approximately is original but is quite similar to that developed concurrently by Shapiro and Mewes (1999).

In Section 2.4, I describe the formulation of the weak constraint method and compare it to the method in Section 2.3. It is difficult to quantify the magnitude of errors in real airborne Doppler observations. However, when even small errors are present in the observations, the weak constraint dual-Doppler synthesis gives a more accurate wind field than the method in which the radial velocity equations are satisfied exactly. The most original contributions described in Section 2.4 are the comparison of the two variational methods and the demonstration of how the weak-constraint synthesis depends on the relative weighting factor.

The discussion in Sections 2.5 and 2.6 centers on the issue of temporal errors (movement and evolution). The spatial resolution in the ELDORA observations of the McLean storm is greater than in the ground-based datasets mentioned above, but the non-simultaneity is more severe. I tried two new methods for handling the non-simultaneity problem. The more productive of these for ELDORA data from VORTEX was to choose an optimal reference frame for the dual-Doppler analysis.

This chapter concludes (Section 2.7) with a summary of how I applied the pseudo-dual-Doppler methodology to the McLean storm case.

2.2 Test Cases

Verification of the dual-Doppler methods described in the following sections requires knowledge of the exact wind fields to which to compare the synthesized dual-Doppler winds. Since the "truth" is not known for real observations, I instead test the synthesis methods with simulated radar data. A dual-Doppler analysis of simulated radar data involves sampling each point within a precisely known wind field from two different viewing angles and then reconstructing the 3D wind field from the simulated radar observations.

Some of the tests in later sections employ analytic wind fields, that is, specifications of velocities that satisfy mass continuity and that vary spatially according to some mathematical function. The analytic wind field ("test case A") I will use for several tests is that of Sperow et al. (1995):

$$u = \overline{U}\sin\left(\frac{2\pi x}{L_H}\right)\cos\left(\frac{2\pi y}{L_H}\right)\cos\left(\frac{2\pi z}{L_V}\right) \tag{2.2.1}$$

$$v = \overline{U}\cos\left(\frac{2\pi x}{L_H}\right)\sin\left(\frac{2\pi y}{L_H}\right)\cos\left(\frac{2\pi z}{L_V}\right) \tag{2.2.2}$$

$$w = -2\overline{U}\frac{L_V}{L_H}\cos\left(\frac{2\pi x}{L_H}\right)\cos\left(\frac{2\pi y}{L_H}\right)\sin\left(\frac{2\pi z}{L_V}\right) \tag{2.2.3}$$

where $\overline{U}$ is the amplitude of the horizontal wind, L_H is the horizontal wavelength, and L_V is the vertical wavelength. This wind field, which satisfies Boussinesq mass continuity, consists of a checkerboard pattern of updrafts and downdrafts with corresponding horizontal winds containing both divergence and deformation (Fig. 2.2.1). I chose this analytic wind field because it contains significant gradients in vertical velocity (as in real thunderstorms) and is readily adjustable by wavelength.

The domain for the Sperow et al. (1995) test case is 20 km wide, is 10 km tall, and has a grid spacing of 500 m in both the horizontal and vertical. I selected a constant vertical wavelength L_V of 10 km and varied the horizontal wavelength L_H for the tests. I varied the magnitude of $\overline{U}$ according to the horizontal wavelength ($\overline{U}$ =10 m s^{-1} for L_H =5 km, $\overline{U}$ =20 m s^{-1} for L_H =10 km, and $\overline{U}$ =40 m s^{-1} for L_H =20 km) so that the maximum vertical velocity (40 m s^{-1}) in each case would be identical.

The simulated pseudo-dual-Doppler samples of this and the following wind fields are like those collected by an aircraft flying eastward and westward 5 km to the south of the domain at 1.0 km AGL. The simulated aircraft tilt angle is 20°. With the specified scanning geometry, the elevation angles of the observations in the Sperow wind field are as great as 60°, which means that a traditional iterative dual-Doppler analysis would not converge to a solution. Unlike real data, the fore and aft scans of the Sperow wind field are effectively instantaneous and simultaneous (since there is no time dependence in Equations 2.2.1-2.2.3).

Although it is easy to create wind fields that satisfy mass continuity, it is not easy to find analytic solutions that also satisfy the non-linear equations of motion. Shapiro (1993) describes some of the few known time-dependent analytic solutions of the equations of motion. This limited class of solutions is useful for understanding the ability of a dual-Doppler technique to resolve wind fields of varying complexity. Analytic wind fields can also be used to examine the impact of local time rates of change in the velocities resulting from advection. However, I am unaware of an analytic wind field that both satisfies the equations of motion and appropriately represents true evolution like that in thunderstorms (i.e., formation and dissipation of updrafts and downdrafts).

The second class of test cases for the dual-Doppler syntheses in the following sections consists of output from a numerical cloud model. Numerical thunderstorm simulations can contain evolution on time and space scales similar to those in supercell thunderstorms, and they are therefore ideal test cases (Clark et al. 1980) for the present study. I selected two numerical simulations as test cases for the dual-Doppler synthesis methods; each was produced with the Klemp and Wilhelmson (1978) model.

The first numerical model test case (test case B: "Colliding Cold Pools") is a simulation of the descent of four Gaussian spheres of cold air, followed by the subsequent spreading out and collision of the cold air near the surface (Fig. 2.2.2). I initialized this simulation of dry dynamics with the cold bubbles (maximum temperature perturbation of −20 K) centered at 3.0 km AGL. The domain for this simulation is shallow (5 km tall but 20 km wide) and is represented by a grid with horizontal and vertical resolutions of 500 m and 250 m, respectively. I included strong vertical wind shear in the model initialization so that regions of local cyclonic and anticyclonic vertical vorticity would quickly be produced by tilting within downdrafts and updrafts; the initialization wind profile matches that in the McLean storm environment (Fig. 1.4). I selected test case B for the dual-Doppler synthesis tests because it contains high resolution, rapid evolution, multiple vertical velocity maxima/minima, sharp low-level boundaries, and a variety of characteristic translation velocities.

Some of the dual-Doppler tests are for simulated fore and aft observations that are simultaneous and instantaneous. For other tests, the fore and aft observations are based on model output at two different times. The use of two model times imitates the time lag in real observations. Since the goal in Sections 2.5 and 2.6 will be primarily to examine the impact of this time lag, rather than the total time required to scan a volume, all fore observations are assumed to be instantaneous, and all aft observations are assumed to be instantaneous (but at a later time).

For ELDORA data from VORTEX, the time lag between observations is ~120 s, while the time between consecutive aircraft passes of a storm is ~300 s. Since the test case B simulation evolves on a more rapid time scale than these times, I scaled down the time lag between observations and the time between passes for the simulated data while maintaining the same ratio between the two (5:2). For the dual-Doppler analyses of non-simultaneous test case B observations, the times between passes and times between fore and aft observations in each pass are 200 s and 80 s, respectively.

One drawback of using cloud-model test cases is that the numerical model employs a different grid from that of the dual-Doppler analysis. In the Klemp and Wilhelmson (1978) model, the u, v, and w wind components are staggered one-half grid point east/west, north/south, and up/down of the center of the grid box, respectively. In contrast, in the dual-Doppler analysis, the velocities are collocated at each grid point. To determine the wind components for simulated Doppler sampling and for verification of the Doppler analyses, I interpolated the model velocities to common grid points. This interpolation from the staggered grid to the regular grid introduces some uncertainty into the verification of the dual-Doppler analyses, since the interpolated winds do not necessarily satisfy continuity.

The second numerical model test case (test case C: "Line of Storms") is from Bluestein and Weisman (1999). The convective-storm simulation begins with a series of warm bubbles along a north-south oriented line in an environment in which the vertical shear of the horizontal wind is perpendicular to the line of initiation (increasing westerlies with height). This configuration favors isolated supercells at the ends of the line and collisions of left-moving and right-moving cells in between (Bluestein and Weisman 1999). The horizontal grid spacing of the simulation is 1000 m, and the vertical spacing varies from 250 m at low levels to 750 m at the top of the domain.

Since the test case C domain is very large, I only selected a portion of the domain (the southern end of the line) for the dual-Doppler tests (Fig. 2.2.3). In this portion, there is a relatively steady cell at the southern end of the line (near x=17, y=10 in Fig. 2.2.3.a). Farther north, there is a new cell (x=27, y=27 in Fig. 2.2.3.a) developing along the surface gust front. Even farther north, a left-moving (x=24, y=37 in Fig. 2.2.3.a) and a right-moving (x=20, y=44 in Fig. 2.2.3.a) cell are colliding; the result is a single cell (x=26, y=43 in Fig. 2.2.3.b).

I selected test case C because it contains more evolution than a typical classic supercell simulation. (However, evolution still does not occur as quickly as in the McLean storm.) For the dual-Doppler analyses of non-simultaneous test case C observations, the times between passes and times between fore and aft observations are similar to those for VORTEX data: 300 s and 120 s, respectively.

For both of the numerical simulation test cases, portions of the domain contain relatively uniform winds. Instead of including these portions, I instead selected smaller regions with significant velocity gradients when computing error statistics. The windowed regions for the statistics are outlined in Fig. 2.2.2 and 2.2.3.

2.3 Strong Constraint Dual-Doppler Analysis Scheme

2.3.1 Formulation

In 1997, I began to work on a 3D variational dual-Doppler analysis method with two boundary conditions on w in which the radial velocity equations are satisfied exactly (i.e., as "strong constraints"). Shapiro and Mewes (1999) independently developed a similar formulation around the same time. The method is reminiscent of a traditional dual-Doppler synthesis with an O'Brien (1970) correction. An advantage of the variational scheme in this section over the traditional method is that it will converge on a solution even when there are data at high elevation angles. Ziegler (1978) was perhaps the first to design a variational dual-Doppler scheme with two boundary conditions. However, the variational adjustment in his technique is a separate process that follows the wind synthesis.

In the strong-constraint formulation, the 2D velocity components within some plane are known directly from the observations at each point (Fig. 2.1.3). The orientation of this plane is that which contains the dual-Doppler beams that intersect at the grid point.

The Doppler measurements can be represented as vectors:

$$\vec{V}_1 = V_1\left(c_1^{(1)}\hat{i} + c_2^{(1)}\hat{j} + c_3^{(1)}\hat{k}\right) \tag{2.3.1}$$

$$\vec{V}_2 = V_2\left(c_1^{(2)}\hat{i} + c_2^{(2)}\hat{j} + c_3^{(2)}\hat{k}\right) \tag{2.3.2}$$

where V_1 and V_2 are the magnitudes of the radial air velocity in the fore and aft measurements, and the geometric coefficients (c_1, c_2, c_3) are as defined in Equations (2.1.6)-(2.1.8). For the strong-constraint formulation, the essence of the dual-Doppler wind synthesis is to determine a third velocity component, the unknown component V_n oriented in a direction normal to the common plane of the dual-Doppler observations (Fig. 2.1.3). This component, as represented by a vector, is

$$\vec{V}_n \equiv V_n\hat{n} \equiv V_n\left(n_1\hat{i} + n_2\hat{j} + n_3\hat{k}\right) \equiv V_n\frac{\vec{N}}{|\vec{N}|} \tag{2.3.3}$$

where

$$\begin{aligned}\vec{N} &\equiv \left(c_1^{(1)}\hat{i} + c_2^{(1)}\hat{j} + c_3^{(1)}\hat{k}\right)\times\left(c_1^{(2)}\hat{i} + c_2^{(2)}\hat{j} + c_3^{(2)}\hat{k}\right) \\ &= \left(c_2^{(1)}c_3^{(2)} - c_3^{(1)}c_2^{(2)}\right)\hat{i} + \left(c_3^{(1)}c_1^{(2)} - c_1^{(1)}c_3^{(2)}\right)\hat{j} + \left(c_1^{(1)}c_2^{(2)} - c_2^{(1)}c_1^{(2)}\right)\hat{k}.\end{aligned} \tag{2.3.4}$$

In the determination of V_n, the way I proposed setting up the problem was to seek the velocities that satisfy mass continuity in a least squares sense over the domain while still satisfying the radial velocity equations exactly. The velocities that meet this requirement are associated with the minimum of a functional defined by

$$J = \iiint_{R^{(3)}} \left[\begin{array}{l}\lambda_1\left(c_1^{(1)}u + c_2^{(1)}v + c_3^{(1)}w - V_1\right) + \lambda_2\left(c_1^{(2)}u + c_2^{(2)}v + c_3^{(2)}w - V_2\right) \\ + \left(\dfrac{\partial u}{\partial x} + \dfrac{\partial v}{\partial y} + \dfrac{\partial w}{\partial z} + \kappa w\right)^2\end{array}\right] dx\,dy\,dz \tag{2.3.5}$$

where λ_1 and λ_2 are Lagrange multipliers, and $R^{(3)}$ is a bounded three-dimensional domain. The initial steps in the derivation of the solution are identical to those of Shapiro and Mewes (1999).

A local (and potentially a global) minimum in J occurs where the variations of J with respect to u, v, and w are all zero. The variation with respect to u is

$$\delta_u J = \iiint_{R^{(3)}} \left[\lambda_1 c_1^{(1)} \delta u + \lambda_2 c_1^{(2)} \delta u + 2\left(\frac{\partial u}{\partial x} + \frac{\partial v}{\partial y} + \frac{\partial w}{\partial z} + \kappa w \right) \frac{\partial(\delta u)}{\partial x} \right] dx dy dz \\ = 0. \tag{2.3.6}$$

This expression can be simplified by integrating the third term by parts:

$$\delta_u J = \iiint_{R^{(3)}} \delta u \left(\lambda_1 c_1^{(1)} + \lambda_2 c_1^{(2)} \right) dx dy dz + \iint_{R^{(2)}} \left[2\left(\frac{\partial u}{\partial x} + \frac{\partial v}{\partial y} + \frac{\partial w}{\partial z} + \kappa w \right) \delta u \right]_{x_{west}}^{x_{east}} dy dz \\ - \iiint_{R^{(3)}} 2\delta u \frac{\partial}{\partial x}\left(\frac{\partial u}{\partial x} + \frac{\partial v}{\partial y} + \frac{\partial w}{\partial z} + \kappa w \right) dx dy dz \\ = 0. \tag{2.3.7}$$

The double integral term can be eliminated by either of two natural boundary conditions: u is specified (and thus δu=0) at the east and west boundaries of the domain, or the mass continuity equation is satisfied exactly at these sides. In the application of the strong-constraint method to the test cases and real data, I will choose the latter boundary condition. However, it is conceivable that for some applications, the former boundary condition would be more desirable.

I enforce the mass-continuity condition at the sides by expanding the grid of u velocities by one layer on both the west and east sides. In each step of the solution method, I choose u values outside the edges such that the centered finite-difference form of the continuity equation is satisfied exactly at every point along the actual west and east sides of the domain. The dual-Doppler technique uses these extra velocities beyond the analysis domain, but I discard them at the end of the procedure.

With the double integral term eliminated, Equation (2.3.7) becomes

$$\delta_u J = \iiint_{R^{(3)}} \delta u \left[\lambda_1 c_1^{(1)} + \lambda_2 c_1^{(2)} - 2\frac{\partial}{\partial x}\left(\frac{\partial u}{\partial x} + \frac{\partial v}{\partial y} + \frac{\partial w}{\partial z} + \kappa w\right)\right] dxdydz \tag{2.3.8}$$
$$= 0.$$

For Equation (2.3.8) to be zero for arbitrary δu, the term in brackets must be identically zero; this gives the first Euler-Lagrange equation:

$$\lambda_1 c_1^{(1)} + \lambda_2 c_1^{(2)} = 2\frac{\partial}{\partial x}\left(\frac{\partial u}{\partial x} + \frac{\partial v}{\partial y} + \frac{\partial w}{\partial z} + \kappa w\right). \tag{2.3.9}$$

The second Euler-Lagrange equation is found in a similar manner. By taking the variation of J in Equation (2.3.5) with respect to v, using natural boundary conditions on the north and south sides, and solving for the case in which the variation is zero, one may obtain

$$\lambda_1 c_2^{(1)} + \lambda_2 c_2^{(2)} = 2\frac{\partial}{\partial y}\left(\frac{\partial u}{\partial x} + \frac{\partial v}{\partial y} + \frac{\partial w}{\partial z} + \kappa w\right). \tag{2.3.10}$$

The natural boundary conditions are that either v is specified on the north and south sides of the domain, or that continuity is satisfied exactly on these sides. With a similar procedure to that for computing u, I choose the latter option by expanding the grid of v velocities on both the north and south sides. I calculate the values of v at the grid points just outside the domain by solving the finite-difference form of the continuity equation centered at grid points along the north and south sides. As mentioned previously, I discard the extra layers of velocities at the end.

The third Euler-Lagrange equation is obtained by taking the variation of J in Equation (2.3.5) with respect to w, employing natural boundary conditions, and solving for the case in which the variation is zero:

$$\lambda_1 c_3^{(1)} + \lambda_2 c_3^{(2)} = 2\left(-\kappa + \frac{\partial}{\partial z}\right)\left(\frac{\partial u}{\partial x} + \frac{\partial v}{\partial y} + \frac{\partial w}{\partial z} + \kappa w\right) \tag{2.3.11}$$

In this case, there is an extra term involving κ. The boundary conditions that simplified the derivation of Equation (2.3.11) are either that w is specified at the bottom and top of the domain, or that continuity is satisfied exactly there. For w, I will choose the former option, specifying w=0 at the surface and at the top of the domain (or top of the storm). With these boundary conditions, the strong-constraint variational method is similar to a traditional dual-Doppler synthesis employing an O'Brien (1970) correction. However, the strong-constraint method is based on a global minimization of how well the continuity equation is satisfied, whereas the O'Brien adjustment is based on a column-by-column adjustment without regard for how individual columns are related.

At this point, the solution technique will diverge from that of Shapiro and Mewes (1999). The strong-constraint method described below is an iterative method applied in Cartesian coordinates. In contrast, Shapiro and Mewes (1999) solve the Euler-Lagrange equations in cylindrical coordinates.

Equations (2.1.2), (2.1.3), (2.3.9), (2.3.10), and (2.3.11) are a system of five equations and five unknowns (u, v, w, λ_1, and λ_2). A more useful form is obtained by algebraic elimination of the λ terms, resulting in one equation relating three unknowns (u, v, and w):

$$\begin{aligned}\left(c_2^{(1)}c_3^{(2)} - c_3^{(1)}c_2^{(2)}\right)\frac{\partial}{\partial x}\left(\frac{\partial u}{\partial x} + \frac{\partial v}{\partial y} + \frac{\partial w}{\partial z} + \kappa w\right) + \left(c_3^{(1)}c_1^{(2)} - c_1^{(1)}c_3^{(2)}\right)\frac{\partial}{\partial y}\left(\frac{\partial u}{\partial x} + \frac{\partial v}{\partial y} + \frac{\partial w}{\partial z} + \kappa w\right) \\ + \left(c_1^{(1)}c_2^{(2)} - c_2^{(1)}c_1^{(2)}\right)\left(-\kappa + \frac{\partial}{\partial z}\right)\left(\frac{\partial u}{\partial x} + \frac{\partial v}{\partial y} + \frac{\partial w}{\partial z} + \kappa w\right) = 0.\end{aligned} \tag{2.3.12}$$

The coefficients in Equation (2.3.12) are simply those of $\vec{N}$ in Equation (2.3.4). Dividing Equation (2.3.12) by $\left|\vec{N}\right|$, one obtains

$$n_1\frac{\partial}{\partial x}\left(\frac{\partial u}{\partial x}+\frac{\partial v}{\partial y}+\frac{\partial w}{\partial z}+\kappa w\right)+n_2\frac{\partial}{\partial y}\left(\frac{\partial u}{\partial x}+\frac{\partial v}{\partial y}+\frac{\partial w}{\partial z}+\kappa w\right)$$
$$+n_3\left(-\kappa+\frac{\partial}{\partial z}\right)\left(\frac{\partial u}{\partial x}+\frac{\partial v}{\partial y}+\frac{\partial w}{\partial z}+\kappa w\right)=0. \tag{2.3.13}$$

This equation is inherently cylindrical, as it describes the gradient of 3D divergence in the solution along coplane azimuthal coordinate curves. This is perhaps a strong argument for why the solution should be obtained in cylindrical coordinates (Shapiro and Mewes 1999). Nevertheless, I will forge ahead in Cartesian coordinates. Equation (2.3.13) is a simple partial differential equation in terms of 3D divergence, and a solution of it would be direct if boundary conditions were known in advance. However, it is not known initially what divergence values will eventually allow the other constraints to be satisfied.

Finding a Cartesian solution method that satisfies Equations (2.1.2), (2.1.3), and (2.3.13) is difficult. However, I have found that the following algorithm converges on a solution. This algorithm requires repeated transformations between the velocity components of the local coordinate system at each grid point (V_1, V_2, and V_n) and the Cartesian velocity components (u, v, and w).

1. Initialize V_1 and V_2 from observations. Set V_n=0.
2. Compute Cartesian velocities corresponding to the current values of V_1, V_2, and V_n from the following system of equations:

$$c_1^{(1)}u + c_2^{(1)}v + c_3^{(1)}w = V_1$$
$$c_1^{(2)}u + c_2^{(2)}v + c_3^{(2)}w = V_2$$
$$n_1 u + n_2 v + n_3 w = V_n.$$

3. Update side boundary conditions.
4. Compute new estimates of V_n with one of the following options. (The method for choosing the best option is described later.)
   a. Compute $u^{(new)}$ with Equation (2.3.14) below. Then,

$$V_n^{(new)} = n_1 u^{(new)} + n_2 v^{(old)} + n_3 w^{(old)}.$$

b. Compute $v^{(new)}$ with Equation (2.3.15) below. Then,

$V_n^{(new)} = n_1 u^{(old)} + n_2 v^{(new)} + n_3 w^{(old)}$.

c. Compute $w^{(new)}$ with Equation (2.3.16) below. Then,

$V_n^{(new)} = n_1 u^{(old)} + n_2 v^{(old)} + n_3 w^{(new)}$.

5. Repeat the process beginning at step 2 if the solution has not converged sufficiently.

The estimates of $u^{(new)}$, $v^{(new)}$, and $w^{(new)}$ are obtained from Equation (2.3.13) by expanding the finite difference forms of the second derivatives of u with respect to x, of v with respect to y, and of w with respect to z:

$$u^{(new)} = \frac{(\Delta x)^2}{2}\left[\begin{array}{r}\dfrac{u_{i-1}+u_{i+1}}{(\Delta x)^2} + \dfrac{\partial}{\partial x}\left(\dfrac{\partial v}{\partial y} + \dfrac{\partial w}{\partial z} + \kappa w\right) + \dfrac{n_2}{n_1}\dfrac{\partial}{\partial y}\left(\dfrac{\partial u}{\partial x} + \dfrac{\partial v}{\partial y} + \dfrac{\partial w}{\partial z} + \kappa w\right) \\ + \dfrac{n_3}{n_1}\left(-\kappa + \dfrac{\partial}{\partial z}\right)\left(\dfrac{\partial u}{\partial x} + \dfrac{\partial v}{\partial y} + \dfrac{\partial w}{\partial z} + \kappa w\right)\end{array}\right] \tag{2.3.14}$$

$$v^{(new)} = \frac{(\Delta y)^2}{2}\left[\begin{array}{r}\dfrac{n_1}{n_2}\dfrac{\partial}{\partial x}\left(\dfrac{\partial u}{\partial x} + \dfrac{\partial v}{\partial y} + \dfrac{\partial w}{\partial z} + \kappa w\right) + \dfrac{v_{j-1}+v_{j+1}}{(\Delta y)^2} + \dfrac{\partial}{\partial y}\left(\dfrac{\partial u}{\partial x} + \dfrac{\partial w}{\partial z} + \kappa w\right) \\ + \dfrac{n_3}{n_2}\left(-\kappa + \dfrac{\partial}{\partial z}\right)\left(\dfrac{\partial u}{\partial x} + \dfrac{\partial v}{\partial y} + \dfrac{\partial w}{\partial z} + \kappa w\right)\end{array}\right] \tag{2.3.15}$$

$$w^{(new)} = \frac{1}{\kappa^2 - \dfrac{\partial \kappa}{\partial z} + \dfrac{2}{(\Delta z)^2}}\left[\begin{array}{r}\dfrac{n_1}{n_3}\dfrac{\partial}{\partial x}\left(\dfrac{\partial u}{\partial x} + \dfrac{\partial v}{\partial y} + \dfrac{\partial w}{\partial z} + \kappa w\right) + \dfrac{n_2}{n_3}\dfrac{\partial}{\partial y}\left(\dfrac{\partial u}{\partial x} + \dfrac{\partial v}{\partial y} + \dfrac{\partial w}{\partial z} + \kappa w\right) \\ + \dfrac{w_{k-1}+w_{k+1}}{(\Delta z)^2} + \left(-\kappa + \dfrac{\partial}{\partial z}\right)\left(\dfrac{\partial u}{\partial x} + \dfrac{\partial v}{\partial y}\right)\end{array}\right] \tag{2.3.16}$$

The other derivative terms are also computed from centered finite differences; however, the partial derivative notation has been maintained to keep the equations compact.

The strategy I use in step 4 of the algorithm is essentially to compute V_n by updating the estimate of the most poorly observed Cartesian wind component. For example, if the direction of $\hat{n}$ is within 35° of the orientation of x axis, then u is the most poorly observed velocity component. Therefore, I would update V_n with option "a" in step 4. In some cases, though, the choice is not clear cut. For example, with an east-west oriented baseline and a scan at a 45° elevation angle, V_n contains significant contributions from both v and w. An arbitrary choice of the component to be updated can lead to a solution that blows up. In such situations, my program chooses the option in step 4 (either "b" or "c" in this case) that produces the minimum change in V_n relative to the previous estimate. This maintains the stability of the algorithm while still allowing it to converge on the solution that minimizes the cost function.

Although the strong-constraint solution just described is obtained in Cartesian coordinates, it is important to keep in mind the cylindrical nature of the data (Fig. 2.3.1). Equation (2.3.13) is a relationship describing the derivative of 3D divergence in the direction $\hat{n}$. The direction $\hat{n}$ is simply the direction of coplane azimuthal coordinate curves (i.e., curves of constant radius from the radar baseline) along which integration of the continuity equation in cylindrical coordinates would occur (Armijo 1969, Shapiro and Mewes 1999). For a Cartesian domain, some of these lines are bounded on two sides, while others are not. For example, in Fig. 2.3.1, the coplane azimuthal coordinate line on the right is bounded at both the lower surface and the storm top by the w=0 boundary conditions. This is not true for the curve on the left, which is bounded at the bottom of the domain but which passes out the side of the domain beneath the storm top.

I was concerned that the presence of coplane azimuthal curves with less than two bounds would result in implausible velocity values on the unbounded side of the domain (i.e., large values of v in the upper south portion of the domain) in the test cases and real data. Although v did tend to be noisy there, the velocities did not grow to extreme values. I believe this is an indication of smoothing of the underlying cylindrical geometry by the Cartesian representation of the solution. For real data especially, the curves parallel to $\hat{n}$ follow contorted paths among the grid points, and these cannot be represented properly by the Cartesian finite differences.

One last note is necessary for the upper and lower boundaries. In certain situations, the specification of w=0 at these levels may be inconsistent with the radial velocity equations. For example, for observations directly above the flight track, the common plane of the dual-Doppler observations (Fig. 2.1.3) is vertical. Therefore, the vertical velocity can be determined unambiguously by the observations. For such observations at the upper boundary of the domain, this vertical velocity value may or may not agree with the specified upper boundary condition (w=0). Although the strong constraint solution satisfies the radial velocity equations exactly in the interior of the domain, it does not necessarily do so at the upper and lower boundaries.

2.3.2 Tests

The strong-constraint dual-Doppler algorithm converged to solutions for all three test cases (the Sperow analytic wind field and the two numerical simulations). Error statistics for the synthesized wind fields are shown in Tables 2.1-2.3. (The tables also include results for comparison from other wind synthesis methods, including a weak constraint method described in Section 2.4.) For test case B, the solution converged in 200 iterations to the point where the statistics did not change further. Test cases A and C required 500 iterations.

Error statistics for wind syntheses with upward and downward integration of the continuity equation are also given in Tables 2.1-2.3. The test cases (except for the shallow test case B) contain radial velocities at high elevation angles on the upper south side of the domain, and therefore the traditional iterative wind synthesis is unstable for these cases. Therefore, I used the Sperow et al. (1995) method of integrating the continuity equation.

For the experiments in Tables 2.1-2.3, the simulated fore and aft observations are simultaneous and instantaneous. The first experiments for each test case are for "error free" observations. Errors in the wind syntheses for the Sperow analytic wind field in these experiments are associated with inadequate representation of the continuous functions on the discrete grid. Errors in the wind syntheses for the numerical simulations are associated with interpolation error from the staggered model grid to the regular Doppler analysis grid.

The later experiments include random noise with a standard deviation of 1.5 m s^{-1} added to the radial velocities. To generate the random noise, I used a standard random number generator (Sedgewick 1988) to generate a series of numbers between 0 and 1. Interpreting each random number as the cumulative probability distribution of a normal curve with a standard deviation of 1.5 m s^{-1}, I created a series of velocity perturbations corresponding to the random cumulative probabilities. I then added this series of velocity perturbations to the series of gridded radial velocity values to produce the set of simulated noisy observations.

It is difficult to simulate adequately errors associated with real radar observations. The 1.5 m s^{-1} value is typical of random errors in airborne Doppler measurements (Jorgensen et al. 1983, Hildebrand et al. 1994). Although truly random small-scale errors are smoothed out in objective analysis and other filtering in a dual-Doppler wind synthesis, the bias errors (e.g., from antenna pointing errors) remain. The 1.5 m s^{-1} random noise should provide insight into how the dual-Doppler methods handle small-scale, unphysical features in the data, but it is likely an underestimate of the amount of total error in real data.

The winds in the strong-constraint variational synthesis satisfy the observations exactly. The same is true for the traditional synthesis methods (upward or downward integration), which include only one boundary condition for w. With the specified geometry, u is the along-track velocity component and therefore is exactly determined by the observations. Thus, errors in u are identical for all three analysis methods.

The larger errors for downward integration (experiments 2 and 6 in Tables 2.1.a-2.1.c) than for upward integration (experiments 1 and 5) in the Sperow test case are contrary to the usual notion that downward integration is preferable to upward integration (Ray et al. 1980). There are two reasons for this. First, the Sperow wind field is a flow with constant density; therefore, errors do not damp with downward integration as in the case of atmospheric flows with a density stratification (Ray et al. 1980). Secondly, the high incidence angles in the upper south portion of the domain result in significant errors in the estimates of v. These initial errors are carried downward through the depth of the domain during the integration.

As expected, for the experiments with noise, the strong-constraint method is superior to upward and downward integration, especially in the estimation of w, for all three test cases. The strong-constraint formulation contains more physical information about the solution (two boundary conditions for w) than the latter two methods (one boundary condition for w). A comparison of the w error at low levels only (the last column in the tables) for upward integration versus the strong-constraint methods reveals that the most significant improvement in w with the strong-constraint method is occurring higher up. The magnitude of improvement offered by the strong-constraint method does not appear to vary significantly with horizontal wavelength (experiments 5-7 in Tables 2.1.a-2.1.c).

A more interesting question is whether the strong-constraint method is better than the traditional method with an O'Brien (1970) correction, since these two methods use identical boundary conditions. The shallow domain of test case B contains observations at low enough elevation angles such that the O'Brien method converges on a solution. For the experiments with "error free" observations, the analysis with the O'Brien method (experiment 3 in Table 2.2) does not differ significantly from that with the strong-constraint method (experiment 4). However, with errors in the observations, the strong-constraint method yields over 7% improvement (domain-averaged) in the estimates of w compared to the O'Brien method.

Experiments 9 and 10 in Table 2.3 test whether the same is true for observations of a deeper flow. These experiments are like the others for test case C (the numerical simulation of the line of storms), except that the wind field was sampled as if by an aircraft farther from the domain (flying along y=-15 km at z=1 km). With this geometry, all elevation angles are below 45°. In these experiments, the strong-constraint method is again superior to the O'Brien method, offering 11% and 23% improvements in the estimates of v and w, respectively. This may be a reflection of the fact that the variational formulation involves a global minimization of how well the continuity equation is satisfied, whereas the O'Brien formulation does not.

2.4 Weak Constraint Dual-Doppler Analysis Scheme

2.4.1 Formulation

Gamache (1997) and Shapiro and Mewes (1999) describe a formulation of the dual-Doppler problem in which the radial velocity and continuity equations are all satisfied approximately (i.e., as weak constraints):

$$J = \iiint_{R^{(3)}} \left[\begin{array}{l} \left(c_1^{(1)}u + c_2^{(1)}v + c_3^{(1)}w - V_1\right)^2 + \left(c_1^{(2)}u + c_2^{(2)}v + c_3^{(2)}w - V_2\right)^2 \\ + \beta\left(\frac{\partial u}{\partial x} + \frac{\partial v}{\partial y} + \frac{\partial w}{\partial z} + \kappa w\right)^2 \end{array} \right] dx\,dy\,dz \tag{2.4.1}$$
$$= \text{minimum}.$$

In the above cost function, the weights of the geometric equations for the two radars are identical. The constant multiplier β determines the weight given to the continuity equation relative to the radial velocity equations. The motivation for this scheme is that the most accurate solution is one that does not exactly satisfy the observations, which contain errors. In contrast, the solution precisely matches the observations in the strong-constraint formulation.

The weak-constraint formulation appears in other recent publications in more elaborate forms. Bousquet and Chong's (1998) method is essentially a 3D weak-constraint technique, even though they obtain the solution on a plane-by-plane basis. Bousquet and Chong (1998) include a Laplacian velocity smoother in the cost functional, as originally proposed by Gamache (1997). They also incorporate weighted interpolation of observations directly into the cost functional, and thus, the objective analysis and wind synthesis are not separate as in traditional methods. Gao et al.'s (1999) variational dual-Doppler formulation is similar to Bousquet and Chong's (1998) but does include one additional feature. The general framework described by Gao et al. (1999) also allows one to give weight in the solution to a background field when measurements are available from independent sources.

Shapiro and Mewes (1999) solve the Euler-Lagrange equations associated with (2.4.1) in cylindrical coordinates. In contrast, Gamache (1999, personal communication) obtains the velocities that minimize Equation (2.4.1) in Cartesian coordinates by a matrix method. I will adopt Gamache's procedure of working in Cartesian coordinates but will instead solve the Euler-Lagrange equations iteratively.

The variation of J with respect to u, which must be zero at a minimum in J, is

$$\delta_u J = \iiint_{R^{(3)}} \left[\begin{matrix} 2\left(c_1^{(1)}u + c_2^{(1)}v + c_3^{(1)}w - V_1\right)c_1^{(1)}\delta u + 2\left(c_1^{(2)}u + c_2^{(2)}v + c_3^{(2)}w - V_2\right)c_1^{(2)}\delta u \\ +2\beta\left(\frac{\partial u}{\partial x} + \frac{\partial v}{\partial y} + \frac{\partial w}{\partial z} + \kappa w\right)\frac{\partial(\delta u)}{\partial x} \end{matrix} \right] dxdydz \tag{2.4.2}$$
$$= 0.$$

The term with a derivative of δu can be simplified by integration by parts:

$$\begin{aligned} \frac{1}{2}\delta_u J &= 0 \\ &= \iiint_{R^{(3)}} \left[\left(c_1^{(1)}u + c_2^{(1)}v + c_3^{(1)}w - V_1\right)c_1^{(1)} + \left(c_1^{(2)}u + c_2^{(2)}v + c_3^{(2)}w - V_2\right)c_1^{(2)}\right]\delta u \, dxdydz \\ &+ \iint_{R^{(2)}} \left[\beta\left(\frac{\partial u}{\partial x} + \frac{\partial v}{\partial y} + \frac{\partial w}{\partial z} + \kappa w\right)\delta u\right]_{x_{west}}^{x_{east}} dydz - \iiint_{R^{(3)}} \left[\beta\frac{\partial}{\partial x}\left(\frac{\partial u}{\partial x} + \frac{\partial v}{\partial y} + \frac{\partial w}{\partial z} + \kappa w\right)\right]\delta u \, dxdydz. \end{aligned} \tag{2.4.3}$$

The double integral term above can be eliminated by the same boundary conditions used in the strong-constraint dual-Doppler method: either u is specified at the east and west sides, or continuity is satisfied exactly there. I will again choose the latter option.

With the boundary term eliminated, Equation (2.4.3) becomes

$$0 = \iiint_{R^{(3)}} \left[\begin{matrix} u\left(\left\{c_1^{(1)}\right\}^2 + \left\{c_1^{(2)}\right\}^2\right) + v\left(c_1^{(1)}c_2^{(1)} + c_1^{(2)}c_2^{(2)}\right) + w\left(c_1^{(1)}c_3^{(1)} + c_1^{(2)}c_3^{(2)}\right) \\ -c_1^{(1)}V_1 - c_1^{(2)}V_2 - \beta\frac{\partial}{\partial x}\left(\frac{\partial u}{\partial x} + \frac{\partial v}{\partial y} + \frac{\partial w}{\partial z} + \kappa w\right) \end{matrix} \right] \delta u \, dxdydz. \tag{2.4.4}$$

For Equation (2.4.4) to be true for arbitrary δu, the sum of the bracketed terms must be zero. This leads to the first Euler-Lagrange equation:

$$\begin{aligned} &u\left(\left\{c_1^{(1)}\right\}^2 + \left\{c_1^{(2)}\right\}^2\right) + v\left(c_1^{(1)}c_2^{(1)} + c_1^{(2)}c_2^{(2)}\right) + w\left(c_1^{(1)}c_3^{(1)} + c_1^{(2)}c_3^{(2)}\right) \\ &\qquad = c_1^{(1)}V_1 + c_1^{(2)}V_2 + \beta\frac{\partial}{\partial x}\left(\frac{\partial u}{\partial x} + \frac{\partial v}{\partial y} + \frac{\partial w}{\partial z} + \kappa w\right). \end{aligned} \tag{2.4.5}$$

Similarly, equating the variations of J with respect to v and w to zero yields the other two Euler-Lagrange equations:

$$
\begin{aligned}
u\left(c_1^{(1)}c_2^{(1)}+c_1^{(2)}c_2^{(2)}\right)+v\left(\left\{c_2^{(1)}\right\}^2+\left\{c_2^{(2)}\right\}^2\right)+w\left(c_2^{(1)}c_3^{(1)}+c_2^{(2)}c_3^{(2)}\right)& \\
=c_2^{(1)}V_1+c_2^{(2)}V_2+\beta\frac{\partial}{\partial y}\left(\frac{\partial u}{\partial x}+\frac{\partial v}{\partial y}+\frac{\partial w}{\partial z}+\kappa w\right)&
\end{aligned}
\tag{2.4.6}
$$

$$
\begin{aligned}
u\left(c_1^{(1)}c_3^{(1)}+c_1^{(2)}c_3^{(2)}\right)+v\left(c_2^{(1)}c_3^{(1)}+c_2^{(2)}c_3^{(2)}\right)+w\left(\left\{c_3^{(1)}\right\}^2+\left\{c_3^{(2)}\right\}^2\right)& \\
=c_3^{(1)}V_1+c_3^{(2)}V_2+\beta\left(-\kappa+\frac{\partial}{\partial z}\right)\left(\frac{\partial u}{\partial x}+\frac{\partial v}{\partial y}+\frac{\partial w}{\partial z}+\kappa w\right).&
\end{aligned}
\tag{2.4.7}
$$

Again, I choose the same boundary conditions used in the strong-constraint dual-Doppler formulation. Satisfying continuity exactly on the north and south sides of the domain, and satisfying w=0 at the top and bottom of the domain, eliminates the boundary terms in the derivation of the Euler-Lagrange equations.

The Euler-Lagrange equations are a set of three equations with three unknowns (u, v, and w). The finite difference forms of (2.4.5)-(2.4.7) can be solved simply in Cartesian coordinates by iteration. If the second derivative of u in Equation (2.4.5) is represented with finite differences, and if terms involving u at the center grid point are then collected, the following expression results:

$$
u_i=\frac{\left[\begin{aligned}&\frac{\beta}{(\Delta x)^2}\left(u_{i-1}+u_{i+1}\right)-v\left(c_1^{(1)}c_2^{(1)}+c_1^{(2)}c_2^{(2)}\right)-w\left(c_1^{(1)}c_3^{(1)}+c_1^{(2)}c_3^{(2)}\right)\\&\qquad\qquad+c_1^{(1)}V_1+c_1^{(2)}V_2+\beta\frac{\partial}{\partial x}\left(\frac{\partial v}{\partial y}+\frac{\partial w}{\partial z}+\kappa w\right)\end{aligned}\right]}{\frac{2\beta}{(\Delta x)^2}+\left(c_1^{(1)}\right)^2+\left(c_1^{(2)}\right)^2}.
\tag{2.4.8}
$$

Similarly,

$$v_j = \frac{\left[\begin{array}{r}\frac{\beta}{(\Delta y)^2}\left(v_{j-1}+v_{j+1}\right)-u\left(c_1^{(1)}c_2^{(1)}+c_1^{(2)}c_2^{(2)}\right)-w\left(c_2^{(1)}c_3^{(1)}+c_2^{(2)}c_3^{(2)}\right)\\ +c_2^{(1)}V_1+c_2^{(2)}V_2+\beta\frac{\partial}{\partial y}\left(\frac{\partial u}{\partial x}+\frac{\partial w}{\partial z}+\kappa w\right)\end{array}\right]}{\frac{2\beta}{(\Delta y)^2}+\left(c_2^{(1)}\right)^2+\left(c_2^{(2)}\right)^2} \tag{2.4.9}$$

and

$$w_k = \frac{\left[\begin{array}{r}\frac{\beta}{(\Delta z)^2}\left(w_{k-1}+w_{k+1}\right)-u\left(c_1^{(1)}c_3^{(1)}+c_1^{(2)}c_3^{(2)}\right)-v\left(c_2^{(1)}c_3^{(1)}+c_2^{(2)}c_3^{(2)}\right)\\ +c_3^{(1)}V_1+c_3^{(2)}V_2+\beta\left(-\kappa+\frac{\partial}{\partial z}\right)\left(\frac{\partial u}{\partial x}+\frac{\partial v}{\partial y}\right)\end{array}\right]}{\frac{2\beta}{(\Delta z)^2}-\beta\frac{\partial\kappa}{\partial z}+\beta\kappa^2+\left(c_3^{(1)}\right)^2+\left(c_3^{(2)}\right)^2}. \tag{2.4.10}$$

The other derivative terms in the above expressions are also computed by finite differences.

The algorithm I use to solve for the Cartesian velocity components in the weak-constraint formulation updates the components one at a time.

1. Initialize u, v, and w with a first guess.
2. a. Solve for u at each grid point with Equation (2.4.8).
   b. Solve for v at each grid point with Equation (2.4.9).
   c. Solve for w at each grid point with Equation (2.4.10).
3. Update the side boundary conditions.
4. Repeat the process beginning at step 2 if the solution has not converged.

As in the case of the strong-constraint method, the above algorithm for the weak-constraint formulation converges to a solution even with data at high incidence angles.

For the first guess field in the weak-constraint method, I use w=0 and compute u and v according to Equations (2.1.9) and (2.1.10). At grid points where the denominator in (2.1.9) and (2.1.10) is small (i.e., at elevation angles above 60°), I instead use a 2D horizontal Laplacian hole filler to determine first guesses for u and v. This procedure gives a first guess field that varies smoothly outside the region where u and v can be estimated directly from the observations. More details of the hole-filling procedure are given in Section 2.7.

A disadvantage of iterative dual-Doppler schemes in Cartesian coordinates like the one above is that the procedure does not necessarily lead to a unique solution (Shapiro and Mewes 1999). Although the algorithm may converge on a solution, and the value of the cost function may decrease during each iteration, the solution is not necessarily a global minimum of the cost function. To test the hypothesis that the algorithm may converge on separate local minima in the cost function, I applied the weak-constraint algorithm with the usual first guess field and with an alternate first guess field of u=v=w=0.

For the Sperow analytic wind field and the numerical simulation test cases, the solution of the weak-constraint algorithm was *identical* for both types of first guesses. The same was nearly true for similar tests applied to real data, lending some confidence to the use of the solution procedure in practice. For sample data of the McLean storm, the weak-constraint algorithm converged to indistinguishable solutions throughout most of the domain. However, each first guess resulted in different velocities in a few locations on the south side of the domain at upper levels (Fig. 2.4.1). For example, the winds on the southeast side of the domain are more westerly in the analysis with the zero first guess, and there is a stronger updraft near x=-15, y=-22 (Fig. 2.4.1). The McLean storm ELDORA observations contain regions with missing data. In order to solve the variational problem, I "hole-fill" the velocities in the locations of missing data during the dual-Doppler analysis, as described in Section 2.7. (This procedure during the iterative solution is separate from the issue of hole-filling in the first guess field because in the latter case the synthesized velocities at grid points with valid data are eventually constrained by the observations.) The procedure I have chosen for handling missing data may increase the likelihood of multiple local minima in the weak-constraint cost function.

An important issue in the use of the weak-constraint wind synthesis is the choice of β, the relative weight given to the continuity equation. When there are errors in the observations, the use of a β that is too small results in a noisy solution that poorly satisfies continuity (Fig. 2.4.2.a), while the use of a β that is too large results in an excessively smoothed wind field (Fig. 2.4.2.b). The control of β in smoothing is seen directly in the finite difference expressions (2.4.8)-(2.4.10) in the $\frac{\beta}{(\Delta x)^2}(u_{i-1} + u_{i+1})$, $\frac{\beta}{(\Delta y)^2}(v_{j-1} + v_{j+1})$, and $\frac{\beta}{(\Delta z)^2}(w_{k-1} + w_{k+1})$ terms.

Inspection of Equation (2.4.1) reveals that β has units of length squared. In the tests below, I use a first guess of β equal to the square of the horizontal grid spacing (and then see how the solution varies for larger or smaller values). This gives the terms in brackets in Equations (2.4.8)-(2.4.10) the same order of magnitude. In a sense, the weights of the three constraints in the variational problem are equal.

2.4.2 Tests

Tables 2.1-2.3 provide a comparison of RMS errors in the synthesized wind components from weak-constraint analyses to those from the traditional and strong-constraint methods. As in the case of the strong-constraint method, test case B required approximately 200 iterations for the statistics to be stable, while test cases A and C required approximately 500 iterations.

An obvious difference in the results for the strong and weak constraint schemes is in how well the radial velocity equations are satisfied. In the former, the synthesized wind field satisfies the observations exactly (except perhaps at the upper and lower boundaries). In the latter, the mean difference between the observed radial air motion and the radial projection of the Cartesian velocities varies from 0.01 m s^{-1} for small values of β with noise-free observations (experiment 5a in Table 2.2), to 1.40 m s^{-1} for large values of β with noisy observations (experiment 8c in Table 2.1.a).

In terms of RMS velocity error in the synthesized wind field, ***the weak-constraint formulation provides no advantage over the strong-constraint formulation for perfect observations. However, the opposite is true when the observations are noisy.*** When there is random noise in the observations, there exists a value of β in each test case for which the weak-constraint method results in less error than the strong-constraint method for all three wind components. Improvements can be quite significant. In test case B, the RMS error is 39% less for w, and 48% less for the total velocity magnitude, in the weak-constraint analysis (with β=2.5×10^6 m^2) than in the strong-constraint analysis (experiments 9 and 10c in Table 2.2).

The challenge is in determining the optimal value of β. Physically, one would anticipate that a greater value of β (i.e., less weight to observations) would be desirable for observations with errors than for error-free observations. This idea is confirmed by the tests. For example, in test case C (Table 2.3), a wind synthesis with error-free observations is better for β=10^5 m^2 than for β=10^6 m^2, and vice versa for a synthesis with random errors in the observations. The issue is complicated because errors in u, v, and w are not necessarily minimized for the same value of β (e.g., experiments 8a and 8b in Table 2.1.a).

The use of β as the square of the grid spacing appears to be a reasonable first guess, resulting in the lowest RMS errors in the analyses with noisy observations for three of the five examples. However, there also appears to be a dependence on the scale of the observed features (Fig. 2.4.3). For the Sperow analytic wind fields with horizontal wavelengths of 5 km, 10 km , and 20 km, $\sqrt{\beta}$ values of 160 m, 300 m, and 400 m, respectively, yield the most accurate vertical velocities.

Further work is needed to understand how one may choose an optimal value of β without knowledge of the true wind field. However, even with the uncertainty in the choice of β, the tests (Tables 2.1-2.3) suggest that the weak-constraint scheme is still better than the strong-constraint scheme for noisy observations. After trying a first guess of $\sqrt{\beta}$ equal to the grid spacing, one may then adjust β if there is too much or too little noise in the solution. This procedure is subjective and requires the analyst to have some knowledge of what the synthesized wind field should look like.

The use of the weak-constraint method for real data results in a smoother wind field than for the strong-constraint method (Fig. 2.4.4). (Although the differences in horizontal velocity are difficult to detect, the differences in w are noticeable.) The strong-constraint analysis is required to resolve every small-scale detail (whether it is real or noise) in the observations. In contrast, the weak-constraint synthesis may slightly disregard small features in the observations if the result is a lower value of the global cost function.

It is common practice to apply a scale-selective filter to the output of a dual-Doppler synthesis algorithm (Brandes 1978, Dowell and Bluestein 1997, Wakimoto et al. 1998). One may ask whether the weak-constraint synthesis is simply a filtered version of the strong-constraint synthesis. In experiments 11 and 12 in Tables 2.2 and 2.3, a one-pass Leise (1982) filter has been applied to each of the Cartesian velocity components before the calculation of the error statistics. This filter eliminates features with a wavelength of twice the horizontal grid spacing and damps features with a wavelength of four times the grid spacing by approximately 25% (Leise 1982). The filtering results in more accurate velocities for both the strong and weak constraint methods (Tables 2.2 and 2.3). However, the filtered strong-constraint syntheses are still not as accurate as either the filtered or unfiltered weak-constraint syntheses for the optimal range of β.

2.5 Reference Frame

2.5.1 Formulation for Moving Radars

There is no provision for time evolution in the standard dual-Doppler equations (2.1.2)-(2.1.4). This would not be a problem for instantaneous, simultaneous observations. However, real observations typically consist of samples of moving, evolving phenomena collected over periods of ~5 min with dual-Doppler observations at individual points that aren't necessarily simultaneous. I will primarily consider here the non-simultaneity problem for airborne Doppler radar. For ELDORA storm observations during VORTEX, there was typically a time lag of up to 2 min between fore and aft radar samples.

Gal-Chen (1982) describes a strategy for minimizing the impact of non-simultaneous observations by employing a moving reference frame for the dual-Doppler analysis. The use of a moving frame ensures that local time derivatives in the observed velocities (which are not allowed by the dual-Doppler equations) are the result of evolution only, rather than both movement and evolution.

Gal-Chen's (1982) general methodology is to find a constant horizontal reference frame velocity (U_s, V_s) that minimizes, in a least squares sense over the domain, the local time derivatives of a quantity f:

$$J = \int_{R^{(4)}} \left(\frac{\partial f'}{\partial t'} \right)^2 dR^{(4)} = \text{minimum} \tag{2.5.1}$$

where $R^{(4)}$ is a bounded region in time and 3D space, and primes refer to measurements defined in the moving frame. For a variable f that is Galilean invariant,

$$\frac{\partial f'}{\partial t'} = \frac{\partial f}{\partial t} + U_s \frac{\partial f}{\partial x} + V_s \frac{\partial f}{\partial y}. \tag{2.5.2}$$

Gal-Chen (1982) calls the velocity (U_s, V_s) of the optimal moving reference frame the "advection velocity." However, since motion is not determined by advection alone, I believe this terminology is poor. For example, in purely horizontal motion, the rate of change of f is governed by

$$\frac{\partial f}{\partial t} = -u \frac{\partial f}{\partial x} - v \frac{\partial f}{\partial y} + F(x, y, t) \tag{2.5.3}$$

where F is a forcing (source or sink) term. The quantity that is minimized by Equation (2.5.1) is thus

$$J = \int_{R^{(4)}} \left[F + (U_s - u)\frac{\partial f}{\partial x} + (V_s - v)\frac{\partial f}{\partial y} \right]^2 dR^{(4)}. \tag{2.5.4}$$

In the absence of forcing, the solution for (U_s, V_s) could be thought of as a characteristic velocity of advection. However, with nonzero F, this is not the case. I will refer to (U_s, V_s) as the "translation velocity" of the system.

An example of the importance of the reference frame choice for the McLean storm data is shown in Fig. 2.5.1. The first analysis (Fig. 2.5.1.a) is in a reference frame moving at the velocity of the southwestern member of a vortex pair ("V1"), as determined from an inspection of consecutive Doppler volumes. The reference frame motion of the second analysis (Fig. 2.5.1.b) is roughly that of the storm reflectivity core. Significant differences exist between the two analyses. For example, the winds on the south sides of V1 and V2 are weaker in the second analysis than in the first. More obvious differences are apparent in the convergence field associated with the velocities. The sign of the convergence changes both east of V1 and south of V2 in the two analyses. In addition, the use of the second reference frame greatly increases the magnitude of divergence northeast of V1.

An important question about the moving reference frame approach for a dual-Doppler analysis is what variable (f in Equation 2.5.1) should be used for the minimization. Gal-Chen (1982) proposed a method for two Doppler radars based on the quantity $v_r r$, where r is the distance from the radar to the observed point. However, this method is useless for moving (e.g., airborne) radars, in which the location from which the point is observed may change from one Doppler volume to the next.

Instead, I propose using the Cartesian velocity components as roughly conserved variables for the minimization in Equation (2.5.1). It would be possible to apply Gal-Chen's (1982) technique on Cartesian winds synthesized from a complete dual-Doppler analysis in each step of the procedure. However, I have opted for approximate forms of the velocities that can be calculated more quickly. For scans at mostly low elevation angles, I use estimates of u and v from Equations (2.1.2)-(2.1.3) with the assumption that $w \sin e$ is negligible in those expressions:

$$u \approx \frac{c_2^{(2)} V_1 - c_2^{(1)} V_2}{c_1^{(1)} c_2^{(2)} - c_2^{(1)} c_1^{(2)}} \equiv f_1 \qquad (2.5.5)$$

$$v \approx \frac{c_1^{(1)} V_2 - c_1^{(2)} V_1}{c_1^{(1)} c_2^{(2)} - c_2^{(1)} c_1^{(2)}} \equiv f_2. \qquad (2.5.6)$$

This choice for f_1 and f_2 works for the test cases and for most of the data levels in the McLean storm data. However, for the McLean storm, many of the data at upper grid levels are nearly overhead. Since the flight legs are approximately east-west, I use approximate values of u and w from Equations (2.1.2)-(2.1.3) for f_1 and f_2 at these upper levels, with the assumption that $v\cos a$ is negligible.

The goal of the (modified) Gal-Chen (1982) technique is to find the reference frame translation velocity (U_s, V_s) that minimizes the following functional:

$$J = \int_{R^{(4)}} \left[\left(\frac{\partial f_1'}{\partial t'} \right)^2 + \left(\frac{\partial f_2'}{\partial t'} \right)^2 \right] dR^{(4)}. \tag{2.5.7}$$

In terms of a ground-relative reference frame, Equation (2.5.7) is equivalent to

$$J = \int_{R^{(4)}} \left[\left(\frac{\partial f_1'}{\partial t} + U_s \frac{\partial f_1'}{\partial x} + V_s \frac{\partial f_1'}{\partial y} \right)^2 + \left(\frac{\partial f_2'}{\partial t} + U_s \frac{\partial f_2'}{\partial x} + V_s \frac{\partial f_2'}{\partial y} \right)^2 \right] dR^{(4)}. \tag{2.5.8}$$

The solution for the optimal U_s and V_s is found by requiring the variation of J with respect to both U_s and V_s to be zero (Gal-Chen 1982):

(2.5.9)

$$\delta_{U_s} J = \int_{R^{(4)}} 2\delta U_s \left[\frac{\partial f_1'}{\partial t}\frac{\partial f_1'}{\partial x} + \frac{\partial f_2'}{\partial t}\frac{\partial f_2'}{\partial x} + U_s \left(\frac{\partial f_1'}{\partial x} \right)^2 + U_s \left(\frac{\partial f_2'}{\partial x} \right)^2 + V_s \frac{\partial f_1'}{\partial x}\frac{\partial f_1'}{\partial y} + V_s \frac{\partial f_2'}{\partial x}\frac{\partial f_2'}{\partial y} \right] dR^{(4)}$$
$$= 0$$

(2.5.10)

$$\delta_{V_s} J = \int_{R^{(4)}} 2\delta V_s \left[\frac{\partial f_1'}{\partial t}\frac{\partial f_1'}{\partial y} + \frac{\partial f_2'}{\partial t}\frac{\partial f_2'}{\partial y} + U_s \frac{\partial f_1'}{\partial x}\frac{\partial f_1'}{\partial y} + U_s \frac{\partial f_2'}{\partial x}\frac{\partial f_2'}{\partial y} + V_s \left(\frac{\partial f_1'}{\partial y} \right)^2 + V_s \left(\frac{\partial f_2'}{\partial y} \right)^2 \right] dR^{(4)}$$
$$= 0.$$

The above equations are true for arbitrary δU_s and δV_s if

$$AU_s + BV_s = D \tag{2.5.11}$$

$$BU_s + CV_s = E \tag{2.5.12}$$

where

$$A = \int_{R^{(4)}} \left[\left(\frac{\partial f_1'}{\partial x} \right)^2 + \left(\frac{\partial f_2'}{\partial x} \right)^2 \right] dR^{(4)} \tag{2.5.13}$$

$$B = \int_{R^{(4)}} \left[\frac{\partial f_1'}{\partial x} \frac{\partial f_1'}{\partial y} + \frac{\partial f_2'}{\partial x} \frac{\partial f_2'}{\partial y} \right] dR^{(4)} \tag{2.5.14}$$

$$C = \int_{R^{(4)}} \left[\left(\frac{\partial f_1'}{\partial y} \right)^2 + \left(\frac{\partial f_2'}{\partial y} \right)^2 \right] dR^{(4)} \tag{2.5.15}$$

$$D = -\int_{R^{(4)}} \left[\frac{\partial f_1'}{\partial t} \frac{\partial f_1'}{\partial x} + \frac{\partial f_2'}{\partial t} \frac{\partial f_2'}{\partial x} \right] dR^{(4)} \tag{2.5.16}$$

$$E = -\int_{R^{(4)}} \left[\frac{\partial f_1'}{\partial t} \frac{\partial f_1'}{\partial y} + \frac{\partial f_2'}{\partial t} \frac{\partial f_2'}{\partial y} \right] dR^{(4)}. \tag{2.5.17}$$

The primes have been carried through in the above equations because the velocity estimates f_1' and f_2' depend on the reference frame. These may be calculated during each step of the method as

$$f_1' = f_1 - U_s \tag{2.5.18}$$

$$f_2' = f_2 - V_s. \tag{2.5.19}$$

Gal-Chen (1982) employed an iterative technique to find the solution of Equations (2.5.11)-(2.5.19), and that's how I solve the problem as well. The process begins with a first guess of $(U_s, V_s)=(0, 0)$. For the test cases, approximately five iterations lead to the optimal values of U_s and V_s.

Multiple dual-Doppler volumes are required for estimation of the time derivatives in (2.5.16) and (2.5.17). My dual-Doppler program is set up to estimate translation velocity for three consecutive dual-Doppler volumes. The U_s and V_s values are then most appropriate for the middle volume.

2.5.2 Non-uniform Moving Reference Frame

Gal-Chen (1982) described his moving reference frame method as being applied uniformly to the entire multiple-Doppler analysis domain. However, this does not account for the fact that individual features within a storm can move at different velocities. For example, in the McLean storm (Fig. 1.7) at 2318 UTC, the dissipating tornado #2 was moving northwestward, the overall storm updraft and developing vortex of tornado #4 were moving northward, and the trailing gust front was moving eastward (not shown). The use of a single constant velocity for a moving reference frame does not seem appropriate for this flow.

I propose instead that a translation velocity be calculated for each grid point in the domain, based on observations within a small sub-domain centered around the point (Fig. 2.5.2). A reference frame motion $U_s(x, y, z)$ and $V_s(x, y, z)$ that is a function of space can account for the variety of characteristic velocities of the features in the domain. I will call this type of frame a "non-uniform moving reference frame." The procedure for determining the velocity of the moving frame is the same as before, except that the integrals in Equations (2.5.13)-(2.5.17) apply to smaller regions centered around each grid point.

Each observation in each of the three dual-Doppler volumes has the following coordinates in the moving frame:

$$x' = x - U_s t \tag{2.5.20}$$

$$y' = y - V_s t \tag{2.5.21}$$

where t=0 is the reference time, and x and y are the coordinates on the original regular grids, which I choose to be identical for all volumes. As in the case of the traditional approach with a uniform moving reference frame, the interpolation of the observations in the moving frame to common grid points simplifies the computation of the derivatives in Equations (2.5.13)-(2.5.17). (For the non-uniform moving frame, the spacing between translated observations in the moving frame becomes irregular.) Interpolation to common grid points is also necessary for the dual-Doppler analysis, which is carried out on a regular grid after the determination of the reference frame translation velocity. I use the method described in Appendix D for the interpolation.

2.5.3 Tests

To test the non-uniform moving reference frame algorithm, I first applied it to the following analytic wind field (Fig. 2.5.3), which has inconsistent dynamics but does satisfy continuity:

$$u = u_o \tag{2.5.22}$$

$$v = v_o \sin\left[\frac{4\pi}{L}\left(x - \frac{u_o y t}{2L}\right)\right] \tag{2.5.23}$$

$$w = \frac{2\pi u_o v_o t z}{L^2} \cos\left[\frac{4\pi}{L}\left(x - \frac{u_o y t}{2L}\right)\right]. \tag{2.5.24}$$

In this analytic wind field, sinusoidal waves move at a phase speed $\frac{u_o y}{2L}$ that varies in the y direction. In the upper (lower) half of the domain, the waves move to the right (left). Both the density and horizontal winds are independent of height. The values of the constants in the test are L=10.0 km, u_o = 20.0 m s^{-1}, and v_o = 15.0 m s^{-1}. The maximum speed of the waves is thus 10.0 m s^{-1} (at the north and south edges).

I produced three simulated pseudo-dual-Doppler volumes (centered around t=0) of the analytic wind field like those collected from a plane flying back and forth along y=0 at z=500 m. As with some of the experiments with test case C, the interval between consecutive dual-Doppler volumes is 5 min, and the time lag between fore and aft observations in each volume is 2 min.

Owing to the symmetry of the analytic wind field, the optimal *constant* reference frame motion for the Doppler wind synthesis (Gal-Chen 1982) has zero velocity. A cross section from a traditional dual-Doppler synthesis with upward integration in this (fixed) reference frame is shown in Fig. 2.5.3.c. A comparison with the exact wind field (Fig. 2.5.3.a) reveals noteworthy differences. Although there is still some evidence of a wavetrain, the wind speed in the valleys (peaks) is overestimated (underestimated). More importantly, spurious divergence appears in the derived wind field. The divergence is associated with erroneous vertical velocity of over 30 m s^{-1} at 1.0 km AGL (Fig. 2.5.3.c).

I applied a second dual-Doppler analysis (Fig. 2.5.3.d) in a reference frame with a *non-uniform* translation velocity. The local sub-domains for the reference frame scheme were cubical with 5-km long sides; this size matches the wavelength in the analytic wind field. I am yet to determine a rigorous method for selecting the optimal sub-domain size for real data. The choice should certainly depend on the scale of the phenomenon being observed and on the quality of the data. One can choose a reasonable sub-domain size subjectively. If the sub-domain size is too small, the field of translation velocities is noisy; if it is too large, there is little impact compared to the use of a uniform moving reference frame.

The eastward translation velocity (for 5-km sub-domains) for the analytic wind field is shown in Fig. 2.5.3.e. These U_s values agree rather closely to the exact values out to $|y| = 6$ km. However, the large (8-10 m s^{-1}) values near the boundaries are not captured.

The dual-Doppler winds in the non-uniform reference frame (Fig. 2.5.3.d) much more closely approximate the exact solution (Fig. 2.5.3.a) than those in the fixed frame (Fig. 2.5.3.c). RMS errors at 1.0 km of u and w are 1.05 and 1.29 m s^{-1}, respectively, in the second analysis, as opposed to 9.86 and 11.13 m s^{-1} in the first. The loss of data near the edges in Fig. 2.5.3.d is an indication of a translation velocity that requires analysis of data from outside the domain; the interpolation scheme (Appendix D) avoids extrapolation beyond the limits of the data. The loss of data near the flight track is the result of the scheme avoiding interpolation across the sharp gradient in azimuth angles there.

The remaining experiments (Tables 2.4-2.5) are for the numerical model test cases. The time lags between fore and aft observations are as described in Section 2.2: 80 s for test case B and 120 s for test case C. The experiments are in three different reference frames: one that is stationary with respect to the ground, one that is moving at uniform velocity (Gal-Chen 1982), and one that is moving with a non-uniform translation velocity. Since the numerical model itself employs a moving reference frame, the translation velocity components for the fixed frame (Tables 2.4-2.5) are nonzero.

As in the tests with the analytic wind field, the use of 5-km wide sub-domains proved to be ideal (not shown) for the determination of local translation velocities. The translation velocity vectors for test case B (Fig. 2.5.4.a) reflect the overall divergent character of the flow as the cold air spreads out at low levels, while those for test case C (Fig. 2.5.4.b) depend more on local details in the flow.

In some regions of the numerical model output (e.g., close to the edges in Fig. 2.2.2.c), the horizontal velocity gradients are very weak. In these regions, the determinant of the coefficient matrix $\begin{pmatrix} A & B \\ B & C \end{pmatrix}$ of Equations (2.5.11) and (2.5.12) is small. To account for this problem, I do not allow the magnitude of the determinant to be less than 1.0 $m^6\ s^{-2}$ when computing the translation velocity. This forces the values of U_s and V_s to approach zero in the weak-gradient areas.

The results in Tables 2.4-2.5 clearly demonstrate the advantage (Gal-Chen 1982) of a moving reference frame (experiments 3, 4, 9, and 10) over a stationary frame (experiments 1, 2, 7, and 8). The use of non-uniform values of U_s and V_s (experiments 5, 6, 11, and 12) over constant ones provides a small but consistent additional positive impact. The improvements in the RMS errors in u, v, and w range from 8-19%, 0-11%, and 2-9%, respectively.

The results hold up when noise is present in the observations, although the magnitude of the improvement typically decreases slightly. (The differences between the experiments with noisy and with noise-free observations are less than in previous sections because the interpolation of observations from the moving frame coordinates to the regular grid smoothes out some of the random noise.) Also, the magnitude of the improvement with a non-uniform moving frame is generally slightly less when the dual-Doppler synthesis is based on the weak constraint formulation than on the strong constraint formulation. This is likely an indication of the weak constraint method itself smoothing out some of the temporal error.

2.6 Incorporation of Time Derivatives

2.6.1 Formulation

The method in the previous section is an attempt to minimize the impact of non-simultaneous observations on a dual-Doppler analysis by employing a moving reference frame. The motivation here is to further minimize the impact by accounting for slow evolution of the flow. By slow I mean with a time scale greater than the time between observations.

Gal-Chen (1978) and Clark et al. (1980) recommend a procedure of linear time interpolation of radial velocities from two successive radar scans to a common time level. However, such a procedure is not possible when the radar sites are not fixed (e.g., for airborne radar). Instead, I propose another simple procedure for accounting for evolution. The fundamental assumption is that the velocities are linear functions of time over the time period of the observations:

$$u(x,y,z,t) = U(x,y,z) + tD_u(x,y,z) \tag{2.6.1}$$

$$v(x,y,z,t) = V(x,y,z) + tD_v(x,y,z) \tag{2.6.2}$$

$$w(x,y,z,t) = W(x,y,z) + tD_w(x,y,z) \tag{2.6.3}$$

where U, V, and W are the velocities at the reference time (t=0), and D_u, D_v, and D_w are the estimates of the time derivatives. This approach is designed to be applied in the moving frame of reference.

The solution for the six unknown variables (U, V, W, D_u, D_v, and D_w) requires six equations. Substitution of Equations (2.6.1)-(2.6.3) into the continuity equation provides two relationships:

$$\frac{\partial U}{\partial x} + \frac{\partial V}{\partial y} + \frac{\partial W}{\partial z} + \kappa W = 0 \tag{2.6.4}$$

$$\frac{\partial D_u}{\partial x} + \frac{\partial D_v}{\partial y} + \frac{\partial D_w}{\partial z} + \kappa D_w = 0. \tag{2.6.5}$$

The former equation guarantees that anelastic mass continuity is satisfied at t=0. The latter equation follows from requiring mass continuity to be valid at all t.

Closure of the system requires four consecutive radial velocity observations (e.g, Fig. 2.6.1) from at least two different viewing angles:

$$c_1^{(1)}(U+t_1D_u)+c_2^{(1)}(V+t_1D_v)+c_3^{(1)}(W+t_1D_w)=V_1 \qquad \text{(previous pass, aft)} \qquad (2.6.6)$$

$$c_1^{(2)}(U+t_2D_u)+c_2^{(2)}(V+t_2D_v)+c_3^{(2)}(W+t_2D_w)=V_2 \qquad \text{(current pass, fore)} \qquad (2.6.7)$$

$$c_1^{(3)}(U+t_3D_u)+c_2^{(3)}(V+t_3D_v)+c_3^{(3)}(W+t_3D_w)=V_3 \qquad \text{(current pass, aft)} \qquad (2.6.8)$$

$$c_1^{(4)}(U+t_4D_u)+c_2^{(4)}(V+t_4D_v)+c_3^{(4)}(W+t_4D_w)=V_4. \qquad \text{(next pass, fore)} \qquad (2.6.9)$$

As is the case for a traditional dual-Doppler analysis, the use of multiple boundary conditions for the continuity equation (in this case, W=0 and D_w =0 at both the surface and at the storm top) makes the problem overdetermined.

I choose to split the problem into two parts – one a variational problem for U, V, and W and the other a variational problem for D_u, D_v, and D_w. Since the values of U, V, and W depend on the estimates of D_u, D_v, and D_w (and vice versa), I solve the two problems concurrently. I use the observations closest in time to the reference time (Equations 2.6.7 and 2.6.8) to compute U, V, and W:

$$c_1^{(2)}U+c_2^{(2)}V+c_3^{(2)}W \approx V_2-t_2\left(c_1^{(2)}D_u+c_2^{(2)}D_v+c_3^{(2)}D_w\right)\equiv Q_2 \qquad (2.6.10)$$

$$c_1^{(3)}U+c_2^{(3)}V+c_3^{(3)}W \approx V_3-t_3\left(c_1^{(3)}D_u+c_2^{(3)}D_v+c_3^{(3)}D_w\right)\equiv Q_3 \qquad (2.6.11)$$

and the other two radial velocity equations (2.6.6 and 2.6.9) to compute D_u, D_v, and D_w:

$$c_1^{(1)}D_u+c_2^{(1)}D_v+c_3^{(1)}D_w \approx \frac{1}{t_1}\left(V_1-c_1^{(1)}U-c_2^{(1)}V-c_3^{(1)}W\right)\equiv Q_1 \qquad (2.6.12)$$

$$c_1^{(4)}D_u+c_2^{(4)}D_v+c_3^{(4)}D_w \approx \frac{1}{t_4}\left(V_4-c_1^{(4)}U-c_2^{(4)}V-c_3^{(4)}W\right)\equiv Q_4. \qquad (2.6.13)$$

For each of the solutions, I will employ a weak-constraint formulation like that in Section 2.4:

$$J_1 = \iiint_{R^{(3)}} \left[\begin{array}{l} \left(c_1^{(2)}U + c_2^{(2)}V + c_3^{(2)}W - Q_2\right)^2 + \left(c_1^{(3)}U + c_2^{(3)}V + c_3^{(3)}W - Q_3\right)^2 \\ + \beta\left(\dfrac{\partial U}{\partial x} + \dfrac{\partial V}{\partial y} + \dfrac{\partial W}{\partial z} + \kappa W\right)^2 \end{array} \right] dx\,dy\,dz$$
$$= \text{minimum} \tag{2.6.14}$$

$$J_2 = \iiint_{R^{(3)}} \left[\begin{array}{l} \left(c_1^{(1)}D_u + c_2^{(1)}D_v + c_3^{(1)}D_w - Q_1\right)^2 + \left(c_1^{(4)}D_u + c_2^{(4)}D_v + c_3^{(4)}D_w - Q_4\right)^2 \\ + \beta\left(\dfrac{\partial D_u}{\partial x} + \dfrac{\partial D_v}{\partial y} + \dfrac{\partial D_w}{\partial z} + \kappa D_w\right)^2 \end{array} \right] dx\,dy\,dz$$
$$= \text{minimum.} \tag{2.6.15}$$

The derivation of the Euler-Lagrange equations for the above cost functions parallels that in Section 2.4. The result is

$$U\left(\left\{c_1^{(2)}\right\}^2 + \left\{c_1^{(3)}\right\}^2\right) + V\left(c_1^{(2)}c_2^{(2)} + c_1^{(3)}c_2^{(3)}\right) + W\left(c_1^{(2)}c_3^{(2)} + c_1^{(3)}c_3^{(3)}\right)$$
$$= c_1^{(2)}Q_2 + c_1^{(3)}Q_3 + \beta\frac{\partial}{\partial x}\left(\frac{\partial U}{\partial x} + \frac{\partial V}{\partial y} + \frac{\partial W}{\partial z} + \kappa W\right) \tag{2.6.16}$$

$$U\left(c_1^{(2)}c_2^{(2)} + c_1^{(3)}c_2^{(3)}\right) + V\left(\left\{c_2^{(2)}\right\}^2 + \left\{c_2^{(3)}\right\}^2\right) + W\left(c_2^{(2)}c_3^{(2)} + c_2^{(3)}c_3^{(3)}\right)$$
$$= c_2^{(2)}Q_2 + c_2^{(3)}Q_3 + \beta\frac{\partial}{\partial y}\left(\frac{\partial U}{\partial x} + \frac{\partial V}{\partial y} + \frac{\partial W}{\partial z} + \kappa W\right) \tag{2.6.17}$$

$$U\left(c_1^{(2)}c_3^{(2)} + c_1^{(3)}c_3^{(3)}\right) + V\left(c_2^{(2)}c_3^{(2)} + c_2^{(3)}c_3^{(3)}\right) + W\left(\left\{c_3^{(2)}\right\}^2 + \left\{c_3^{(3)}\right\}^2\right)$$
$$= c_3^{(2)}Q_2 + c_3^{(3)}Q_3 + \beta\left(-\kappa + \frac{\partial}{\partial z}\right)\left(\frac{\partial U}{\partial x} + \frac{\partial V}{\partial y} + \frac{\partial W}{\partial z} + \kappa W\right) \tag{2.6.18}$$

$$D_u\left(\left\{c_1^{(1)}\right\}^2+\left\{c_1^{(4)}\right\}^2\right)+D_v\left(c_1^{(1)}c_2^{(1)}+c_1^{(4)}c_2^{(4)}\right)+D_w\left(c_1^{(1)}c_3^{(1)}+c_1^{(4)}c_3^{(4)}\right)$$
$$=c_1^{(1)}Q_1+c_1^{(4)}Q_4+\beta\frac{\partial}{\partial x}\left(\frac{\partial D_u}{\partial x}+\frac{\partial D_v}{\partial y}+\frac{\partial D_w}{\partial z}+\kappa D_w\right) \tag{2.6.19}$$

$$D_u\left(c_1^{(1)}c_2^{(1)}+c_1^{(4)}c_2^{(4)}\right)+D_v\left(\left\{c_2^{(1)}\right\}^2+\left\{c_2^{(4)}\right\}^2\right)+D_w\left(c_2^{(1)}c_3^{(1)}+c_2^{(4)}c_3^{(4)}\right)$$
$$=c_2^{(1)}Q_1+c_2^{(4)}Q_4+\beta\frac{\partial}{\partial y}\left(\frac{\partial D_u}{\partial x}+\frac{\partial D_v}{\partial y}+\frac{\partial D_w}{\partial z}+\kappa D_w\right) \tag{2.6.20}$$

$$D_u\left(c_1^{(1)}c_3^{(1)}+c_1^{(4)}c_3^{(4)}\right)+D_v\left(c_2^{(1)}c_3^{(1)}+c_2^{(4)}c_3^{(4)}\right)+D_w\left(\left\{c_3^{(1)}\right\}^2+\left\{c_3^{(4)}\right\}^2\right)$$
$$=c_3^{(1)}Q_1+c_3^{(4)}Q_4+\beta\left(-\kappa+\frac{\partial}{\partial z}\right)\left(\frac{\partial D_u}{\partial x}+\frac{\partial D_v}{\partial y}+\frac{\partial D_w}{\partial z}+\kappa D_w\right). \tag{2.6.21}$$

The algorithm with which I solve the finite difference forms of the Euler-Lagrange equations is:

1. Initialize U, V, W, D_u, D_v, and D_w with a first guess.
2. Compute Q_2 and Q_3.
3. a. Solve for U at each grid point with Equation (2.6.16).
   b. Solve for V at each grid point with Equation (2.6.17).
   c. Solve for W at each grid point with Equation (2.6.18).
4. Update the side boundary conditions for U, V, and W.
5. Compute Q_1 and Q_4.
6. a. Solve for D_u at each grid point with Equation (2.6.19).
   b. Solve for D_v at each grid point with Equation (2.6.20).
   c. Solve for D_w at each grid point with Equation (2.6.21).
7. Update the side boundary conditions for D_u, D_v, and D_w.
8. Repeat the process beginning at step 2 if the solution has not converged sufficiently.

For the first guess field, I compute *U, V, W* as described in Section 2.4 and use $D_u=D_v=D_w=0$. The boundary conditions are also like those in Section 2.4: $W=0$ and $D_w=0$ satisfied at the top and bottom, and continuity (and the time derivative of continuity) satisfied exactly on the sides.

Before describing the results of the tests, I should mention that in my research prospectus I outlined a strategy for including a dynamical constraint in dual-Doppler wind syntheses. (This is in contrast to traditional methods, which involve purely geometrical and kinematic constraints.) In particular, I had proposed a variational scheme that included the frictionless vertical vorticity equation (Dowell and Bluestein 1999):

(2.6.22)

$$J = \int_{R^{(3)}} \left\{ \left[\frac{\partial U}{\partial x} + \frac{\partial V}{\partial y} + \frac{\partial W}{\partial z} + \kappa W \right]^2 + \alpha \left[\frac{d\zeta}{dt} + \left(\frac{\partial U}{\partial x} + \frac{\partial V}{\partial y}\right)\zeta + \hat{k} \cdot \left(\nabla W \times \frac{\partial \vec{V}}{\partial z} \right) \right]^2 \right\} dx\, dy\, dz$$

$$= \text{minimum}$$

where $\zeta = \frac{\partial V}{\partial x} - \frac{\partial U}{\partial y}$ and α is a weight given to the vorticity equation relative to the continuity equation. This formulation is related to the other methods described in this section because it requires estimates of the velocity time derivatives (in the $d\zeta / dt$ term).

The vorticity equation includes second derivatives of the velocities, while the continuity equation includes first derivatives. Therefore, when errors are present in the observations, one would anticipate less information to be provided by the vorticity equation relative to the continuity equation owing to a lower signal-to-noise ratio in the former case. However, I had still hoped that the inclusion of the dynamical constraint in the dual-Doppler synthesis would improve the estimates of vertical velocity. This may be possible in some cases. However, with the tests in the following sub-section, I will argue that we are not able to estimate well the velocity time derivatives from VORTEX airborne Doppler data. This means that the dynamical equation is of limited utility in this case. I have currently abandoned attempts to use the vorticity equation in the dual-Doppler analysis of ELDORA data from VORTEX.

2.6.2 Tests

Tables 2.6 and 2.7 summarize statistics for the weak-constraint wind syntheses of the test cases, both with and without velocities that vary linearly with time. The results were mixed overall. For test case B, the inclusion of time derivatives improves the estimates of *U*, has a very small impact on *W*, but actually increases the RMS errors in *V*.

The results for test case C (Table 2.7) are tabulated separately for the steady storm at the southern end of the line and for the northern, more rapidly evolving cells (Fig. 2.2.3). The inclusion of time derivatives for the noise-free observations of the southern storm has almost no impact on the results. This is not surprising given the relatively steady nature of the storm; i.e., the change in the velocities over the 8-min time period between the first and last observation is relatively small compared to the mean magnitude of the velocities.

When noise is included in the observations, the use of time-varying velocities slightly increases the RMS error in *U*, *V*, and *W* for the southern storm. This indicates that the perceived trend in the velocities is pure noise and has no basis in the actual simulation.

The situation is different for the northern storms. The evolution of these cells includes a merging of two updrafts over a relatively long time scale (Fig. 2.2.3). For the northern storms, the inclusion of time derivatives has a positive impact on the results (Table 2.7), decreasing the RMS errors in *U*, *V*, and *W* by 22%, 7%, and 4%, respectively. The results hold when noise is present in the observations.

In summary, the results of these experiments suggest that one can not confidently use velocities that vary linearly with time without knowledge of the characteristics of the storm evolution. For the time derivative approach to succeed, there must exist significant evolution in the observed fields with a time scale greater than the time interval over which the observations are collected. I would anticipate that the following condition must be satisfied on average for the scheme to be useful: $|\vec{v}_4 - \vec{v}_1|\frac{t_3 - t_2}{t_4 - t_1} > E_{\vec{v}}$, where $\vec{v}_1$ and $\vec{v}_4$ are the actual velocities at times 1 and 4, and $E_{\vec{v}}$ is the magnitude of error in the velocity estimates. For airborne data during VORTEX, the interval between the first aft radar scan and the second fore radar scan (Fig. 2.6.1) was typically ~8 min. This is likely too long to capture mesocyclone-scale evolution in supercells.

The inclusion of time derivatives in dual-Doppler wind syntheses of supercells may be more productive in situations in which the total scan time is more rapid. For example, the Doppler on Wheels radars (Wurman et al. 1997) repeat volume scans every 2 min (J. Wurman 1999, personal communication). In the case of completely uncoordinated scans by two radars, the total time required to scan a point in the storm twice with each radar could be as little as 3 min. As a second example, during VORTEX the P-3 and Electra aircraft occasionally followed each other in the same flight leg. A combination of the two datasets from a flight leg would also contain the required four Doppler observations over a small (~4 min) time period.

2.7 Application of Analysis Methodology to Real Data

Appendix A contains a summary of the editing and objective analysis of raw data from each of the McLean storm flight legs (Table 1.2). The objectively-analyzed fields are on grids with a 400 m horizontal and a 500 m vertical spacing.

For the pseudo-dual-Doppler analyses of the McLean storm, I used the weak-constraint method (Section 2.4) in a non-uniform moving reference frame (Section 2.5.2). I had originally set out to analyze the ELDORA data with the strong-constraint method that I had developed (Section 2.3). However, the results from the comparison with the other technique were convincing enough that I opted for the weak-constraint method. I did not include time-varying velocities (Section 2.6) owing to the coarse time resolution of the ELDORA data compared to the rapid evolution of the storm.

The dual-Doppler syntheses in both Chapters 2 and 3 were created with computer code that contained a boundary condition error (A. Shapiro 1999, personal communication). I learned this too late in the project to go back and run the wind syntheses again. Although I did employ the proper boundary conditions for u (v) on the west and east (north and south) sides, I also erroneously applied zero-gradient conditions in the other velocity components. I recently compared examples of wind syntheses with the correct and incorrect boundary conditions. The use of the correct boundary condition tended to give a noisier solution at the edge of the domain closest to the flight track.

However, the locations and magnitudes of the updrafts and downdrafts within the interior of the domain were not significantly affected by the change in boundary conditions.

The size of the sub-domains for the determination of local translation velocities was 3 km. This yielded detailed, but not noisy, translation velocities inside the storm. One drawback of the use of the non-uniform moving reference frame is that interpolation of the observations occurs twice – once in the gridding of the raw data with REORDER (Oye and Case 1992) (Appendix A), and a second time in the interpolation from the coordinates in the moving reference frame to the regular grid (Appendix D). I would prefer to include the translation velocity algorithm in REORDER so that interpolation occurs only once. However, my efforts to modify REORDER proved to be unsuccessful owing to incompatibility of software versions currently distributed by NCAR.

The value of β for the weak-constraint wind syntheses was 250000 m^2. This value is consistent with the results in Section 2.4 and yielded smooth wind fields that appear to be plausible depictions of the updraft-scale features (e.g., Fig. 2.4.4.b). For the McLean storm analyses, the mean difference between the objectively-analyzed radial air velocities and the radial projections of the Cartesian wind components is 0.5 m s^{-1}.

Real observations such as those of the McLean storm do not completely fill the analysis domain. To keep the weak-constraint solution method simple, I used a hole filler in each iteration to compute u, v, and w in regions of bad or missing ELDORA data. Hole-filled values satisfy the 2D Laplace equations:

$$\frac{\partial^2 u}{\partial x^2} + \frac{\partial^2 u}{\partial y^2} = 0 \tag{2.7.1}$$

$$\frac{\partial^2 v}{\partial x^2} + \frac{\partial^2 v}{\partial y^2} = 0 \tag{2.7.2}$$

$$\frac{\partial^2 w}{\partial x^2} + \frac{\partial^2 w}{\partial y^2} = 0. \tag{2.7.3}$$

This method of hole-filling minimizes the introduction of spurious horizontal convergence/divergence in the solution (Ellis 1997). After solving the variational dual-Doppler analysis problem, I discard the hole-filled values.

The complexity of the pseudo-dual-Doppler synthesis makes it difficult to derive a response function for how features of varying sizes will be resolved. The horizontal grid spacing in the McLean storm analyses is 400 m (which is roughly equal to the radar beamwidth and to the along-track distance between consecutive sweeps). Therefore, features less that 1600 m (= $4\Delta x$) wide will be poorly represented. Since the 1600-m resolution is larger than tornado scale, I consider here how the velocity signatures of the tornadoes in the McLean storm might appear in the dual-Doppler analyses.

Results from traditional dual-Doppler analyses of combined Rankine vortices are shown in Fig. 2.7.1. The goal of these experiments in particular is to see how the objective analysis smears the structure of the vortex. I do not consider the Doppler sampling issue but instead assume that perfect point measurements of radial velocity are known at a density much greater than the grid spacing. The 1200-m radius of influence for the Cressman (1959) interpolation of the simulated dual-Doppler measurements to the grid matches that in the analyses of the McLean storm (Appendix A). The 400-m horizontal grid spacing also matches that for the McLean storm.

The objective analysis and dual-Doppler analysis both expand the apparent size of the vortex core (Fig. 2.7.1.a) and diminish the maximum wind speed (Fig. 2.7.1.b). The distance from the vortex center to the grid location with the maximum wind speed in the dual-Doppler synthesis is 800 m for the Rankine vortices of core radius 100-600 m and 1200 m for core radius 700-1200 m (not shown). In each combined Rankine vortex, the actual maximum wind speed (at the edge of the core) is 100 m s^{-1}. However, this magnitude is underestimated by over 50% in the dual-Doppler analyses of vortices of core radius up to 600 m (Fig. 2.7.1.b).

Contamination of the data by ground return (Appendix A) limits the lowest level with usable velocity measurements to around 500 m AGL for the McLean storm ELDORA scans. Therefore, the lowest level in the pseudo-dual-Doppler analyses is at this height. Even with the missing data near the ground, I still employ a w boundary condition by assuming that convergence/divergence at 500 m is representative of the entire layer below that level. I then integrate the continuity equation upward from the surface, where w=0. Changing w at the lowest grid level (500 m) is inconsistent with the boundary conditions in the derivation of the weak constraint Euler-Lagrange equations

(Section 2.4) and can make the analysis scheme unstable. Therefore, I only update *w* at 500 m AGL once every 25 of the 500 total iterations so that the scheme converges on a solution.

Since convergence can be concentrated near the surface in supercell storms (Dowell and Bluestein 1997) and especially in tornadoes (Appendix E), the assumption of constant convergence at low levels introduces error into the dual-Doppler synthesis. I considered using the scheme of Mewes and Shapiro (1999), in which the vertical vorticity equation is a constraint for determining vertical velocity at the lowest grid level. (This strategy for incorporating the vorticity equation differs from that mentioned in Section 2.6.) However, this scheme did not give plausible values of vertical velocity at 500 m AGL for the McLean storm data (not shown). This is not surprising given the poor time resolution available with the ELDORA data. Tests by Mewes and Shapiro (1999) also suggest that the vorticity method works best when the layer of missing data near the ground is deeper (≥1500 m).

Since the ELDORA data extend to storm top (e.g., Fig. 2.1.1), the upper boundary condition of w=0 is easier to apply. However, it is harder to justify this constraint. This boundary condition is certainly in error when the storm top is rising or falling. However, the impact of error in this boundary condition (even if it is ~10 m s^{-1}) is small on the vertical velocities at low and mid levels, owing to the great distance from the upper boundary.

I apply the w=0 boundary condition at a height that varies by vertical column, either at z=12 km or at the highest level with 20+ dBZ reflectivity, whichever is greater. (The height z=12 km is the approximate observed height of the top of the storm anvil and lies near the middle of the moderately stable layer around 200 mb in Fig. 1.4.) This accounts for storm tops that protrude much higher than the anvil (Fig. 2.1.1).

Analyses of temperature would complement the dual-Doppler wind syntheses. Since thermodynamic measurements were not collected while the ELDORA was scanning the McLean storm (except by the aircraft itself), I applied a thermodynamic retrieval to the wind fields. I used the traditional method of Gal-Chen (1978) and Hane and Ray (1985), including estimates of velocity time derivatives like in Section 2.6. I also compared the retrievals to others without the time tendency terms. Leaving these terms out did affect the results but did not change the overall structures of the temperature fields.

The results of the thermodynamic retrievals were unacceptable in general (Fig. 2.7.2). For example, at 0.5 km AGL (Fig. 2.7.2.a), the retrievals generally indicated positive buoyancy within the updrafts. Since the storm was lifting stable air at this height (Fig. 1.4), the results should be the opposite. In addition, the retrievals did not show much evidence of a low-level cold pool with the storm.

Aloft, the retrieval at 2318 UTC (Fig. 2.7.2.b) incorrectly does not indicate positive buoyancy within the updrafts. The analysis at 2318 is one of the worst cases, though. Some of the other retrievals did suggest a correlation between positive buoyancy and updrafts aloft, but they also included other implausible noisy features.

Thermodynamic retrievals are very sensitive to estimates of $\partial w / \partial t$ (Crook 1994). With dual-Doppler data, w is typically the most poorly observed velocity component. Furthermore, with poor time resolution in data like those from VORTEX, we cannot compute good estimates of time tendencies. This may be a source of significant error in the thermodynamic retrievals.

3. McLEAN, TEXAS STORM

3.1 Reflectivity Features

The NCAR Electra aircraft arrived at the McLean supercell over 15 minutes before the storm produced the first tornado. At this time, the storm had a large high-reflectivity core with a less intense low-level reflectivity appendage (Fig. 3.1.1.a and b). Such appendages often precede the formation of tornadoes (Forbes 1981). The appendages were hook shaped later on (e.g., Fig. 3.1.1.r).

In the following sections of the text, I will suggest that the McLean storm had a single dominant updraft while the research planes were scanning it. Although the storm was isolated from a complex of other tornadic storms to the north (Fig. 1.6), the McLean storm updraft (cell "A" in Fig. 3.1.1) was anything but isolated from other updrafts. A video recorded from the P-3 aircraft and my personal observations from the ground both indicated a field of abundant towering cumulus near the storm. Many of these clouds persisted beyond the time at which the ELDORA dataset ends (0015 UTC 9 June 1995).

Some of the updrafts near the McLean storm were significant enough to produce precipitation. The most noticeable separate feature is the companion storm that matured to the northwest and west of the McLean storm (Fig. 3.1.1). It is not unusual for supercells to persist side by side (e.g., Brandes et al. 1988). In this particular case, the western member of the pair, which produced only a brief, weak tornado (R. Satkus 1995, personal communication), was less severe than the eastern storm. With surface storm-relative flow from the east (Fig. 1.4), some of the inflow to the western storm was likely outflow from the McLean storm. This may have diminished the magnitude of instability available to the western storm.

At 2247 UTC, new low-level echoes appeared south of the McLean storm (Fig. 3.1.1c). The new region of reflectivity (cell "B") moved northward faster than the main storm (cell "A") and eventually merged into the larger core. At 2249 UTC, raw ELDORA scans indicated neither a bounded weak echo region (BWER) in the reflectivity (Browning and Donaldson 1963, Lemon 1977) nor a convergent velocity signature at low levels in cell "B" (Fig. 3.1.2.b and c). This indicates that the updraft that had produced the precipitation was already dead. The remnant precipitation began to fall into the tornadic region of the McLean storm around the time of the formation of tornado #1 (Fig. 3.1.1.d). However, the timing may have been merely coincidental, as the formation of the first tornado was well underway at this point (Fig. 3.1.2.b and c).

Other reflectivity features associated with separate updrafts are visible only upon close inspection of the images. At 2322 UTC, new echoes at low levels appeared on the southwest side of the McLean storm (Fig. 3.1.1.j and k). Pseudo-dual-Doppler analyses of the storm (later in this chapter) show that although there was one precipitation core aloft associated with the new updraft "C", the low-level echoes initially appeared both east and west of the updraft. In Section 3.2, I will suggest that updraft "C" (Fig. 3.1.2.l) had more important dynamical consequences for the McLean storm than other surrounding updrafts.

The presence of cells "B" and "C", plus the elongation of the southwest side of the main cell at 2317 UTC (Fig. 3.1.1.i), gave the storm an unsteady appearance on the WSR-88D during much of the time that the ELDORA was operating. However, at the end of the ELDORA dataset, the storm did have a rather steady classic supercell appearance (intense round core with a narrow hook-shaped appendage) on radar (Fig. 3.1.1.r). In general, the size of the reflectivity core increased with time (Fig. 3.1.1).

High up, the storm had a dome of reflectivity (e.g., Fig. 2.1.1 and 3.1.2.d) that penetrated above the tropopause level, which was near 14.2 km AGL (Fig. 1.4). The maximum height of the 20-dBZ reflectivity rose from around 17 km AGL to over 19 km AGL during the early stages of tornado #1. For the remainder of the time that the ELDORA scanned the supercell, the storm top height fluctuated between 18 and 19.5 km. Fujita et al. (1976) noted that storm tops tend to collapse at the time when tornadoes form. However, such a phenomenon was not observed in the McLean storm, nor in other cyclic storms studied by Burgess et al. (1982).

Numerous examples of narrow BWERs in reflectivity appear in the ELDORA scans of the McLean storm (Fig. 3.1.2). These are associated with both updrafts and tornadoes. In the former case, the BWER indicates rising air in which precipitation has not yet had time to form (Browning and Donaldson 1963, Lemon 1977), and the reflectivity feature usually corresponds to a deep convergence signature (Lemon and

Burgess 1993) in the radial velocities (Fig. 3.1.2.a, b, and l). In the case of BWERs associated with tornadoes (Fig. 3.1.2.d, e, f, i, and l), the reflectivity minimum is presumably due to centrifuging of precipitation (Appendix E), and the radial velocities in consecutive scans indicate strong cyclonic shear.

3.2 Tornado Formation, Maintenance, and Dissipation

3.2.1 Background

A complete discussion of tornado dynamics is beyond the scope of this section. Instead, the goal here is to introduce a few of the key issues about how tornadoes form and persist. I will begin with a review of relevant dynamical equations.

The equation of motion, with the Coriolis force neglected, is

$$\frac{\partial \vec{v}}{\partial t} = -(\vec{v} \cdot \nabla)\vec{v} - \frac{1}{\rho}\nabla p' + B\hat{k} + \vec{F} \tag{3.2.1}$$

where p' is the perturbation pressure (hydrostatic portion of the base state removed), ρ is the total density, B is buoyancy, F is turbulent friction, and the other variables have their usual meteorological definitions. For the processes considered in this section (with length scales ~1000 m and time scales ~100 s), the Coriolis force should not have a direct impact and is therefore not included.

Analyses of thunderstorm dynamics typically include a Boussinesq approximation in the derivation of the vorticity equation (e.g., Klemp and Rotunno 1983). However, for completeness, I will not make this simplification at the start. (Another motivation is that in the scale analysis below, I am not able to discard the solenoidal term in the horizontal vorticity equation.) One may obtain the full vorticity equation by applying the $\nabla \times$ operator to Equation (3.2.1). The result is

$$\frac{\partial \vec{\omega}}{\partial t} = -(\vec{v} \cdot \nabla)\vec{\omega} + (\vec{\omega} \cdot \nabla)\vec{v} - \vec{\omega}\nabla \cdot \vec{v} - \nabla\left(\frac{1}{\rho}\right) \times \nabla p' + \nabla \times \left(B\hat{k}\right) + \nabla \times \vec{F} \tag{3.2.2}$$

where $\vec{\omega}$ is the 3-D vorticity:

$$\vec{\omega} \equiv (\omega_x, \omega_y, \zeta) \equiv \nabla \times \vec{v}. \tag{3.2.3}$$

The derivation of (3.2.2) required two vector identities: $(\vec{A} \cdot \nabla)\vec{A} = (\nabla \times \vec{A}) \times \vec{A} + \frac{1}{2}\nabla(\vec{A} \cdot \vec{A})$ and $\nabla \times (\vec{A} \times \vec{B}) = \vec{A}\nabla \cdot \vec{B} + (\vec{B} \cdot \nabla)\vec{A} - \vec{B}\nabla \cdot \vec{A} - (\vec{A} \cdot \nabla)\vec{B}$.

Expansion of the terms in Equation (3.2.2) on a component-by-component basis produces a few that cancel. The resulting equations are

$$\frac{\partial \omega_x}{\partial t} = -(\vec{v} \cdot \nabla)\omega_x + \left(\frac{\partial v}{\partial x}\frac{\partial u}{\partial z} - \frac{\partial w}{\partial x}\frac{\partial u}{\partial y}\right) - \left(\frac{\partial v}{\partial y} + \frac{\partial w}{\partial z}\right)\omega_x + F_{\omega_x} + \frac{1}{\rho^2}\left(\frac{\partial p'}{\partial z}\frac{\partial \rho}{\partial y} - \frac{\partial p'}{\partial y}\frac{\partial \rho}{\partial z}\right) + \frac{\partial B}{\partial y} \tag{3.2.4}$$

$$\frac{\partial \omega_y}{\partial t} = -(\vec{v} \cdot \nabla)\omega_y + \left(\frac{\partial w}{\partial y}\frac{\partial v}{\partial x} - \frac{\partial u}{\partial y}\frac{\partial v}{\partial z}\right) - \left(\frac{\partial u}{\partial x} + \frac{\partial w}{\partial z}\right)\omega_y + F_{\omega_y} + \frac{1}{\rho^2}\left(\frac{\partial p'}{\partial x}\frac{\partial \rho}{\partial z} - \frac{\partial p'}{\partial z}\frac{\partial \rho}{\partial x}\right) - \frac{\partial B}{\partial x} \tag{3.2.5}$$

$$\frac{\partial \zeta}{\partial t} = -(\vec{v} \cdot \nabla)\zeta + \left(\frac{\partial u}{\partial z}\frac{\partial w}{\partial y} - \frac{\partial v}{\partial z}\frac{\partial w}{\partial x}\right) - \left(\frac{\partial u}{\partial x} + \frac{\partial v}{\partial y}\right)\zeta + F_{\zeta} + \frac{1}{\rho^2}\left(\frac{\partial p'}{\partial y}\frac{\partial \rho}{\partial x} - \frac{\partial p'}{\partial x}\frac{\partial \rho}{\partial y}\right). \tag{3.2.6}$$

The first term on the right-hand side of each equation represents advection of vorticity. The physical meaning of the second term is tilting of the orientation of vorticity from one direction into another. The third term, commonly called the "stretching" or "convergence" term, is a representation of conservation of angular momentum. Term four in each equation is turbulent mixing of vorticity. The fifth term is solenoidal generation, which describes how a perturbation pressure gradient force accelerates air parcels of different densities at different rates. The horizontal vorticity equations each contain a sixth term – baroclinic generation of vorticity owing to a gradient in buoyancy.

For a scale analysis of the terms in the vertical vorticity equation applied to a thunderstorm updraft and mesocyclone (Heymsfield 1978), I will assume that velocities are ~10 m s^{-1} and that variations occur over a length of ~1 km. In addition, I will assume that $p' \sim 1$ mb, $\rho \sim 1.0$ kg m^{-3}, and that horizontal variations in density are ~0.01 kg m^{-3} km^{-1} (corresponding to a temperature gradient ~3 K km^{-1}). In this case, the advection, tilting, and stretching terms on the right-hand side of (3.2.6) are all ~10^{-4} s^{-2}. In contrast, the solenoidal term is much smaller (~10^{-6} s^{-2}) and should be negligible in most cases. The mixing term is more difficult to quantify, but it is likely that this effect is most significant very close to the surface and in the turbulent upper levels of the storm (Lewellen 1993).

Similar terms appear in the horizontal vorticity equations. The advection, tilting, and stretching terms are ~10^{-4} s^{-2}. However, there is a significant difference between the solenoidal terms in the horizontal vorticity equations and those in the vertical vorticity equation. Terms in both (3.2.4) and (3.2.5) involve $\frac{\partial \rho}{\partial z}$, which is typically an order of magnitude greater (~0.1 kg m^{-3} km^{-1}) than horizontal density variation. Therefore, the solenoidal effect is more important in generating horizontal vorticity than in generating vertical vorticity. The solenoidal terms involving $\frac{\partial \rho}{\partial z}$ in Equations (3.2.4) and (3.2.5) are ~10^{-5} s^{-2}, which is great enough to be significant in certain situations. However, for some of the simple scenarios I can envision (not shown), the $\frac{\partial p'}{\partial z}\frac{\partial \rho}{\partial y}$ and $-\frac{\partial p'}{\partial y}\frac{\partial \rho}{\partial z}$ terms in (3.2.4) would tend to oppose each other. (The same is true for the other horizontal vorticity equation). The solenoidal terms are likely of secondary importance but can not be discarded completely.

For a strong temperature gradient (~3 K km^{-1}), the baroclinic generation terms in Equations (3.2.4) and (3.2.5) can be as great as ~10^{-4} s^{-2}. Complex dynamics are embedded in these seemingly simple terms (Fig. 3.2.1). The primary forcing is the acceleration by buoyancy, which acts to increase the horizontal vorticity by inducing a horizontal gradient of vertical motion. A secondary circulation is forced by hydrostatic perturbation pressure gradients associated with the buoyancy field. In the vertical, the pressure forcing acts in the opposite direction of the buoyancy, diminishing what the vertical motions would have been as a result of buoyancy alone. However, accelerations associated with the same pressure field increase the vertical shear of the horizontal wind, thus producing horizontal vorticity with the same sense as from the vertical motion. The reason I emphasize the secondary circulation is that it is the vertical shear portion of horizontal vorticity ($\frac{\partial u}{\partial z}$ and $\frac{\partial v}{\partial z}$) that eventually enters into the tilting terms in the vertical vorticity equation. A vertical velocity gradient tilts horizontal vorticity associated with the vertical shear; the vertical shear does *not* tilt the horizontal vorticity associated with the vertical velocity gradient.

Following the convention of Fujita (1981), "mesocyclone" will refer here to a vortex with horizontal dimensions of greater than 4 km and vertical vorticity ~0.01 s^{-1}. The upper end of the mesocyclone size range (400 km) as defined by Fujita (1981) greatly exceeds thunderstorm scales, so in the present discussion I will be focusing on mesocyclones at the extreme low end of the scale. Tornadoes themselves are concentrated regions of rotation with diameters ~100 m to ~1000 m and vertical vorticity ~0.1 s^{-1} to ~10 s^{-1} (Fujita 1981). The size may or may not be related to the size of the visible condensation funnel (Davies-Jones 1986).

Since Browning (1964) first described the basic airflow within supercells, there have been numerous studies attempting to explain how rotation develops in a storm. The general consensus of these studies is that a mesocyclone first develops aloft in storms as a result of tilting of horizontal vorticity into the vertical by the updraft (Browning and Landry 1963, Barnes 1968, Lilly 1982, Brandes 1984b, Rotunno and Klemp 1985). The instantaneous tilting of a vortex line by an updraft produces a vertical-vorticity pair at the sides of the updraft, with one vortex cyclonic and the other anticyclonic (Fig. 3.2.2.a). After this tilting begins, non-linear effects then become important. If there is updraft-relative flow along the direction of the horizontal vorticity (i.e., streamwise horizontal vorticity), then the vertical vorticity and updraft tend to be more correlated (Fig. 3.2.2.b). In the convergent flow beneath the updraft maximum, the vertical vorticity can be further amplified by stretching (Rotunno 1981). In addition, the development of mesolows aloft associated with the vortices enhances the upward motion beneath them and promotes lateral propagation of the updraft (Rotunno and Klemp 1982, Weisman and Klemp 1984).

Nearly 30 years after the first organized tornado research field programs (Bluestein and Golden 1993), the development of rotation at low levels (in particular, the formation of tornadoes) remains as controversial as ever. Low-level rotation tends to develop later than that aloft but tends to be stronger (Brandes 1978, Rotunno and Klemp 1985). Most numerical simulations (e.g., Rotunno and Klemp 1985, Adlerman et al. 1999) have produced strong low-level vorticity maxima that are still too weak to be classified as tornado-like. Simulating a vortex of tornadic intensity within a full thunderstorm model (Wicker and Wilhelmson 1995, Grasso and Cotton 1995) continues to be an ambitious task. However, I believe that the general concepts from the simulations are applicable to the discussion of tornadogenesis. The formation of realistic tornado structures in the simulations may simply require higher resolution and better treatment of the no-slip condition in the boundary layer (Rotunno 1993).

The exponential nature of amplification by the stretching term in the vertical vorticity equation makes it the most plausible explanation for how vertical vorticity can increase to the unusually large values characteristic of tornadoes. Thus, the ingredients for tornadogenesis are vertical vorticity and convergence (Lewellen 1993). Laboratory simulations have shown that the structure of a vortex itself is even related to the ratio of the two (Ward 1972, Davies-Jones 1973). However, we are yet to determine the general relationship between tornado formation and storm-scale processes. In particular, some of the key questions are:

- What is the source of the vertical vorticity in tornadoes, and does it vary from storm to storm?
- Why do most supercells *not* produce tornadoes? In other words, which of the two ingredients (vorticity and convergence) is missing, and why?

Rasmussen and Straka (1997) summarize a number of theories of tornadogenesis. I will discuss the major points from a few of them here.

In one theory, Wakimoto and Atkins (1996) and Wakimoto et al. (1998) imply that many tornadoes in supercells form as the convergent bottom of the updraft concentrates vertical vorticity from a source independent of the storm. For example, Wakimoto et al. (1998) argue that the low-level mesocyclone of the 16 May 1995 Garden City storm "began as an incipient shallow circulation along a synoptic scale trough." The simple concentration of pre-existing vertical vorticity by an updraft, which is the same process that apparently produces many non-supercell tornadoes (Brady and Szoke 1989, Wakimoto and Wilson 1989), is not widely accepted as a mechanism for producing a majority of significant supercell tornadoes.

Many other tornadogenesis theories involve a two-step process. The first step is tilting of horizontal vorticity into the vertical, and the second is amplification of the vertical vorticity by stretching at the base of an updraft (Brandes 1984b, Rotunno and Klemp 1985, Davies-Jones and Brooks 1993, Walko 1993, Wicker and Wilhelmson 1995, Rasmussen and Straka 1997). The controversy in these tornadogenesis theories centers on the nature of the horizontal vorticity and on the configuration of the vertical motion field that accomplishes the tilting.

In the discussion of horizontal vorticity, I will distinguish between "barotropic" and "baroclinic" sources, in a similar manner to Davies-Jones and Brooks (1993). "Baroclinic" refers to horizontal vorticity produced by the temperature gradient (Fig. 3.2.1) within a storm's pool of rain-cooled air. "Barotropic" instead refers to horizontal vorticity available to the updraft in the inflow from the environment. The latter term does not imply that the original source of horizontal vorticity was not baroclinic, merely that it was not influenced directly by the storm's cold pool. For example, a temperature gradient beneath the edge of the McLean storm anvil may have enhanced the horizontal vorticity in the low-level inflow (Markowski et al. 1998). However, this source would still be classified as "barotropic" here because it originated far away from the updraft and from the rain-cooled air. Storms may also modify the low-level shear by accelerating the low-level inflow (Weisman et al. 1998). For the P-3 legs flown in east-west directions at low levels to the south of the McLean storm, in situ measurements generally indicated the highest wind speeds in those portions of the legs closest to the main updraft (not shown). Again, this is a barotropic process.

The first multiple-Doppler studies of tornadic storms (e.g., Brandes 1978) focused primarily on qualitative relationships between the tornado and the parent storm. Detailed attempts to diagnose the formation of low-level rotation in supercells did not begin in earnest until numerical simulations began to reproduce some of the low-level features seen originally in the Doppler analyses. The analysis of a numerical simulation by

Klemp and Rotunno (1983) and Rotunno and Klemp (1985) yielded the unsuspected result that the low-level rotation originated from baroclinic horizontal vorticity. Before the mid 1980's, this source had been primarily neglected.

Rotunno and Klemp (1985) simulated a storm in an environment with unidirectional shear. The vortex lines in the low-level southeasterly storm inflow pointed toward the north owing to the westerly shear (Fig. 3.2.3). (For the discussion of storm dynamics in this section, I will use compass directions, rather than "upshear", "downshear", etc. I will assume that the storm is moving eastward.) However, this air primarily fed the updraft and mesocyclone aloft. The flow into the *low-level* vortex came from the northeast, where the vortex lines pointed toward the southwest (along the direction of the flow). A temperature gradient existed in this inflow region between the warm environmental air and the air cooled by precipitation within the storm. Baroclinic generation reoriented the vortex lines and increased their magnitude (Fig. 3.2.3). When the horizontal vorticity reached the updraft, it was first tilted into the vertical and then stretched.

A highlight of the baroclinic theory for low-level vortex formation (Rotunno and Klemp 1985) is that it would appear to explain why low-level rotation develops much later than rotation aloft. It simply takes time for precipitation to form and for the low-level baroclinic zone to develop. Recent work has continued to highlight the importance of baroclinically-generated horizontal vorticity for low-level vortex formation (Davies-Jones and Brooks 1993, Adlerman et al. 1999).

Some researchers working primarily with observations have not been convinced of the necessity of baroclinic horizontal vorticity for tornadogenesis. In a study of the 8 June 1974 Harrah storm by Brandes (1984a), the configuration of the retrieved buoyancy field relative to the flow direction was inconsistent with the Rotunno and Klemp (1985) theory. More recently, Dowell and Bluestein (1997) argued that barotropic low-level horizontal vorticity in the environment of the 17 May 1981 Arcadia storm (plus possible enhancement by stretching in the inflow) may have been a sufficient source of rotation for the low-level mesocyclone. In both of the storms, the low-level horizontal vorticity in the environment was stronger than in the simulated storm (Rotunno and Klemp 1985), and the orientation of the barotropic horizontal vorticity (toward the west-southwest) was already along the direction of storm-relative inflow into the low-level mesocyclone. However, errors and gaps in observations such as those in the Harrah and Arcadia cases make it difficult to obtain definitive conclusions from real data (Johnson et al. 1987).

A few numerical simulations have added some fuel to the argument that baroclinic generation of horizontal vorticity is not necessary to produce rotation near the surface. In a pseudo-storm numerical experiment by Walko (1993), the source of rotation in a low-level vortex was barotropic horizontal vorticity associated with the environmental shear. The vortex was embedded in a temperature gradient, as would be expected based on potential vorticity considerations (Rotunno and Klemp 1985). However, baroclinic effects acted to *diminish* the magnitude of the rotation in this particular case.

Wicker (1996) considered the impact of the environmental wind shear over the lowest two grid levels on full thunderstorm simulations. He concluded that the magnitude and direction of the low-level barotropic horizontal vorticity strongly modulated the eventual low-level evolution, and that the strongest low-level vortices formed when the barotropic and baroclinic contributions were in phase.

A logical conclusion from the argument over the vorticity source may be that the importance of barotropic versus baroclinic horizontal vorticity varies from one storm to the next. Understanding how much the two sources vary, and how much they complement or counteract each other, will likely be necessary if we are to predict which supercells will produce tornadoes and which will not.

It has long been observed that tornadoes form in a region of strong vertical velocity gradient between the updraft and a rear downdraft that wraps around the back side of the updraft (Fig. 3.2.4) (Lemon and Doswell 1979). Early discussions of the rear downdraft (e.g., Lemon and Doswell 1979, Brandes 1984b) implied at best a secondary role of the downdraft in tornadogenesis. (Enhanced convergence at the edge of spreading outflow air from the rear downdraft is an example of a secondary role.) In more recent studies, Davies-Jones and Brooks (1993) and Walko (1993) have demonstrated that the downdraft may play a primary role by providing the vertical velocity gradient that originally tilts horizontal vorticity into the vertical. It is the sign of the vertical velocity *gradient*, rather than the sign of the vertical velocity itself, that matters in the tilting term in Equation (3.2.6).

The process of tilting in a downdraft has typically been demonstrated in terms of the circulation about a curve moving with the fluid (Rotunno and Klemp 1985, Davies-Jones and Brooks 1993, Walko 1993) (Figure 3.2.5). Circulation is defined by

$$C \equiv \oint \vec{v} \cdot d\vec{l} = \int_A \vec{\omega} \cdot d\vec{A} \tag{3.2.7}$$

where the integration is along a closed path, $d\vec{l}$ is a length element along the path, A is a region bounded by the path, and $d\vec{A}$ is an area element vector normal to this region. The right-hand side of Equation (3.2.7) is by Stokes' theorem, which states that circulation is equivalent to the vorticity flux through a surface traced out by the circuit. By Bjerknes' theorem

$$\frac{dC}{dt} = \oint B\hat{k} \cdot d\vec{l} \tag{3.2.8}$$

circulation about a material curve in inviscid Boussinesq flow is altered only by baroclinic effects.

In the particular example in Fig. 3.2.5, a component of the horizontal vorticity is normal to the initially tilted circuit. Therefore, the circuit starts with a nonzero circulation. In the absence of a baroclinic contribution, this circulation is conserved as the vertical velocity gradient near the edge of a downdraft tips the circuit so that it becomes horizontal. (Equivalently, some of the horizontal vorticity is tilted into the vertical.) Since tilting occurs in a low-level downdraft, some of the vertical vorticity is destroyed by divergence. Therefore, if this process is to be significant, it must occur over a broad region in order to produce a large amount of circulation about a vertical axis (Walko 1993).

In the final step of tornadogenesis in the Walko (1993) and Davies-Jones and Brooks (1993) theories, the horizontal flow advects the vertical vorticity (which was created by tilting in the downdraft) into the convergent base of an updraft, where it is strongly stretched (Fig. 3.2.5). Therefore, these theories require a complicated scenario involving air passing from the bottom of a downdraft to the base of a nearby updraft. In the simulated thunderstorm, this scenario occurs along trajectories that approach the tornado from the north or northwest (Fig. 3.2.4).

A key argument for the importance of the downdraft mechanism is that the updraft-only process described by Rotunno and Klemp (1985) cannot explain rotation close to the ground. Since the updraft-only process occurs in rising air, the air parcels are far from the surface by the time tilting and stretching have produced significant vertical vorticity (Davies-Jones and Brooks 1993, Walko 1993). Instead, if the downdraft is the agent for tilting horizontal vorticity into the vertical, then air parcels near the surface already have vertical vorticity when they later enter the convergent base of an updraft.

The process of tilting upstream of the updraft in the Davies-Jones and Brooks (1993) simulation does not actually differ significantly from that in the original Rotunno and Klemp (1985) simulation. The real difference is in the interpretation. The analysis by Rotunno and Klemp (1985) does show trajectories descending into the low-level vorticity maximum; however, the authors did not highlight the process of tilting in the descending inflow.

An attractive feature of the tornadogenesis theories with a downdraft is that they also explain why it takes a while for rotation to develop at low levels. It simply takes time for the storm to form a downdraft next to the updraft, in a location where air passes from the former to the latter. The complexity of the required flow structure may be a clue why many storms fail to produce tornadoes.

Once a tornado has formed, it will persist as long as it is the focus of a convergent velocity field with significant circulation. Low pressure associated with the tornado sustains the convergence by accelerating parcels inward until they approach cyclostrophic balance (Ward 1972). Close to the surface, where cyclostrophic balance is disrupted by friction, air penetrates closer to the center of the circulation than it would have otherwise (Lilly 1969, Ward 1972, Lewellen 1993). Observations and numerical experiments (Hoecker 1960, Lewellen 1993, Fiedler 1993) indicate that the convergent layer in which the rotation spins up becomes very shallow (tens of meters deep) near the surface.

If the low-level mass convergence is not to fill the circulation, then upward exhaust of mass from the boundary layer is necessary. Buoyancy is the overall driving force of the exhaust (Lilly 1969, Smith and Leslie 1979, Lewellen 1993). However, supercell tornadoes tend to occur in stable boundary layers (Fig. 1.4) below the level of free convection (LFC). Therefore, an upward-directed perturbation pressure gradient force is required to lift air parcels to their LFC. Such a pressure gradient is associated with the magnitude of convergence decreasing with height and/or the magnitude of rotation increasing with height (Weisman and Klemp 1984, Trapp and Davies-Jones 1997).

The most common explanation for tornado dissipation is that cold outflow (which is too negatively buoyant to be lifted) is drawn into the circulation (Lemon and Doswell 1979, Brandes 1981, Burgess et al. 1982, Klemp 1987, Adlerman et al. 1999). Another possibility is that the tornado simply loses its source of vertical vorticity.

A vorticity budget for the McLean storm will not be possible owing to poor time resolution, missing data near the surface, and a lack of thermodynamic measurements. However, the dual-Doppler wind syntheses contain clues for a qualitative analysis of whether the evolution is consistent with the proposed mechanisms of tornadogenesis.

3.2.2 Pre-Tornadic and Tornadic Stages

The McLean storm already had rotation both aloft and at the surface (Fig. 3.2.6.a) when the Electra aircraft first arrived. Although the ELDORA dataset does not capture the development of the first low-level rotation, it does begin 15 min before the formation of the first visible tornado.

During the early aircraft passes, the updraft structure was particularly unsteady. The analyses from the first two passes show two updrafts on the southwest side of the storm (Fig. 3.2.6.a and 3.2.6.b at 4.0 km AGL, Fig. 3.2.7.a). (The separation between the updrafts during the first pass shows up more clearly in the single-Doppler scans [Fig. 3.1.2.a] than in the smoother dual-Doppler analysis [Fig. 3.2.6.a].) By the time of the fourth aircraft pass, this structure was gone, and the storm had a single rotating updraft aloft (Fig. 3.2.6.d). This early evolution is inconsistent with Browning's (1964) unicellular model of a supercell, but it is not surprising in light of more recent observations (e.g., Weaver and Nelson 1982). Since the time of Browning's paper, the term "supercell" has come to refer to a process in which perhaps multiple updrafts during the lifetime of a storm are correlated with vertical vorticity, and in which rightward movement (relative to the shear) of the updraft(s) is enhanced by dynamically induced vertical pressure gradients associated with a mesolow (Weisman and Klemp 1984).

It is not entirely clear what was process was occurring early on. The most plausible explanation to me is that a new updraft pulse had just begun forming to the southeast of the older portion of the updraft. Then, the new updraft became the dominant feature by 2248 UTC. The formation of a new vortex couplet aloft with the southeastern updraft (Fig. 3.2.6.b) between the times of the first and second aircraft passes is consistent with a new updraft beginning to tilt horizontal vorticity and/or advect vertical vorticity upward from below. Another clue is provided by a change in the northwestern updraft. At 2242 UTC (Fig. 3.2.6.b, Fig. 3.2.7.a), the roots of the updraft were not as close to the surface as they had been at 2236 UTC (near x=-19, y=-21 in Fig. 3.2.6.a). The loss of low-level roots is compatible with the description of the northwestern updraft as a dissipating feature.

The pre-tornadic parent vortex of tornado #1 extended upward through the west side of the southeastern updraft at 2242 UTC (Fig. 3.2.6.b). By 2249 UTC, this portion of the storm had an unusual reflectivity structure (Fig. 3.1.2.b) that has previously not been documented in other studies. There was a "bump" in a reflectivity streamer extending southward from the storm; the location of this feature is marked with a "B" in the horizontal cross sections (Fig. 3.2.6.b and c). It appears that falling precipitation in the reflectivity appendage at low levels (Fig. 3.2.6.b at z=0.5 km) was blown southward in the northerly winds (in a storm-relative sense). Then, it was drawn back up by the growing southeastern updraft (Fig. 3.2.6.b at z=4.0 km). This reflectivity structure persisted into the next aircraft pass (Fig. 3.2.6.c at z=4.0 km) but was not apparent in the following pass, when it was masked by precipitation from cell "B" approaching the McLean storm from the south (Fig. 3.1.1, Fig. 3.1.2.b and c, Fig. 3.2.6.d).

Although there was a closed circulation at low levels at 2236 UTC (Fig. 3.2.6.a), the vortex was not strong enough to produce noticeable damage at this stage according to *Storm Data* (U. S. Dept. of Commerce 1995). The vorticity maximum did not have a visible tornado condensation funnel associated with it until 2252 UTC. The eventual tightening of the vortex into a tornado is not clear in the smooth dual-Doppler analyses (Fig. 3.2.6) but is apparent in the single-Doppler scans (Fig. 3.1.2).

The single-Doppler depiction of the formation of tornado #1 (Fig. 3.1.2.b-e) is similar to that for the other two major tornadoes (Fig. 3.1.2.g-l). In the pre-tornadic stage, the circulation was broad and confined primarily below 5 km AGL (Fig. 3.1.2.b and c). During the mature stage, the wind speeds were higher, the horizontal scale of the circulation was slightly less (~800 m wide) (Table 1.3), and the circulation extended through a greater depth (Fig. 3.1.2.d and e). The single-Doppler scans show evidence of tornado #1 very high in the storm during the mature stage (14 km AGL in Fig. 3.1.2.e); the same was true for tornadoes #2 and #4 (not shown). The Doppler slices through the tornado at high elevation angles (Fig. 3.1.2.d and e) cross from one side of the vortex to the other owing to the tilts of both the tornado and of the conical radar sweeps.

To determine the exact locations of the tornadoes in the figures, I computed the locations of the tornado signatures in the raw ELDORA scans relative to the origin of the dual-Doppler grid. (The distinguishing features of the tornadoes are the BWER in reflectivity and the strong cyclonic shear in velocity.) I also verified these locations against known points of damage at the surface. To determine the times along the damage path, I had to visit the sites from which photographs and videos of the tornadoes were taken. After documenting the location of each site, I recorded a compass reading of the line of sight to the tornado, based on features in the foreground of the photos and videos.

A comparison of the tornado location to the dual-Doppler analysis reveals that tornado #1 formed on the south side of an elliptical (Brandes 1977b) low-level circulation (Fig. 3.2.6.d, Fig. 3.2.8.c). The dual-Doppler analysis at 500 m AGL indicates small values of vertical velocity in the tornado #1 location, as it does also for the tornadoes in later analyses (Fig. 3.2.6). Presumably, there was a strong low-level updraft associated with the tornado circulation itself, but its roots were too small and shallow to be resolved (Appendix E). The maximum wind speeds around the tornado at 500 m AGL at 2254 UTC are only ~25 m s^{-1} (ground-relative) in the dual-Doppler analysis, which is weaker even than some of the storm inflow at this level (Fig. 3.2.6.d). However, winds in the tornado, as measured by the single-Doppler scans, were as high as 60 m s^{-1} (Table 1.3).

It would be desirable to know the source of rotation for tornado #1, and to understand why it took so long for the tornado to form, given that there was already a significant low-level circulation 16 min previously (Fig. 3.2.6.a). However, these are challenging questions, especially given the start of the dataset after the first development of the low-level rotation and the lack of observations below 500 m AGL. The horizontal vorticity plots from the early aircraft passes don't help clarify the situation because they are so dissimilar (Fig. 3.2.8.a-c). At 2236 UTC, the analysis indicates that the strongest horizontal vorticity was on the east side of the updraft (Fig. 3.2.8.a). Six minutes later, the horizontal vorticity was greatest in magnitude on the northwest side of the updraft (Fig. 3.2.8.b), which is where vorticity is typically enhanced by a low-level baroclinic zone (Fig. 3.2.3). Twelve minutes later, just after the formation of tornado #1, the horizontal vorticity was equally intense in both regions (Fig. 3.2.8.c), although the overall magnitudes had decreased somewhat. Some of the changes are related to the distance from the plane to the storm, which was greater between 2248-2318 UTC than during the first two aircraft passes. (At long ranges, the wider beamwidth smoothes the sharp velocity gradient at low levels.) However, the range to the storm was similar during the first two passes.

Wicker and Wilhelmson (1995) suggest that tornadogenesis follows an updraft pulse above cloud base, which is itself forced dynamically by increasing mesocyclone rotation aloft. This process probably occurs too quickly (over a period of ~5 min) (Wicker and Wilhelmson 1995) to be resolved in data like those of the McLean storm. The scenario depicted in the McLean storm dual-Doppler analyses appears to be more one of increasing overall storm organization during the formation stage of tornado #1. Vertical velocity at 4 km and rotation in the updraft both increased significantly during this stage (Fig. 3.2.6.a-d at z=4.0 km, Fig. 3.2.9), but there is no clear evidence of a response (a "pulse") in the low-level vertical velocities (Fig. 3.2.9.a). I chose the criteria for identifying the updraft regions (Fig. 3.2.9.b) so that the areas of the updraft would be roughly the same at each height for the majority of analysis times. However, at 2248, 2259, 2306, 2338, and 2356 UTC, the area at 4.0 km was over 50% larger than below. At the other times, the plots of average vertical vorticity may be more appropriately related to vertical profiles of rotation in the updraft. At all of these times, updraft rotation generally increased with height. The formation stage of tornado #1 also coincided with increases with time in updraft rotation at all levels (Fig. 3.2.9.b).

At low levels, the most significant storm-scale changes appear to be an increasing amount of precipitation to the west of the vorticity maximum (Fig. 3.2.6.b and c) and increasing northerly winds to the north and west (Fig. 3.2.6.b-d). Low-level rear-flank downdrafts (Fig. 3.2.4) in these locations tended to be weak in all of the dual-Doppler analyses (Fig. 3.2.6). In the figures, the downdrafts are often too weak to make the first level of shading. (If the layers of divergence beneath the downdrafts were shallow, then the missing Doppler data below 500 m would introduce serious errors in the analysis.) However, the tornado did form near the nose of the rear downdraft (Fig. 3.2.6.d, Fig. 3.2.8.c) at the time when the rear downdraft became more prominent.

If the rear downdraft is a key ingredient in tornadogenesis (Walko 1993, Davies-Jones and Brooks 1993), then this begs the question of why the downdraft itself forms. Both negative buoyancy and downward-directed pressure gradient forces are potential candidates for inducing a rear downdraft (Lemon and Doswell 1979, Klemp and Rotunno 1983). The analysis of Klemp and Rotunno (1983) implies that much of the rear downdraft is supported by cooling from evaporation of rain, while a small portion of it (the "occlusion downdraft") (Fig. 3.2.4) is dynamically forced by low pressure associated with strong rotation near the ground. In contrast, Lemon and Doswell (1979) and Dowell and Bluestein (1997) attribute some of the downward acceleration in portions of the rear downdraft to the development of high pressure aloft.

In the McLean storm, the increase in low-level northerlies to the north and west of the pre-tornadic circulation (Fig. 3.2.6.b-d) is consistent with an increase in outflow from the west side of the precipitation core. However, the microphysical reasons for an outflow increase at this time are beyond what can be explained with this dataset.

To consider the effect of pressure forcing, I applied a retrieval of the dynamic pressure to the dual-Doppler analyses, with the dynamic pressure partitioned into three individual contributions (Klemp and Rotunno 1983):

$$\begin{aligned}\nabla^2 p_{dn} &= -\nabla \cdot \left[\rho(\vec{v}\cdot\nabla)\vec{v}\right] \\ &= -\rho\left[\left(\frac{\partial u}{\partial x}\right)^2 + \left(\frac{\partial v}{\partial y}\right)^2 + \left(\frac{\partial w}{\partial z}\right)^2 - w^2\frac{d}{dz}\left(\frac{1}{\rho}\frac{d\rho}{dz}\right)\right] \quad \text{"fluid extension"} \\ &\quad -2\rho\left[\frac{\partial v}{\partial x}\frac{\partial u}{\partial y}\right] \quad \text{"curvature"} \\ &\quad -2\rho\left[\frac{\partial u}{\partial z}\frac{\partial w}{\partial x} + \frac{\partial v}{\partial z}\frac{\partial w}{\partial y}\right] \quad \text{"shear"} \\ &= \nabla^2 p_e + \nabla^2 p_c + \nabla^2 p_s.\end{aligned} \tag{3.2.9}$$

I have more confidence in this retrieval of pressure than in that of buoyancy (Section 2.7) because this retrieval does not depend on time derivatives of the velocities, except in the side boundary conditions (Klemp and Rotunno 1983).

The northeast-to-southwest oriented portion of the low-level downdraft far away from the tornado (Fig. 3.2.6.d) does *not* appear to be associated with a downward-directed dynamic perturbation pressure gradient force (Fig. 3.2.10). In contrast, the northwest-to-southeast oriented portion closer to the tornado (Fig. 3.2.6.d) *is* nearly coincident with a maximum in the $\partial p_{\mathrm{dn}} / \partial z$ field.

Dowell and Bluestein (1997) noted the development of convergence and deformation aloft to the west and south of the intensifying mesocyclone in the Arcadia storm (17 May 1981). Convergence involves negative forcing in Equation (3.2.9) through the fluid extension term. Deformation also involves negative forcing (but in the curvature term). Therefore, each flow characteristic tends to be associated with a local maximum in dynamic pressure. The development of a high pressure center aloft induces downward acceleration below it. This mechanism seems to apply to the McLean storm as well. As the mesocyclone aloft matured (Fig. 3.2.6.a-d at z=4.0 km), a storm-relative stagnation point (Lemon and Doswell 1979) developed west of the mesocyclone (near x=-14, y=-12 in Fig. 3.2.6.d at z=4.0 km). This is near the location of the ridge in $\partial p_{\mathrm{dn}} / \partial z$ below.

The pre-tornadic stages of the other two large tornadoes (#2 and #4) are similar to each other and are more completely captured in the ELDORA dataset. At 2254 UTC, a gust front with strong convergence along it surged ahead of the developing tornado #1

(Fig. 3.2.6.d at z=0.5 km). During the next aircraft pass, when tornado #1 was at its mature stage (Fig. 1.8.a), the convergence along the gust front was weaker (Fig. 3.2.6.e). However, the subtle first step of cyclic tornado formation had already begun. At low levels, there was a local region of cyclonic curvature and shear (marked "V2" in Fig. 3.2.6.e and Fig. 3.2.8.d) in a southeastern lobe of the updraft. This new vorticity maximum was already a deep feature and was more prominent aloft at this stage (Fig. 3.2.11.d) as a small local maximum in cyclonic flow within the larger mesocyclone (Fig. 3.2.6.e). An increase in vorticity with height (observed also preceding tornado #4 [Fig. 3.2.11.g]) is a common feature of pre-tornadic vortices (Brandes 1978, Dowell and Bluestein 1997). Such a distribution favors further intensification of vortices because the associated dynamically induced pressure gradient force induces lift (and thus convergence) within the low-level air (Leslie 1971, Smith and Leslie 1979, Trapp and Davies-Jones 1997).

During the aircraft pass at 2306 UTC, the new low-level vorticity maximum was no longer a subtle feature (Fig. 3.2.6.f, Fig. 3.1.2.g and h). Although a condensation funnel was not yet observed at the ground, there was already a well developed circulation. Vortex #2, which had initially formed on the southeast side of the low-level updraft (Fig. 3.2.6.e at z=0.5 km), was now on the western side of the overall main updraft area and south of the updraft maximum (Fig. 3.2.6.f). Farther southwest, the weakening tornado #1 had fallen behind the main updraft. The vertical velocity band from its south to its northwest was apparently at the leading edge of an outflow feature.

Seven minutes later, the single-Doppler data (Fig. 3.1.2.i) and the pseudo-dual-Doppler analysis (Fig. 3.2.6.g) both indicated a tighter vortex. At this time, there was a significant, expanding tornado condensation funnel (Fig. 1.8.b and 1.8.c). Maximum velocities in the raw single-Doppler scans of tornado #2 were 52 m s^{-1} at this time (Table 1.3). As was the case with the first tornado, the tornado formed on the extreme back (west) side of the updraft in the vertical velocity gradient between the updraft and weak rear downdraft.

As tornado #2 formed, the gust front bowed out to its east (Fig. 3.2.6.f and g). The same evolution as before was beginning to occur east of the mature tornado. At low levels, there was a new region of weak cyclonic vorticity ("V4" in Fig. 3.2.6.g and Fig.

3.2.8.e) on the east side of the updraft. Aloft, this new vorticity maximum was already much stronger (Fig. 3.2.6.g).

Low-level rotation slowly increased with time in the new vortex (Fig. 3.2.6.h-k), which eventually became tornado #4 (Fig. 1.8.e). The brief tornado #3 (Fig. 1.8.d) was also apparently embedded within the new parent vortex but occurred while the Electra was turning around after the 2318 UTC pass. The beginnings of vortex #4 (Fig. 3.1.2.j and k) in the single-Doppler data look much like those for tornado #2 (Fig. 3.1.2.g and h). The clues that a tornado was about to form were the small region of anomalous inbound (northerly) velocities at low levels and the enhancement in outbound (southerly) velocities just to the east.

For a northeastward moving storm, baroclinic generation of horizontal vorticity typically occurs in inflow to the updraft from the north because this is the location where environmental air and rain-cooled air meet (Fig. 3.2.3) (Rotunno and Klemp 1985, Davies-Jones and Brooks 1993). However, new low-level vorticity maxima in the McLean storm formed in *southeasterly* inflow into the *east* side of the updraft, suggesting that the source air was purely environmental (Fig. 3.2.6.e and 3.2.6.g, Fig. 3.2.8.d and e). One might argue that the flow parallel to the reflectivity contours at 2313 UTC (east of the updraft in Fig. 3.2.6.g) and later was along a baroclinic zone. However, the horizontal vorticity field in the inflow was rather uniform and did not appear to be enhanced along the edge of the reflectivity core (Fig. 3.2.8.e).

The pattern of the low-level horizontal vorticity field in the McLean storm (Fig. 3.2.8.d-g, Fig. 3.2.12.b) is unlike that in many numerical supercell simulations (Fig. 3.2.12.a). In the Klemp and Rotunno (1983) simulation, low-level horizontal vorticity was approximately five times weaker in the environment than in the baroclinic zone north of the updraft, where horizontal vorticity was as great as 0.025 s^{-1} (Fig. 3.2.12.a). The opposite was true in the McLean storm (Fig. 3.2.12.b, left panel). The 500-1000 m AGL analysis indicates that the horizontal vorticity south and east of the updraft (i.e., in the near environment) was stronger (up to 0.02 s^{-1}) than on the other side of the updraft. The McLean storm is not unusual in this respect. For example, dual-Doppler analyses of the Del City storm (20 May 1977) (Brandes 1984b) also indicate stronger horizontal vorticity in the environmental inflow. The comparison of the observations to the simulations is not entirely appropriate since it involves data at different levels (above 500 m AGL in the McLean storm, and at 250 m AGL in the simulation). However, I would not expect the impact of a baroclinic zone associated with rain cooled air to be confined entirely below 500 m.

Images of foreground vegetation in a video of the McLean storm tornadoes, as viewed from the southeast (B. Haynie 1995, personal communication), do not show evidence that conditions were particularly windy at the surface. In other words, the inflow at 500 m AGL of up to 30 m s^{-1} (Fig. 3.2.6) was not experienced at the surface. Much later in the life of the McLean storm, a mobile mesonet vehicle (Rasmussen et al. 1994) sampled the low-level storm inflow 12 km southeast of tornado #4 (Fig. 3.2.13.a). The ground-relative surface winds (corresponding to the storm-relative winds plotted in the figure) were 9.5 m s^{-1} from 120°. In the same tornado-relative location a few minutes earlier, an ELDORA dual-Doppler analysis indicates a wind of 28 m s^{-1} from 150° at 500 m AGL (not shown). The magnitude of horizontal vorticity associated with this vertical shear at very low levels (~0.04 s^{-1}) is roughly twice that in the ELDORA analyses in the 500-1000 m layer (Fig. 3.2.12.b). (The orientation of the horizontal vorticity in the surface-to-500 m layer [directed just south of west] also differs from that in the dual-Doppler analyses of the layer higher up [generally directed toward the north-northwest].) Therefore, the importance of low-level shear in the southeasterly inflow into the updraft may be even greater than indicated in the dual-Doppler analyses.

Numerical simulations of the Del City storm (e.g., Klemp and Rotunno 1983, Adlerman et al. 1999), on which much of present supercell theory is based, do not start with, nor do they develop, the magnitude of vertical shear in the low-level inflow that was observed in the McLean storm. Therefore, I would not expect them to model accurately the evolution in a storm like the latter. Recent work by Wicker (1996) indicates that the environmental wind profile very near the surface can have a more important impact on the development of low-level rotation than previously thought (Rotunno and Klemp 1985). Furthermore, if there is low-level vertical shear present in the environment, it can be greatly enhanced as air parcels pass through the accelerated storm inflow (Weisman et al. 1998) on the way to the updraft.

The new pre-tornadic vortices (#2 and #4) in the McLean storm apparently formed by tilting of barotropic horizontal vorticity into the vertical at the edge of the updraft, followed by stretching of vertical vorticity in the updraft. For the early stages of the vortices, the dual-Doppler analyses indicate local maxima in tilting approximately upstream of the vorticity maxima (Fig. 3.2.14.a and d, Fig. 3.2.8.d and e), where the low-level horizontal vorticity and sharp vertical velocity gradient are rather parallel. The agreement is not exact, though. Vortex #4 is roughly 2 km north of where it would be if it were exactly downstream of the apparent maximum in tilting (Fig. 3.2.8.e, Fig. 3.2.14.d). By accounting for horizontal vorticity below 500 m pointing more toward the west (Fig. 3.2.12.b, right panel), one would shift the maximum in tilting farther north where the vertical-velocity gradient is more east-west oriented. This leads to a more consistent picture of how the vortex formed.

Although the new vortices formed by tilting and stretching of environmental vorticity, the source of low-level rotation in the mature tornadoes is more complicated. The low-level vortices, which had formed on the east side of the updraft (Fig. 3.2.8.d and e), did not have tight low-level rotation associated with them until they had moved to the west side of the updraft (Fig. 3.2.8.e-g). (The development of intense low-level rotation is implied by the formation of a tornado condensation funnel and confirmed by single-Doppler wind measurements.) In this part of the storm, low-level inflow was more from the north (Fig. 3.2.8.g). Given the lack of data below 500 m, we cannot have great confidence in the streamlines in the figures. However, it does appear likely that the storm-relative flow near the surface in this region had a significantly weaker component from the east and a greater component from the north than on the east side of the updraft.

Updraft inflow trajectories from the north tend to be through a baroclinic zone associated with rain-cooled air (Fig. 3.2.3, Fig. 3.2.12.a). Without direct temperature measurements, though, we do not know that this was the case in the McLean storm before 0000 UTC. Sometimes the temperature field can be counter-intuitive. For example, mobile mesonet observations collected much later indicate that the surface air west of tornado #4 was *warmer* (26-28 °C) than the surroundings (25-26 °C), even though the radar measured high reflectivity there (Fig. 3.2.13.b).

The analyses during tornado #4 indicate a gradual turning of the low-level horizontal vorticity from a southeast-to-northwest orientation in the environment to a more northeast-to-southwest orientation on the north side of the updraft (Fig. 3.2.8.f and g, Fig. 3.2.12.b left panel). Horizontal vorticity in the tornado inflow in the latter region may have been the sum of barotropic and baroclinic contributions (Wicker 1996). The presence of a weak baroclinic zone is confirmed by the mobile mesonet data just beyond the time of the last ELDORA data, which show a small temperature drop (2°C) from over 10 km southeast of the tornado to just northeast of the tornado.

All three large tornadoes in the McLean storm formed and matured in the vertical-velocity gradient between the weak rear downdraft and the west side of the updraft (Fig. 3.2.6 at z=0.5 km). This tornado location, which is common for supercell tornadoes (Lemon and Doswell 1979), indicates a possibly important role of the downdraft in producing and maintaining the rotation near the surface (Walko 1993, Davies-Jones and Brooks 1993). However, if that portion of the rear downdraft to the *west* of the updraft (near "B" and "D" in Fig. 3.2.12.b) did help produce cyclonic low-level vertical vorticity, its positive impact must have been confined below 500 m AGL. Above 500 m, the weak horizontal vorticity in this region pointed more from updraft toward downdraft (Fig. 3.2.8.c-g, Fig. 3.2.12.b near "B"), rather than vice versa. Tilting would have thus produced anticyclonic vertical vorticity (Fig. 3.2.14.a near x=-10, y=-12; Fig. 3.2.14.d near x=-5, y=-2; Fig. 3.2.14.g near x=11, y=14). For tilting in a downdraft to produce cyclonic vertical vorticity, the horizontal vorticity must point away from the strongest downdraft (Fig. 3.2.5).

Since the low-level horizontal vorticity vector turned clockwise with increasing height in the environment (Fig. 1.4), I suspect that the same was true in low-level inflow approaching the updraft from the northeast (near "A" and "C" in Fig. 3.2.12.b). With horizontal vorticity vectors pointing more from north to south near the surface (near "C" in Fig. 3.2.12.b), the portion of the rear downdraft to the *north* of the updraft could have produced cyclonic vertical vorticity by tilting (Davies-Jones and Brooks 1993). However, with Doppler velocities only above 500 m available, the only picture painted by the data is a process of tilting and then stretching in cyclonically curved trajectories along the eastern, northern, and western periphery of the *updraft* (Fig. 3.2.8, Fig. 3.2.14).

3.2.3 Steady Phase (Tornado #4)

By 2313 UTC, a new updraft had formed on the back side of the McLean storm, approximately 10 km southwest of the main storm updraft (Fig. 3.2.15.a). This new updraft "C" moved closer to the main updraft (Fig. 3.2.15.b) and then lost its separate identity; the resulting structure was elongated and bow shaped (Fig. 3.2.15.c). In the wake of this cell, a surge of strong southwesterly winds near the surface appeared on the back side of the storm (near x=-13, y=-11 in Fig. 3.2.15.a and x=-10, y=-8 in Fig. 3.2.15.b). This surge eventually moved into the region of the main storm updraft (Fig. 3.2.15.c). The timing of the arrival of the strong southwesterly winds coincided with the formation of tornado #4.

Trailing the new updraft, a blob of reflectivity (Fig. 3.1.1.j and k, Fig. 3.2.15.c near x=-7, y=-4) emerged from the elongated southwest part of the main core (Fig. 3.2.15.a and b) and moved eastward (in a storm-relative sense). The collocation of this reflectivity feature with the low-level southwesterly surge (Fig. 3.2.15.c) suggests that the outflow surge was air cooled from evaporation of precipitation. The development of cell "C" at the rear of the storm resulted in much more precipitation aloft to the southwest of the primary storm updraft (Fig. 3.2.6.f-i at z=4.0 km). As environmental air aloft with stronger southwesterly flow (Fig. 1.4, Fig. 3.2.6) impinged on this precipitation from the southwest, it may have cooled and descended, resulting in a local region of southwesterlies at lower levels. The winds in a vertical cross section through the outflow surge (left side of Fig. 3.2.7.b) are rather uniform at low and mid levels, which is consistent with the hypothesis of mixing of momentum down to the surface in downdrafts. On the other hand, there is no evidence of descent at the edge of the storm (Fig. 3.2.7.b). Another possibility is that cell "C" was the effect, rather than the cause, of the outflow surge. With WSR-88D data from Amarillo, Texas, I tried to identify an outflow surge approaching the McLean storm from the southwest prior to 2313 UTC. This attempt returned inconclusive results.

Although the formative stages of tornado #4 are captured in the ELDORA dataset, the first aircraft pass that followed the development of the condensation funnel itself (Fig. 1.8.e) suffers from a data gap (Fig. 3.2.6.j). During this pass at 2331 UTC, the radar data recording tape filled up and had to be changed while the fore radar beams were scanning the tornado. Fortunately, the scans from the following pass are more complete. At 2338 UTC, the ELDORA scanned the early stages of a large, long-lived, violent tornado (Fig. 1.7, 1.8.f, and 2.1.1).

According to single-Doppler ELDORA wind measurements, tornado #4 reached its maximum intensity (~90 m s^{-1} winds) from 2337 to 2346 UTC (Table 1.3, Fig. 3.1.2.1), *shortly after the arrival of the low-level outflow surge*. The strength of the winds in this time period, and the unusual donut-shaped updraft structure at 2338 (Fig. 3.2.6.k), are unlike what was observed in tornado #4 later on, or in any of the other tornadoes. Perhaps the early stages of tornado #4 included an extra "boost" from the outflow surge.

For tornadoes #1 and #2, circulation at 500 m AGL was 0.10-0.20 km^2 s^{-1} in the near environment of the vortices (Fig. 3.2.16). (In this discussion, circulation is best thought of as a measure of the average vertical vorticity over a region, times the area of the region.) With the appearance of the outflow surge from the southwest, circulation around the developing vortex #4 increased sharply at large radii to at least 0.4 km^2 s^{-1} at 2325 UTC (Fig. 3.2.16). Circulation increased to this magnitude at smaller radii 13 minutes later, when tornado #4 was most intense. This evolution suggests that simple convergence acting on rotation organized on a large (r>5 km) scale may have led to a stronger tornado than earlier in the lifetime of the storm. Without data below 500 m AGL, it is not possible to verify this by a Lagrangian analysis of material circuits in the fluid (Rotunno and Klemp 1985).

As a side note, I should point out that circulation remained intense beyond the passing of the outflow surge from cell "C", and there was even another increase from 2356 to 0009 UTC (Fig. 3.2.16). This high magnitude of circulation is apparently an indication of large-scale storm organization at low levels. An increase in northerlies to the west of the updraft at 0003 UTC (Fig. 3.2.6.o at z=0.5 km) and a general increase with time in the southeasterly winds to the east of the updraft (Fig. 3.2.6 at z=0.5 km) contributed to this circulation. After a rather erratic relationship between vertical velocity and vertical vorticity during the cyclic stage, the storm updraft steadily increased in rotation during the mature stage of tornado #4 (Fig. 3.2.9.b).

The donut-hole vertical velocity minimum at 2338 UTC (Fig. 3.2.6.k) has the appearance of an occlusion downdraft (Fig. 3.2.4) (Klemp and Rotunno 1983), a small feature that develops behind the gust front as a result of pressure gradient forces when rotation decreases with height. A retrieval of the dynamically-induced perturbation pressure does reveal a downward-directed pressure gradient force (Fig. 3.2.17.a) on the south side of the vortex, just upstream (west) of the vertical velocity minimum. Most of the contribution to the downward forcing comes from the curvature terms (Fig. 3.2.17.b).

However, the situation is not as simple as a decrease in rotation with height in this case. On the average, vertical vorticity in the dual-Doppler analysis of the vortex actually *increases* slightly with height at mid levels (Fig. 3.2.11.h). The couplet of positive and negative $\partial p_c / \partial z$ on the south and north sides of the vortex, respectively, is more associated with a northward tilt with height of the vortex axis, at an angle of approximately 10° with respect to the vertical (Fig. 2.1.1). The lack of symmetry in the couplet (Fig. 3.2.17.b) is related to asymmetry of the vorticity distribution (not shown).

Tornado #4 persisted for at least one hour. After 2346 UTC, the single-Doppler wind speeds (Table 1.3) were weaker (~70 m s^{-1}) but were still greater in magnitude than those in the early tornadoes (50-60 m s^{-1}). Although there were small fluctuations in path (Fig. 1.7) and intensity of the tornado, the storm structure remained rather steady (Fig. 3.2.6.m-p, Fig. 3.2.9.a). Tornado #4 was consistently to the southwest of the updraft maximum at low levels, and the gust front bowed out strongly to its east. Previous studies have typically emphasized the bowing out of the gust front as the beginning of the dissipating stage of a tornado. However, this was not the case with tornado #4 in the McLean storm while the ELDORA was observing it.

3.2.4 Tornado Dissipation

Tornado #1 had a ropelike appearance at 2313 UTC and dissipated two minutes thereafter (B. Haynie 1995, personal communication). The narrowness of the condensation funnel is consistent with a contraction of the width of the single-Doppler velocity anomaly (Table 1.3) to 500 m (Fig. 3.1.2.f) from the earlier width of 800 m (Fig. 3.1.2.d). The dual-Doppler analysis is barely able to resolve weak cyclonic curvature associated with tornado #1 at 2313 UTC (Fig. 3.2.6.g at z=0.5 km). Northerly inflow into the tornado now passed through significant precipitation core over a long distance.

Tornado #2 was obscured by rain (Fig. 3.2.6.h-i) when it dissipated at approximately 2322 UTC (B. Haynie 1995, personal communication). The dual-Doppler analysis at 2325 UTC resolves the remnant low-level vortex far to the west of the main updraft (Fig. 3.2.6.i at z=0.5 km).

Even though the tornadoes were in weakening stages, it is still remarkable how long they persisted when separated from the main storm updraft. Tornado #1 still had a condensation funnel at 2313 UTC when it was approximately 7 km away from the primary storm updraft (Fig. 3.2.6.g). At 2318 UTC, tornado #2 still had a large condensation funnel while it was over 3 km away from the updraft (Fig. 3.2.6.h). The analyses indicate a weak localized region of upward motion (strongest aloft) in the vicinity of tornado #1 in the former case (Fig. 3.2.6.g) and a weak lobe of upward motion behind the main updraft and just northeast of tornado #2 in the latter case (Fig. 3.2.6.h). Presumably the tornadoes were able to persist until the local vorticity source was depleted and/or the stability of the surrounding surface air became too great.

For the highly unstable atmosphere in the eastern Texas Panhandle (Fig. 1.4), the surface air in the vicinity of the tornado could have been much cooler and drier than the environment and still be potentially buoyant aloft. A surface air parcel with a temperature (dewpoint) over 9°C (over 5°C) lower than in the environment would have still realized some positive buoyancy aloft. Late in the lifetime of the storm, mobile mesonet vehicles did not identify deficits of more than 3.5°C in either quantity (relative to the environmental inflow air) in various locations relative to tornado #4 (Fig. 3.2.13). Assuming the outflow characteristics at this time are representative of the earlier nature of the storm, then the air in the vicinity of the dissipating tornadoes #1 and #2 was likely still potentially buoyant, but perhaps too cold to be lifted to its LFC.

For the mature stages of tornadoes #1 and #2, the vertical vorticity distributions in the dual-Doppler analyses exhibited maxima at low levels (Fig. 3.2.11.b and e). In the weakening stages, the maximum vertical vorticity was aloft (Fig. 3.2.11.c and f), although there was a weaker secondary maximum near the surface with tornado #2 (Fig. 3.2.11.f). This pattern in the tornado weakening stage is contrary to what has been documented previously in the ground-based dual-Doppler tornadic supercell datasets

(Brandes 1978, Dowell and Bluestein 1997). This finding may be related to the overall health of the storms. The Harrah (20 May 1977) (Brandes 1978) and Arcadia (17 May 1981) (Dowell and Bluestein 1997) storms were essentially collapsing, and the observed decreases in rotation with height would have been associated with dynamically-induced downdrafts within the mesocyclone. In contrast, tornadoes #1 and #2 in the McLean storm were dissipating within a healthy overall storm structure.

3.3 Cyclic Tornadogenesis

3.3.1 Background

As defined in the introduction, the term "cyclic tornadogenesis" will refer to the formation of a succession of tornadoes in a single supercell storm. I summarize below published proposed mechanisms of cyclic tornadogenesis. These modes are not mutually exclusive; i.e., more than one mechanism may operate in a given storm.

In the published studies, some of the authors refer to the formation of tornadoes within a "mesocyclone", while others describe the occurrence of tornadoes within a "tornado cyclone". Forbes (1978) defined a "tornado cyclone" as an intermediate scale of rotation larger than a tornado but smaller than a mesocyclone. For two reasons, I will use instead the term "parent vortex" to describe the next larger scale of rotation in which a tornado is embedded. First of all, the existence of three scales of vortex flow is yet to be proven as a universal feature of supercells. Secondly, use of the term "parent vortex" will make the mechanisms described below more general, as it leaves open the possibility that a mesocyclone, rather than a smaller scale vortex, is the parent vortex of a tornado.

a. Repeated tornado development within a single parent vortex that fluctuates in intensity.

This is perhaps the simplest mode by which a thunderstorm may produce multiple tornadoes. Periodicity in tornado formation relates to pulsation in the intensity of the parent thunderstorm (Agee et al. 1976), or more specifically, fluctuations in the magnitude of the rotation and low-level convergence in the tornado parent vortex. Some of the low-level changes may be controlled by fluctuations in the updraft strength aloft (Wicker and Wilhelmson 1995). This type of evolution is implied for the "series mode" tornado family described by Fujita et al. (1970); tornadoes form in the center of the parent vortex, and all tornado paths tend to lie along a straight line.

b. Periodic tornado development within a mesocyclone containing multiple long-lived parent vortices that fluctuate in intensity.

A study of "Superoutbreak" (3 April 1974) tornado tracks by Agee et al. (1976) led the authors to hypothesize that some supercell mesocyclones contain multiple long-lived, small-scale tornado parent vortices that revolve cyclonically about the mesocyclone center (Figure 3.3.1). Individual parent vortices (diameter of 1-3 km) produce tornadoes as they rotate through that portion of the mesocyclone (diameter of 3-10 km) in which the environment is most favorable for tornadogenesis. The favorable part of the mesocyclone for tornado formation is that which feeds upon the warm, moist low-level air from the environment. When the parent vortex and tornado turn cyclonically into the cold storm outflow air, the tornado dissipates. This parent vortex is then inactive until the mesocyclone flow carries it back into the warm air, when it can again produce a tornado. The end result is a family of tornadoes along cycloidal paths (Fig. 3.3.1).

The motivation of the Agee et al. (1976) hypothesis was to explain "left-turn" and "right-turn" tornado families (Fujita 1974). The direction of the tornado turn at the end of the track depends on where the tornado dissipates within the mesocyclone. If it dissipates within the southern half of the mesocyclone, then its final motion is toward the left (Fig. 3.3.1). If the tornado instead survives until it reaches the northern half of the mesocyclone, then the path turns to the right at the end.

The Agee et al. (1976) hypothesis does not agree with more recent theory of supercell dynamics. The discussion of vortices moving into and out of the baroclinic zone is inconsistent with potential vorticity considerations (Rotunno and Klemp 1985), which predict that low-level vortices must lie *within* baroclinic zones. (This argument applies when the vertical vorticity is produced by tilting of horizontal vorticity.)

c. Rollup of a shear zone into multiple vortices.

Barcilon and Drazin (1972) proposed that dust devils are vortices that roll up along a vortex sheet (vertical plane along which there is horizontal wind shear). In their model, individual vortices grow via barotropic (Kelvin-Helmholtz) instability. Unlike the case of Kelvin-Helmholtz instability in a vertically sheared and stratified fluid, in the horizontal shear case the buoyancy force plays no direct role in the instability condition. However, convection in an unstable stratification can intensify the vortices that form by the barotropic process (Barcilon and Drazin 1972).

Since 1972 the concept of Kelvin-Helmholtz instability along zones of horizontal shear has been applied to the storm scale. Carbone (1982) documented a tornado that formed in a cold frontal rainband in an environment of very low CAPE. He attributed the tornado development to Kelvin-Helmholtz instability along the surface front. Forbes and Wakimoto (1983) speculated that many tornadoes in a localized outbreak of severe weather formed via Kelvin-Helmholtz instability in the horizontal shear at the periphery of downbursts. Wakimoto and Wilson (1989) hypothesized that parent vortices of many nonsupercell tornadoes form as shear instabilities along lines of convergence and horizontal shear; these vortices develop into tornadoes when they become collocated with the updraft of a developing storm. More recently, Lee and Wilhelmson (1997) simulated the formation of multiple circulations of 1.6 to 3.2 km scale at the leading edge of an outflow boundary.

Brandes (1977b, 1978) applied the idea of vortex sheet rollup to supercell thunderstorms. Noting multiple small-scale vortices (although only one tornadic vortex) within the elliptical low-level mesocyclone of the Harrah storm (8 June 1974), Brandes hypothesized that tornadoes may form within shear bands in the mesocyclone.

The idea of multiple tornado development within supercells as a Kelvin-Helmholtz instability has received little attention since 1978. However, a recent storm observation in the field reminded me of this hypothesis (Fig. 3.3.2). The storm of interest was in an environment with CAPE of approximately 2000 J kg^{-1} and with vertical shear of over 25 m s^{-1} in the lowest 4 km AGL; these conditions support supercell formation (Weisman and Klemp 1982). The storm reflectivity on the Lubbock, Texas WSR-88D had the characteristics of a classic supercell (not shown). Multiple tornadoes formed in rapid succession below an elongated west-east oriented cloud base (Fig. 3.3.2), perhaps in an elongated region of shear at the interface between the easterly storm inflow and the westerly outflow from the rear downdraft.

Wakimoto et al.'s (1998) extension of the concept of "vortex breakdown" (Ward 1972) to the storm scale is a variation on the theme of this cyclic mode. The authors speculate that the mesocyclone of the Garden City storm (16 May 1995) broke down into multiple vortices (Wakimoto el al. 1998) along the periphery of an occlusion downdraft (Klemp and Rotunno 1983). Although only one of the smaller vortices strengthened into a tornado in the Garden City storm, this theory would allow for the possibility of multiple tornadoes in other cases. A distinguishing characteristic of this version of the shear-zone cyclic mode is that the region of shear in which the vortices develop is circular rather than linear.

d. Tornado formation within cyclic mesocyclone cores.

Burgess et al. (1982) described a conceptual model for the cyclic formation of rotational cores within a low-level mesocyclone (Figure 3.3.3). They defined the mesocyclone as a region of cyclonic swirl about 20 km across with a smaller inner core (or cores) of nearly solid rotation; these inner cores can be the parent vortices of tornadoes. In a dataset of single-Doppler observations, 24% of mesocyclones produced multiple inner cores. Burgess et al. (1982) described the flow in the mesocyclone outside the cores as "vorticity rich," although they also used the term "potential flow" to describe this region (implying by definition no vertical vorticity). For consistency in their conceptual model, it appears that Burgess et al. view the mesocyclone as containing cyclonic vertical vorticity both inside and outside the cores, although much greater in magnitude within the cores.

The Burgess et al. (1982) model resembles synoptic cyclone evolution. During the mature stage of the first mesocyclone core, a gust front wraps cyclonically about the right (southeast) side of the core (Figure 3.3.3). Eventually it wraps around far enough to form an occlusion with the forward-flank boundary. This cuts off the supply of warm environmental air to the core, and the occluded core begins to dissipate. The core (and its accompanying tornado) turn to the left and slow down as they dissipate. Burgess et al. (1982) did not specifically address the reason for the left turn.

While dissipation of the first core occurs, a second vortex core develops rapidly in the region of strong convergence at the occlusion point associated with the first core (Burgess et al. 1982) (Figure 3.3.3). Unlike the first core, which forms rather slowly and follows midlevel mesocyclogenesis, the new core forms rapidly and simultaneously over a large depth because it is in an environment that is now rich in vertical vorticity. The new core becomes the dominant core (and may produce a tornado) until its associated gust fronts occlude, initiating the formation of yet another new core in a similar manner.

For the Burgess et al. (1982) dataset, the most common total number of cyclic cores was three, although one storm produced six. The Burgess et al. conceptual model accounts for left-turn tornado families in which each tornado forms at a regular time interval (40 minutes in their study), and it is thus consistent with striking periodicities in tornado formation intervals noted by Darkow and Roos (1970) and Darkow (1971). Working with perhaps the best dual-Doppler observations of cyclic tornadogenesis before VORTEX, Johnson et al. (1987) suggested that their analysis of the Fort Cobb storm (20 May 1977) was consistent with the Burgess et al. (1982) model.

e. Tornado formation within successive updrafts.

A study by Adlerman et al. (1999) provides a detailed description of a cyclic supercell evolution. Their analysis of a numerical simulation expands on the work of Klemp and Rotunno (1983). The four-hour simulation produced two low-level vortices (and began to produce a third).

By t=5280 s in the Adlerman et al. (1999) simulation, a low-level vortex (called a "mesocyclone" in the paper, but with a slightly smaller scale than defined earlier in this section for mesocyclones) has already formed (Fig. 3.3.4.a). The surging gust front to the east and south of this vortex initiates a deep new updraft rooted near the intersection of the rear gust front and the forward-flank baroclinic zone (Klemp 1987) (Fig. 3.2.3.b). The result is a two-celled updraft structure at both low and mid levels (Fig. 3.3.4.a). Although the updraft has two discrete roots, the storm is unicellular higher up (Fig. 3.3.4.b).

When the low-level vortex associated with the western updraft reaches its maximum intensity, outflow from the occlusion downdraft (Fig. 3.2.4) surrounds the east side of the vortex and updraft, cutting off the supply of conditionally unstable low-level air (Fig. 3.3.4.c). As a result, the updraft and vortex soon weaken. The eastern portion of the updraft continues to separate from the weakening updraft.

In the Adlerman et al. (1999) simulation, a new low-level vortex forms with the new updraft, but only after the gust front slows down and the updraft becomes less tilted (Fig. 3.3.4.d). However, the new vortex still forms more rapidly than the first. The source of rotation in both vortices is identical: horizontal vorticity generated baroclinically in low-level inflow from the north (Klemp 1987). After the development of the first occlusion, the low-level buoyancy contours are oriented so that the baroclinic generation of horizontal vorticity in the new updraft's inflow proceeds immediately. In effect, the processes associated with the old vortex set the stage for the new one. Unlike in the Burgess et al. (1982) model, ambient vertical vorticity did not play a significant role in the formation of new vortices.

Cyclic vortex formation in the Alderman et al. (1999) simulation occurs at roughly 60 min intervals in discrete updrafts as the storm repeatedly re-organizes at low levels farther east. Burgess et al. (1982) do not explicitly discuss updraft structure, making it difficult to distinguish clearly between their conceptual model and the current one. However, one clear distinction is in how the new vortices form. In mode "d", new vortices form in a different manner from the first. In mode "e", all vortices form in the same manner within each successive updraft.

Other storm evolutions may produce multiple tornadoes, but I do not consider some of these to be cyclic mechanisms. For example, supercells occasionally produce cyclonic-anticyclonic tornado pairs (Brown and Knupp 1980, Fujita and Wakimoto 1982, Jensen et al. 1983, Klemp and Rotunno 1983). The cyclonic tornado is typically within the heart of the low-level mesocyclone, while the anticyclonic tornado is farther southeast along the gust front (Figure 3.3.5). The formation of a tornado pair appears to be a simultaneous, rather than cyclic, process.

Umenhofer and Fujita (1977) discuss a series of tornadoes near Great Bend, Kansas (30 August 1974). The location of individual tornado touchdowns progressed from northeast to southwest along a surface wind-shift line over a period of an hour and a half. Radar revealed that the tornadoes were spawned by a complex of individual thunderstorm storm cells, with each tornado touchdown coinciding with new cell growth along the surface boundary.

Although the individual cells in the Great Bend case were not supercells (Umenhofer and Fujita 1977), it is conceivable that a similar evolution could occur in a supercell environment (Weaver and Nelson 1982). I do not consider this example to be in the same class as the other cyclic modes because it involves the interaction of the storm with a larger scale process, rather than processes only within the storm.

One purpose of the current study is to explain the cyclic evolution in the McLean storm. In particular, I will consider the following questions:

- Which of the above modes, if any, occurred in the McLean storm?
- Why did tornado #4 last much longer than the others?
- What scales of motion were present in the McLean storm? Was there a "tornado cyclone"?

3.3.2 Hypothesis for the Cyclic Process

The process of cyclic tornadogenesis in the McLean storm (Fig. 3.3.6, Fig. 3.2.6) is qualitatively similar to conceptual models of this process based on visual observations (Rasmussen et al. 1982), single-Doppler observations (Burgess et al. 1982), and numerical simulations (Klemp 1987, Adlerman et al. 1999). New vortices formed near the leading edge of a gust front that had surged eastward ahead of a mature tornado (Fig. 3.2.6.e and g at z=0.5 km, Fig. 3.3.3, Fig. 3.3.6). A new vortex was first characterized by strong convergence and weak rotation (Fig. 3.2.6.e and g). Later, tangential motion increased substantially, the tornado formed, and a new gust front surge developed near the incipient tornado (Fig. 3.2.6.f and i).

A minor difference in the McLean storm compared to the storms that Burgess et al. (1982) analyzed is that new rotation centers increased in magnitude with height (Fig. 3.2.11.d and g) in the former case; Burgess et al. found more uniform distributions with height. A more significant discrepancy with the Burgess et al. (1982) model (Fig. 3.3.3) is that new vortices did not form at a clearly defined occlusion point between two wind discontinuities. Although there was an elongated region of weak low-level convergence along the forward flank extending northeastward from the updraft maximum during the formation of vortex #2 (Fig. 3.2.6.e at z=0.5 km), the new vortex formed farther south than the intersection of this convergence line with the rear gust front. Furthermore, new development appeared to occur in lobes of the updraft *slightly east of the gust front*, rather than along it (Fig. 3.2.6.e and g at z=0.5 km). The regions where the updraft lobes formed were in a generally favorable environment owing to upward forcing east of the main updraft associated with the dynamically-induced perturbation pressure gradient force (Fig. 3.3.7.a, Fig. 3.3.8.a). The upward forcing east of the updraft center was primarily influenced by the shear term (Equation 3.2.9) (Fig. 3.3.7.b, Fig. 3.3.8.b). Since the pattern persisted (Fig. 3.3.9), it does not explain the periodic nature of the earlier vortex formation.

In the figures, I have drawn the gust fronts along the apparent lines of maximum confluence and/or convergence. At 2259 and 2313 UTC, these are west of the developing vortices (Fig. 3.2.6.e and g at z=0.5 km). However, there may have been some impact of the gust front surge that extended beyond the sharpest boundaries. A dual-Doppler analysis at 2259 UTC with much less smoothing (Appendix A) does indicate weaker storm-relative easterlies just west of vortex #2, indicating that some outflow may have previously surged ahead to this point.

Rotation increased with height in the developing vortices (Fig. 3.2.11.d and g). Therefore, the eastern side of the updraft was also enhanced by the rotationally-induced vertical pressure gradient force. However, this influence appeared to be slightly north of the elongated part of the low-level updraft (Fig. 3.3.8.c).

In the numerical simulations of cyclic vortex formation (Klemp 1987, Adlerman et al. 1999), successive low-level vortices formed within new updrafts (Fig. 3.2.3.b, Fig. 3.3.4). During the intermediate times, the storm needed time to recover (i.e., time for the gust front to slow down). In contrast, the pseudo-dual-Doppler analyses of the McLean storm suggest a more continuous process (Fig. 3.2.6). Only at 2236-2242 UTC (Fig. 3.2.6.a and b at z=4.0 km) was there a two-celled updraft reminiscent of that in the numerical simulations, and this feature *preceded* the formation of any tornadoes.

Cyclic tornadogenesis in the McLean storm appeared to occur within an essentially single-celled updraft (Fig. 3.3.6). New vortices arose on the east side of the same updraft which had spawned an existing tornado. Furthermore, cyclic tornado formation in the McLean storm occurred quickly. New large tornadoes formed at 18-min intervals, which is less than the 40-min and 60-min times between low-level vortices in the Burgess et al. (1982) observational study and the Adlerman et al. (1999) numerical simulation. Important questions to be answered are why a single main updraft would have a cyclic process associated with it, and why the cyclic process effectively ceased with tornado #4.

To investigate these issues, I will return to the vertical vorticity equation and the vertical equation of motion:

$$\frac{\partial\zeta}{\partial t} \approx -(\vec{v}_h \cdot \nabla)\zeta - w\frac{\partial\zeta}{\partial z} + \left(\frac{\partial u}{\partial z}\frac{\partial w}{\partial y} - \frac{\partial v}{\partial z}\frac{\partial w}{\partial x}\right) - \left(\frac{\partial u}{\partial x} + \frac{\partial v}{\partial y}\right)\zeta \tag{3.3.1}$$

$$\frac{\partial w}{\partial t} \approx -(\vec{v}_h \cdot \nabla)w - w\frac{\partial w}{\partial z} + B - \frac{1}{\rho}\frac{\partial p'}{\partial z}. \tag{3.3.2}$$

The solenoidal term in (3.3.1) and the turbulent mixing terms in both equations have been neglected.

In my explanation of the cyclic behavior of the McLean storm, a basic premise is that updrafts and vortices move somewhat independently. Tornado rotation forms and reaches its maximum intensity close to the surface (Lewellen 1993). Therefore, the most important layer in which the processes in Equation (3.3.1) govern vortex motion is at low levels.

The basic driving force of the updraft is positive buoyancy, which is greatest aloft (Fig. 1.4). All of the terms in Equation (3.3.2) tend to be largest well above the surface; therefore, the layer that controls updraft motion is generally higher and deeper than for a tornado.

The motions of updrafts and vortices are not completely independent, however. In the vertical vorticity equation, vertical advection, tilting, and stretching are all processes that would tend to keep a vortex tied to its parent updraft. In contrast, horizontal advection does not necessarily do this.

In the vertical equation of motion, the influence of vorticity enters through the pressure term (Rotunno and Klemp 1982, Weisman and Klemp 1984). Vortices are associated with mesolows, which induce rising (sinking) motion below (above) the level of maximum rotation. The effect of tornadoes on the motion of the main updraft is probably rather small, though, since these vortices are significantly smaller than the overall updraft and mesocyclone aloft (Fig. 3.2.6).

My hypothesis for why some storms are cyclic requires horizontal advection of vertical vorticity to be a significant factor in the evolution (more so than is typically thought). I believe that the end of the cyclic process in the McLean storm occurred because the updraft-relative magnitudes of low-level storm inflow and outflow changed beneath the west side of the updraft.

Initially, inflow dominated, and the low-level flow carried the vortices westward with respect to the updraft (Fig. 3.3.6). In the plots corresponding to the terms in the vorticity equation (Fig. 3.2.14), advection of vertical vorticity by the updraft-relative horizontal wind is consistently of the same order of magnitude as the other large term (stretching). At 2259 UTC, the effect of advection was to move tornado #1 southwestward and vortex #2 westward (Fig. 3.2.14.c). The same was true for the mature tornado #2 and the new vortex #4; advection tended to displace both vortices westward (Fig. 3.2.14.f).

Later in the life of the McLean storm, the low-level flow beneath the back side of the updraft became more westerly (Fig. 3.2.15). Horizontal advection of vorticity continued to be a significant term. In the case of tornado #4 at 0003 UTC (Fig. 3.2.14.i), advection now acted to move the vortex *eastward* – i.e., *toward* the main storm updraft rather than away from it.

To investigate further the role of updraft-relative low-level winds, I compared a time series of the east-west component of motion of the updraft with those of the tornadoes (Fig. 3.3.10). The vortex information is based on analyses at 500 m AGL, since this is the lowest grid level. In contrast, I chose 4 km AGL as the height for determining the locations of the updraft centers because the updraft tended to be more circular aloft. Since the updrafts were not tilted significantly, the results are not sensitive to this choice.

With a few exceptions, the updraft generally was moving eastward at 4-8 m s^{-1} (Fig. 3.3.10). In all three cases, the *u* component of the velocities of the pre-tornadic vortices were initially less than that of the updraft. Vortices #1 and #2 were initially moving eastward more slowly than the updraft, and vortex #4 originally moved westward. When vortex #4 became tornadic, it started moving toward the east (Fig. 3.3.10).

During the mature stages of tornadoes #1 and #4, the vortex speed and updraft speed were nearly identical (Fig. 3.3.10). In contrast, during the weakening stage of tornado #1, it lagged well behind the updraft. Tornado #2 was unable to keep up with the updraft throughout its life. It was always moving significantly westward relative to the updraft.

Fig. 3.3.10 also includes values of the mean *u* component of velocity at 500 m AGL in the neighborhood of the vortices. I computed the average values within 5-km wide circles centered around each vorticity maximum in the dual-Doppler syntheses. The data support the idea that tornado motion is strongly related to the mean low-level flow in which it is embedded. For example, the time series of local mean *u* for vortex #1 follows the pattern of the observed vortex motion (Fig. 3.3.10). The tornado was embedded in westerly flow when it was locked in place with the main updraft, and it was in easterly flow on the average when it lagged behind.

Tornado #2's parent vortex was always within an easterly mean wind (Fig. 3.2.15, Fig. 3.3.10), and it moved rapidly westward relative to the updraft. Given the strong southerly wind component also present at low levels, it is not surprising that the overall motion of tornado #2 was toward the northwest (Fig. 1.7).

The decrease in magnitude of the easterly wind component in the neighborhood of vortex #2 does not agree with the trend in the observed motion (Fig. 3.3.10). Since there was significant vertical shear of the horizontal wind in the boundary layer (Section 3.2.2), the lack of more appropriate radar data below 500 m AGL for the computation of local mean u may account for some of the observed difference in trend.

Vortex #4 was embedded in easterly flow when it formed on the east side of the updraft, but by the time it became tornadic, it was within westerly low-level flow on the west side of the updraft (Fig. 3.3.10). When the outflow surge arrived from the rear of the storm, the flow beneath the west side of the updraft switched from predominantly southerly to more westerly (Fig. 3.2.15). The velocity of the low-level flow was then close enough to that of the main updraft so that tornado #4 could survive in a relatively steady state until the end of the ELDORA dataset.

The flow beneath the back side of the updraft became more westerly around 2330 UTC as a result of the outflow surge from cell "C" (Fig. 3.2.15). However, this outflow surge was a transient feature and does not explain the nature of the later flow around tornado #4. By 2345 UTC, the mean u velocity around tornado #4 had diminished to near zero (Fig. 3.3.10). Approximately 15 minutes later, the local flow became stronger from the west again. The second increase appears to be from an increase in outflow associated with the dynamics of the main storm. Between 2351 and 0009 UTC, the low-level flow wrapped a significant amount of precipitation around the southwest side of the updraft (Fig. 3.2.6.m-p at z=0.5 km). Evaporation of this precipitation may have increased the amount of outflow in this region.

A generalization of the hypothesis for cyclic tornadogenesis in the McLean storm is that there could exist cyclic modes on either side of a quasi-equilibrium state. (I consider tornado #4 to be an example of near equilibrium). *When the storm inflow is slightly too strong beneath the rear side of the updraft, cyclic tornadogenesis occurs because vortices that form are unable to keep up with the updraft* (Fig. 3.3.6). *In contrast, when the storm outflow is too strong, cyclic tornadogenesis can occur each time the storm recovers from the outflow surge ahead of the previous tornado* (Brooks et al. 1994, Adlerman et al. 1999). By "recovers," I mean that the gust front slows down enough so that it does not completely undercut the new updraft aloft. One would expect the former process to occur more quickly since no storm reorganization is involved. Cyclic tornadogenesis in the McLean storm (in the inflow-dominated mode) occurred ~3 times more rapidly than the formation of low-level vortices in the Adlerman simulation.

The pattern of relatively short-lived tornadoes followed by a long-track tornado is common in outbreaks (e.g., the storm "A" tornado family in Fig. 1.1.a and the southernmost family in Fig. 1.1.b). The track of tornado A3 in the Oklahoma City storm (Fig. 1.1.b) is even reminiscent of the anomalous motion of tornado #2 in the McLean storm. The Oklahoma City and McLean storms both later produced a long-lived, violent tornado. In the McLean storm, the buildup of outflow on the back side of the storm, which apparently aided the transition from the cyclic phase to the steady phase, appeared to be first associated with interaction of the main storm with a smaller cell. In other storms, the buildup of outflow may simply be a function of time.

It is not entirely true that the cyclic process in the McLean storm ended with tornado #4. At 0005 UTC, a narrow tornado #5 formed northeast of tornado #4 (Fig. 1.9, Fig. 3.2.8.g). The low-level flow carried the small tornado toward the larger tornado (Fig. 3.2.8.g), and the remnants of tornado #5 were observed visually to be absorbed into the circulation of tornado #4 (D. Ewoldt and C. Kaufman 1995, personal communication). If tornado #4 had moved away from the main updraft and dissipated like previous tornadoes, then perhaps tornado #5 would have had the chance to grow into the next significant tornado. However, tornado #4 remained anchored to the back side of the updraft, and a "survival of the fittest" competition between the two vortices ensued (at the expense of the smaller tornado) as tornado #5 approached.

I will close this section with brief discussion on two issues in the Burgess et al. (1982) conceptual model. First of all, Burgess et al. speculated that new tornadoes in cyclic storms form primarily by vortex stretching in a "vorticity rich" environment. Circulation (and thus, mean vorticity) did increase with time beneath the storm (Fig. 3.2.16), and I speculated earlier that the formation of tornado #4 included convergent flow drawing in circulation from large radii. The strong tilting of horizontal vorticity into the vertical by the updraft (Fig. 3.2.14.g), and the U-shaped trail of cyclonic vertical vorticity (Brandes 1981, Klemp and Rotunno 1983) from the tilting maximum to the tornado (Fig. 3.2.8.g), suggest that other supercell processes continued to be important as well.

Burgess et al. (1982) defined the low-level mesocyclone as a broad region of circulation with embedded intense rotational cores. The analyses of the McLean storm suggest that this definition is appropriate. The plots of circulation (Fig. 3.2.16) show a general increase with radius but indicate that most of the rotation is concentrated in cores with radii of less than 2.5 km. Sometimes, these cores were elliptical, and the tornadoes were located away from the center (Fig. 3.2.6.d and o). More often, the tornadoes appeared to be simply a tightening of the rotation at the center of the core. There does not appear to be evidence of a third intermediate "tornado cyclone" scale (Forbes 1978) in the McLean storm.

4. CONCLUSIONS

4.1 Summary

In contrast with traditional methods, dual-Doppler methods based on variational formulations can yield solutions that converge in Cartesian coordinates regardless of scanning geometry (as long as the dual-Doppler beams are not close to parallel). When two boundary conditions are available for w, a variational formulation in which the radial velocity equations are satisfied exactly and continuity is satisfied in a least squares sense ("strong-constraint method") yields slightly more accurate velocities than a traditional method with an O'Brien (1970) adjustment. When errors are present in the data, a formulation in which all constraints are satisfied approximately ("weak-constraint method") produces a more accurate wind field.

The use of a moving reference frame for the dual-Doppler analysis alleviates the impact of temporal errors, as in the study by Gal-Chen (1982). However, Gal-Chen's technique for dual-Doppler radars, which is based on an expression in terms of radial velocity, cannot be used when the radars are moving. The alternative use of approximations of two Cartesian wind components (Section 2.5.1) worked for the simulated airborne radar data in the current study.

Another twist that I applied to Gal-Chen's (1982) method for the current study was the use of a non-uniform moving reference frame (i.e., one in which the reference frame velocity changes from grid point to grid point). This technique provided consistent minimal improvement over the standard Gal-Chen method.

The allowance for velocities that vary linearly with time does not in general appear to minimize errors further owing to evolution, although it does do so in some cases. This approach may be more promising for other types of datasets, in which the interval between dual-Doppler volumes is shorter than for airborne radar datasets.

The ELDORA observations of the 8 June 1995 McLean, Texas storm are unique in two senses: they are the first to provide a detailed glimpse of the 3D wind field within a storm producing a family of tornadoes, and they are the first to document the relatively steady structure of a storm producing a long-lived, violent tornado (#4). Pseudo-dual-

Doppler analyses (based on a weak-constraint formulation in a non-uniform moving reference frame) depict the 2+ km scale features in the storm during the formation of three large tornadoes. Some of the significant findings of this study are:

- New vortices formed by tilting of *environmental* horizontal vorticity into the vertical by the *updraft*, followed by stretching of vertical vorticity in the updraft. The new vortices were weaker near the surface than aloft.
- The vortices did not become tornadoes (i.e., intensify at low levels) until they were in the vertical-velocity gradient between the updraft and the (weak) rear downdraft. However, there is no direct evidence of cyclonic vertical vorticity production by tilting in a downdraft (Walko 1993, Davies-Jones and Brooks 1993). If this process were important, it was occurring below 500 m AGL.
- In the low-level storm-relative inflow from the north into the mature tornadoes, horizontal vorticity was oriented more from north to south than in the environment. This suggests that baroclinic generation of horizontal vorticity was more important during tornadogenesis than during the initial formation of the vortices.
- Cyclic tornado production within an otherwise quasi-steady storm can occur if rearward low-level flow repeatedly separates the vortices from the main updraft. In this mode, formation of new tornadoes can occur quickly.
- Outflow from a neighboring storm cell can affect both the nature of the main cell (i.e., cyclic versus non-cyclic) and the strength of its tornado(es).

In the cyclic stage of the McLean storm, the tornadic region at low levels (i.e., southwest of the updraft maximum) was slightly dominated by storm inflow (Fig. 4.1). Therefore, the tornadoes were carried away from the main updraft by the easterly storm-relative winds. At the same time, new vortices formed on the east side of the updraft (Fig. 3.3.6). This is a different process from what appears to be occurring in some numerical simulations (Klemp 1987, Adlerman et al. 1999). In the simulations, new vortices form within *new updrafts* that develop along the gust front (Fig. 3.2.3.b, Fig. 3.3.4). I consider the simulations to be examples of a more outflow-dominated cyclic process (Fig. 4.1). Tornado #4 in the McLean storm may be an example of an equilibrium state in between the inflow-dominated and outflow-dominated states.

The development of a new cell to the southwest of the McLean storm updraft was associated with a surge of outflow (Fig. 4.2.a), which approached the developing tornado #4 at low levels from the southwest. This surge had two effects: increasing the magnitude of circulation at large radii around the developing tornado, and increasing the westerly momentum beneath the back side of the updraft. These effects apparently produced a briefly more intense tornado #4 and helped end the cyclic process. In other storms, such a close proximity of cells might aid in the transition of a steady storm to one that behaves like that in the Adlerman et al. (1999) simulation, or even in the transition of a tornadic storm to an outflow-dominated non-tornadic storm.

A simple gradual build up of outflow as a result of continuous evaporation of precipitation at the rear of a storm may also be responsible for transitions in storm behavior. A low-level mesohigh (Fig. 4.2.b) is associated with the development of the cold pool. If the cold pool to the west of the updraft is significant, the pressure gradient force on the east side of the mesohigh will slow the westward motion of air parcels and/or accelerate eastward parcel motions.

An understanding of these issues is potentially useful to a forecaster in a real time situation. Since the cyclic process depends on the low-level flow beneath the rear (with respect to storm motion) edge of the updraft, the storm must be close to the radar and at an azimuth angle where the radar measures the flow component toward/away from the left rear portion of the storm. A viewing angle toward either the west or the east would have been ideal for the McLean storm.

If a forecaster is observing short-lived tornadic vortex signatures in an inflow-dominated region, then he/she might anticipate that the storm will later produce a stronger, longer-lived tornado after outflow builds up at the rear of the storm. In storm-relative single-Doppler velocity images, "inflow-dominated" would mean stronger flow in the side of the rotational velocity couplet directed *toward* the left rear portion of the storm.

On the other hand, if there is little inflow beneath the apparent back side of the updraft region, then one might anticipate that an existing tornado will dissipate, or that later tornadogenesis will be delayed. For severely outflow-dominated storms, there may also be clues in the reflectivity data. WSR-88D reflectivity images often show fine lines (indicative of gust fronts) just ahead of the main storm echo in severely outflow-dominated storms. In current practice, some of the more skilled warning forecasters at the National Weather Service do monitor the relationship of the velocity and reflectivity structures in storms (D. Speheger 1999, personal communication). However, I am not aware that much significance is placed on clues in velocity asymmetry.

4.2 Future Work

I recommend the following avenues of future work based on the present study of dual-Doppler analysis techniques. First of all, further work is needed to determine a general method for determining the optimal choice of β in the weak-constraint scheme.

Secondly, I used approximations of two Cartesian velocity components as the scalars for determining the optimal reference frame translation velocity (Section 2.5). It would be interesting to see if I would get more accurate results by instead using all three Cartesian components, with each component determined from a complete dual-Doppler analysis in each iteration of the method.

The dual-Doppler analyses of the McLean storm required two interpolations – one in the gridding of the raw data, and another in mapping the data in the moving frame to a regular grid. A third suggestion for future work is to incorporate the moving reference frame methodology directly into the objective analysis program so that only one interpolation is necessary.

One of the variational dual-Doppler methods in Chapter 2 is based on mass continuity as a weak constraint, and the other is based on continuity and the radial velocities all as weak constraints. Shapiro and Mewes (1999) describe a third formulation in which the radial velocity equations are approximate and mass continuity is satisfied exactly. I am interested in finding a solution method for solving the Euler-Lagrange equations of this formulation directly in Cartesian coordinates. When errors are present in the radial velocity data, this formulation should yield more accurate winds than the method in Section 2.3 and may be competitive with the method in Section 2.4. In addition, the output of a dual-Doppler analysis with mass continuity as a strong constraint would be more valuable if the data were to be used to initialize a numerical model.

In future work on cyclic tornadogenesis, I am interested in verifying the hypothesis for cyclic tornadogenesis in the McLean storm by reproducing it in a numerical experiment. One possible experiment would be based on the simulation by Walko (1993). In the simulation, Walko (1993) produced a low-level vortex in a vertically-sheared environment by imposing a constant cylindrical heat source (which drives an updraft) near a mid-level heat sink to its southwest (which forces a rear downdraft). The low-level vortex was produced by tilting of horizontal vorticity into the vertical in the downdraft, followed by stretching of the vertical vorticity at the base of the updraft. By introducing a strong easterly initial flow and maintaining a small heat sink so that the cold pool builds up very gradually, it might be possible to produce a transition from a cyclic phase to a long-lived vortex phase.

The lack of data near the surface and the lack of temperature measurements limit the utility of ELDORA datasets alone for quantitative analysis of tornadic storms. My experience with mobile ground-based radars suggests that even they do not resolve the convergent tornado inflow near the surface. I am not sure what instrumentation will eventually give us the needed information near the ground. VORTEX showed us that mobile mesonet vehicles observations are of limited utility, simply because too many observations are required to resolve the low-level flow, and the standard road network is not dense enough.

Buoyancy is an even more problematic quantity since it is more difficult to measure remotely. However, if we are able to find ways to 1. improve the time resolution of multiple-Doppler radar datasets, and 2. extend the coverage down to the surface, then I believe that thermodynamic retrievals might start producing more realistic results.

To obtain more consistent fields in the current case, I am considering analyzing the McLean storm case by assimilating the radar data into a numerical cloud model. If a model simulation based on an initial state from the assimilation can reproduce the observed evolution of storm, then it might be possible to obtain a more quantitative analysis of the storm. I have already attempted simulations initialized with a warm bubble in a homogeneous environment. These simulations with the Klemp and Wilhemson (1978) model failed to produce a long-lived storm unless I significantly lowered the evaporation rate in the warm-rain microphysics scheme. Therefore, the representation of realistic precipitation microphysics may be the most difficult hurdle to overcome in the data assimilation.

REFERENCES

Adlerman, E. J., K. K. Droegemeier, and R. Davies-Jones, 1999: A numerical simulation of cyclic mesocyclogenesis. *J. Atmos. Sci.*, **56**, 2045-2069.

Agee, E. M., J. T. Snow, and P. R. Clare, 1976: Multiple vortex features in the tornado cyclone and the occurrence of tornado families. *Mon. Wea. Rev.*, **104**, 552-563.

Armijo, L., 1969: A theory for the determination of wind and precipitation velocities with Doppler radars. *J. Atmos. Sci.*, **26**, 570-573.

Atlas, D., R. C. Srivastava, and R. S. Sekhon, 1973: Doppler radar characteristics of precipitation at vertical incidence. *Rev. Geophys. Space Phys.*, **11**, 1-35.

Barcilon, A., and P. Drazin, 1972: Dust devil formation. *Geophys. Fluid Dyn.*, **4**, 147-159.

Barnes, S. L., 1968: On the source of thunderstorm rotation. ESSA Tech. Memo. ERLTM-NSSL 38, 28 pp.

Bluestein, H. B., and J. H. Golden, 1993: A review of tornado observations. *The Tornado: Its Structure, Dynamics, Prediction, and Hazards, Geophys. Monogr.*, No. 79, Amer. Geophys. Union, 319-352.

Bluestein, H. B., and M. L. Weisman, 1998: The interactions of numerically simulated supercells initiated along lines. *Preprints, 19th Conf. on Severe Local Storms*, Amer. Meteor. Soc., 265-268.

Bousquet, O., and M. Chong, 1998: A multiple-Doppler synthesis and continuity adjustment technique (MUSCAT) to recover wind components from Doppler radar measurements. *J. Atmos. Oceanic Technol.*, **15**, 343-359.

Brady, R. H., and E. J. Szoke, 1989: Case study of nonmesocyclone tornado development in northeast Colorado: Similarities to waterspout formation. *Mon. Wea. Rev.*, **117**, 843-856.

Brandes, E. A., 1977a: Flow in severe thunderstorms observed by dual-Doppler radar. *Mon. Wea. Rev.*, **105**, 113-120.

Brandes, E. A., 1977b: Gust front evolution and tornado genesis as viewed by Doppler radar. *J. Appl. Meteor.*, **16**, 333-338.

Brandes, E. A., 1978: Mesocyclone evolution and tornadogenesis: Some observations. *Mon. Wea. Rev.*, **106**, 995-1011.

Brandes, E. A., 1981: Finestructure of the Del City-Edmond tornadic mesocirculation. *Mon. Wea. Rev.*, **109**, 635-647.

Brandes, E. A., 1984a: Relationships between radar-derived thermodynamic variables and tornadogenesis. *Mon. Wea. Rev.*, **112**, 1033-1052.

Brandes, E. A., 1984b: Vertical vorticity generation and mesocyclone sustenance in tornadic thunderstorms: The observational evidence. *Mon. Wea. Rev.*, **112**, 2253-2269.

Brandes, E. A., R. P. Davies-Jones, B. C. Johnson, 1988: Streamwise vorticity effects on supercell morphology and persistence. *J. Atmos. Sci.*, **45**, 947-963.

Brooks, H. E., C. A. Doswell, and R. B. Wilhelmson, 1994: The role of midtropospheric winds in the evolution and maintenance of low-level mesocyclones. *Mon. Wea. Rev.*, **122**, 126-136.

Brown, J. M., and K. R. Knupp, 1980: The Iowa cyclonic-anticyclonic tornado pair and its parent thunderstorm. *Mon. Wea. Rev.*, **108**, 1626-1646.

Browning, K. A., 1964: Airflow and precipitation trajectories within severe local storms which travel to the right of the winds. *J. Atmos. Sci.*, **21**, 634-639.

Browning, K. A., and R. J. Donaldson, Jr., 1963: Airflow and structure of a tornadic storm. *J. Atmos. Sci.*, **20**, 533-545.

Browning, K. A., and C. R. Landry, 1963: Airflow within a tornadic storm. *Preprints, 10th Weather Radar Conference*, Amer. Meteor. Soc., 116-122.

Burgess, D. W., V. T. Wood, and R. A. Brown, 1982: Mesocyclone evolution statistics. *Preprints, 12th Conf. on Severe Local Storms*, Amer. Meteor. Soc., 422-424.

Carbone, R. E., 1982: A severe frontal rainband. Part I: Stormwide hydrodynamic structure. *J. Atmos. Sci.*, **39**, 258-279.

Chong, M. and C. Campos, 1996: Extended overdetermined dual-Doppler formalism in synthesizing airborne Doppler radar data. *J. Atmos. Oceanic Technol., 13*, 581-597.

Chong, M., and J. Testud, 1996: Three-dimensional air circulation in a squall line from airborne dual-beam Doppler radar data: A test of coplane methodology software. *J. Atmos. Oceanic Technol.*, **13**, 36-53.

Clark, T. L., F. I. Harris, and C. G. Mohr, 1980: Errors in wind fields derived from multiple-Doppler radars: Random errors and temporal errors associated with advection and evolution. *J. Appl. Meteor.*, **19**, 1273-1284.

Conway, J. W., and D. S. Zrnic, 1993: A study of embryo production and hail growth using dual-Doppler and multiparameter radars. *Mon. Wea. Rev.*, **121**, 2511-2528.

Cressman, G. P., 1959: An operational objective analysis system. *Mon. Wea. Rev.*, **87**, 367-374.

Crook, A., 1994: Numerical simulations initialized with radar-derived winds. Part I: Simulated data experiments. *Mon. Wea. Rev.*, **122**, 1189-1203.

Darkow, G. L., 1971: Periodic tornado production by long-lived parent thunderstorms. *Preprints, 7th Conf. on Severe Local Storms*, Amer. Meteor. Soc., 214-217.

Darkow, G. L., and J. C. Roos, 1970: Multiple tornado producing thunderstorms and their apparent cyclic variations in intensity. *Preprints, 14th Conf. on Radar Meteorology*, Amer. Meteor. Soc., 305-308.

Davies, J. M., C. A. Doswell III, D. W. Burgess, and J. F. Weaver, 1994: Some noteworthy aspects of the Hesston, Kansas tornado family of 13 March 1990. *Bull. Amer. Meteor. Soc.*, **75**, 1007-1017.

Davies-Jones, R. P., 1973: The dependence of core radius on swirl ratio in a tornado simulator. *J. Atmos. Sci.*, **30**, 1427-1430.

Davies-Jones, R. P., 1986: Tornado dynamics. *Thunderstorm Morphology and Dynamics* (2nd Ed.), University of Oklahoma Press, Norman, OK, 411 pp.

Davies-Jones, R. P., and H. E. Brooks, 1993: Mesocyclogenesis from a theoretical perspective. *The Tornado: Its Structure, Dynamics, Prediction, and Hazards, Geophys. Monogr.*, No. 79, Amer. Geophys. Union, 105-114.

Doswell, C. A. III, and D. W. Burgess, 1988: On some issues of United States tornado climatology. *Mon. Wea. Rev.*, **116**, 495-501.

Doviak, R. J., P. S. Ray, R. G. Strauch, and L. J. Miller, 1976: Error estimation in wind fields derived from dual-Doppler radar measurement. *J. Appl. Meteor.*, **15**, 868-878.

Dowell, D. C., and H. B. Bluestein, 1997: The Arcadia, Oklahoma storm of 17 May 1981: Analysis of a supercell during tornadogenesis. *Mon. Wea. Rev.*, **125**, 2562-2582.

Dowell, D. C., and H. B. Bluestein, 1999: Dual-Doppler analysis of non-simultaneous observations. *Preprints, 29th Conf. on Radar Meteorology*, Montreal, Quebec, 529-532.

Dowell, D. C., H. B. Bluestein, and D. P. Jorgensen, 1997: Airborne Doppler radar analysis of supercells during COPS-91. *Mon. Wea. Rev.*, **125**, 365-383.

Ellis, S., 1997: Hole-filling data voids in meteorological fields. M.S. thesis, School of Meteorology, University of Oklahoma, Norman, 198 pp.

Fiedler, B. H., 1993: Numerical simulation of axisymmetric tornadogenesis in forced convection. *The Tornado: Its Structure, Dynamics, Prediction, and Hazards, Geophys. Monogr.*, No. 79, Amer. Geophys. Union, 41-48.

Foote, G. B., and P. S. duToit, 1969: Terminal velocity of raindrops aloft. *J. Appl. Meteor.*, **8**, 249-253.

Forbes, G. S., 1978: *Three scales of motions associated with tornadoes*. Prepared for the Nuclear Regulatory Commission. Available from Nat. Tech. Info. Svc., 359 pp.

Forbes, G. S., 1981: On the reliability of hook echoes as tornado indicators. *Mon. Wea. Rev.*, **109**, 1457-1466.

Forbes, G. S., and R. M. Wakimoto, 1983: A concentrated outbreak of tornadoes, downbursts and microbursts, and implications regarding vortex classification. *Mon. Wea. Rev.*, **111**, 220-235.

Fujita, T. T., 1974: Jumbo tornado outbreak of 3 April 1974. *Weatherwise*, **27**, 116-126.

Fujita, T. T., 1981: Tornadoes and downbursts in the context of generalized planetary scales. *J. Atmos. Sci.*, **38**, 1511-1534.

Fujita, T. T., D. L. Bradbury, and C. F. Van Thullenar, 1970: Palm Sunday tornadoes of April 11, 1965. *Mon. Wea. Rev.*, **98**, 29-69.

Fujita, T. T., G. S. Forbes, and T. A. Umenhofer, 1976: Close-up view of 20 March 1976 tornadoes: Sinking cloud tops to suction vortices. *Weatherwise*, **29**, 116-131.

Fujita, T. T., and R. M. Wakimoto, 1982: Anticyclonic tornadoes in 1980 and 1981. *Preprints, 12th Conf. on Severe Local Storms*, Amer. Meteor. Soc., 401-404.

Gal-Chen, T., 1978: A method for the initialization of the anelastic equations: Implications for matching models with observations. *Mon. Wea. Rev.*, **106**, 587-606.

Gal-Chen, T., 1982: Errors in fixed and moving frame of references: Applications for conventional and Doppler radar analysis. *J. Atmos. Sci.*, **39**, 2279-2300.

Gamache, J. F., 1997: Evaluation of a fully three-dimensional variational Doppler analysis technique. *Preprints, 28th Conf. on Radar Meteor.*, Amer. Meteor. Soc., 422-423.

Gao, J., M. Xue, A. Shapiro, and K. K. Droegemeier, 1999: A variational method for the analysis of three-dimensional wind fields from two Doppler radars. *Mon. Wea. Rev.*, **127**, 2128-2142.

Gilchrist, B., and G. Cressman, 1954: An experiment in objective analysis. *Tellus*, **6**, 309-318.

Grasso, L. D., and W. R. Cotton, 1995: Numerical simulation of a tornado vortex. *J. Atmos. Sci.*, **52**, 1192-1203.

Haltiner, G. J., and R. T. Williams, 1980: *Numerical Prediction and Dynamic Meteorology*. John Wiley & Sons, 477 pp.

Hane, C. E., and P. S. Ray, 1985: Pressure and buoyancy fields derived from Doppler radar data in a tornadic thunderstorm. *J. Atmos. Sci.*, **42**, 18-35.

Heymsfield, G. M., 1978: Kinematic and dynamic aspects of the Harrah tornadic storm analyzed from dual-Doppler radar data. *Mon. Wea. Rev.*, **106**, 233-254.

Hildebrand, P. H., and C. K. Mueller, 1985: Evaluation of meteorological airborne Doppler radar. Part I: Dual-Doppler analyses of air motions. *J. Atmos. Oceanic Technol.*, **2**, 362-380.

Hildebrand, P. H., C. A. Walther, C. L. Frush, J. Testud, and F. Baudin, 1994: The ELDORA/ASTRAIA airborne Doppler weather radar: Goals, design, and first field tests. *Proc. of the IEEE*, **82**, 1873-1890.

Hoecker, W. H., 1960: Wind speed and airflow patterns in the Dallas tornado of April 2, 1957. *Mon. Wea. Rev.*, **88**, 167-180.

Jensen, B., E. N. Rasmussen, T. P. Marshall, and M. A. Mabey, 1983: Storm scale structure of the Pampa storm. *Preprints, 13th Conf. on Severe Local Storms*, Amer. Meteor. Soc., 85-88.

Johnson, K. W., P. S. Ray, B. C. Johnson, and R. P. Davies-Jones, 1987: Observations related to the rotational dynamics of the 20 May 1977 tornadic storms. *Mon. Wea. Rev.*, **115**, 2463-2478.

Jorgensen, D. P., and J. D. DuGranrut, 1991: A dual-beam technique for deriving wind fields from airborne Doppler radar. *Preprints, 25th Conf. on Radar Meteor.*, Amer. Meteor. Soc., 458-461.

Jorgensen, D. P., P. H. Hildebrand, and C. L. Frush, 1983: Feasibility test of an airborne pulse-Doppler meteorological radar. *J. Climate Appl. Meteor.*, **22**, 744-757.

Jorgensen, D. P., and F. D. Marks, Jr., 1984: Airborne Doppler radar study of the structure and three-dimensional airflow within a hurricane rainband. *Preprints, 22nd Conf. on Radar Meteor.*, Amer. Meteor. Soc., 572-577.

Jorgensen, D. P., and B. F. Smull, 1993: Mesovortex circulations seen by airborne Doppler radar within a bow-echo mesoscale convective system. *Bull. Amer. Meteor. Soc.*, **74**, 2146-2157.

Joss, J., and A. Waldvogel, 1970: Raindrop size distribution and Doppler velocities. *Preprints, 14th Conf. Radar Meteorology*, Amer. Meteor. Soc., 153-156.

Kangieser, P. C., 1954: A physical explanation of the hollow structure of waterspout tubes. *Mon. Wea. Rev.*, **82**, 147-152.

Klemp, J. B., 1987: Dynamics of tornadic thunderstorms. *Ann. Rev. Fluid Mech.*, **19**, 369-402.

Klemp, J. B., and R. Rotunno, 1983: A study of the tornadic region within a supercell thunderstorm. *J. Atmos. Sci.*, **40**, 359-377.

Klemp, J. B., and R. B. Wilhelmson, 1978: The simulation of three-dimensional convective storm dynamics. *J. Atmos. Sci.*, **35**, 1070-1096.

Lateef, M. A., 1967: Vertical motion, divergence, and vorticity in the troposphere over the Caribbean, August 3-5, 1963. *Mon. Wea. Rev.*, **95**, 778-790.

Lee, B. D., and R. B. Wilhelmson, 1997: The numerical simulation of non-supercell tornadogenesis. Part I: Initiation and evolution of pre-tornadic misocyclone circulations along a dry outflow boundary. *J. Atmos. Sci.*, **54**, 32-60.

Lee, W.-C., P. Dodge, F. D. Marks, Jr., and P. H. Hildebrand, 1994: Mapping of airborne Doppler radar data. *J. Atmos. Oceanic Technol.*, **11**, 572-578.

Leise, J. A., 1982: A multidimensional scale-telescoped filter and data extension package. NOAA Tech. Memo. ERL WPL-82, 18 pp. [NTIS PB82-164104.]

Lemon, L. R., 1977: *New Severe Thunderstorm Radar Identification Techniques and Warning Criteria: A Preliminary Report*. NOAA Tech. Memo. NWS NSSFC-1, TDU, NSSFC, Kansas City.

Lemon, L. R., and D. W. Burgess, 1993: Supercell associated deep convergence zone revealed by a WSR-88D. *Preprints, 26th Conf. on Radar Meteor.*, Amer. Meteor. Soc., 206-208.

Lemon, L. R., and C. A. Doswell, 1979: Severe thunderstorm evolution and mesocyclone structure as related to tornadogenesis. *Mon. Wea. Rev.*, **107**, 1184-1197.

LeMone, M. A., and D. P. Jorgensen, 1991: Precipitation and kinematic structure of an oceanic mesoscale convective system. Part II: Momentum transport and generation. *Mon. Wea. Rev.*, **119**, 2638-2653.

Leslie, L. M., 1971: The development of concentrated vortices: A numerical study. *J. Fluid Mech.*, **48**, 1-21.

Lewellen, W. S., 1993: Tornado vortex theory. *The Tornado: Its Structure, Dynamics, Prediction, and Hazards, Geophys. Monogr.*, No. 79, Amer. Geophys. Union, 19-39.

Lhermitte, R. M., 1968: New developments in Doppler radar methods. *Proceedings, 13th Conf. on Radar Meteor.*, Amer. Meteor. Soc., 14-17.

Lilly, D. K., 1969: Tornado dynamics. Manuscript 69-117, Natl. Center for Atmos. Res., Boulder, CO.

Lilly, D. K, 1982: The development and maintenance of rotation in convective storms. *Intense Atmospheric Vortices*, Springer-Verlag, 149-160.

Markowski, P. M., E. N. Rasmussen, J. M. Straka, and D. C. Dowell, 1998: Observations of low-level baroclinity generated by anvil shadows. *Mon. Wea. Rev.*, **126**, 2942-2958.

Marks, F. D., Jr., and R. A. Houze, Jr., 1984: Airborne Doppler radar observations in Hurricane Debby. *Bull. Amer. Meteor. Soc.*, **65**, 569-582.

Marks, F. D., Jr., and R. A. Houze, Jr., 1987: Inner core structure of Hurricane Alicia from airborne Doppler radar observations. *J. Atmos. Sci.*, **44**, 1296-1317.

Mewes, J. J., and A. Shapiro, 1999: Dual-Doppler analysis using the anelastic vertical vorticity equation. *Preprints, 29th Conf. on Radar Meteor.*, Amer. Meteor. Soc, 33-36.

O'Brien, J. J., 1970: Alternative solutions to the classical vertical velocity problem. *J. Appl. Meteor.*, **9**, 197-203.

Ogura, Y., and N. A. Phillips, 1962: Scale analysis of deep and shallow convection in the atmosphere. *J. Atmos. Sci.*, **19**, 173-179.

Oye, R., and M. Case, 1992: *REORDER: A program for gridding radar data.* NCAR Field Observing Facility, Boulder, Colorado, 36 pp.

Rasmussen, E. N., R. E. Peterson, J. E. Minor, and B. D. Campbell, 1982: Evolutionary characteristics and photogrammetric determination of windspeeds within the Tulia outbreak tornadoes 28 May 1980. *Preprints, 12th Conf. Severe Local Storms*, Amer. Meteor. Soc., 301-304.

Rasmussen, E. N., and J. M. Straka, 1997: Tornadogenesis: A review and a new conceptual model. Submitted to *Mon. Wea. Rev.*

Rasmussen, E. N., J. M. Straka, R. Davies-Jones, C. A. Doswell, F. H. Carr, M. D. Eilts, and D. R. MacGorman, 1994: Verification of the origins of rotation in tornadoes experiment: VORTEX. *Bull. Amer. Meteor. Soc.*, **75**, 995-1006.

Ray, P. S., B. C. Johnson, K. W. Johnson, J. S. Bradberry, J. J. Stephens, K. K. Wagner, R. B. Wilhelmson, and J. B. Klemp, 1981: The morphology of several tornadic storms on 20 May 1977. *J. Atmos. Sci.*, **38**, 1643-1663.

Ray, P. S., and D. P. Jorgensen, 1988: Uncertainties associated with combining airborne and ground-based Doppler radar data. *J. Atmos. Oceanic Technol.*, **5**, 177-196.

Ray, P. S., D. P. Jorgensen, and S. L. Wang, 1985: Airborne Doppler radar observations of a convective storm. *J. Climate Appl. Meteor.*, **24**, 687-698.

Ray, P. S., and M. Stephenson, 1990: Assessment of the geometric and temporal errors associated with airborne Doppler radar measurements of a convective storm. *J. Atmos. Oceanic Technol.*, **7**, 206-217.

Ray, P. S., C. L. Ziegler, W. Bumgarner, and R. J. Serafin, 1980: Single- and multiple-Doppler radar observations of tornadic storms. *Mon. Wea. Rev.*, **108**, 1607-1625.

Richtmyer, R. D., and D. W. Morton, 1967: *Difference Methods for Initial Value Problems*. Interscience, 405 pp.

Rogers, R. R., and M. K. Yau, 1989: *A Short Course in Cloud Physics*. Butterworth and Heinemann, 290 pp.

Rotunno, R., 1981: On the evolution of thunderstorm rotation. *Mon. Wea. Rev.*, **109**, 577-586.

Rotunno, R., 1993: Supercell thunderstorm modeling and theory. *The Tornado: Its Structure, Dynamics, Prediction, and Hazards, Geophys. Monogr.*, No. 79, Amer. Geophys. Union, 57-73.

Rotunno, R., and J. Klemp, 1985: On the rotation and propagation of simulated supercell thunderstorms. *J. Atmos. Sci.*, **42**, 271-292.

Sasaki, Y, 1970: Some basic formalisms in numerical variational analysis. *Mon. Wea. Rev.*, **98**, 875-883.

Schneider, J. M., 1991: Dual Doppler measurement of a sheared, convective boundary layer. Ph. D. dissertation, University of Oklahoma, Norman, 134 pp.

Scialom, G., and Y. Lemaitre, 1990: A new analysis for the retrieval of three-dimensional mesoscale wind fields from multiple Doppler radar. *J. Atmos. Oceanic Technol.*, **7**, 640-665.

Sedgewick, R., 1988: *Algorithms*. Addison-Wesley, 657 pp.

Shapiro, A., 1993: The use of an exact solution of the Navier-Stokes equations in a validation test of a three-dimensional nonhydrostatic numerical model. *Mon. Wea. Rev.*, **121**, 2420-2425.

Shapiro, A., and J. J. Mewes, 1999: New formulations of dual-Doppler wind analysis. *J. Atmos. Oceanic Technol.*, **16**, 782-792.

Sirmans, D., D. Zrnic, B. Baumgarner, 1976: Extensions of maximum unambiguous Doppler velocity by use of two sampling rates. *Preprints, 17th Conf. on Radar Meteor.*, Amer. Meteor. Soc., 23-28.

Smith, R. K. and L. M. Leslie, 1979: A numerical study of tornadogenesis in a rotating thunderstorm. *Q. J. R. Meteor. Soc.*, **105**, 107-127.

Snow, J. T., 1984: On the formation of particle sheaths in columnar vortices. *J. Atmos. Sci.*, **41**, 2477-2491.

Snow, J. T., and E. M. Agee, 1975: Vortex splitting in the mesocyclone and the occurrence of tornado families. *Preprints, 9th Conf. on Severe Local Storms*, Amer. Meteor. Soc., 270-277.

Sperow, K. S., H. B. Bluestein, and T. Gal-Chen, 1995: Testing a Doppler analysis method: The two-step, second order Lax-Wendroff scheme. *Preprints, 27th Conf. on Radar Meteor.*, Amer. Meteor. Soc., 296-298.

Trapp, R. J., and R. Davies-Jones, 1997: Tornadogenesis with and without a dynamic pipe effect. *J. Atmos. Sci.*, **54**, 113-133.

Umenhofer, T. A., and T. T. Fujita, 1977: Great Bend tornadoes of August 30, 1974. *Preprints, 10th Conf. on Severe Local Storms*, Amer. Meteor. Soc., 457-462.

U. S. Dept. of Commerce, 1995: *Storm Data*, Vol. 37, No. 6, NOAA, NESDIS, NCDC.

Wakimoto, R. M., and N. T. Atkins, 1996: Observations on the origins of rotation: The Newcastle tornado during VORTEX-94. *Mon. Wea. Rev.*, **124**, 384-407.

Wakimoto, R. M., W.-C. Lee, H. B. Bluestein, C.-H. Liu, and P. H. Hildebrand, 1996: ELDORA observations during VORTEX 95. *Bull. Amer. Meteor. Soc.*, **77**, 1465-1481.

Wakimoto, R. M., C. Liu, and H. Cai, 1998: The Garden City, Kansas storm during VORTEX 95. Part I: Overview of the storm's life cycle and mesocyclogenesis. *Mon. Wea. Rev.*, **126**, 372-392.

Wakimoto, R. M., and J. W. Wilson, 1989: Nonsupercell tornadoes. *Mon. Wea. Rev.*, **117**, 1113-1140.

Walko, R. L., 1993: Tornado spin-up beneath a convective cell: Required basic structure of the near-field boundary layer winds. *The Tornado: Its Structure, Dynamics, Prediction, and Hazards, Geophys. Monogr.*, No. 79, Amer. Geophys. Union, 89-95.

Ward, N. B., 1972: The exploration of certain features of tornado dynamics using a laboratory model. *J. Atmos. Sci.*, **29**, 1194-1204.

Weaver, J. F., and S. P. Nelson, 1982: Multiscale aspects of thunderstorm gust fronts and their effects on subsequent storm development. *Mon. Wea. Rev.*, **110**, 707-718.

Webster, J. P, and R. Lukas, 1992: TOGA-COARE: The TOGA coupled ocean-atmosphere response experiment. *Bull. Amer. Meteor. Soc.*, **73**, 1377-1416.

Weisman, M. L., M. S. Gilmore, and L. J. Wicker, 1998: The impact of convective storms on their local environment: What is an appropriate ambient sounding? *Preprints, 19th Conf. on Severe Local Storms.*, Amer. Meteor. Soc., 238-241.

Weisman, M. L., and J. B. Klemp, 1984: The structure and classification of numerically simulated convective storms in directionally varying wind shears. *Mon. Wea. Rev.*, **112**, 2479-2498.

Wicker, L. J., 1996: The role of near surface wind shear on low-level mesocyclone generation and tornadoes. *Preprints, 18th Conf. on Severe Local Storms*, Amer. Meteor. Soc., 115-119.

Wicker, L. J., and R. B. Wilhelmson, 1995: Simulation and analysis of tornado development and decay within a three-dimensional supercell thunderstorm. *J. Atmos. Sci.*, **52**, 2675-2703.

Wurman, J, J. M. Straka, and E. N. Rasmussen, 1996: Fine-scale Doppler radar observations of tornadoes. *Science*, 272, 1774-1777.

Wurman, J., J. Straka, E. Rasmussen, M. Randall, and A. Zahrai, 1997: Design and deployment of a portable, pencil-beam, pulsed, 3-cm Doppler radar. *J. Atmos. Oceanic Technol.*, **14**, 1502-1512.

Zamora, R. J., M. A. Shapiro, and C. A. Doswell III, 1987: The diagnosis of upper tropospheric divergence and ageostrophic wind using profiler wind observations. *Mon. Wea. Rev.*, **115**, 871-884.

Ziegler, C. L., 1978: A dual Doppler variational objective analysis as applied to studies of convective storms. Master's thesis, University of Oklahoma, Norman, 115 pp.

APPENDIX A. PROCESSING OF RAW ELDORA DATA

Characteristics of the ELDORA (while scanning in convective mode) are given in Table 1.1. The ELDORA transmits pulses at two different pulse repetition frequencies (PRFs). This yields an effective unambiguous velocity (±79 m s^{-1}) much greater than the individual unambiguous velocities associated with each PRF (±20 m s^{-1} at 2500 Hz and ±16 m s^{-1} at 2000 Hz) (Sirmans et al. 1976, Hildebrand et al. 1994, Wakimoto et al. 1996). However, this method of extending the Nyquist velocity range can fail if the Doppler samples are noisy. For example, if one of the velocity measurements is in error by a few m s^{-1}, the unfolded velocity may fall into an interval much different from that of the actual velocity. The result is speckles of erroneous velocity (Fig. 2.1.1).

It is possible to correct a velocity speckle by discarding the bad velocity measurement and then manually unfolding the good velocity estimate corresponding to the other PRF. However, since a small fraction of gates was affected by speckling in the McLean storm (Fig. 2.1.1 is a worst-case example), I opted to simply remove the erroneous gates. Manual removal of the velocity speckles was the most time consuming step of the raw data editing.

I removed all velocity speckles below 10 km AGL. However, owing to the overwhelming number of speckles at upper levels in the storm (Fig. 2.1.1), I removed only the speckles that were very far off (>50 m s^{-1}) from the apparent true velocity. To make sure that this was not a problem, I did attempt to completely clean up data for one analysis time (the aircraft pass at 2306 UTC). The analyses with and without upper-level speckles did not differ significantly at low and mid levels but did contain minor differences very high up in the storm.

Other steps in the editing include removing noisy data outside the storms, unfolding velocities with greater magnitude than the effective unambiguous velocity, and removing data affected by return from the ground. There were only a few locations in the McLean storm (e.g., in the tornado in Fig. 2.1.1) in which unfolding was necessary because the Nyquist velocity (79 m s^{-1}) is so large. However, many data were affected by ground clutter. In clear air, the velocities at low levels approach zero near the ground (Fig. 2.1.1). Removal of velocity (and reflectivity) data where reflectivity exceeded 12 dBZ eliminated the ground clutter in these regions. Within the storm, the impact of the ground return on the velocities was not as sharp owing to the relatively larger fraction of power returned from the precipitation (Fig. 2.1.1). At the bottom of the storm, I removed all reflectivity and velocity data below 0 km AGL and deleted data where there was a distinct maximum in reflectivity associated with the ground.

I interpolated edited data (reflectivity, radial velocity, azimuth angle, elevation angle, and time fields) to Cartesian grids with REORDER (Oye and Case 1992). The interpolation of quantities that are not Galilean invariant (i.e., radial velocity, azimuth angle, and elevation angle) introduces error into the analysis (Gal-Chen 1982, Bousquet and Chong 1998). However, this error is small except near the flight track. Bousquet and Chong (1998) describe a more precise approach of including the interpolation step directly in the dual-Doppler wind synthesis.

Each Cartesian grid is 20 km wide and up to 20 km tall (variable according to the height of the storm). The horizontal and vertical grid spacings are 400 m and 500 m, respectively, which is roughly the radar beamwidth at 15 km range. The radius of influence for the Cressman (1959) interpolation was 1.2 km. A value this large prevents data gaps within the storm interior (Fig. A.1) and also smoothes the data sufficiently such that post-filtering of the dual-Doppler winds is unnecessary. However, the use of such a large radius of influence also potentially eliminates important small details in the flow. For example, a synthesis at 2259 UTC with a 0.6-km Cressman radius of influence (Fig. A.1.a) has stronger convergence in the southeastern lobe of the updraft and a stronger rear downdraft than in the other synthesis (Fig. A.1.b). I chose the 1.2-km radius of influence based on the results with the strong-constraint wind synthesis method (Section 2.3). In future work with the McLean storm case, I may choose a slightly smaller Cressman radius of influence for the weak-constraint syntheses (Section 2.4).

The Cressman scheme expands the coverage of the data beyond the actual limits by extrapolation. After the objective analysis, the first step in my dual-Doppler synthesis is to remove the outermost three data points along the edges of the good data, thus eliminating most of the extrapolated data in the analysis.

Determination of the motion of the optimal moving reference frame (Section 2.5) requires information from three consecutive aircraft passes. Therefore, in addition to the data for the analysis time of interest, I also interpolated data from the previous and following aircraft passes to identical grids. In order to keep the grids filled with data for each pass, I included a first guess of the translation velocity in the interpolation with REORDER.

APPENDIX B. STABILITY OF AN ITERATIVE DUAL-DOPPLER ANALYSIS

It is common knowledge that an iterative dual-Doppler analysis in Cartesian coordinates is unstable if some portion of the domain contains measurements at high incidence angles. However, I am unaware of any publication that provides much detail on the nature of the instability. The writings on this subject by T. Gal-Chen in 1983 and by D. Lilly in 1986 (Schneider 1991) have apparently been lost. An article by Ray et al. (1985) is the only one I know of that actually gives a specific stability constraint, but the paper does not include its derivation. The lack of published information on this subject motivated me to tackle the problem myself.

The dual-Doppler Equations (2.1.9) and (2.1.10) may be expressed in the form

$$u = A + Bw \tag{B.1}$$

$$v = C + Dw \tag{B.2}$$

where the coefficients A, B, C, and D are functions of the radial velocities, the azimuth angles, the elevation angles, and the precipitation fall speed. To keep the expressions below manageable, I will use the forms of the coefficients appropriate for radars at fixed sites (Armijo 1969, Ray et al. 1980), with the simplification that both radars are at the same height. I will define a coordinate system with radar #1 at the origin and with the radar baseline along the y axis. The coordinates of radar #1, radar #2, and the observed point are therefore (0, 0, 0), (0, y_2, 0), and (x, y, z), respectively. With this geometry, the coefficients in the dual-Doppler equations are

$$A = \frac{d_1 V_1 (y_2 - y) + d_2 V_2 y}{x y_2} \tag{B.3}$$

$$B = -\frac{z}{x} \tag{B.4}$$

$$C = \frac{d_1 V_1 - d_2 V_2}{y_2} \tag{B.5}$$

$$D = 0 \tag{B.6}$$

where $d_1 = \sqrt{x^2 + y^2 + z^2}$ and $d_2 = \sqrt{x^2 + (y - y_2)^2 + z^2}$. To simplify things further, I will employ the Boussinesq form of the continuity equation

$$\frac{\partial u}{\partial x} + \frac{\partial v}{\partial y} + \frac{\partial w}{\partial z} = 0. \tag{B.7}$$

rather than the anelastic form.

In a traditional iterative dual-Doppler analysis (Ray et al. 1980), one iteratively adjusts the estimates of the velocities at a particular vertical level before proceeding to the next level. If the solution procedure is stable, then each iteration will produce smaller and smaller changes in the velocity estimates. (If it is not, then the increments will grow quickly with each iteration.) For upward integration of the continuity equation with centered finite differencing, iteration at a particular level k proceeds as follows:

1. Determine a first guess of $w_{i,j,k}$ for all i and j.

2. For all i and j, compute
$$\begin{aligned} u_{i,j,k} &= A_{i,j,k} + B_{i,j,k} w_{i,j,k} \\ v_{i,j,k} &= C_{i,j,k} + D_{i,j,k} w_{i,j,k}. \end{aligned} \qquad \text{(B.8) and (B.9)}$$

3. Compute
$$\begin{aligned} w_{i,j,k} = w_{i,j,k-1} &- \Delta z\left[\frac{1}{2}\left(\frac{u_{i+1,j,k} - u_{i-1,j,k}}{2\Delta x} + \frac{u_{i+1,j,k-1} - u_{i-1,j,k-1}}{2\Delta x}\right)\right] \\ &- \Delta z\left[\frac{1}{2}\left(\frac{v_{i,j+1,k} - v_{i,j-1,k}}{2\Delta y} + \frac{v_{i,j+1,k-1} - v_{i,j-1,k-1}}{2\Delta y}\right)\right] \end{aligned} \tag{B.10}$$
at every location i and j.

4. Repeat steps 2 and 3 until the solution converges.

By substituting (B.8) and (B.9) into (B.10), one may obtain a scheme with a single unknown $w_{i,j,k}$:

$$
\begin{aligned}
w_{i,j,k}^{n+1} = w_{i,j,k-1} &- \frac{\Delta z}{4\Delta x}\left[A_{i+1,j,k} - A_{i-1,j,k} + A_{i+1,j,k-1} - A_{i-1,j,k-1}\right] \\
&- \frac{\Delta z}{4\Delta x}\left[B_{i+1,j,k-1}w_{i+1,j,k-1} - B_{i-1,j,k-1}w_{i-1,j,k-1}\right] \\
&- \frac{\Delta z}{4\Delta y}\left[C_{i,j+1,k} - C_{i,j-1,k} + C_{i,j+1,k-1} - C_{i,j-1,k-1}\right] \\
&- \frac{\Delta z}{4\Delta y}\left[D_{i,j+1,k-1}w_{i,j+1,k-1} - D_{i,j-1,k-1}w_{i,j-1,k-1}\right] \\
&- \frac{\Delta z}{4\Delta x}\left[B_{i+1,j,k}w^{n}_{i+1,j,k} - B_{i-1,j,k}w^{n}_{i-1,j,k}\right] \\
&- \frac{\Delta z}{4\Delta y}\left[D_{i,j+1,k}w^{n}_{i,j+1,k} - D_{i,j-1,k}w^{n}_{i,j-1,k}\right]
\end{aligned} \tag{B.11}
$$

where the superscript n refers to the iteration number (analogous to a time step). During the iteration for w at level k, the coefficients A-D and the values of w at level k-1 are known (i.e., they do not change from one iteration to the next). I will sum the known expressions on the first four lines of (B.11) into one value $q_{i,j,k}$:

$$
\begin{aligned}
q_{i,j,k} \equiv w_{i,j,k-1} &- \frac{\Delta z}{4\Delta x}\left[A_{i+1,j,k} - A_{i-1,j,k} + A_{i+1,j,k-1} - A_{i-1,j,k-1}\right] \\
&- \frac{\Delta z}{4\Delta x}\left[B_{i+1,j,k-1}w_{i+1,j,k-1} - B_{i-1,j,k-1}w_{i-1,j,k-1}\right] \\
&- \frac{\Delta z}{4\Delta y}\left[C_{i,j+1,k} - C_{i,j-1,k} + C_{i,j+1,k-1} - C_{i,j-1,k-1}\right] \\
&- \frac{\Delta z}{4\Delta y}\left[D_{i,j+1,k-1}w_{i,j+1,k-1} - D_{i,j-1,k-1}w_{i,j-1,k-1}\right]
\end{aligned} \tag{B.12}
$$

For the previously specified radar geometry, $B = -\frac{z}{x}$ and D=0. Therefore, Equation (B.11) simplifies to

$$
w_{i,j,k}^{n+1} = q_{i,j,k} + \frac{\Delta z}{4\Delta x}\left[\left(\frac{z}{x+\Delta x}\right)w^{n}_{i+1,j,k} - \left(\frac{z}{x-\Delta x}\right)w^{n}_{i-1,j,k}\right]. \tag{B.13}
$$

One may eliminate the quantity q by considering the change in the estimate of w during a particular iteration:

$$w_{i,j,k}^{n+1} - w_{i,j,k}^{n} = \frac{\Delta z}{4\Delta x}\left[\left(\frac{z}{x+\Delta x}\right)\left(w_{i+1,j,k}^{n} - w_{i+1,j,k}^{n-1}\right) - \left(\frac{z}{x-\Delta x}\right)\left(w_{i-1,j,k}^{n} - w_{i-1,j,k}^{n-1}\right)\right]. \tag{B.14}$$

To determine whether this scheme is stable, I will use the von Neumann method to find out whether errors represented by complex Fourier modes will decay or amplify (Haltiner and Williams 1980):

$$w = \overline{w}e^{I(mx-\sigma t)}. \tag{B.15}$$

In the above expression, $\overline{w}$ is the amplitude, m is the horizontal wavenumber, σ is the frequency, and $I \equiv \sqrt{-1}$. There is actually no time variable in the dual-Doppler equations, but the iterative solution technique is analogous to a time-marching problem. A value Δt represents the interval between consecutive estimates.

Substituting (B.15) into (B.14), one may obtain

$$\overline{w}e^{I(mx-\sigma t)}\left[e^{-I\sigma\Delta t} - 1\right] = \overline{w}e^{I(mx-\sigma t)}\frac{\Delta z}{4\Delta x}\left[\begin{array}{l}\left(\frac{z}{x+\Delta x}\right)\left(e^{Im\Delta x} - e^{Im\Delta x}e^{I\sigma\Delta t}\right)\\ -\left(\frac{z}{x-\Delta x}\right)\left(e^{-Im\Delta x} - e^{-Im\Delta x}e^{I\sigma\Delta t}\right)\end{array}\right]. \tag{B.16}$$

Equation (B.16) may be rearranged and simplified to

$$\begin{aligned} e^{-I\sigma\Delta t} &= \frac{\Delta z}{4\Delta x}\left[\left(\frac{z}{x+\Delta x}\right)e^{Im\Delta x} - \left(\frac{z}{x-\Delta x}\right)e^{-Im\Delta x}\right] \\ &= -\cos(m\Delta x)\left(\frac{\Delta z}{4\Delta x}\right)\left[\frac{2z\Delta x}{x^2-(\Delta x)^2}\right] + i\sin(m\Delta x)\left(\frac{\Delta z}{4\Delta x}\right)\left[\frac{2zx}{x^2-(\Delta x)^2}\right]. \end{aligned} \tag{B.17}$$

In a von Neumann analysis, a scheme is stable if

$$\left|e^{-I\sigma\Delta t}\right| \leq 1. \tag{B.18}$$

Equation (B.17) indicates that the growth rate has special characteristics very close to the radar baseline (where $x \approx 0$). However, we already know to avoid obtaining a solution there because the coefficients A and B become undefined.

Throughout the remainder of the domain, $|x| >> \Delta x$, and the approximate form of Equation (B.17) is

$$e^{-I\sigma\Delta t} = -\cos(m\Delta x)\left(\frac{z\Delta z}{2x^2}\right) + I\sin(m\Delta x)\left(\frac{z\Delta z}{2x\Delta x}\right). \tag{B.19}$$

The magnitude of the imaginary term on the right-hand side is typically much greater than the real one. The imaginary term is greatest in magnitude where $|\sin(m\Delta x)| = 1$. Therefore, the condition for stability becomes

$$\left|\frac{z\Delta z}{2x\Delta x}\right| \leq 1 \tag{B.20}$$

or

$$\left|\frac{z}{x}\right| \leq 2\frac{\Delta x}{\Delta z}. \tag{B.21}$$

The quantity $\frac{z}{x}$ is the tangent of θ, where θ is the elevation angle of the observed point *relative to the radar baseline* (not with respect to the radar). Therefore, an iterative dual-Doppler analysis in Cartesian coordinates with centered finite differencing is stable as long as

$$|\tan\theta| \le 2\frac{\Delta x}{\Delta z}. \tag{B.22}$$

A limitation of Equation (B.22) is that it does not apply to the side of a domain, where centered finite differencing is not possible. The stability constraint changes for one-sided finite differencing at the edge of a domain

$$w_{i,j,k}^{n+1} = q_{i,j,k} + \frac{\Delta z}{2\Delta x}\left[\left(\frac{z}{x+\Delta x}\right)w_{i+1,j,k}^{n} - \left(\frac{z}{x}\right)w_{i,j,k}^{n}\right]. \tag{B.23}$$

With a von Neumann analysis like that employed previously, one may obtain the stability condition for one-sided finite differencing:

$$|\tan\theta| \le \frac{\Delta x}{\Delta z}. \tag{B.24}$$

This condition is more stringent than (B.22) and matches the constraint quoted by Ray et al. (1985). This is the more relevant condition for a domain that does not intersect the radar baseline because the highest elevation angles are found at an edge of the domain.

When the horizontal and vertical grid spacings are identical, the elevation angles (relative to the radar baseline) of all of the grid points at the edge of the domain must be less than 45° to guarantee stability. One may increase the permissible maximum elevation angle by decreasing the vertical grid spacing. Geometrically, the iterative scheme is stable at a particular grid point when the azimuthal coordinate curve (from the representation of the data in coplane coordinates) extending downward from the grid point remains within the grid box at the next lowest level (Fig. B.1) (Shapiro and Mewes 1999).

APPENDIX C. RELATIONSHIP BETWEEN REFLECTIVITY AND FALL SPEED

Solution of the dual-Doppler equations (2.1.2)-(2.1.4) requires a method of estimating the scatterer fall velocity. Dual-Doppler studies of convective storms typically employ an empirical relationship between the reflectivity and the precipitation fall speed (e.g., Brandes 1977a). The frequently-used relationship derived by Joss and Waldvogel (1970)

$$w_t = -2.6Z^{0.107}, \tag{C.1}$$

where w_t is the fall speed of rain in m s^{-1} and Z is the reflectivity factor in mm^6 m^{-3}, was based on rain measurements in a variety of weather systems. These observations included only one thunderstorm, which had reflectivity up to 53 dBZ.

Since the Joss and Waldvogel (1970) conference paper, Atlas et al. (1973) and Conway and Zrnic (1993) concluded that the above relationship was reasonable for rain. However, the subject has in general received little attention.

During the 8 June 1995 flight, the Electra was often close enough to the McLean storm to have high reflectivity (up to 43 dBZ) directly overhead (e.g., Fig. 2.1.1). For scans directly overhead, the common plane of the fore and aft measurements (Fig. 2.1.3) is vertical. Therefore, if the velocities in the observed region are steady between the times of the two measurements, then the horizontal (along-track) and vertical components of scatterer motion can be computed directly (Fig. C.1). Furthermore, if the vertical velocity in the observed region is zero, then the following relationships apply:

$$v_r^{(1)} = v_h \cos e_1 + w_t \sin e_1 \tag{C.2}$$

$$v_r^{(2)} = -v_h \cos e_2 + w_t \sin e_2 \tag{C.3}$$

where v_r is the radial velocity, e is the elevation angle, v_h is the along-track horizontal velocity component, w_t is the fall speed of the scatterers, and the subscripts/superscripts

"1" and "2" refer to the fore and aft measurements, respectively. The solution for w_t, obtained by eliminating v_h from the above equations, is

$$w_t = \frac{v_r^{(1)} \cos e_2 + v_r^{(2)} \cos e_1}{\sin e_1 \cos e_2 + \cos e_1 \sin e_2}. \tag{C.4}$$

With Equation (C.4) and the specified assumptions, one may compute terminal fall speed directly from observations.

Fig. C.2 is a plot of w_t computed from objectively-analyzed ELDORA data from five aircraft passes near the McLean storm. The values are plotted against reflectivity for all locations with greater than 15 dBZ. The precipitation fall speeds have been normalized to a common air density as suggested by Foote and du Toit (1969):

$$w_t^{\text{normalized}} = w_t \left(\frac{\rho_0}{\rho} \right)^{0.4} \tag{C.5}$$

where ρ is the air density at a particular height and ρ_0 is the reference air density (1.2 kg m^{-3} in this case).

There is significant scatter in the data in Fig. C.2. This may be associated with error in the assumption of zero vertical air velocity in Equations (C.2) and (C.3); the overhead ELDORA observations were outside the main updraft but may have still been in regions of some upward or downward air motion. (Error in the steadiness assumption likely also plays a role.) However, the tendency of fall speeds to be greater in magnitude with higher reflectivity is reasonable.

The best fit w_t vs. Z relationship for the data in Fig. C.2, with an exponential form like that specified by Joss and Waldvogel (1970), is

$$w_t = 3.59 - 5.91 Z^{0.114}. \tag{C.6}$$

This empirical relationship is compared to the original Joss and Waldvogel (1970) version in Table C.1. A slightly better fit for the McLean storm observations is obtained with

$$w_t = 0.706 - 0.347 Z_{dB} \tag{C.7}$$

where Z_{dB} is the reflectivity in dBZ.

In the pseudo-dual-Doppler analyses of the McLean storm, I employ the empirical relationship in Equation (C.7). In regions of low reflectivity (2 dBZ or less), I assume the fall speed to be zero. In regions of high reflectivity, I apply Equation (C.7) beyond the range of reflectivity (maximum of 43 dBZ) used in deriving the relationship. However, the fall speed values for the highest reflectivities in the ELDORA data (55 dBZ) are plausible (Table C.1). The terminal fall speed from Equation (C.7) carried out to 55 dBZ lies between the value for rain from Joss and Waldvogel (1970) and a relationship derived for hail by Conway and Zrnic (1993).

The terminal fall speeds (Table C.1) from either Equation (C.6) or (C.7) are greater in magnitude than for the Joss and Waldvogel (1970) equation. I offer a few possible explanations for this. First of all, the reflectivity values in the McLean storm may have been underestimated due to the calibration of the ELDORA; in the storm core, reflectivity tended to be ~4 dBZ lower in the ELDORA data than in the P-3 data. Secondly, the drop size distribution in the McLean storm may have been different than the storm studied by Joss and Waldvogel (1970). Lastly, although the McLean storm was not a prolific hail producer, some of the higher terminal fall speeds may have still been associated with the presence of some hail within the high reflectivity core.

APPENDIX D. LEAST SQUARES INTERPOLATOR

Horizontal interpolation is necessary to map the observations from the coordinates in the non-uniform moving reference frame (Section 2.5) to a regular grid. To minimize the impact of this interpolation on the results, I use a simple interpolator that attempts to preserve local horizontal gradients more accurately than traditional interpolation methods such as the Cressman (1959) scheme. This type of method, which was proposed previously by Gilchrist and Cressman (1954), works well when the spacing between observations is fairly regular. In this scheme, I assume the observations $q_i(x_i, y_i)$ within a small neighborhood of the grid point (x_0, y_0) vary roughly linearly in the horizontal:

$$q_i(x_i, y_i) \approx q(x_0, y_0) + \frac{\partial q}{\partial x}(x_i - x_0) + \frac{\partial q}{\partial y}(y_i - y_0) \qquad i = 1, n \tag{D.1}$$

where n is the number of data points within the neighborhood of the grid point. The least squares solution minimizes the following functional:

$$J = \sum_{i=1}^{n} \left[q(x_0, y_0) + \frac{\partial q}{\partial x}(x_i - x_0) + \frac{\partial q}{\partial y}(y_i - y_0) - q_i(x_i, y_i) \right]^2 = \min. \tag{D.2}$$

The minimization is accomplished by taking the variation of J with respect to $q(x_0, y_0)$, $\frac{\partial q}{\partial x}$, and $\frac{\partial q}{\partial y}$, and setting each equal to zero. The result is

$$n\,q(x_0, y_0) + \frac{\partial q}{\partial x}\sum_{i=1}^{n}(x_i - x_0) + \frac{\partial q}{\partial y}\sum_{i=1}^{n}(y_i - y_0) = \sum_{i=1}^{n} q_i(x_i, y_i) \qquad \text{(D.3)-(D.5)}$$

$$q(x_0, y_0)\sum_{i=1}^{n}(x_i - x_0) + \frac{\partial q}{\partial x}\sum_{i=1}^{n}(x_i - x_0)^2 + \frac{\partial q}{\partial y}\sum_{i=1}^{n}(x_i - x_0)(y_i - y_0) = \sum_{i=1}^{n}(x_i - x_0)\,q_i(x_i, y_i)$$

$$q(x_0, y_0)\sum_{i=1}^{n}(y_i - y_0) + \frac{\partial q}{\partial x}\sum_{i=1}^{n}(x_i - x_0)(y_i - y_0) + \frac{\partial q}{\partial y}\sum_{i=1}^{n}(y_i - y_0)^2 = \sum_{i=1}^{n}(y_i - y_0)\,q_i(x_i, y_i).$$

This is a system of three equations for the three unknowns to $q(x_0, y_0)$, $\frac{\partial q}{\partial x}$, and $\frac{\partial q}{\partial y}$.

The desired quantity $q(x_0, y_0)$, and the gradient values, can be found by Gaussian elimination. At least three non-collinear data points in the neighborhood of the grid point are required for a solution. In the case of n=3 exactly, this scheme is equivalent to the linear vector point methods described by Zamora et al. (1987).

The radius of influence that defines the neighborhood of the grid point must be large enough to ensure that $n \geq 3$ for grid points within regions of good data coverage. The choice of the radius of influence also controls the amount of smoothing by the interpolation scheme. For test case A, test case B, test case C (Section 2.2), and the McLean storm data, the horizontal grid spacings are 500 m, 500 m, 1000 m, and 400 m, respectively. I used the following radii of influence for the interpolation: 750 m (test case A), 900 m (test case B), 1500 m (test case C), and 700 m (McLean storm). This gives typical values of n of 5-10.

A feature of my interpolation routine is that it does not allow for extrapolation (unlike typical objective analysis packages, which both interpolate and extrapolate). This is accomplished by verifying that the grid point is within the convex hull (Sedgewick 1988) of the neighboring data points. The convex hull is the smallest convex polygon containing a set of points. If the grid point falls outside this polygon, then interpolation is not possible.

APPENDIX E. LIMITATIONS OF DOPPLER OBSERVATIONS OF TORNADOES

Errors in pseudo-dual-Doppler analyses arise from a number of sources. Some of these include statistical uncertainty in the Doppler velocity measurements, uncertainty in precipitation fall speeds, smoothing of structure by the beam pattern and by interpolation to a grid, evolution and movement of the storm while data are being collected, biases in the antenna pointing angle, ground-clutter contamination, and inexact boundary conditions for integration of the continuity equation (Doviak et al. 1976; Ray et al. 1980, 1985; Gal-Chen 1982; Jorgensen et al. 1983; Hildebrand and Mueller 1985; Ray and Jorgensen 1988; Ray and Stephenson 1990; LeMone and Jorgensen 1991). Two additional sources of error that are particular to Doppler observations of tornadoes are described below.

First of all, numerical simulations (Lewellen 1993) suggest that the convergence associated with the strong updraft within tornadoes is concentrated very close to the ground -- almost entirely within the lowest 100 m. This represents a significant problem for radar observations, which tend to be contaminated by ground clutter at such low levels. Airborne Doppler radial velocities are typically contaminated by ground clutter within the lowest few hundred meters (LeMone and Jorgensen 1991). An analysis of ELDORA data from 8 June 1995 suggests that the height to which the contamination extends is ~500 m AGL for a range of 15 km to the tornadoes. The ELDORA would thus not be expected to resolve the very shallow convergence found at the base of tornadoes.

Secondly, in regions of large accelerations, radial velocity estimates may be misleading owing to a difference between air parcel motion (the desired quantity) and the motion of individual scatterers (the measured quantity). This is potentially true in vortices such as tornadoes, in which centripetal accelerations are large.

It is possible to imagine a balanced state in a convergent, rotating flow in which scatterers rotate about the vortex center at constant radius (Kangieser 1954). However, I consider here a more typical case away from the surface in tornadoes, where the flow is primarily rotational (Lewellen 1993). In this case, scatterers are constantly centrifuged outward. For simplicity, I will examine the motion of scatterers embedded within a combined Rankine vortex air flow:

$$u_a = 0 \tag{E.1}$$

$$\begin{aligned} v_a &= \frac{Vr}{R},\ r \le R \\ v_a &= \frac{VR}{r},\ r \ge R \end{aligned} \tag{E.2}$$

where u_a is the radial velocity of the air, v_a is the tangential velocity of the air, r is the distance from the vortex center, R is the radius of the vortex core, and V is the maximum tangential velocity within the vortex.

The origin of scatterers in tornadoes (precipitation and/or debris?) is a subject of debate (H. Bluestein and J. Wurman 1998, personal communication). Except in perhaps strong tornadoes, I believe most of the scatterers are still primarily raindrops. The equations governing the horizontal motion of precipitation drops are

$$\frac{\partial u_p}{\partial t} + u_p \frac{\partial u_p}{\partial r} - \frac{v_p^2}{r} = F_{drag}^{(u)} \tag{E.3}$$

$$\frac{\partial v_p}{\partial t} + u_p \frac{\partial v_p}{\partial r} + \frac{u_p v_p}{r} = F_{drag}^{(v)} \tag{E.4}$$

$$\frac{\partial n}{\partial t} + \frac{1}{r}\frac{\partial}{\partial r}(nru_p) = 0 \tag{E.5}$$

where u_p is the radial velocity of the drop, v_p is the tangential velocity of the drop, F_{drag} is the drag force exerted on the drop by the air, and n is the number concentration of the drops (assuming no splitting or coalescence). This problem is similar to that solved by Snow (1984), except that Snow considered small particles (dust) and neglected inertial terms. The pressure gradient force in Equation (E.3) has been neglected according to a scale analysis. In a strong tornado, the $\frac{v_p^2}{r}$ term is $\sim \frac{(100\,\mathrm{m\,s^{-1}})^2}{100\,\mathrm{m}} = 100\,\mathrm{m\,s^{-2}}$. The impact of the pressure gradient force on a drop of water is much smaller in magnitude: $\frac{1}{\rho_w}\frac{\partial P}{\partial r} \sim \frac{1}{1000\,\mathrm{kg\,m^{-3}}}\frac{50\,\mathrm{mb}}{100\,\mathrm{m}} \times \frac{100\,\mathrm{kg\,m^{-1}\,s^{-2}}}{1\,\mathrm{mb}} = 0.05\,\mathrm{m\,s^{-2}}$, where ρ_w is water density.

For spherical raindrops, empirical studies (Rogers and Yau 1989) suggest the following relationship for the drag force (per unit mass):

$$F_{drag} = \left(\frac{\pi}{2} p^2 v^2 \rho_a c_d\right) / m = \frac{3\rho_a c_d v^2}{8 p \rho_w} \tag{E.6}$$

where p is the drop radius, ρ_a is the air density, m is the mass of the drop, v is the difference between air velocity and drop velocity, and c_d=0.45 for drops of radius 0.6 to 2.0 mm. For this drag force, Equations (E.3) and (E.4) become

$$\frac{\partial u_p}{\partial t} + u_p \frac{\partial u_p}{\partial r} - \frac{v_p^2}{r} = -\frac{3\rho_a c_d u_p^2}{8 p \rho_w} \tag{E.7}$$

$$\frac{\partial v_p}{\partial t} + u_p \frac{\partial v_p}{\partial r} + \frac{u_p v_p}{r} = \frac{3\rho_a c_d (v_a - v_p)^2}{8 p \rho_w}. \tag{E.8}$$

I solved Equations (E.5), (E.7), and (E.8) numerically with initial conditions u_p=0.0, v_p=0.0, and n=1.0 (dimensionless). The results for a particular example with p=1.0 mm, R=250 m, and V=50 m s^{-1} are shown in Fig. E.1-E.3. Curves are plotted for every 10 s of the simulation. The 1.0-mm drops quickly accelerate from the initial state and asymptotically reach tangential speeds just below the air tangential speed (Fig. E.1). In the process, the drops are ejected outward at speeds that also approach an asymptotic structure (Fig. E.2). For this particular example, the maximum outward radial velocity of precipitation is just over 7 m s^{-1}, which occurs right at the edge of the core of the Rankine vortex.

The centrifuging process leaves the core relatively free of precipitation, while drops tend to accumulate in an expanding ring outside the vortex core (Fig. E.3). This structure is consistent with particle sheaths observed visually around tornadoes (Snow 1984) and reflectivity donuts observed in high-resolution radar measurements of tornadoes (Fig. 2.1.1) (Fujita 1981, Wurman et al. 1996).

In the steady-state solution, away from the vortex center, and for large vertical vorticity characteristic of tornadoes (~0.1 s^{-1} to ~1.0 s^{-1}), the dominant terms in (E.7) are

$$\frac{v_p^2}{r} \approx \frac{v_a^2}{r} \approx \frac{3c_d \rho_a u_p^2}{8p\rho_w}. \tag{E.9}$$

Right at the edge of a Rankine vortex (r=R), the relationship becomes

$$u_p \approx \sqrt{\left(\frac{V^2}{R^2}\right)\left(\frac{8p\rho_w}{3c_d\rho_a}\right)R} = \frac{\zeta_{core}}{2}\sqrt{\left(\frac{8\rho_w}{3c_d\rho_a}\right)}\sqrt{pR} \tag{E.10}$$

where $\zeta_{core} = 2\frac{V}{R}$ is the vertical vorticity in the core. A Doppler radar would thus observe a mean divergence signature in the vortex core of

$$\delta_p = \frac{2u_p}{R} = 77\zeta_{core}\frac{\sqrt{p}}{\sqrt{R}}. \tag{E.11}$$

This equation is based on ρ_a=1.0 kg m^{-3}, ρ_w=1000 kg m^{-3}, and c_d=0.45. Since the divergence of the air (the desired quantity) is zero in a Rankine vortex, the above expression represents a bias error in the Doppler measurement. For mm-size raindrops, the bias in divergence is directly proportional to the magnitude of vertical vorticity within the vortex, directly proportional to the square root of the drop size, and indirectly proportional to the square root of the vortex size. In the example described previously with 1-mm drops, the error in the divergence estimate would be 0.06 s^{-1}.

The bias in divergence limits the ability of horizontal winds from multiple-Doppler radar to be used to compute vertical motion in tornadoes. A correction for this problem is difficult because the characteristics of the scatterers are unknown.

Table 1.1. Characteristics of the Electra Doppler Radar (ELDORA) when scanning in convective mode during VORTEX-95 (Hildebrand et al. 1994, Wakimoto et al. 1996).

Wavelength (cm)	3.2
Beam Width (deg)	1.8
Antenna Rotation Rate (deg s^{-1})	133
Number of Samples	24
Tilt Angle (fore or aft, deg)	17-20
Pulse Repetition Frequency (Hz)	2500, 2000
Gate Length (m)	150
Along-track Resolution (m)	~300
Maximum Range (km)	60
Individual Unambiguous Velocities (± m s^{-1})	19.7, 15.7
Effective Unambiguous Velocities (± m s^{-1})	78.7

Table 1.2. Summary of ELDORA flight legs near the McLean storm on 8 June 1995. The time given for each pass is roughly the time that the radar scanned the tornadic region of the storm at low levels. "Storm motion" is the approximate velocity (U_v, V_v) of the most intense low-level vortex.

pass	**time (UTC)**	**flight heading**	**storm motion ($\mathbf{m\ s^{-1}}$)**	**comments**
1	2236	W	(5.3, 8.6)	incomplete scan of west side of storm
2	2242	ESE	(5.3, 8.6)	
3	2248	W	(5.8, 10.3)	genesis of tornado #1
4	2254	E	(7.0, 9.5)	
5	2259	W	(4.4, 7.8)	
6	2306	ENE	(-0.5, 8.0)	genesis of tornado #2
7	2313	WSW	(-3.5, 8.1)	dissipation of tornado #1
8	2318	ENE	(-5.6, 6.9)	dissipation of tornado #2
9	2325	WSW	(1.5, 5.6)	genesis of tornado #4; tornado #3 not scanned
10	2331	ENE	(6.4, 6.3)	27 second gap in data (end of data tape) while fore radar was scanning tornado
11	2338	WSW	(7.4, 7.5)	violent tornado #4
12	2345	NE	(7.4, 7.3)	
13	2351	WSW	(4.2, 3.8)	
14	2356	ENE	(5.8, 3.8)	
15	0003	WSW	(6.8, 7.9)	genesis of tornado #5
16	0009	ENE	(6.8, 7.9)	dissipation of tornado #5
17	0015	W		incomplete scan (mission aborted)

Table 1.3. Summary of ELDORA single-Doppler ground-relative velocity measurements in the McLean storm tornadoes. The width refers to the maximum horizontal dimension of the velocity disturbance associated with the tornado in the raw scans (e.g., Fig. 3.1.2.d, f, i, and l). This width is probably somewhat larger than the size of the vortex core.

time (UTC)	range (km) to tornado	maximum velocity value (m s^{-1}) below 2 km AGL in tornado	approximate width (km) of tornado velocity anomaly
2248	14 (T#1)	35	0.9
2254	13 (T#1)	60	0.7
2259	19 (T#1)	55	0.8
2306	13 (T#1), 13 (T#2)	49 (T#1), 34 (T#2)	0.6 (T#1), 0.7 (T#2)
2313	15 (T#1), 17 (T#2)	32 (T#1), 52 (T#2)	0.5 (T#1), 0.7 (T#2)
2318	18 (T#2)	34	0.6
2331	13 (T#4)	57	1.0
2338	13 (T#4)	90	1.2
2345	10 (T#4)	92	1.0
2351	8 (T#4)	78	0.8
2356	6 (T#4)	66	0.6
0003	5 (T#4)	71	0.7
0009	9 (T#4)	57	0.8

Table 2.1. Statistics for pseudo-dual-Doppler analyses of the Sperow et al. (1995) analytic wind field (test case A). The second column gives the domain-averaged value of $|c_1 u + c_2 v + c_3 w - V|$. The third through fifth columns are the domain-averaged errors in u, v, and w (E_u, E_v, and E_w). The sixth column contains the error for w at a single level only. The last column gives the total velocity error $\sqrt{E_u^2 + E_v^2 + E_w^2}$. "Upward" and "downward" refer to traditional iterative methods with w=0 at the lower and upper boundary, respectively. "Strong" refers to the variational formulation (Section 2.3) with both boundary conditions for w and with the radial velocity equations satisfied exactly. "Weak" refers to the variational formulation (Section 2.4) in which all constraints are satisfied approximately and with relative weight of the constraints determined by β.

a) L_H=5 km.

Experiment	Discrepancy with Radial Velocity Eqn.	*u* Error, Global	*v* Error, Global	*w* Error, Global	*w* Error, *z*=2 km	Total Error, Global
1. upward	0.00	0.00	0.96	1.84	1.10	2.08
2. downward	0.00	0.00	1.10	4.34	6.22	4.48
3. strong	0.00	0.00	0.51	1.69	2.39	1.77
4a. weak, β=2.5×10^4 m^2	0.04	0.12	0.64	2.07	2.94	2.17
4b. weak, β=2.5×10^5 m^2	0.26	0.65	0.94	3.25	4.96	3.45
4c. weak, β=2.5×10^6 m^2	0.97	2.04	1.58	5.90	9.83	6.44
5. upward, noise	0.00	2.43	1.94	5.50	3.62	6.32
6. downward, noise	0.00	2.43	2.58	9.92	15.27	10.53
7. strong, noise	0.01	2.43	1.20	2.60	3.62	3.76
8a. weak, noise, β=2.5×10^4 m^2	0.37	1.69	1.15	2.54	3.54	3.26
8b. weak, noise, β=2.5×10^5 m^2	0.80	1.29	1.19	3.37	5.07	3.80
8c. weak, noise, β=2.5×10^6 m^2	1.40	2.21	1.64	5.92	9.85	6.53

b) L_H=10 km.

Experiment	**Discrepancy with Radial Velocity Eqn.**	***u* Error, Global**	***v* Error, Global**	***w* Error, Global**	***w* Error, z=2 km**	**Total Error, Global**
1. upward	0.00	0.01	0.21	0.37	0.36	0.43
2. downward	0.00	0.01	0.33	0.91	1.30	0.97
3. strong	0.00	0.01	0.35	0.94	1.27	1.00
4a. weak, β=2.5×10^4 m^2	0.03	0.09	0.55	1.37	1.71	1.48
4b. weak, β=2.5×10^5 m^2	0.17	0.48	0.67	1.89	2.71	2.06
4c. weak, β=2.5×10^6 m^2	0.77	2.03	1.48	4.10	5.95	4.81
5. upward, noise	0.00	2.43	1.62	5.12	3.49	5.89
6. downward, noise	0.00	2.43	2.24	8.53	13.30	9.15
7. strong, noise	0.01	2.43	1.17	2.40	3.29	3.61
8a. weak, noise, β=2.5×10^4 m^2	0.37	1.69	1.19	2.30	3.02	3.09
8b. weak, noise, β=2.5×10^5 m^2	0.79	1.26	1.05	2.27	3.19	2.80
8c. weak, noise, β=2.5×10^6 m^2	1.30	2.22	1.59	4.16	6.03	4.98

c) L_H=20 km.

Experiment	Discrepancy with Radial Velocity Eqn.	*u* Error, Global	*v* Error, Global	*w* Error, Global	*w* Error, *z*=2 km	Total Error, Global
1. upward	0.00	0.01	0.09	0.13	0.18	0.16
2. downward	0.00	0.01	0.15	0.32	0.44	0.35
3. strong	0.00	0.01	0.28	0.68	0.94	0.74
4a. weak, β=2.5×10^4 m^2	0.03	0.08	0.61	1.28	1.45	1.42
4b. weak, β=2.5×10^5 m^2	0.14	0.39	0.55	1.44	2.08	1.59
4c. weak, β=2.5×10^6 m^2	0.64	1.73	1.16	2.99	4.33	3.64
5. upward, noise	0.00	2.43	1.60	5.10	3.48	5.87
6. downward, noise	0.00	2.43	2.20	8.43	13.15	9.04
7. strong, noise	0.01	2.43	1.15	2.31	3.20	3.54
8a. weak, noise, β=2.5×10^4 m^2	0.37	1.69	1.27	2.32	2.91	3.14
8b. weak, noise, β=2.5×10^5 m^2	0.79	1.25	1.00	1.99	2.76	2.55
8c. weak, noise, β=2.5×10^6 m^2	1.27	1.97	1.33	3.07	4.37	3.88

Table 2.2. As in Table 2.1, except for the pseudo-dual-Doppler analysis of test case B ("Colliding Cold Pools") with simultaneous fore and aft observations at t=360 s. The region in which statistics are computed is outlined in Figure 2.2.2.c.

Experiment	Discrepancy with Radial Velocity Eqn.	u Error, Global	v Error, Global	w Error, Global	w Error, z=1 km	Total Error, Global
1. upward	0.00	0.01	0.38	0.58	0.55	0.69
2. downward	0.00	0.01	0.42	0.58	0.70	0.72
3. O'Brien	0.00	0.01	0.41	0.42	0.51	0.59
4. strong	0.00	0.01	0.41	0.42	0.52	0.59
5a. weak, β=2.5×10^4 m^2	0.01	0.04	0.41	0.43	0.54	0.60
5b. weak, β=2.5×10^5 m^2	0.07	0.19	0.46	0.50	0.66	0.71
5c. weak, β=2.5×10^6 m^2	0.24	0.54	0.65	0.69	0.99	1.09
6. upward, noise	0.00	1.98	0.97	2.78	1.76	3.55
7. downward, noise	0.00	1.98	0.94	2.00	2.55	2.97
8. O'Brien, noise	0.00	1.98	0.95	1.31	1.49	2.56
9. strong, noise	0.00	1.98	0.93	1.21	1.43	2.50
10a. weak, noise, β=2.5×10^4 m^2	0.29	1.48	0.84	1.04	1.23	1.99
10b. weak, noise, β=2.5×10^5 m^2	0.73	0.97	0.62	0.78	0.98	1.39
10c. weak, noise, β=2.5×10^6 m^2	1.06	0.90	0.57	0.74	1.08	1.30
11. strong, noise, one-pass Leise filter	0.53	1.34	0.63	0.93	1.12	1.75
12. weak, noise, β=2.5×10^5 m^2, one-pass Leise filter	0.86	0.82	0.50	0.69	0.90	1.18

Table 2.3. As in Table 2.1, except for the pseudo-dual-Doppler analysis of test case C ("Line of Storms") with simultaneous fore and aft observations at t=5041 s. The regions in which statistics are computed are outlined in Figure 2.2.3.b.

Experiment	Discrepancy with Radial Velocity Eqn.	u Error, Global	v Error, Global	w Error, Global	w Error, z=2 km	Total Error, Global
1. upward	0.00	0.02	0.61	1.75	0.46	1.85
2. downward	0.00	0.02	0.60	1.87	1.82	1.96
3. strong	0.00	0.02	0.43	1.19	0.60	1.27
4a. weak, β=1.0×10^5 m^2	0.03	0.09	0.42	1.19	0.63	1.27
4b. weak, β=1.0×10^6 m^2	0.16	0.39	0.50	1.28	0.80	1.43
4c. weak, β=1.0×10^7 m^2	0.51	1.18	0.87	1.69	1.23	2.24
5. upward, noise	0.00	1.98	2.28	7.24	1.66	7.84
6. downward, noise	0.00	1.98	2.11	4.23	5.05	5.12
7. strong, noise	0.00	1.98	1.17	1.78	1.38	2.91
8a. weak, noise, β=1.0×10^5 m^2	0.30	1.48	1.06	1.62	1.19	2.44
8b. weak, noise, β=1.0×10^6 m^2	0.76	1.05	0.87	1.48	1.01	2.01
8c. weak, noise, β=1.0×10^7 m^2	1.17	1.37	1.01	1.73	1.25	2.43
9. O'Brien, noise, aircraft at y=-15 km	0.00	1.97	1.14	2.06	1.42	3.07
10. strong, noise, aircraft at y=-15 km	0.00	1.97	1.01	1.59	1.33	2.73
11. strong, noise, one-pass Leise filter	0.54	1.35	0.92	1.55	1.07	2.25
12. weak, noise, β=1.0×10^6 m^2, one-pass Leise filter	0.89	0.92	0.78	1.41	0.93	1.86

Table 2.4. As in Table 2.2 (test case B), except with a time lag of 80 s between fore and aft observations. Three different reference frames are used for the Doppler analyses: a reference frame fixed with respect to the ground (U_s=0.0 m s^{-1}, V_s=-14.0 m s^{-1}), a reference frame moving at uniform velocity (U_s=0.8 m s^{-1}, V_s=1.5 m s^{-1}), and a non-uniform moving reference frame (variable U_s and V_s).

Experiment	*u* Error, Global	*v* Error, Global	*w* Error, Global	*w* Error, *z*=1 km	Total Error, Global
1. ground-relative, strong	1.48	0.93	1.07	1.55	2.05
2. ground-relative, weak, β=2.5×10^5 m^2	1.41	0.93	0.99	1.46	1.96
3. uniform moving, strong	0.85	0.67	0.75	1.07	1.32
4. uniform moving, weak, β=2.5×10^5 m^2	0.80	0.69	0.72	1.04	1.28
5. non-uniform moving, strong	0.73	0.67	0.68	0.97	1.20
6. non-uniform moving, weak, β=2.5×10^5 m^2	0.72	0.69	0.67	0.97	1.20
7. ground-relative, noise, strong	1.75	0.99	1.17	1.63	2.33
8. ground-relative, noise, weak, β=2.5×10^5 m^2	1.59	0.97	1.04	1.49	2.13
9. uniform moving, noise, strong	1.19	0.74	0.87	1.18	1.65
10. uniform moving, noise, weak, β=2.5×10^5 m^2	1.03	0.74	0.78	1.10	1.49
11. non-uniform moving, noise, strong	1.09	0.73	0.80	1.11	1.54
12. non-uniform moving, noise, weak, β=2.5×10^5 m^2	0.95	0.73	0.74	1.05	1.41

Table 2.5. As in Table 2.3 (test case C), except with a time lag of 120 s between fore and aft observations. Three different reference frames are used for the Doppler analyses: a reference frame fixed with respect to the ground (U_s=-16.0 m s^{-1}, V_s=-3.0 m s^{-1}), a reference frame moving at uniform velocity (U_s=4.2 m s^{-1}, V_s=-0.1 m s^{-1}), and a non-uniform moving reference frame (variable U_s and V_s).

Experiment	*u* Error, Global	*v* Error, Global	*w* Error, Global	*w* Error, z=2 km	Total Error, Global
1. ground-relative, strong	2.98	1.49	2.94	2.46	4.44
2. ground-relative, weak, β=1.0×10^6 m^2	2.80	1.45	2.67	2.18	4.13
3. uniform moving, strong	1.39	0.91	1.63	0.99	2.33
4. uniform moving, weak, β=1.0×10^6 m^2	1.42	0.92	1.62	0.99	2.34
5. non-uniform moving, strong	1.12	0.81	1.60	0.96	2.11
6. non-uniform moving, weak, β=1.0×10^6 m^2	1.19	0.83	1.59	1.01	2.15
7. ground-relative, noise, strong	3.14	1.57	2.99	2.53	4.61
8. ground-relative, noise, weak, β=1.0×10^6 m^2	2.89	1.51	2.69	2.23	4.23
9. uniform moving, noise, strong	1.67	1.04	1.73	1.13	2.62
10. uniform moving, noise, weak, β=1.0×10^6 m^2	1.56	1.00	1.66	1.05	2.49
11. non-uniform moving, noise, strong	1.43	0.93	1.66	1.08	2.38
12. non-uniform moving, noise, weak, β=1.0×10^6 m^2	1.35	0.92	1.62	1.06	2.30

Table 2.6. RMS errors in U, V, and W for weak constraint analyses (β=2.5×10^5 m^2) of test case B, both with and without incorporation of the time derivatives. The analyses are in a non-uniform moving reference frame. The time lag between fore and aft observations is 80 s.

Experiment	***U* Error, Global**	***V* Error, Global**	***W* Error, Global**	***W* Error, z=1 km**	**Total Error, Global**
1. without time derivatives	0.72	0.69	0.67	0.97	1.20
2. with time derivatives	0.56	0.77	0.67	1.00	1.16
3. without time derivatives, noise	0.95	0.73	0.74	1.05	1.41
4. with time derivatives, noise	0.92	0.82	0.76	1.11	1.45

Table 2.7. RMS errors in U, V, and W for weak constraint analyses (β=1.0×10^6 m^2) of test case C, both with and without incorporation of the time derivatives. The analyses are in a non-uniform moving reference frame. The time lag between fore and aft observations is 120 s. "South storm" and "north storms" labels refer to the outlined regions in Fig 2.2.3.

Experiment	U Error, Global	V Error, Global	W Error, Global	W Error, z=2 km	Total Error, Global
1. south storm, without time derivatives	0.83	0.98	1.52	0.89	1.99
2. south storm, with time derivatives	0.84	0.99	1.51	0.89	1.99
3. south storm, without time derivatives, noise	1.03	1.06	1.55	0.93	2.14
4. south storm, with time derivatives, noise	1.11	1.11	1.57	0.96	2.22
5. north storm, without time derivatives	1.38	0.75	1.63	1.07	2.26
6. north storms, with time derivatives	1.08	0.70	1.57	1.06	2.03
7. north storms, without time derivatives, noise	1.53	0.84	1.66	1.13	2.41
8. north storms, with time derivatives, noise	1.35	0.81	1.59	1.08	2.24

Table C.1. Empirical relationships between reflectivity factor and precipitation fall speed (m s^{-1}). Z is in $mm^6\ m^{-3}$ and Z_{dB} (=10 log Z) is in dBZ.

Empirical Formula	**15 dBZ**	**43 dBZ**	**55 dBZ**
$w_t = -2.6Z^{0.107}$ (Joss and Waldvogel 1970; rain)	-3.8	-7.5	-10.1
$w_t = 3.59 - 5.91Z^{0.114}$ (exponential fit for McLean storm)	-5.2	-14.7	-21.4
$w_t = 0.706 - 0.347Z_{dB}$ (linear fit for McLean storm)	-4.5	-14.2	-18.4
$w_t = -3.95Z^{0.148}$ (Conway and Zrnic 1993; hail)			-25.7

Figure 1.1. Examples of tornado families during outbreaks.

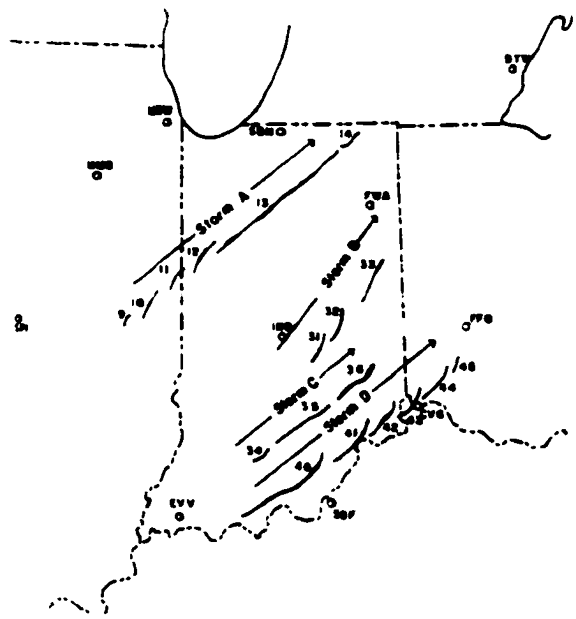

a) Tornado tracks in Indiana within four of the "Superoutbreak" storms on 3 April 1974 (from Agee et al. 1976, courtesy of the American Meteorological Society).

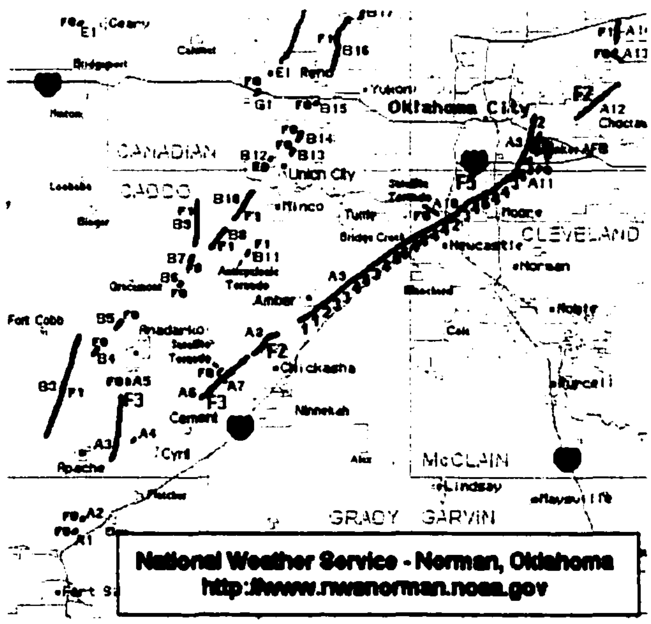

b) Tornadoes (with F-scale ratings) during the Oklahoma outbreak on 3 May 1999 (from National Weather Service, Norman, Oklahoma).

Figure 1.2. Photograph (copyright by Howard Bluestein) of tornadoes near Canadian, Texas at 2236 UTC on 7 May 1986. The view is toward the northwest. A new wall cloud and tornado (right) formed while the previous wall cloud and tornado (left) were dissipating.

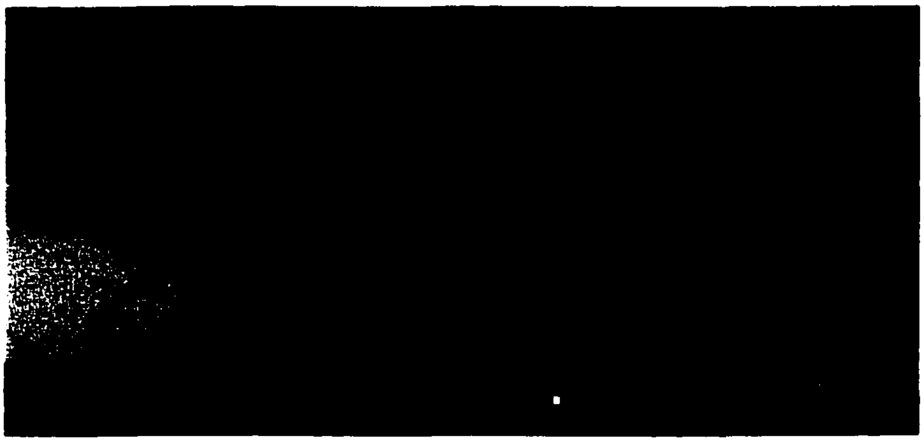

Figure 1.3. 500 mb analysis at 1200 UTC 8 June 1995.

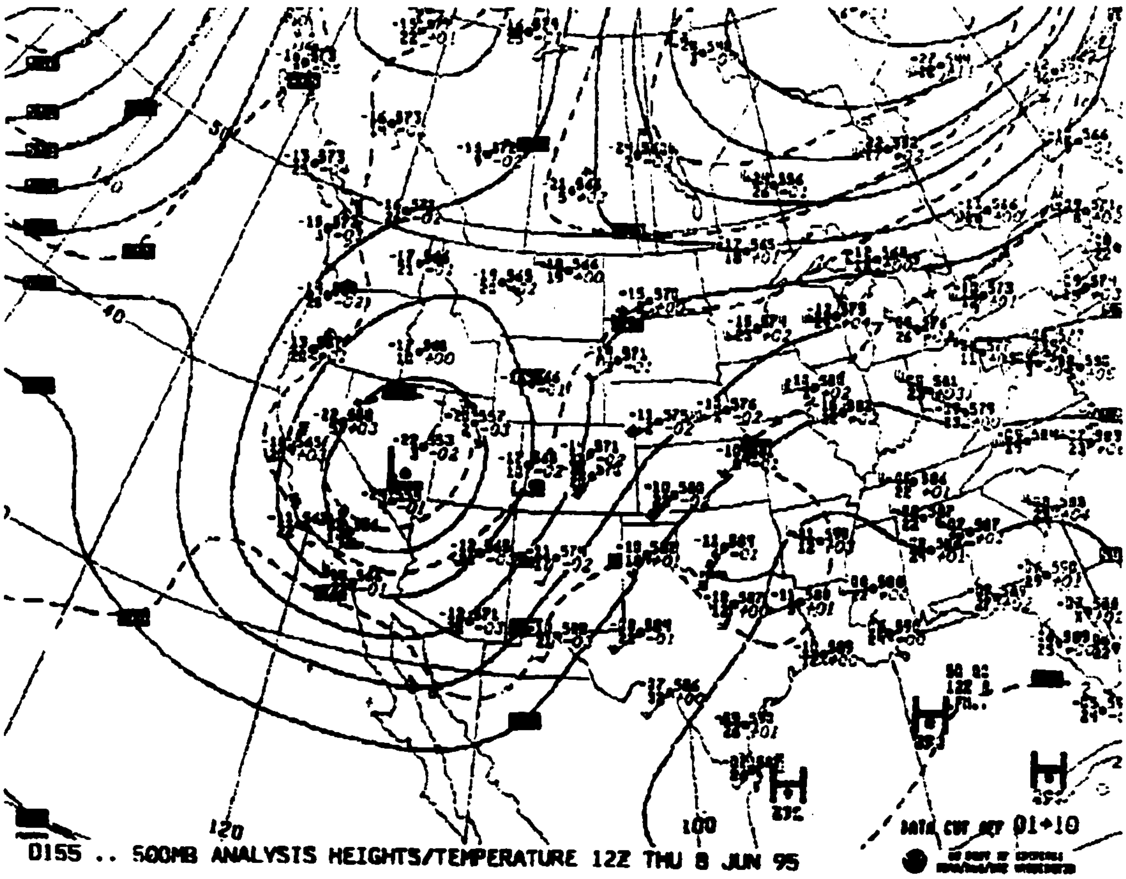

Figure 1.4. Estimated sounding and hodograph 20 km south of the McLean storm at 2300 UTC 8 June 1995. Heights are in km AGL. The heavy line on the sounding plot is an approximate moist adiabat of an undiluted boundary layer parcel. Wind barbs and flags represent 10 kt (≈5 m s^{-1}) and 50 kt (≈25 m s^{-1}), respectively. The rings on the hodograph are at 5 m s^{-1} intervals. The "X" indicates the mean motion of the McLean storm. The observations between 860 mb and 590 mb are in situ measurements by the P-3 during a descent at 2240 UTC. Thermodynamic measurements at upper levels are from the Amarillo, Texas (110 km west of McLean) sounding at 2300 UTC. Upper-level winds are horizontal averages from pseudo-dual-Doppler analyses of ELDORA data collected at 2225 UTC 60 km east-northeast of the storm. (The data sources for upper levels were selected based upon how well the measurements at mid levels agreed with the P-3 observations.) The surface observations are from mobile mesonet vehicles around 0010 UTC 9 June.

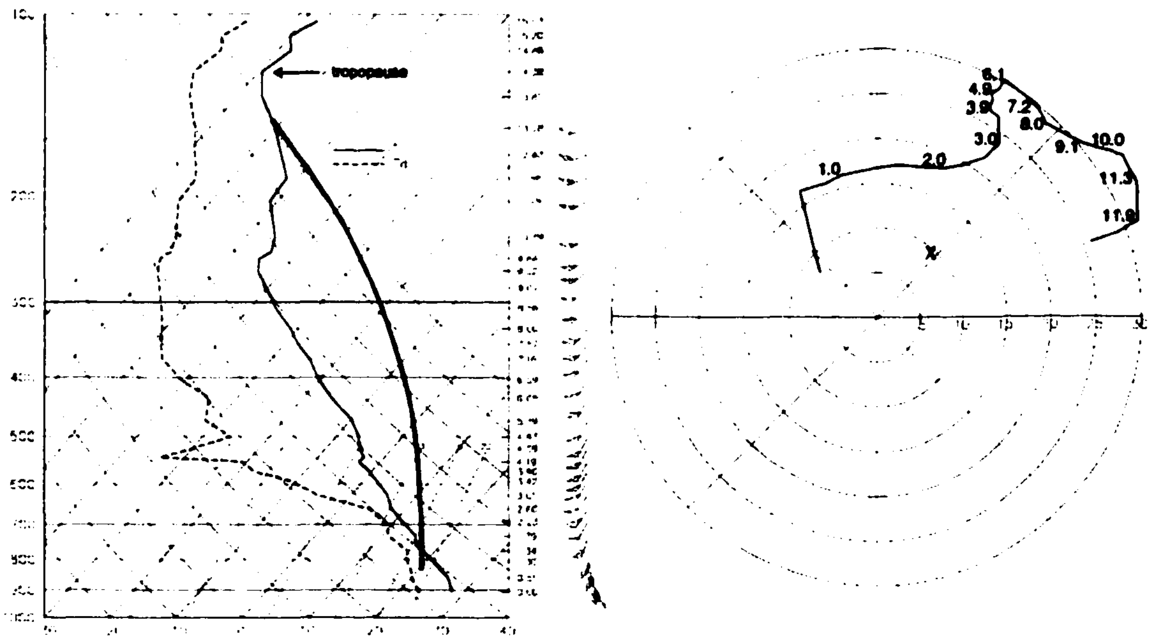

Figure 1.5. Regional surface analysis at 0100 UTC 9 June 1995. For each station, temperature (upper left) and dewpoint (lower left) are in °C, altimeter setting (upper right) is in tenths of mb with leading "10" removed, and full wind barbs are 10 kt (≈5 m s^{-1}). The approximate positions of the front (usual notation), outflow boundary (dashed line), and dryline (scalloped line) are shown. The location of McLean, Texas is noted with a star.

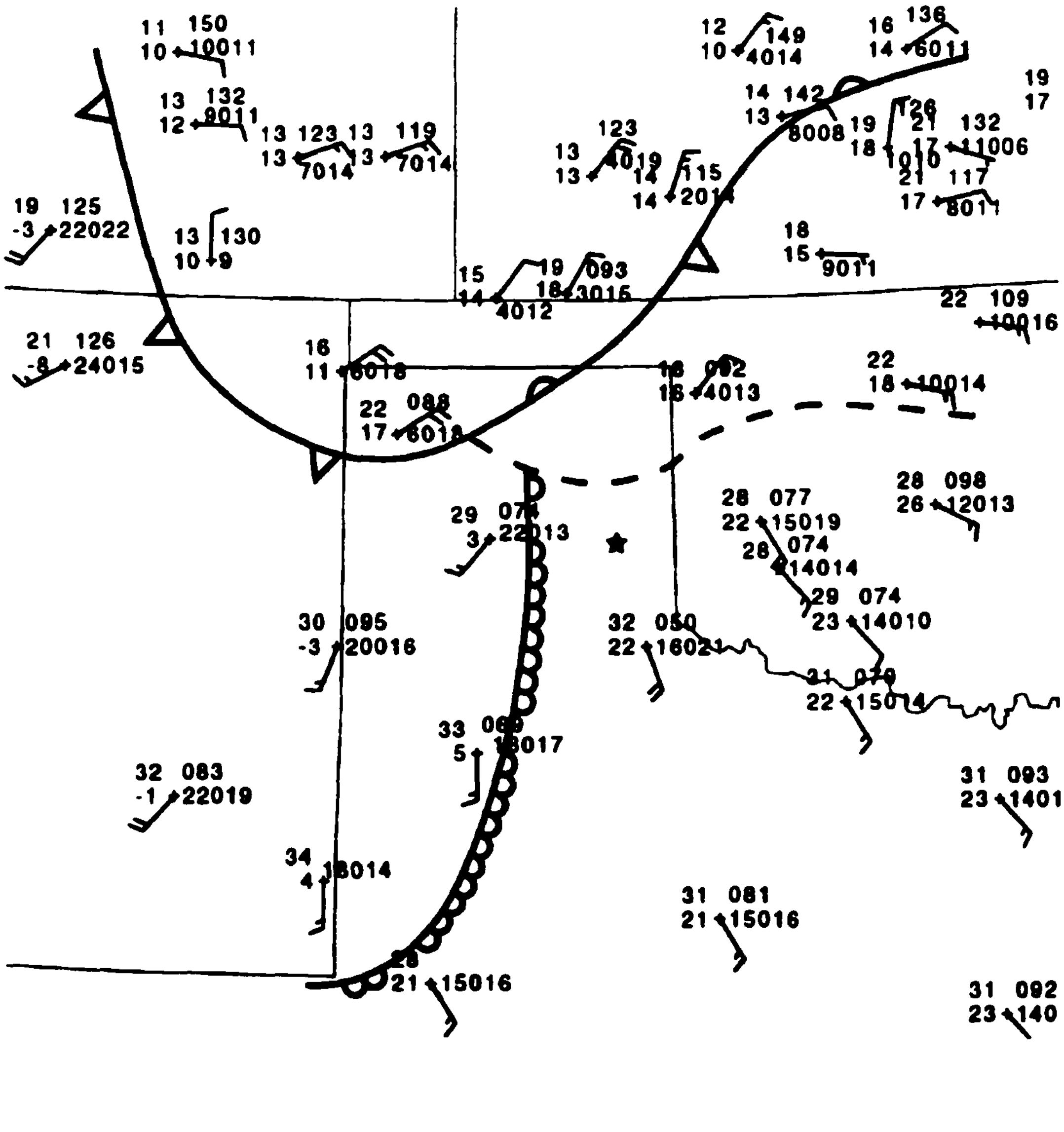

Figure 1.6. NIDS reflectivity images at 0.5° elevation angle from Amarillo, Texas.

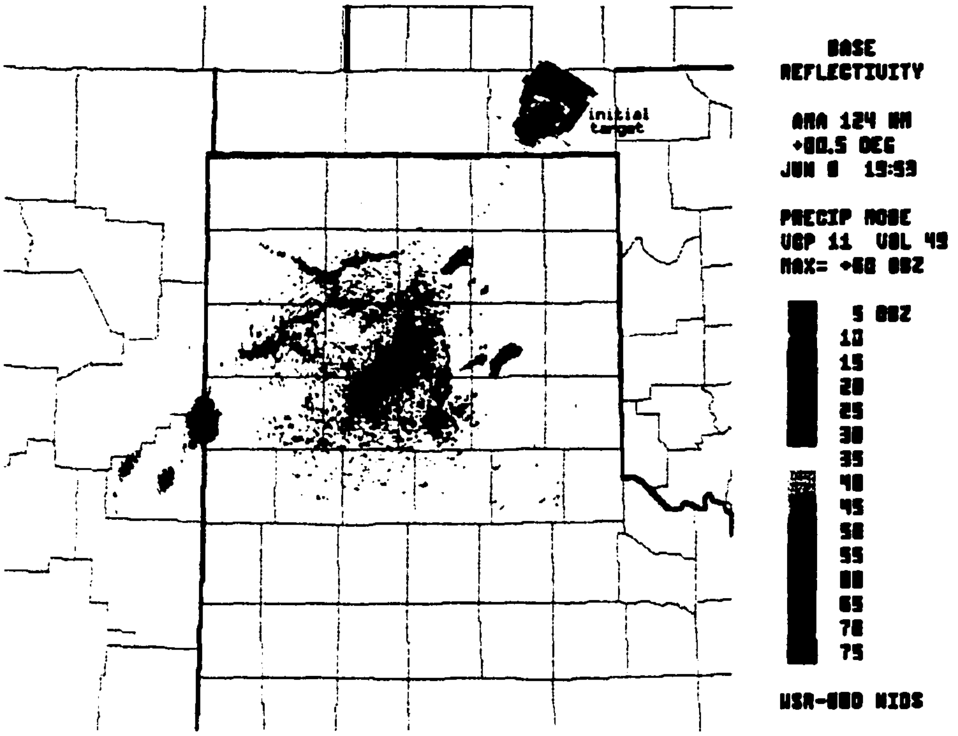

a) 1953 UTC 8 June 1995.

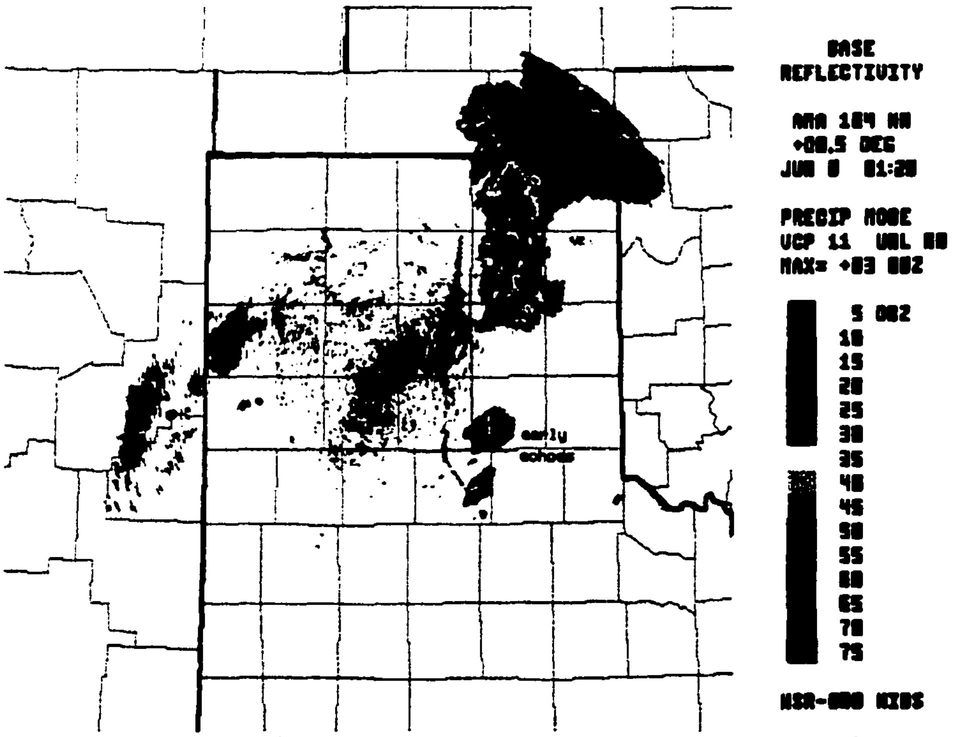

b) 2128 UTC 8 June 1995. The north-south oriented dryline is evident in the east-central Texas Panhandle.

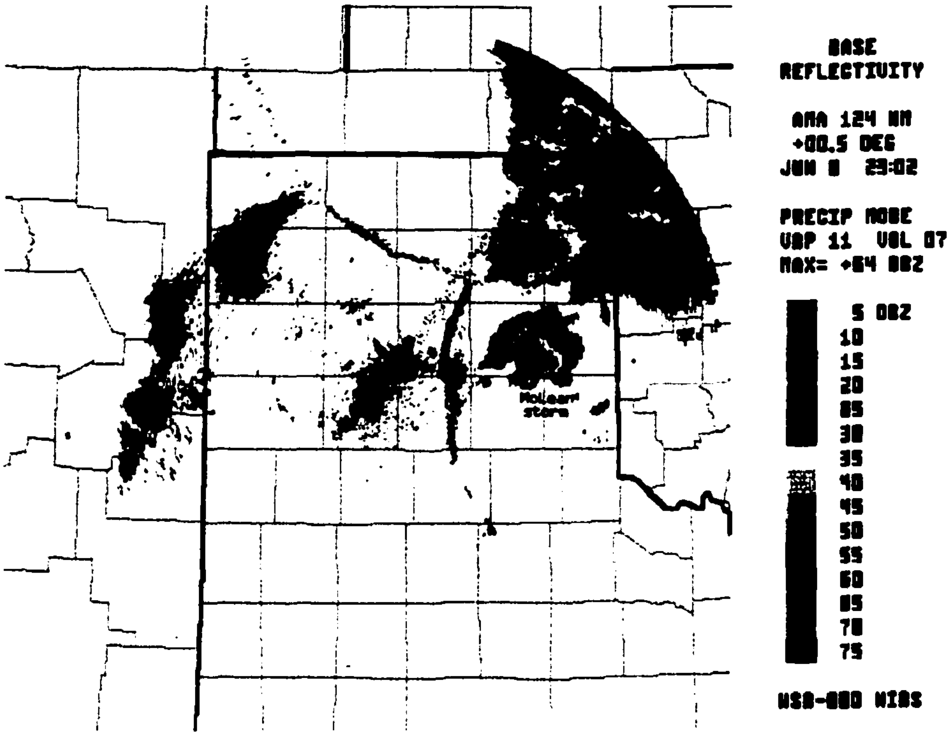

c) 2302 UTC 8 June 1995.

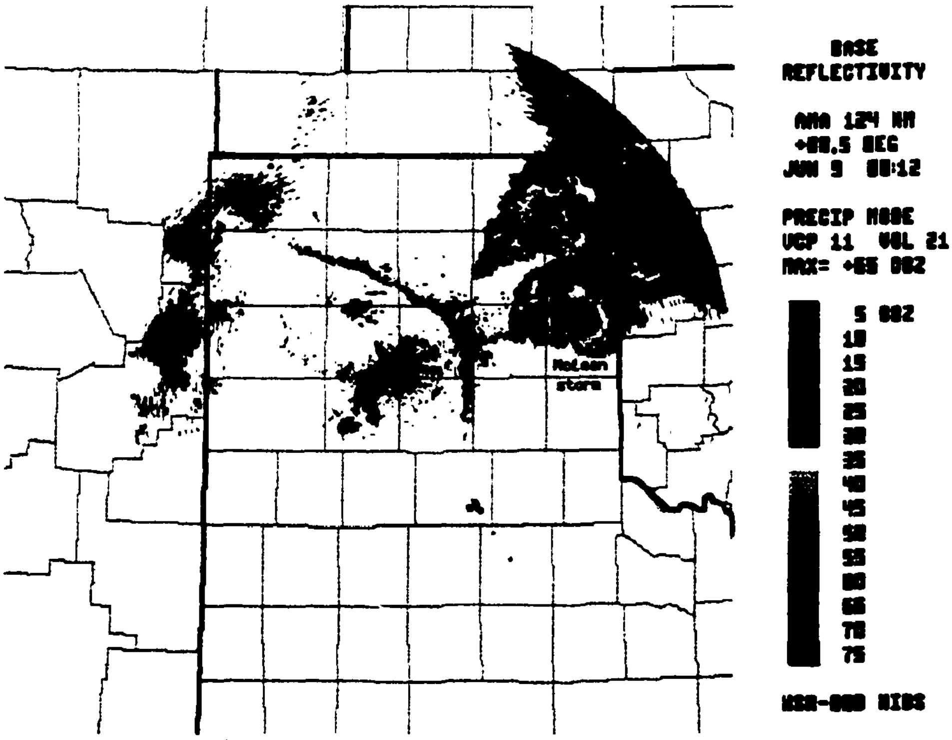

d) 0012 UTC 9 June 1995.

Figure 1.7. Tornado tracks on 8 June 1995, with local road network near McLean, Texas. The tracks are approximate and were determined from information from a variety of sources: damage surveys, raw ELDORA scans, storm reports, and photographs and videos of the storm.

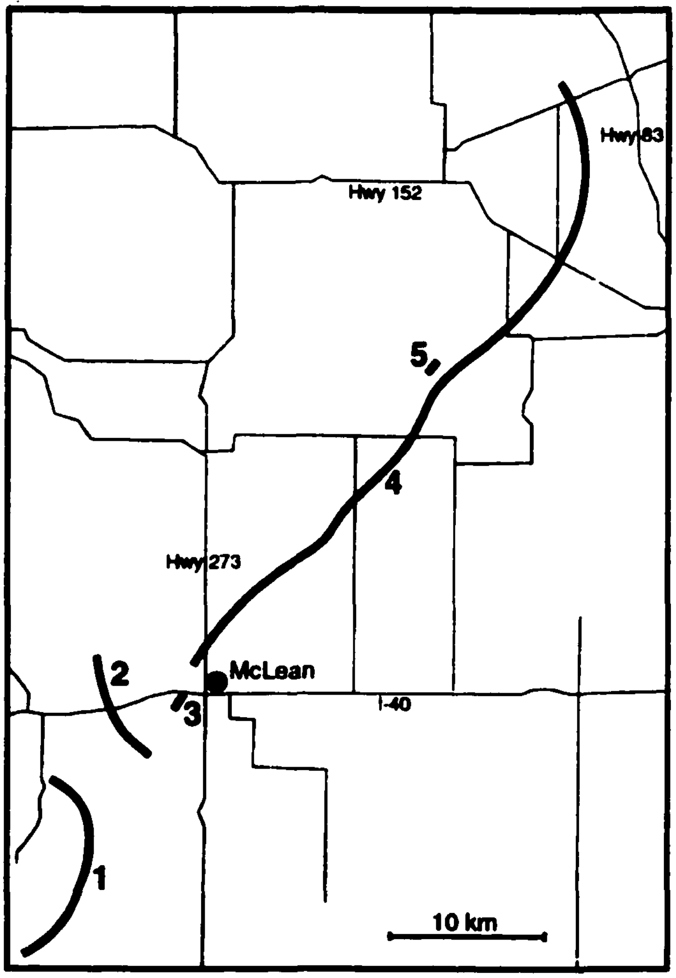

Figure 1.8. Video captures of the tornadoes near McLean, Texas (copyright by Bruce Haynie).

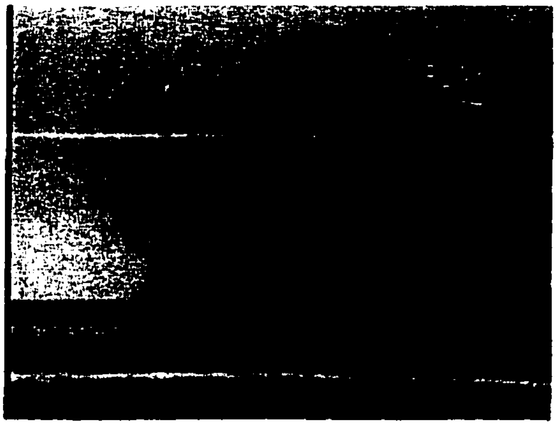

a) Tornado #1 to WNW at 2302 UTC.

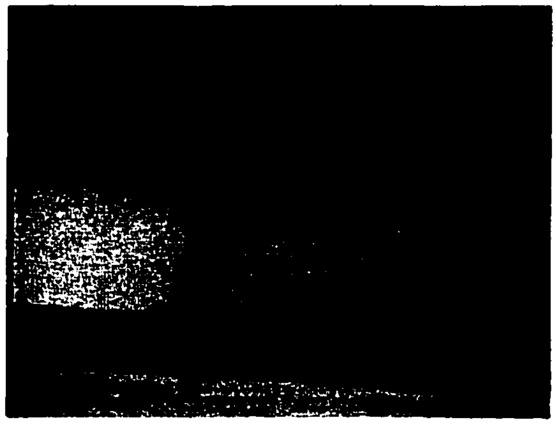

b) Tornado #2 to NW at 2312 UTC.

c) Tornado #2 to NW at 2315 UTC.

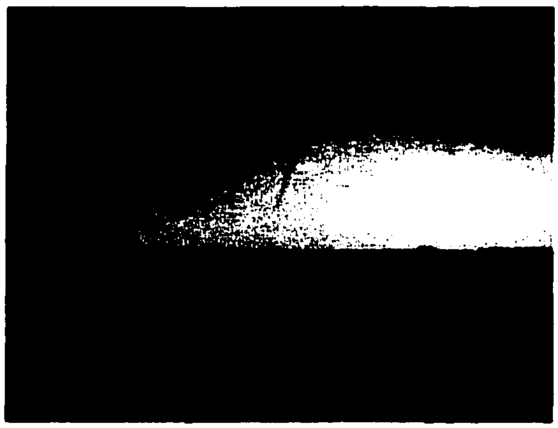

d) Tornado #3 to NW at 2321 UTC.

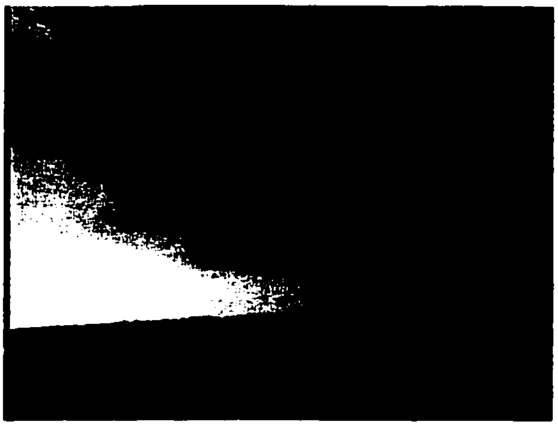

e) Tornado #4 to NNW at 2328 UTC.

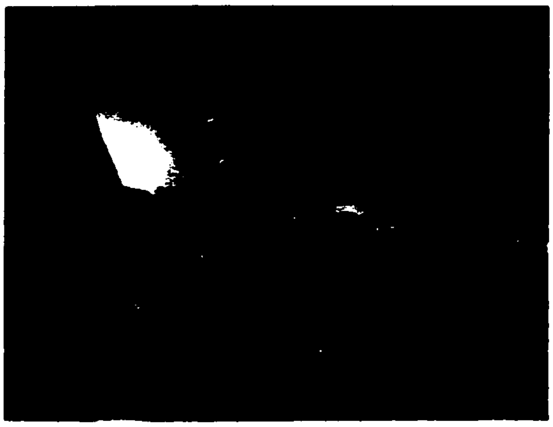

f) Tornado #4 to NW at 2345 UTC.

Figure 1.9. Photograph of tornado #4 (left) and tornado #5 (right) to west at 0004 UTC 9 June 1995 (copyright by David Ewoldt).

Figure 2.1.1. Raw display of an ELDORA aft radar scan at 23:38 UTC 8 June 1995. The image is a projection of a cone-shaped scan onto a flat surface. The view to the right is roughly toward the north. The left panel is the reflectivity factor (dBZ$_e$), and the right panel is radial velocity (m s^{-1}, positive velocities away from radar). The 30 dBZ$_e$ echo extends as high as 18 km AGL in this image. The small data void in the lower left part of each panel indicates the location of the aircraft.

Figure 2.1.2. ELDORA dual-beam scanning (from Hildebrand et al. 1994, copyright by IEEE). The tilt angle, τ, of the radar beam with respect to a plane normal to the aircraft axis is ~20°.

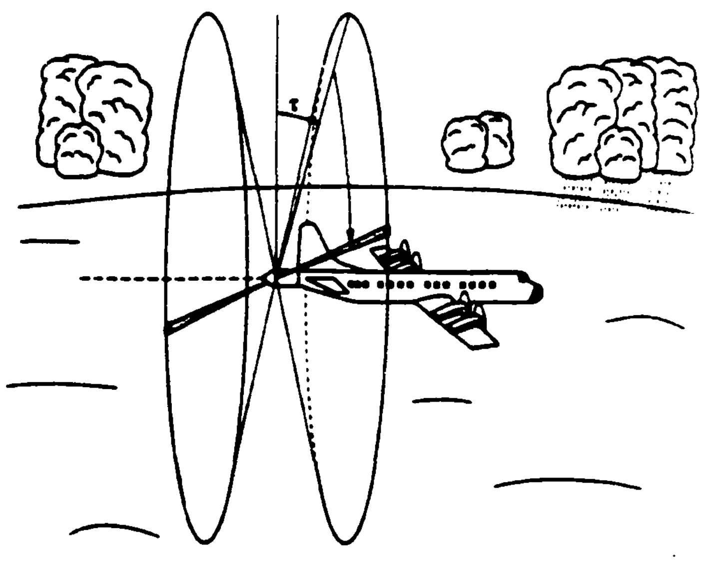

Figure 2.1.3. Geometry of an airborne pseudo-dual-Doppler synthesis. V_1 and V_2 are the estimates of the air radial velocity at a particular point from the fore and aft radar measurements, respectively. V_n is the unmeasured velocity component normal to the common plane of the two observations (in the direction $\vec{V}_1 \times \vec{V}_2$).

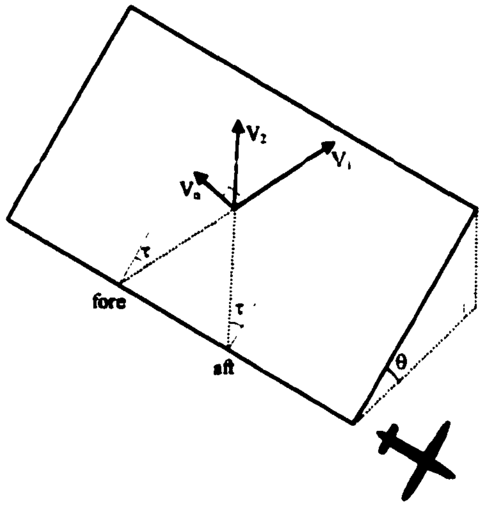

Figure 2.2.1. Horizontal winds (vectors) and vertical velocity (shading) at z=1.0 km for test case A, the Sperow et al. (1995) analytic wind field (L_H=10 km).

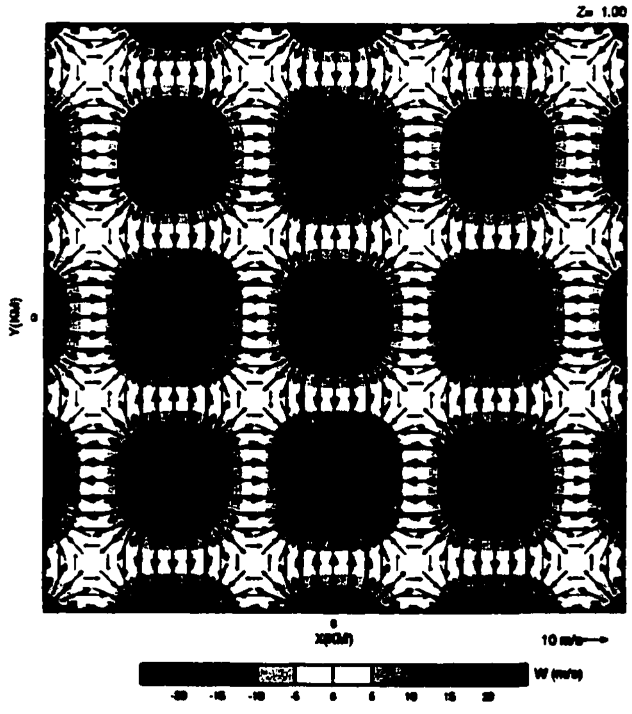

Figure 2.2.2. Horizontal cross sections of the test case B ("Colliding Cold Pools") simulation. Winds are relative to the model domain velocity (0.0 m s^{-1}, 14.0 m s^{-1}).

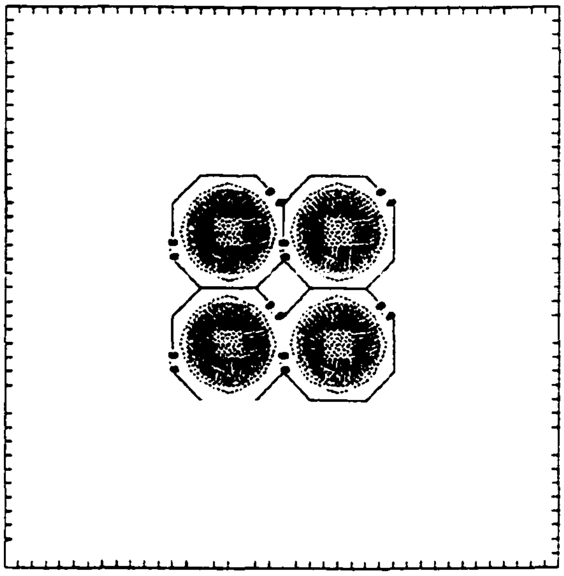

a) Contours of temperature perturbation at t=0 s and z=2.4 km. The maximum perturbation at this level is −13.5 K.

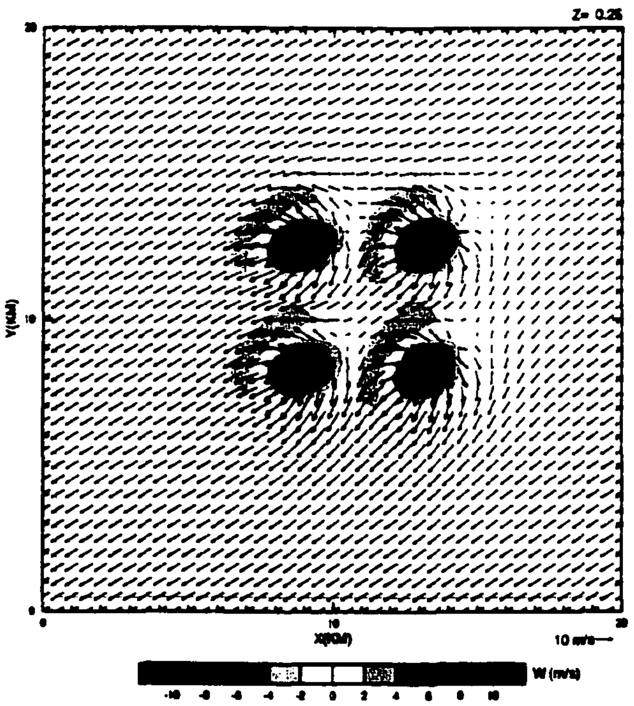

b) Horizontal winds (vectors) and vertical velocity (shading) at t=200 s and z=0.25 km.

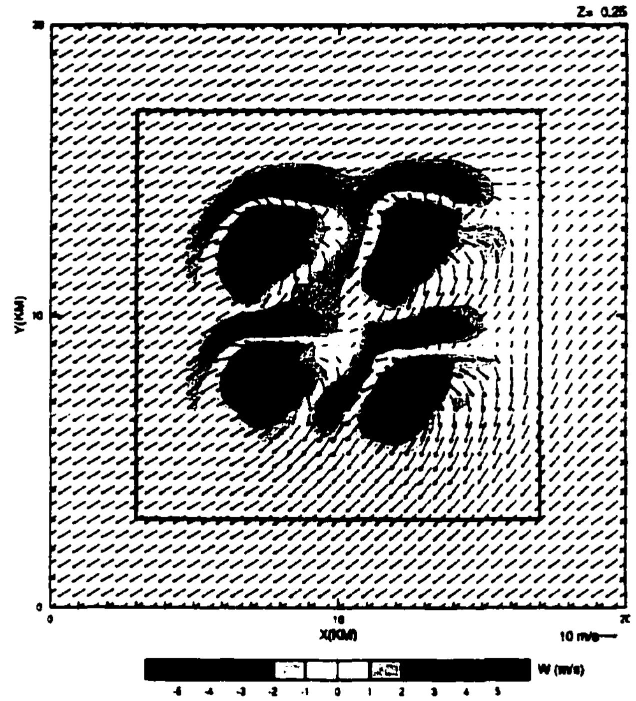

c) As in b) except at t=360 s. The region in which dual-Doppler statistics are computed is outlined in green.

Figure 2.2.3. Horizontal cross sections of the test case C ("Line of Storms") simulation. Winds are relative to the model domain velocity (16.0 m s^{-1}, 3.0 m s^{-1}).

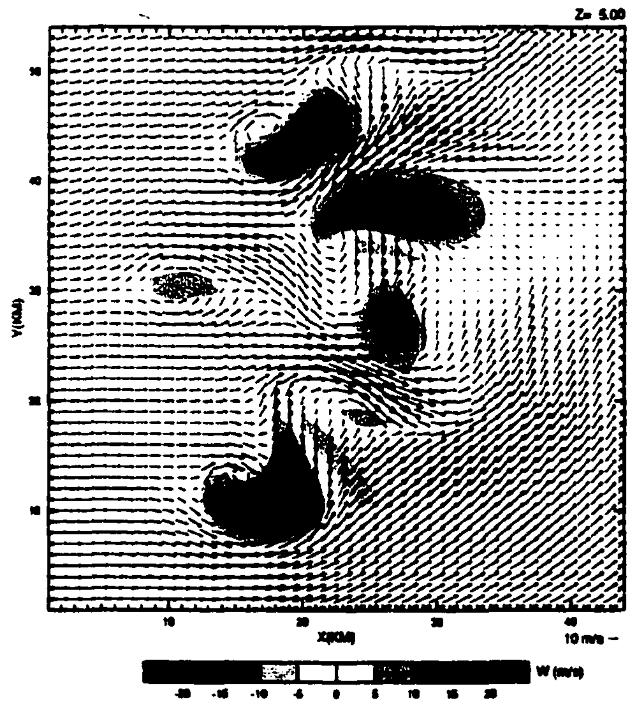

a) Horizontal winds (vectors) and vertical velocity (shading) at t=4501 s and z=5.0 km.

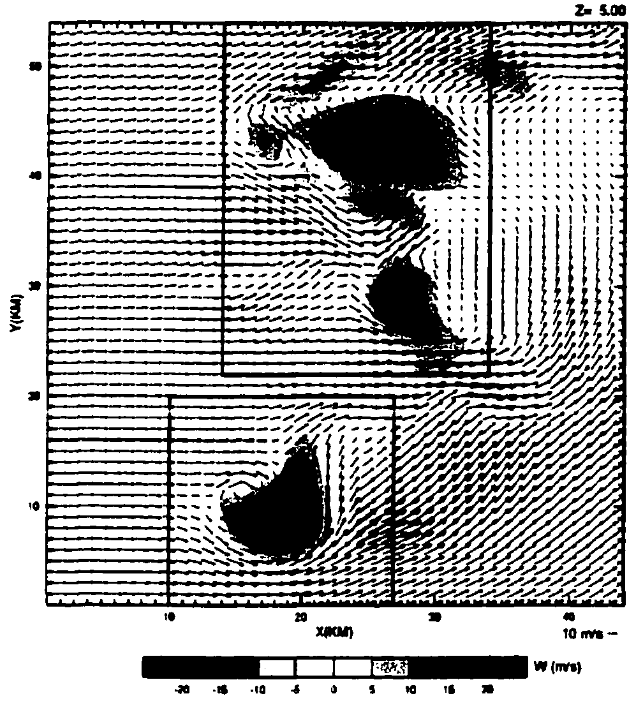

b) As in a) except at t=5041 s. The regions in which dual-Doppler statistics are computed are outlined in green.

Figure 2.3.1. Vertical cross section through a typical storm. The cross section is oriented perpendicular to the flight track. The intersection of the flight track and the cross section is indicated by the dot. Examples of coplane azimuthal coordinate lines are dashed.

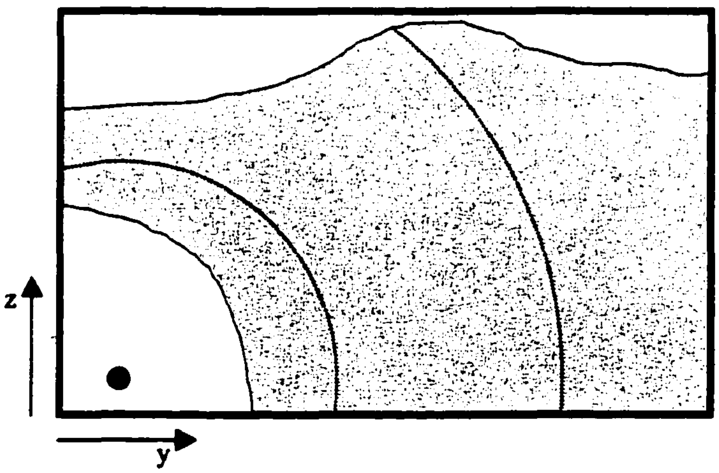

Figure 2.4.1. Cross sections of horizontal velocity (vectors) and vertical velocity (contours) in the McLean storm at z=9 km at 2254 UTC. The velocities were determined by the weak-constraint scheme (β=250000 m^2) with two different first guess fields.

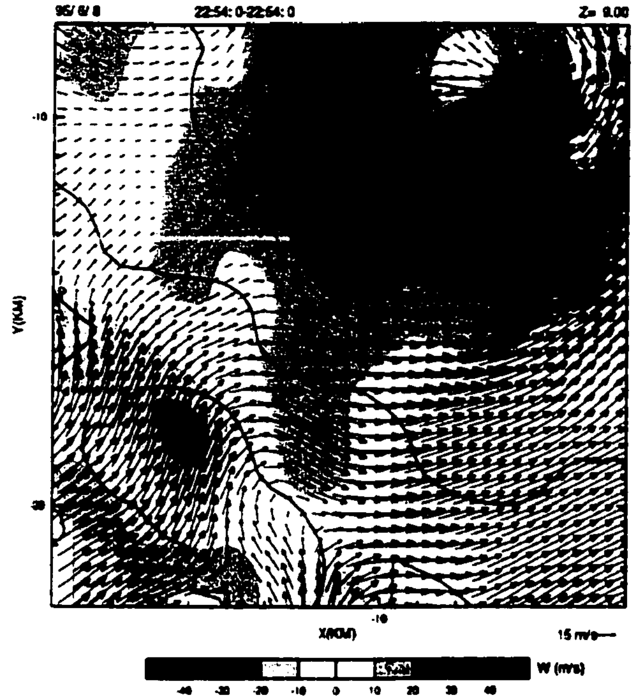

a) First guess with u and v determined from Equations (2.1.9) and (2.1.10) and w=0.

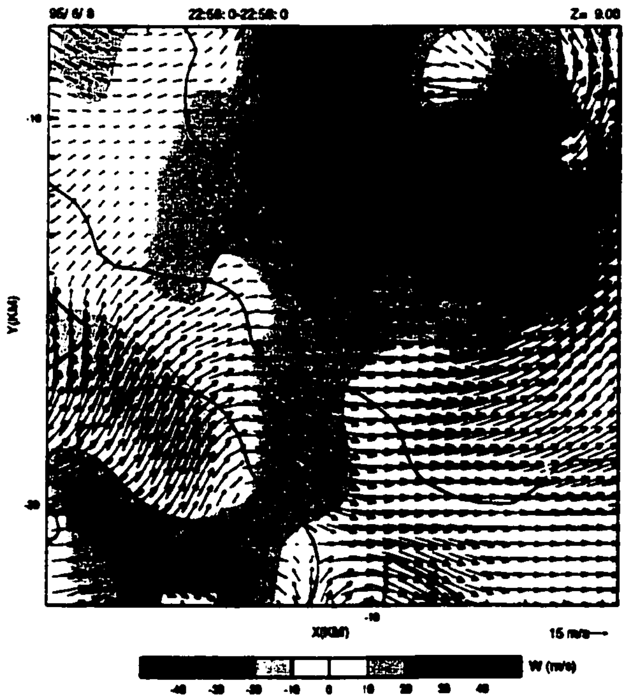

b) First guess of u=v=w=0.

Figure 2.4.2. Horizontal cross sections of wind (vectors) and vertical velocity (shading) at z=0.25 km for the weak-constraint dual-Doppler analysis of test case A.

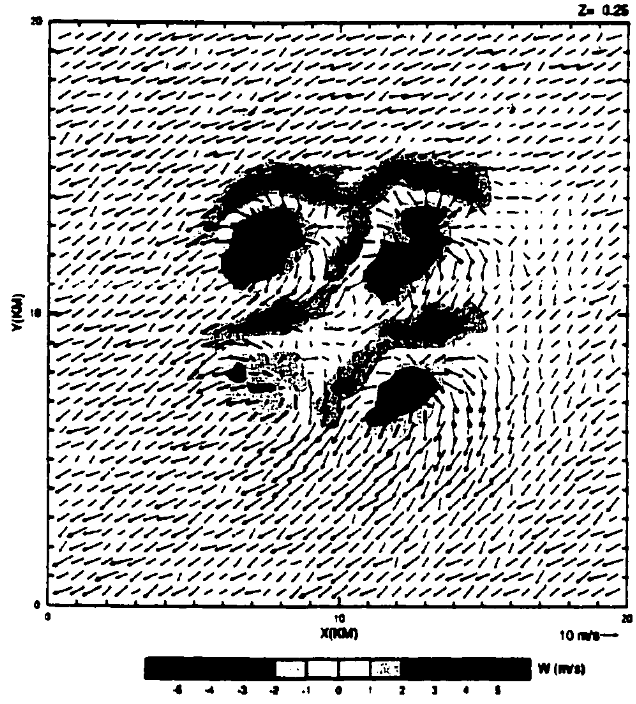

a) β=2.5 m^2.

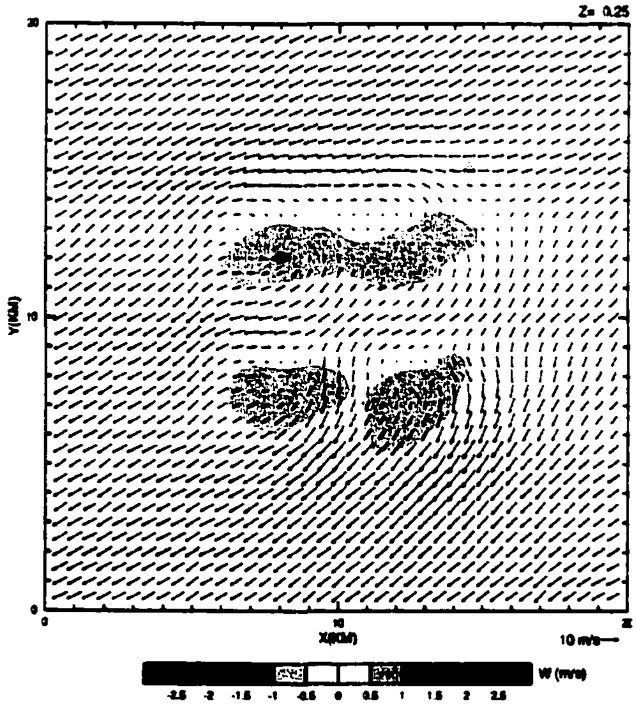

b) β=2.5 × 10^7 m^2.

Figure 2.4.3. RMS error in w (m s^{-1}) as a function of $\sqrt{\beta}$ (m) for weak-constraint dual-Doppler analyses of the Sperow et al. (1995) analytic wind field. Noise was added to the radial velocities. The errors are plotted for three different horizontal wavelengths.

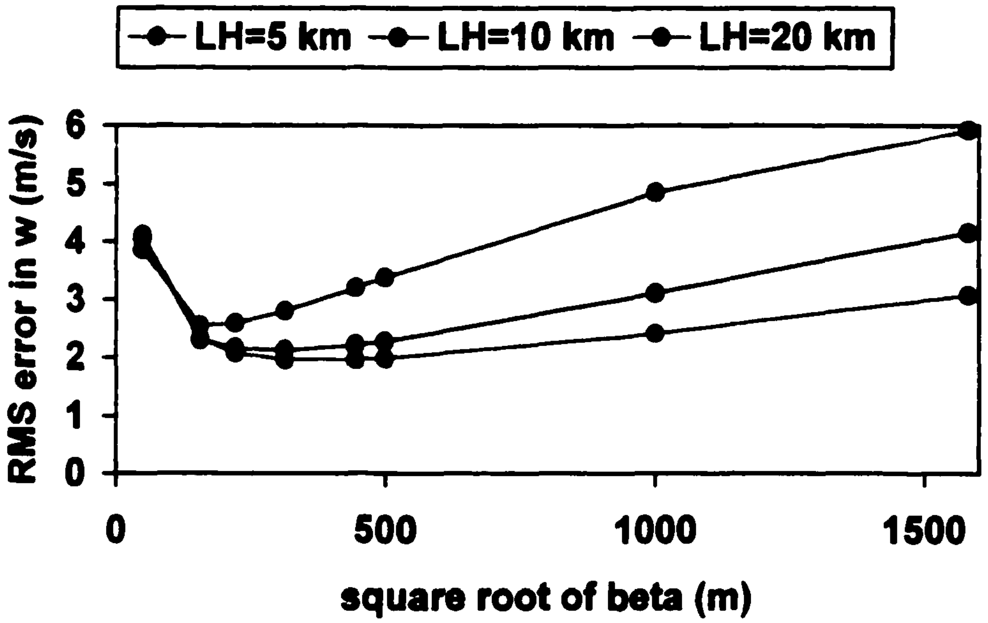

Figure 2.4.4. Cross sections of horizontal velocity (vectors) and vertical velocity (shading) in dual-Doppler analyses of the McLean storm at z=0.5 km at 2254 UTC.

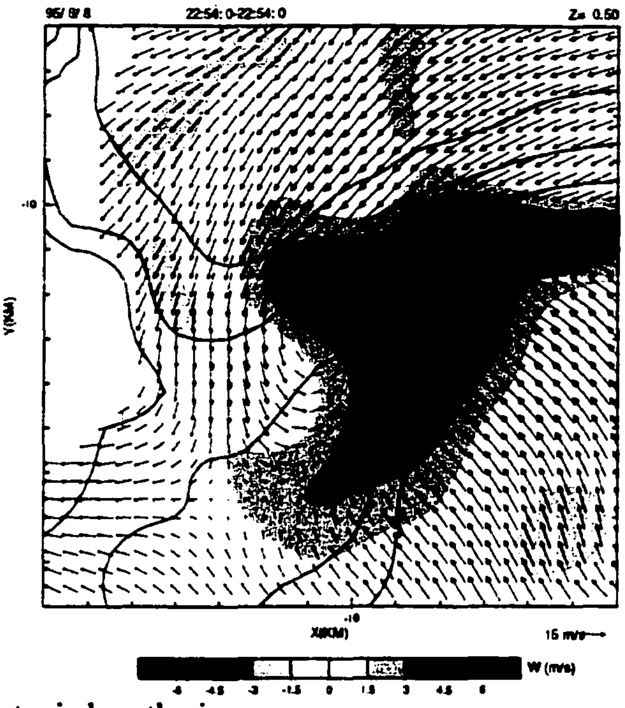

a) Strong-constraint wind synthesis.

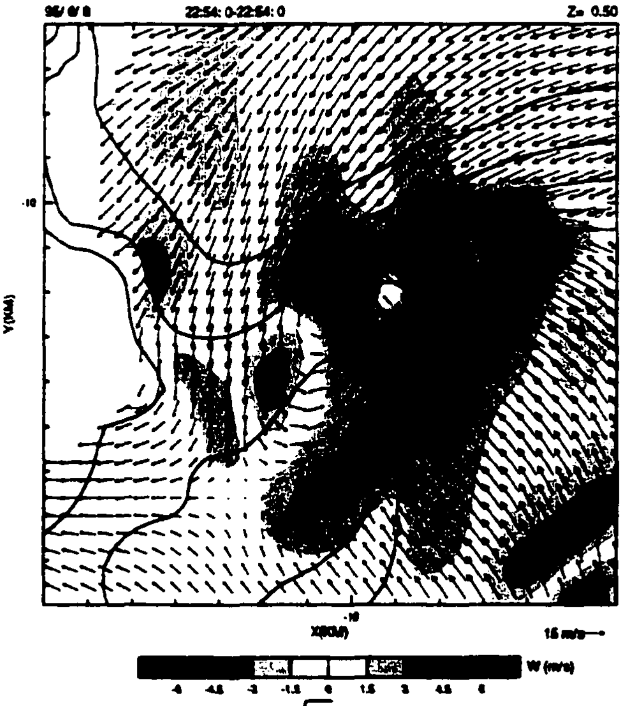

b) Weak-constraint wind synthesis with $\sqrt{\beta}$=500 m.

Figure 2.5.1. Horizontal winds (vectors) and horizontal convergence (shading at intervals of 0.002 s^{-1}) at z=1.0 km AGL from a traditional pseudo-dual-Doppler analysis of the McLean storm at 2306 UTC 8 June 1995.

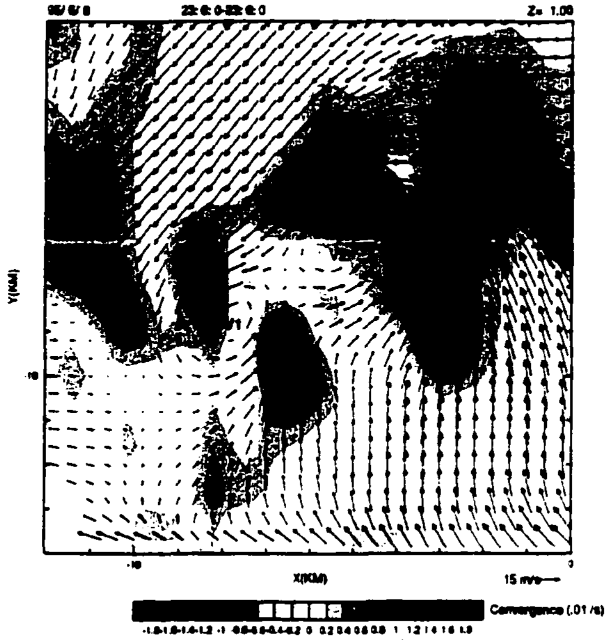

a) Analysis in a reference frame moving at 6.2 m s^{-1} from 175°, which is the approximate motion of the southwestern vortex.

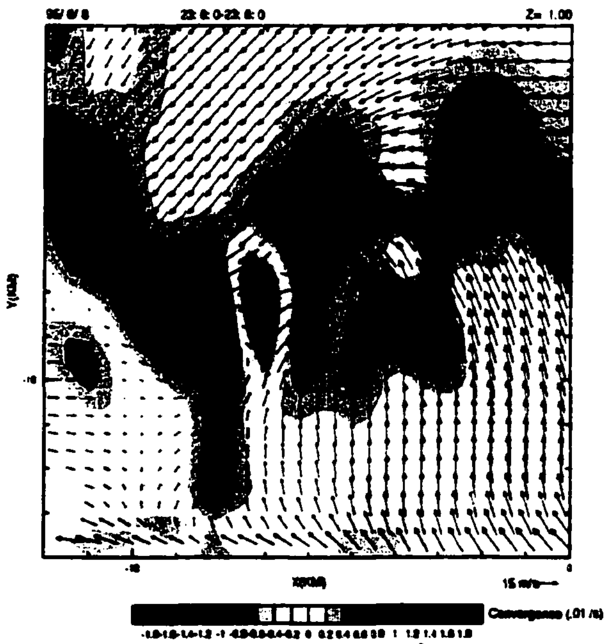

b) Analysis in a reference frame moving at 10.6 m s^{-1} from 209°, which is the approximate motion of the overall storm reflectivity core.

Figure 2.5.2. Geometry for the determination of the local reference frame motion. The outer box represents the overall dual-Doppler analysis domain, and the inner box represents the local sub-domain surrounding a grid point.

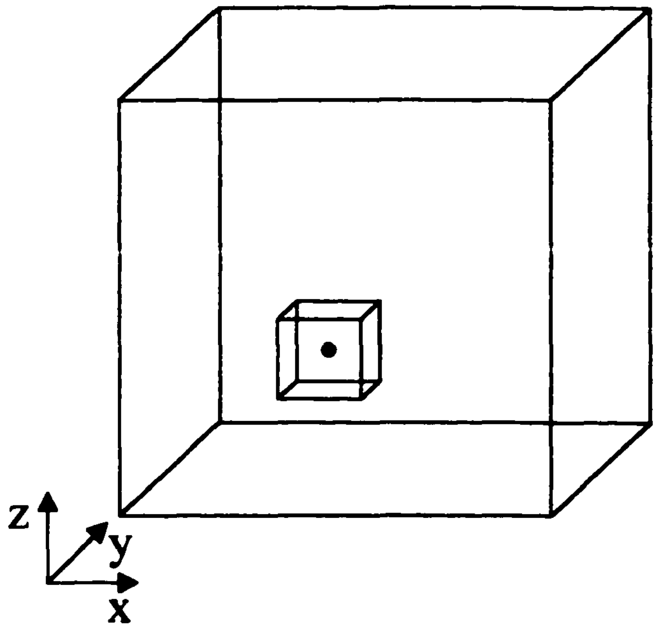

Figure 2.5.3. Horizontal winds at z=1.0 km AGL for the analytic wind field described in Section 2.5.3 of the text. The x and y distances are in km.

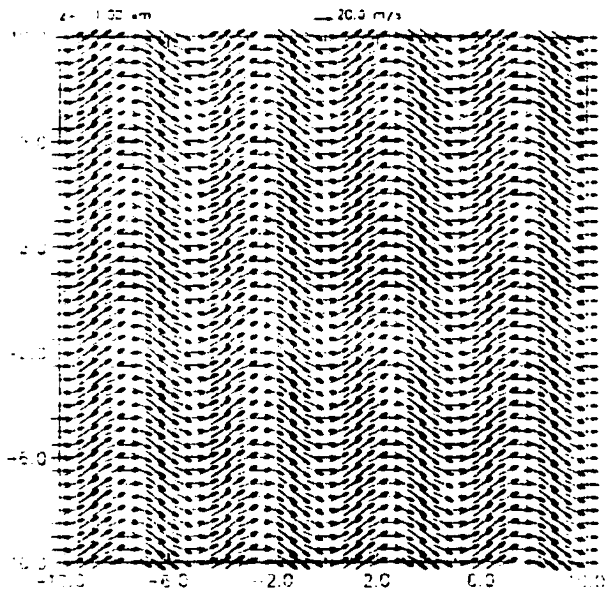

a) Exact wind field at t=0 s. The vertical velocity is zero at this time.

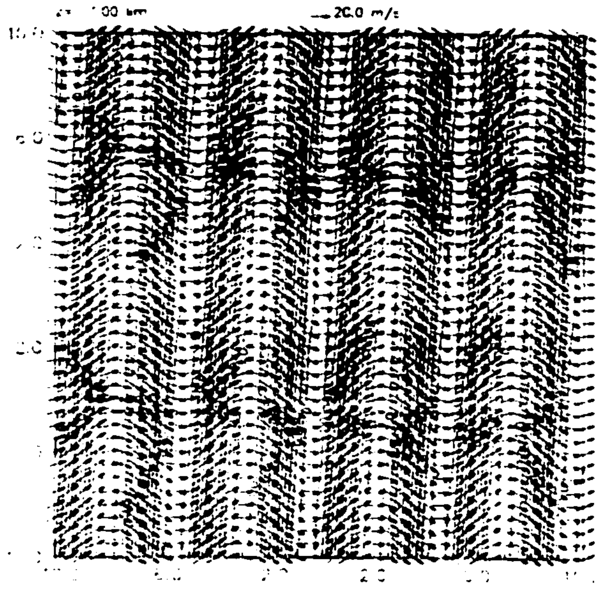

b) **Exact wind field at t=60 s, with contours of vertical velocity. The contour interval is 0.5 m s^{-1}.**

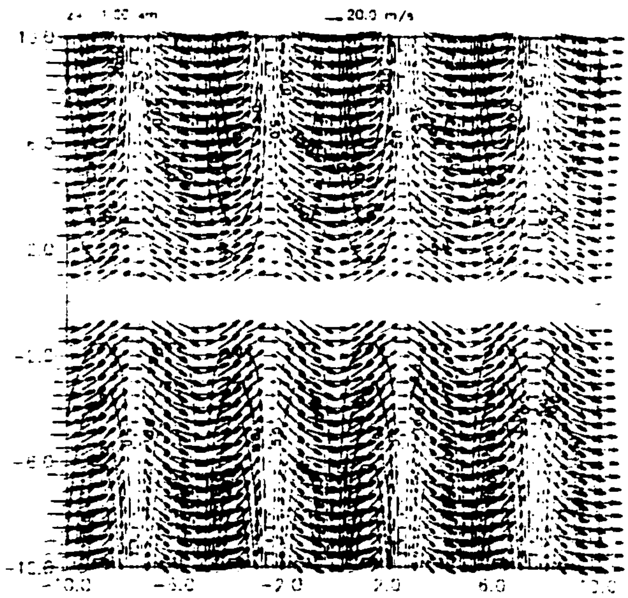

c) **Dual-Doppler wind synthesis (centered at t=0 s) in the fixed reference frame, with contours of vertical velocity. The contour interval is 5.0 m s^{-1}.**

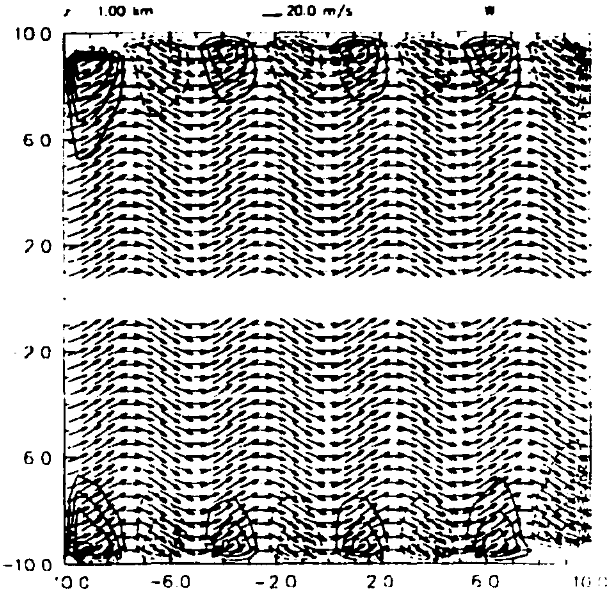

d) **Dual-Doppler wind synthesis (centered at t=0 s) in the non-uniform moving frame, with contours of vertical velocity. The contour interval is 2.0 m s^{-1}.**

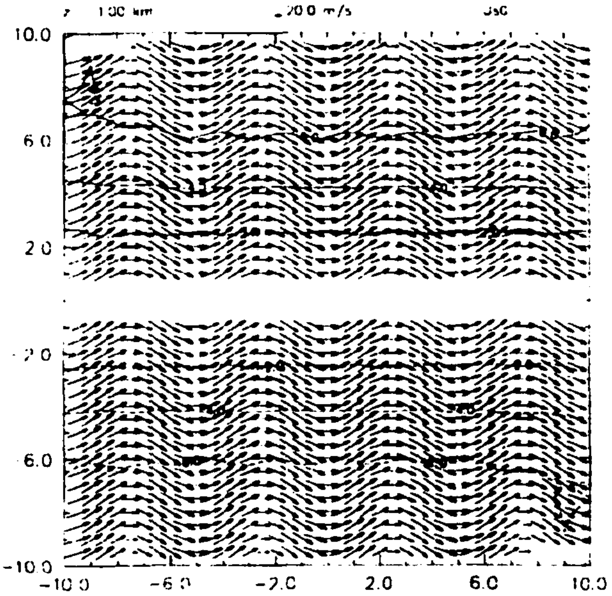

e) ***U_s* for the non-uniform moving frame. The contour interval is 2.0 m s^{-1}.**

Figure 2.5.4. Translation velocity (U_s, V_s) vectors for the non-uniform moving reference frames.

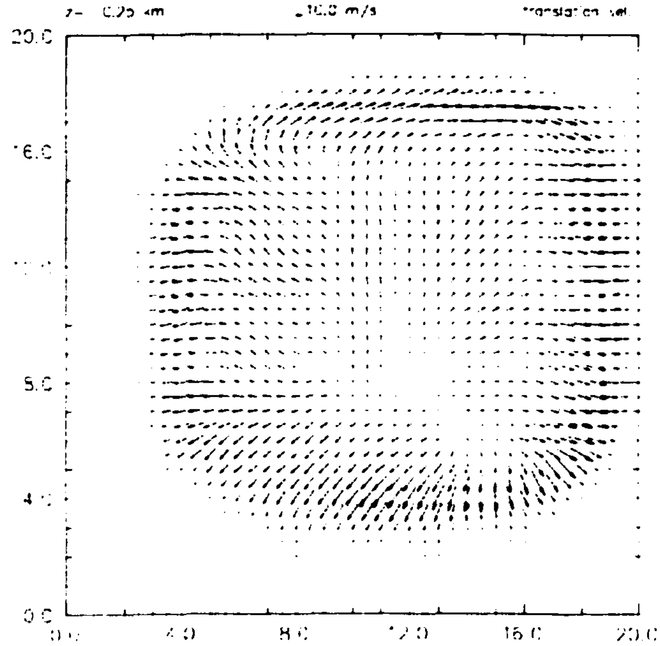

a) For test case B.

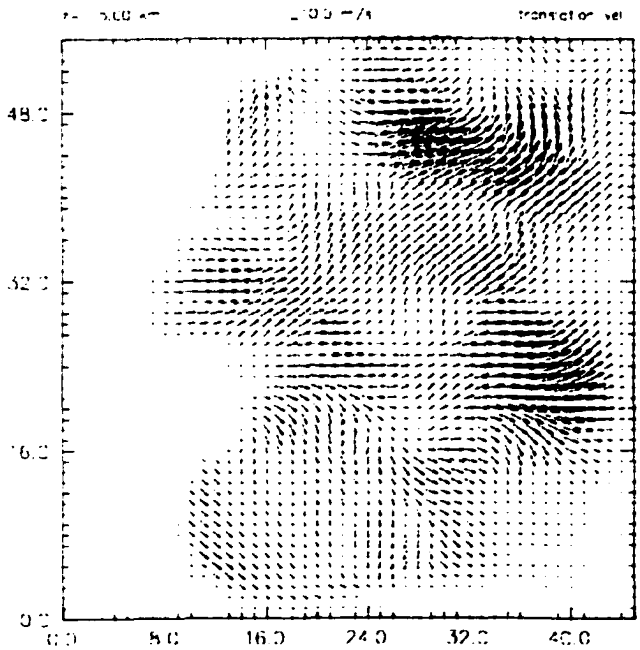

b) For test case C.

Figure 2.6.1. Schematic of aircraft passes near a supercell thunderstorm during VORTEX. Estimation of velocity time derivatives (Section 2.6) requires four consecutive radial velocity observations.

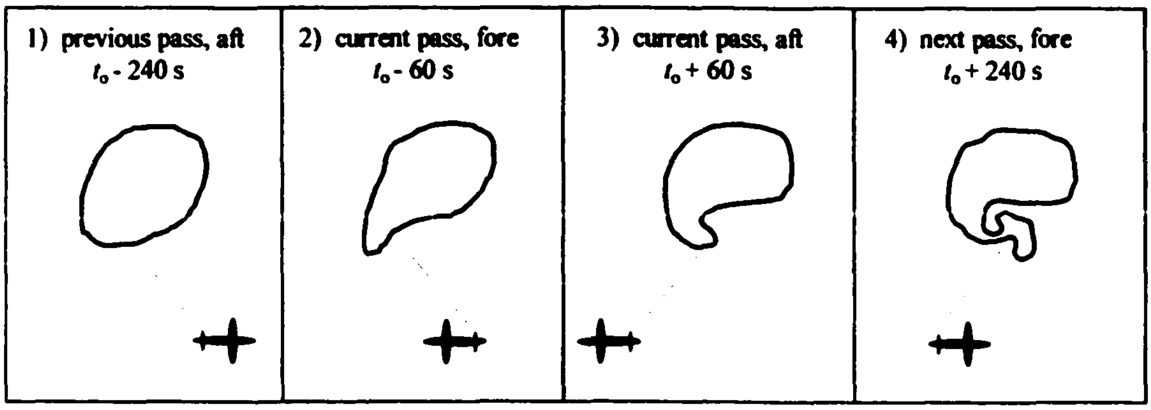

Figure 2.7.1. Traditional dual-Doppler analyses of combined Rankine vortices. The radius of influence for the Cressman (1959) objective analysis of the simulated radial velocity observations is 1200 m. The horizontal grid spacing is 400 m. The actual wind speed at the edge of the vortex core is 100 m s^{-1} in each case.

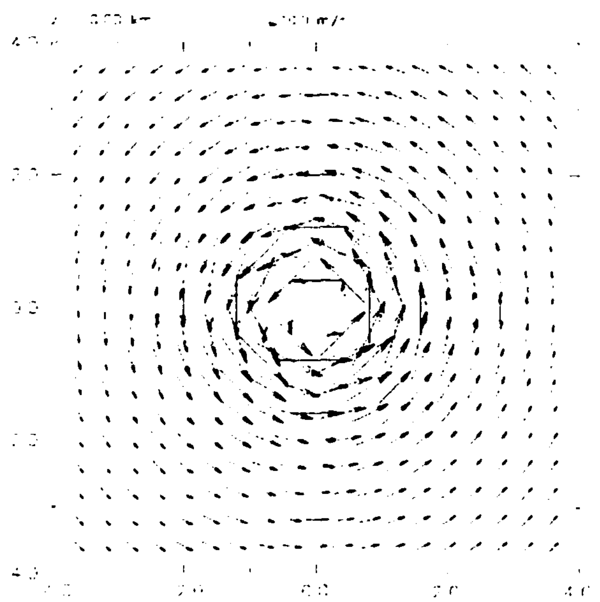

a) Horizontal wind (vectors) in the dual-Doppler analysis of a vortex with a 200-m core radius. The apparent radius of maximum wind in the analysis is 800 m.

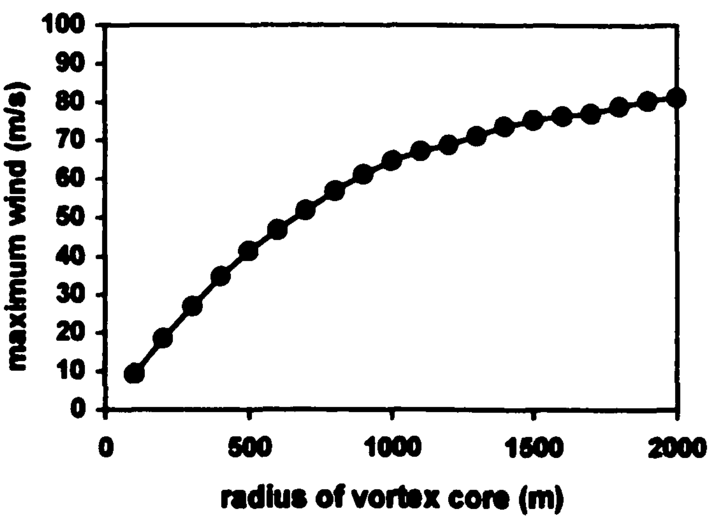

b) Maximum wind speeds in the dual-Doppler analyses as a function of actual core radius.

Figure 2.7.2. Storm-relative wind (vectors), vertical velocity (contours), and retrieved buoyancy (cm s^{-2}) in the McLean storm at 2318 UTC.

a) z=0.5 km.

b) z=4.0 km.

Figure 3.1.1. Reflectivity factor (dBZ) at 0.5° elevation angle from the Amarillo, Texas WSR-88D on 8-9 June 1995. The storm is approximately 100 km east of the radar site. Counties are outlined in orange. The red line is the 35° N parallel. If a tornado was in progress at the time of the image, then it is noted in parentheses after the time.

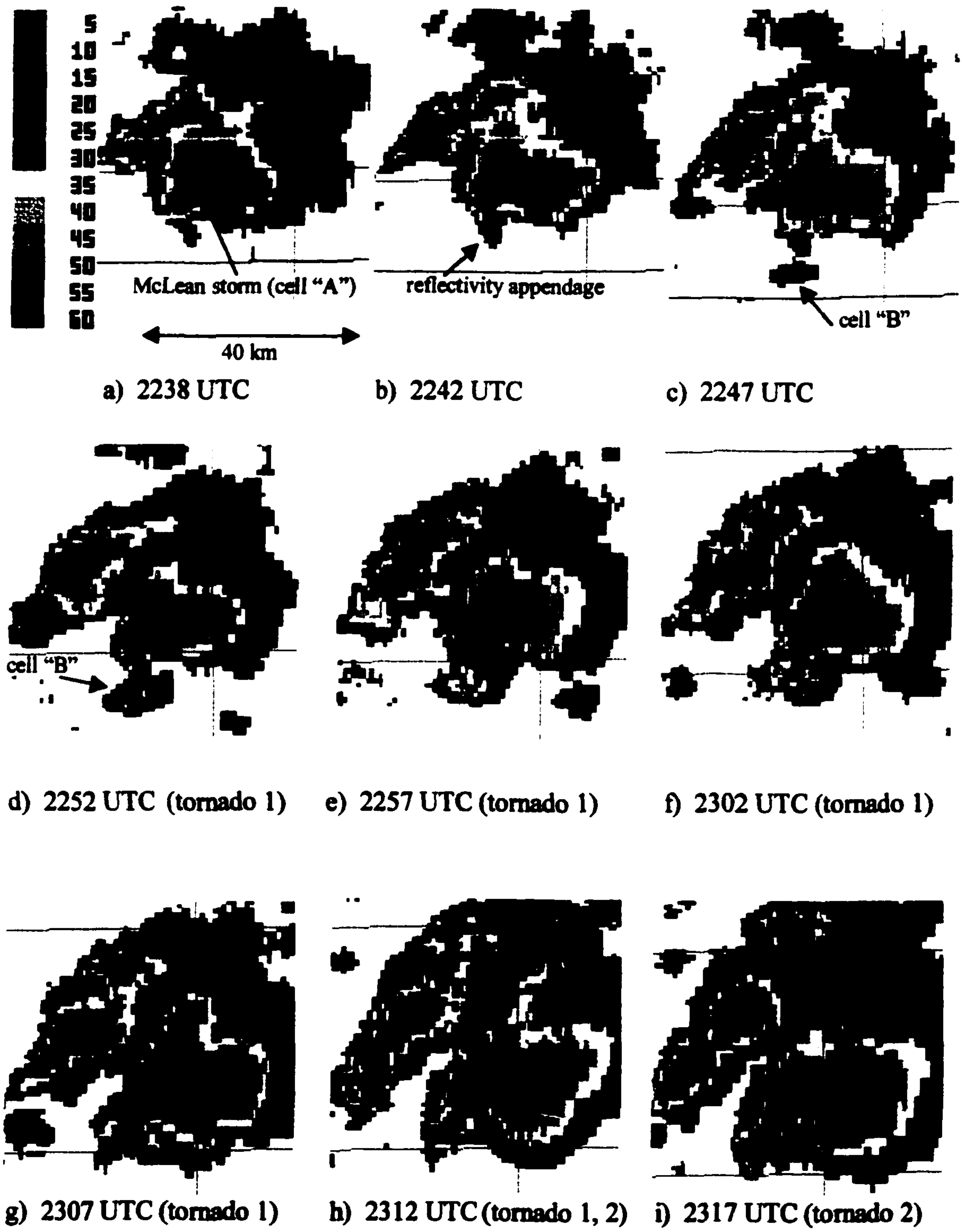

j) 2322 UTC (tornado 2, 3)

k) 2327 UTC

l) 2332 UTC (tornado 4)

m) 2337 UTC (tornado 4)

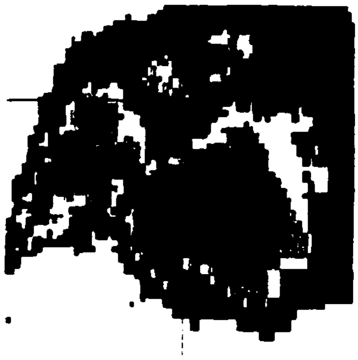

n) 2342 UTC (tornado 4)

o) 2347 UTC (tornado 4)

p) 2352 UTC (tornado 4)

q) 2357 UTC (tornado 4)

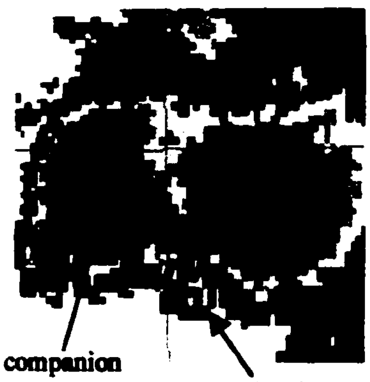

r) 0002 UTC (tornado 4)

Figure 3.1.2. Edited scans of reflectivity (left, dBZ) and radial velocity (right, m s^{-1}) by the ELDORA. The range rings are at 10 km intervals. The arrow indicates the scanning direction of horizontal beams.

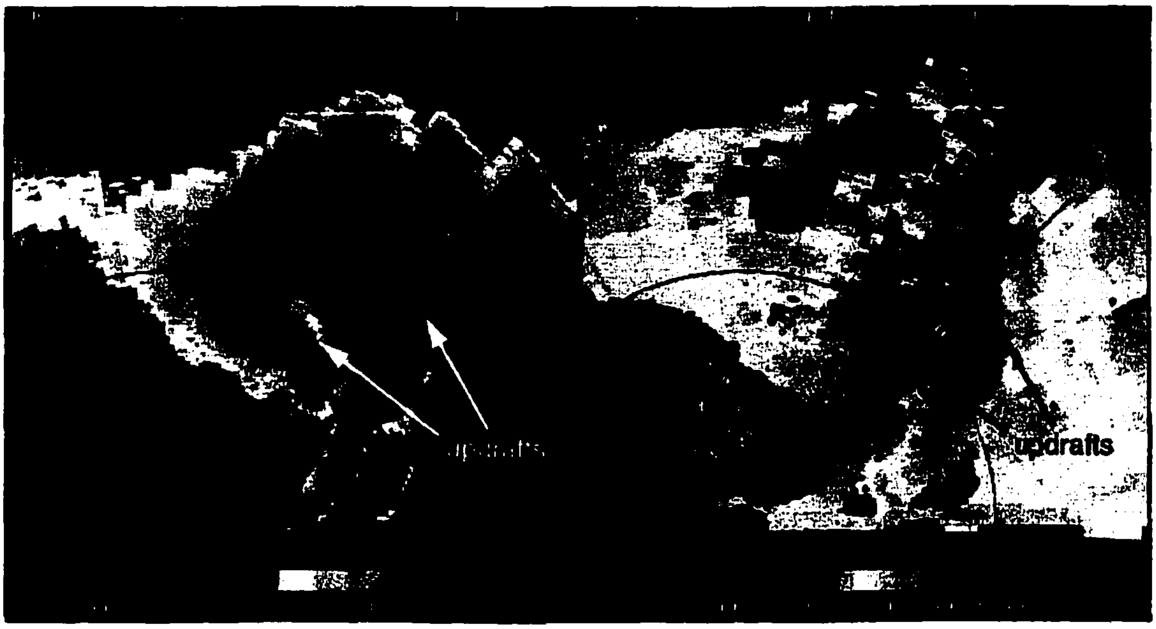

north

a) Aft radar scan at 22:36:14 UTC.

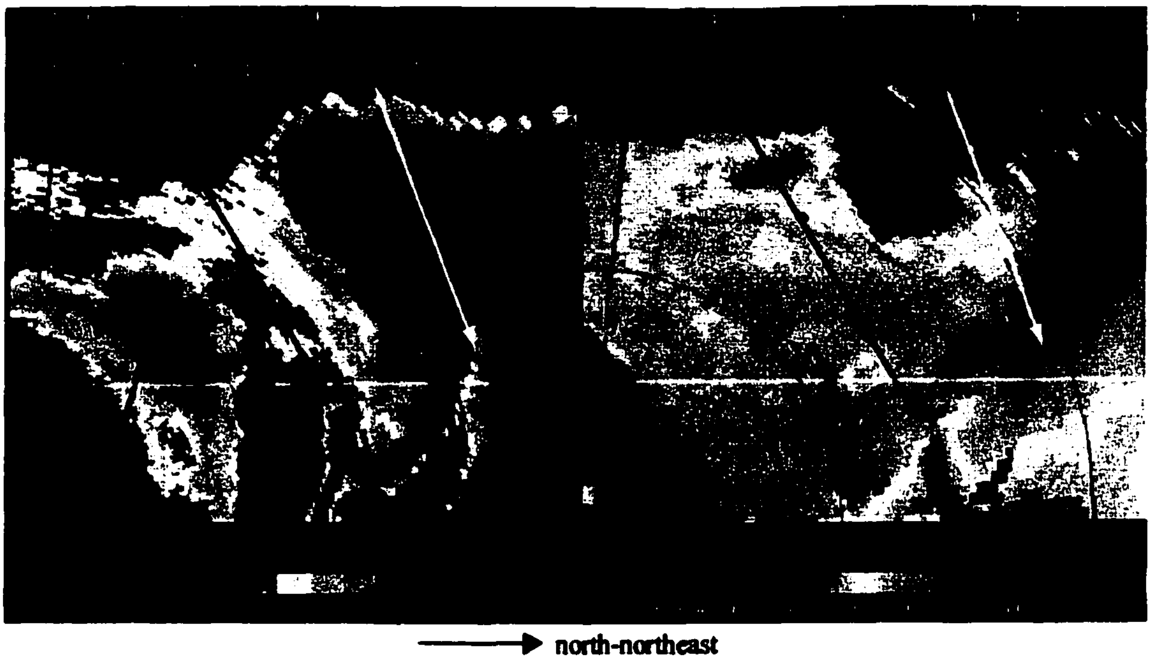

b) Aft radar scan at 22:48:59 UTC.

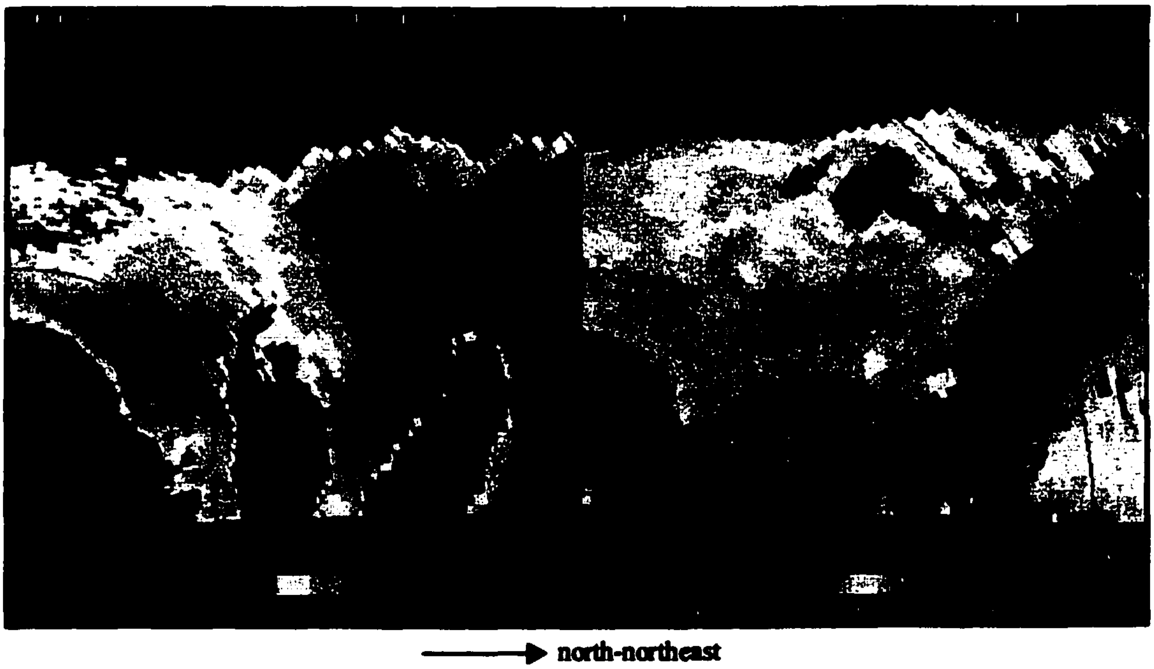

c) Aft radar scan 9 seconds earlier than in b).

(Figure 3.1.2)

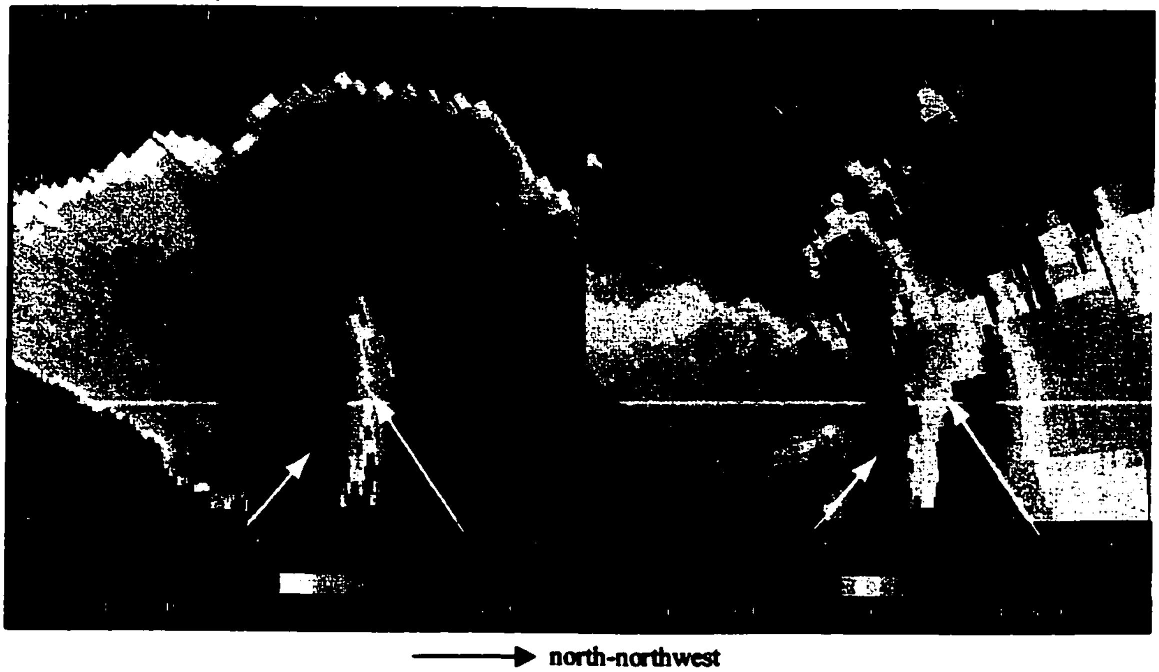

d) Fore radar scan at 22:58:39 UTC.

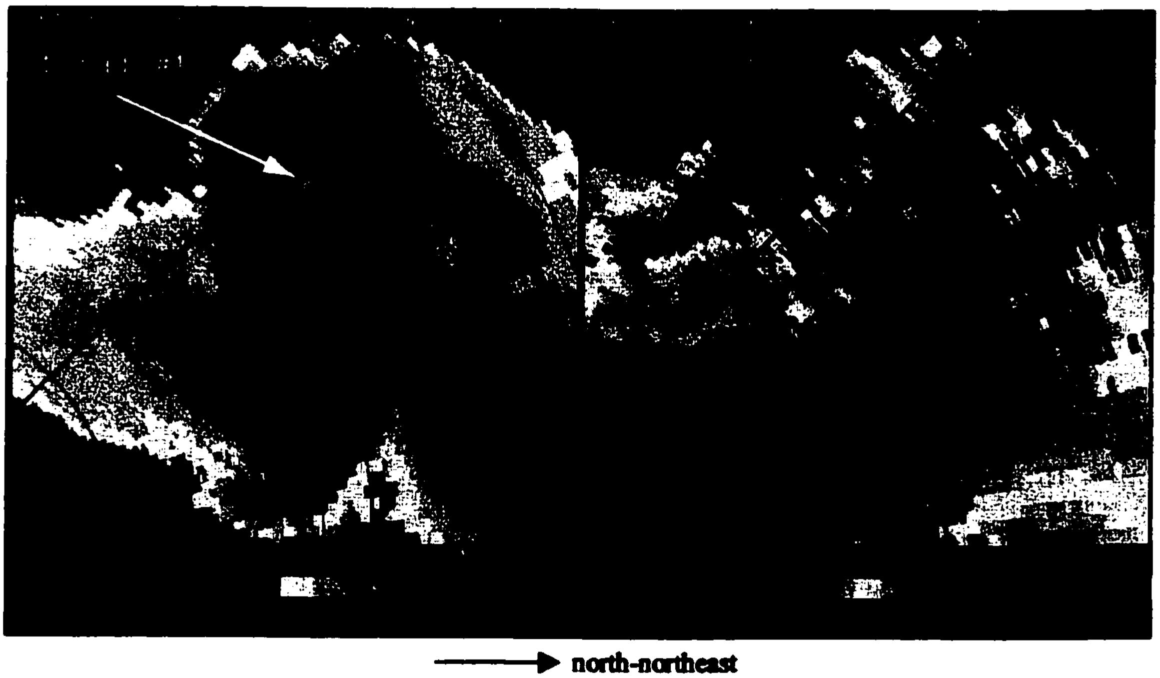

e) Aft radar scan at 22:59:46 UTC.

(Figure 3.1.2)

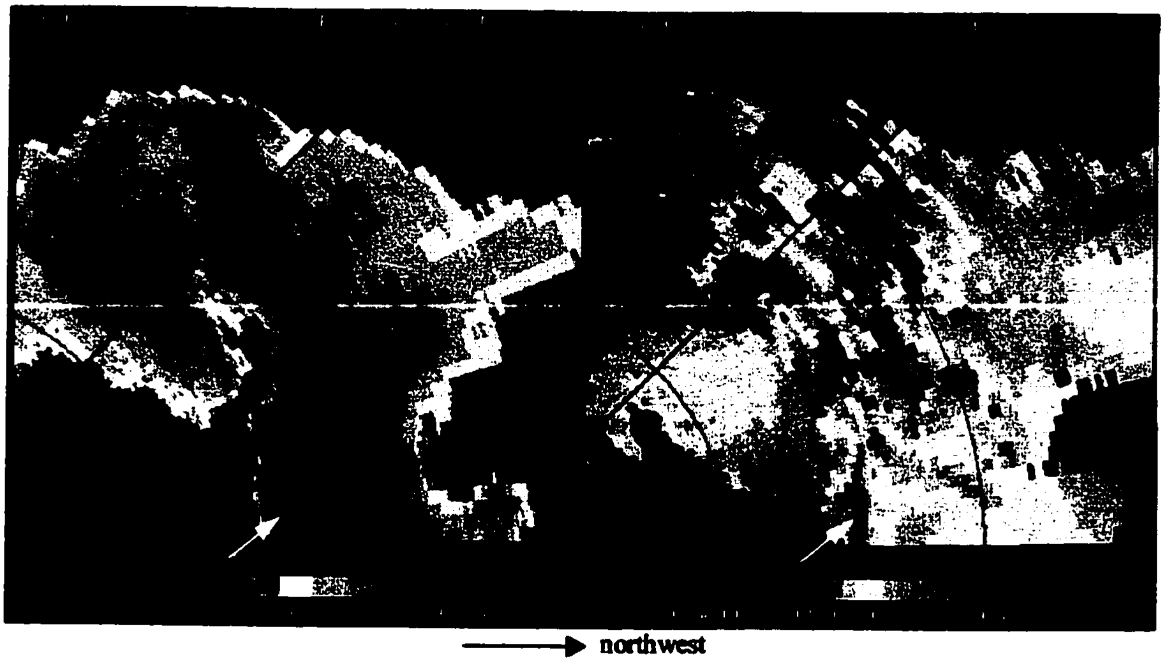

f) Fore radar scan at 23:12:37 UTC.

(Figure 3.1.2)

north ←

g) Fore radar scan at 23:05:34 UTC.

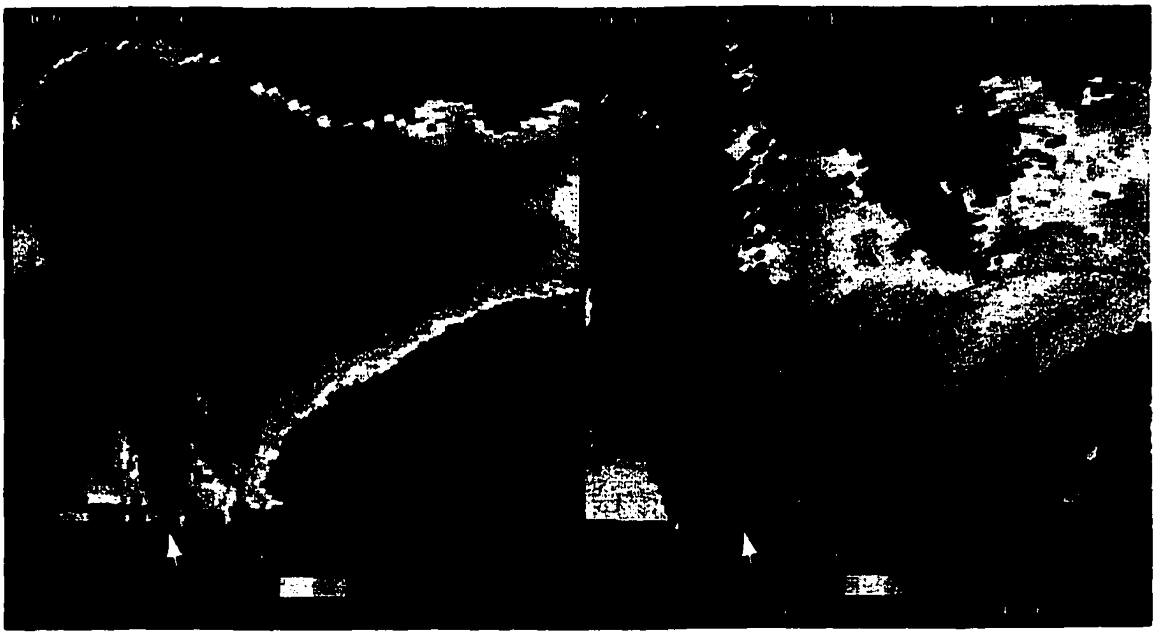

north ←

h) Fore radar scan 5 seconds later than in g).

(Figure 3.1.2)

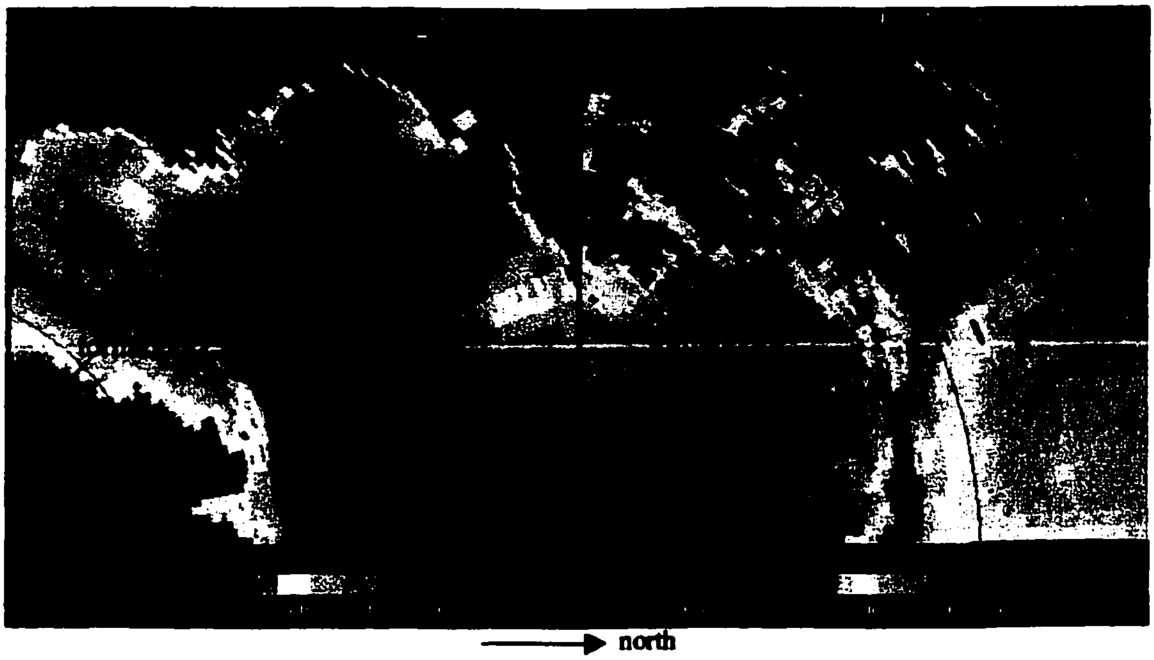

i) Aft radar scan at 23:13:18 UTC.

(Figure 3.1.2)

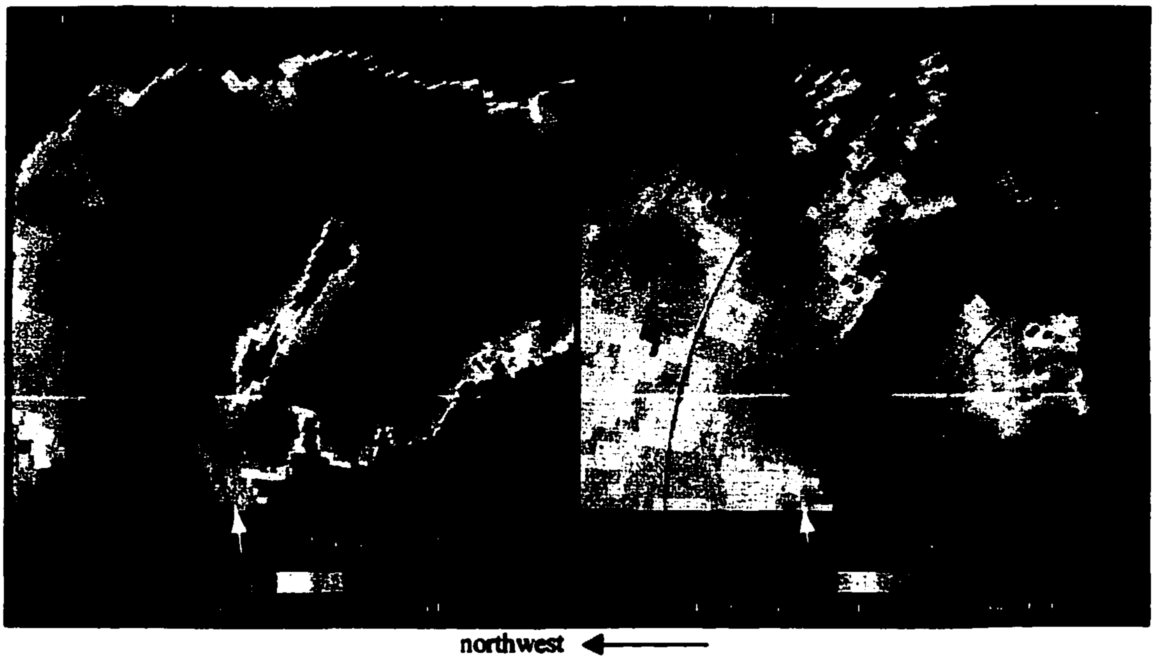

j) Aft radar scan at 23:19:47 UTC.

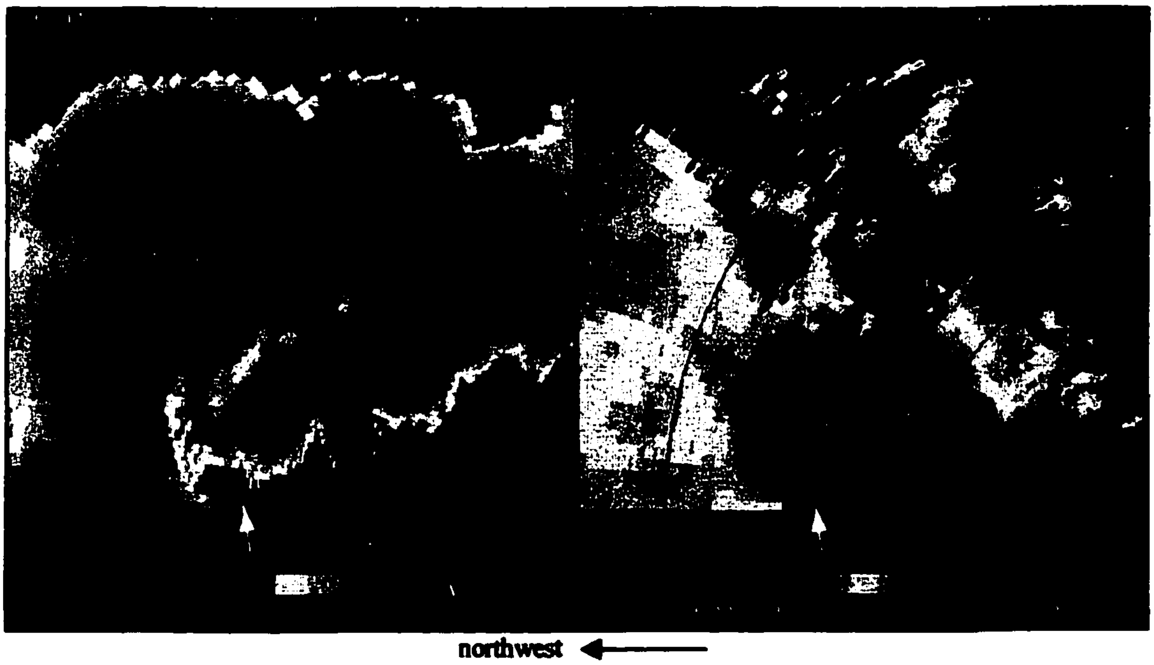

k) Aft radar scan 16 seconds later than in j).

(Figure 3.1.2)

l) Fore radar scan at 23:37:22 UTC.

(Figure 3.1.2)

Figure 3.2.1. Force diagram for baroclinic generation of horizontal vorticity. "H" and "L" indicate hydrostatic high and low pressure perturbations, respectively. "B" and "P" indicate accelerations associated with buoyancy and pressure, respectively.

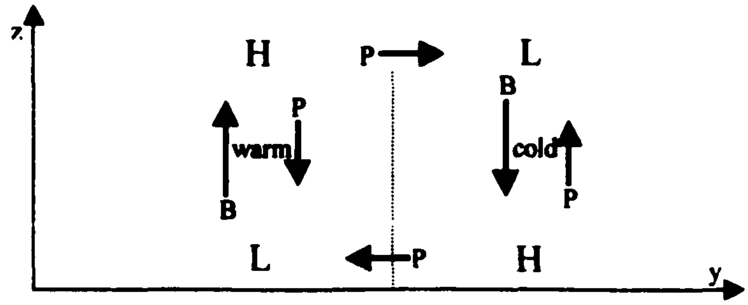

Figure 3.2.2. Tilting of horizontal vorticity into the vertical by an updraft (from Lilly 1982, copyright by Springer-Verlag). The coils represent the sense of the 3-D vorticity. The arrows represent the magnitude of vertical displacement by the updraft.

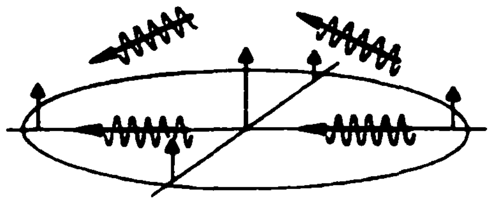

a) Rectilinear shear case. In this example, tilting produces cyclonic vertical vorticity on the right side of the updraft and anticyclonic vertical vorticity on the left side.

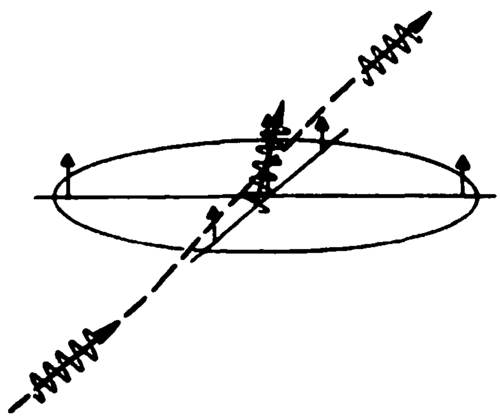

b) Directional shear case. In this example, the updraft-relative flow carries the cyclonic vertical vorticity produced by tilting into the center of the updraft. Then, the vorticity is tilted back into the horizontal on the downstream side of the updraft maximum.

Figure 3.2.3. Three-dimensional schematic of a supercell thunderstorm, as viewed from the southeast (from Klemp 1987, copyright by Annual Reviews, Inc.). The storm is evolving in an environment in which the westerly component of the wind increases with height. The thick lines (tubes) represent the flow in and near the storm. The thin lines are vortex lines.

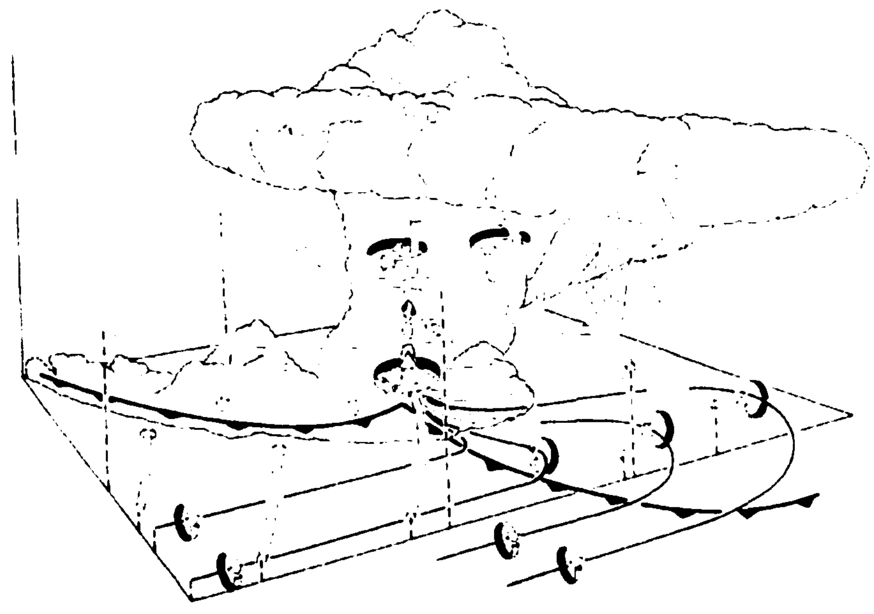

a) Intensification of the low-level rotation.

b) Formation of a new updraft and vortex farther east after the intensification of the rear flank downdraft.

Figure 3.2.4. Summary of low-level features in a simulated storm (from Klemp and Rotunno 1983, courtesy of the American Meteorological Society). The arrows are storm-relative streamlines. Updrafts (downdrafts) are enclosed with solid (dashed) contours. The cold front marks the −1°C isotherm.

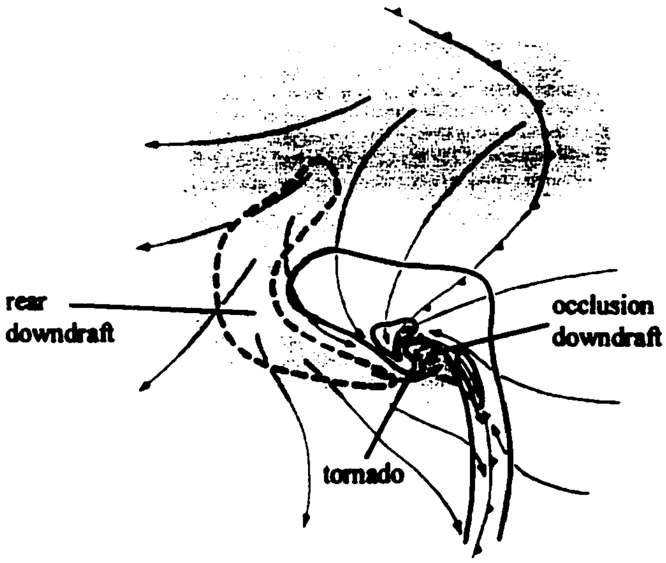

Figure 3.2.5. Depiction of the formation of vertical vorticity by tilting of horizontal vorticity in a downdraft, followed by stretching of the vertical vorticity at the base of an updraft (adapted from Dowell and Bluestein 1997). The parallelogram represents a material circuit in the fluid, and the arrow represents the orientation of the 3-D vorticity vector. The effects of deformation acting on the material curve are neglected for ease of interpretation. Initially (left panel), there is circulation about the tilted circuit owing to horizontal vorticity in the environment. After the circuit is flattened out (middle panel) by a downdraft on the left side, a small component of the vorticity is vertical. When the circuit later enters a convergent region, the vertical component is amplified (right panel).

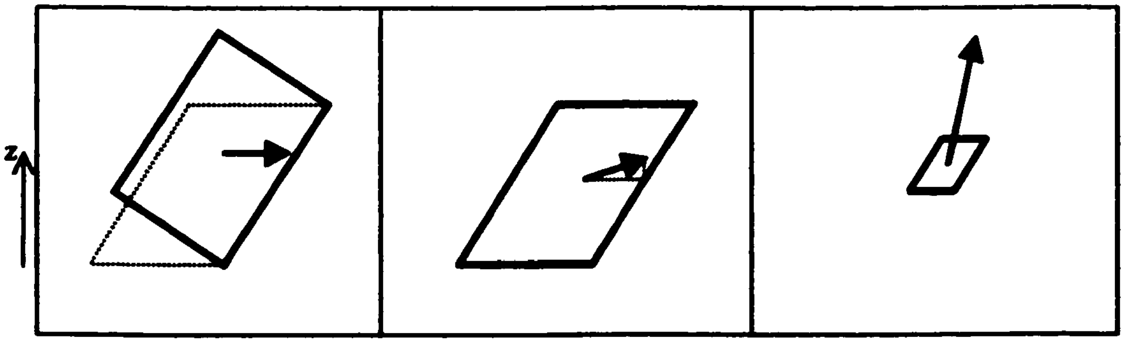

Figure 3.2.6. Horizontal storm-relative velocity (vectors), vertical velocity (shading), and reflectivity (contours at 10 dBZ intervals) at z=0.5 (left) and 4.0 (right) km AGL in the pseudo-dual-Doppler analyses of the McLean, Texas storm. "Storm-relative" refers to the motion of the dominant low-level vortex (Table 1.2), which changes from one pass to the next. This constant value, which is given on the lower left-hand side of each panel, is approximately equal to the variable velocity (U_s, V_s) at the vortex location but not necessarily elsewhere in the domain. The x and y distances are relative to the center of McLean. Approximate tornado tracks and gust front locations are marked with heavy gray and black lines, respectively. "T1", "T2", and "T4" denote the locations of tornadoes #1, #2, and #4. "V1", "V2", and "V4" refer to the locations of the parent vorticity maxima before they are tornadic. "C" and "A" denote local maxima in cyclonic and anticyclonic vertical vorticity not clearly associated with a tornado. "B" marks the location of the "bump" in reflectivity (Fig. 3.1.2.b).

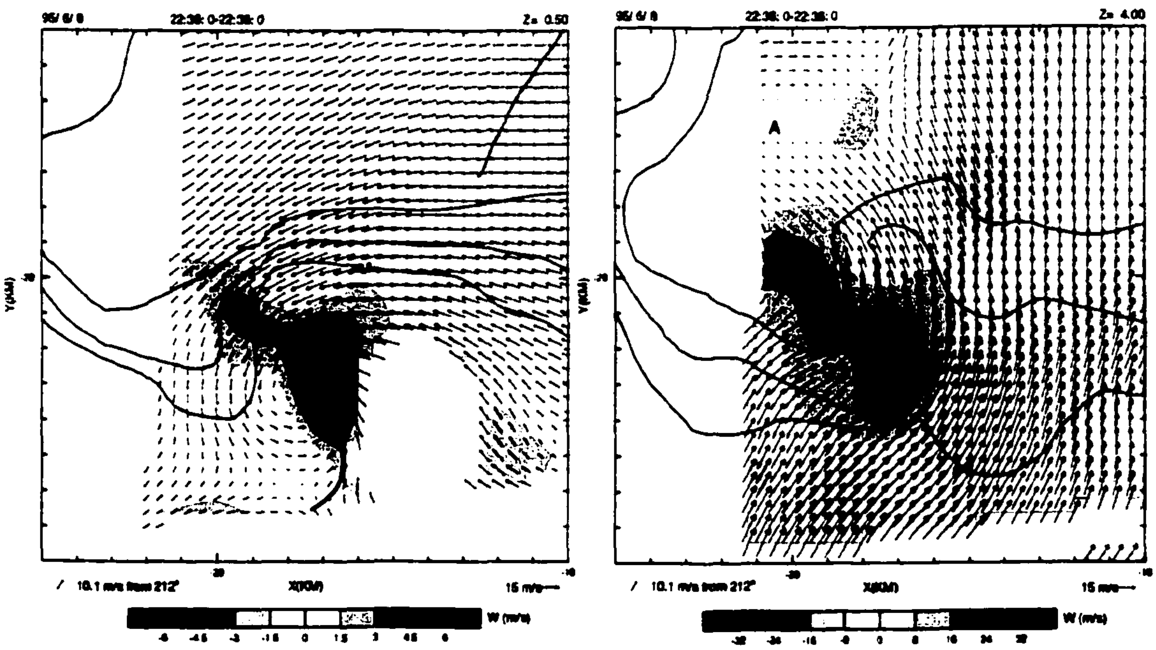

a) 2236 UTC

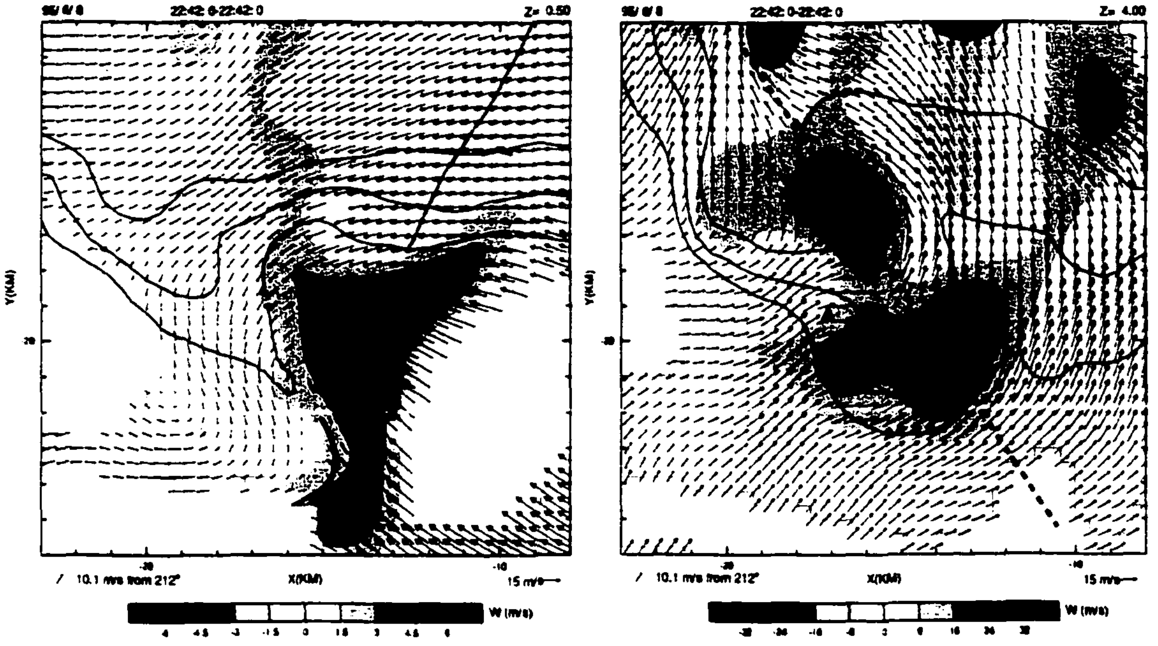

b) 2242 UTC

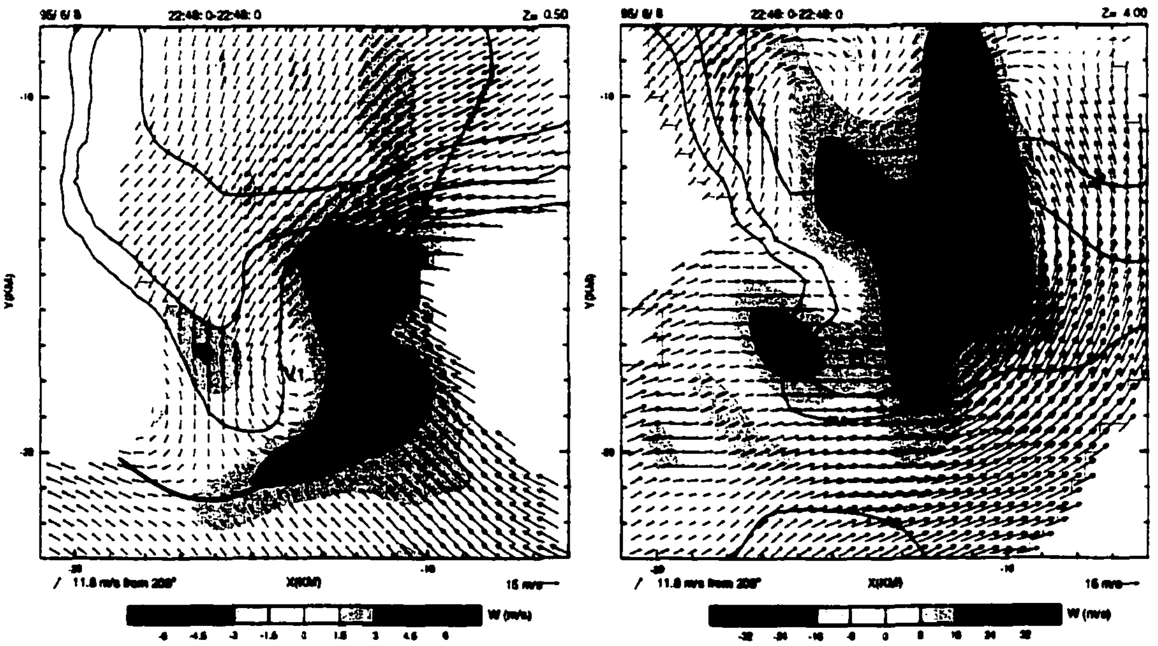

c) 2248 UTC

(Figure 3.2.6)

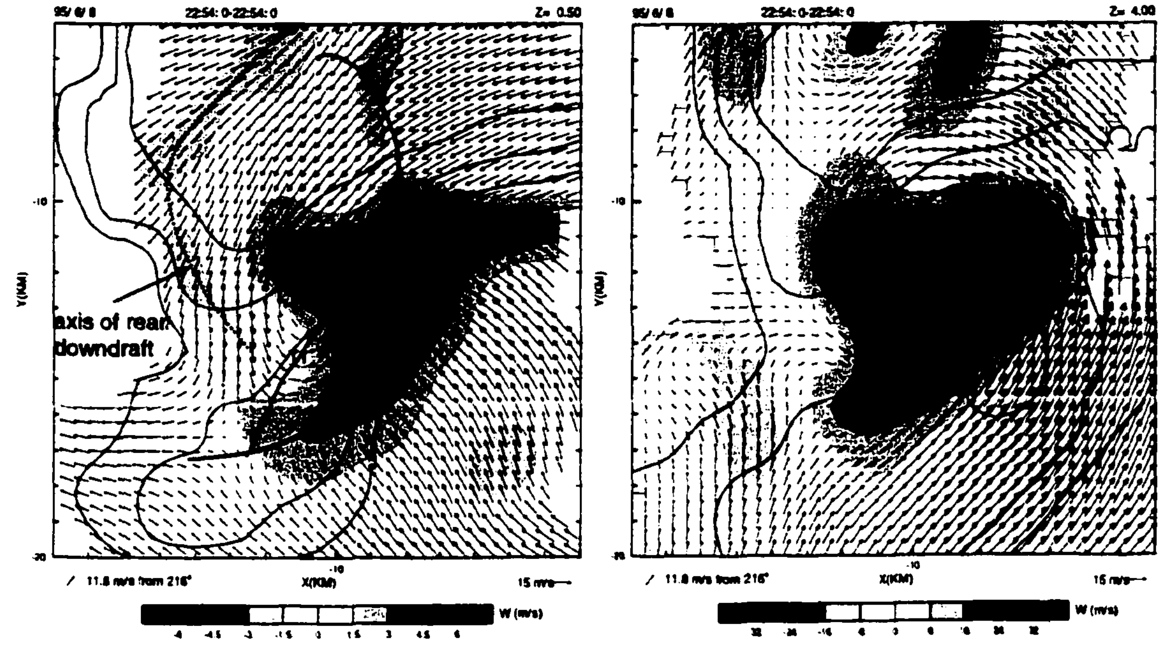

d) 2254 UTC

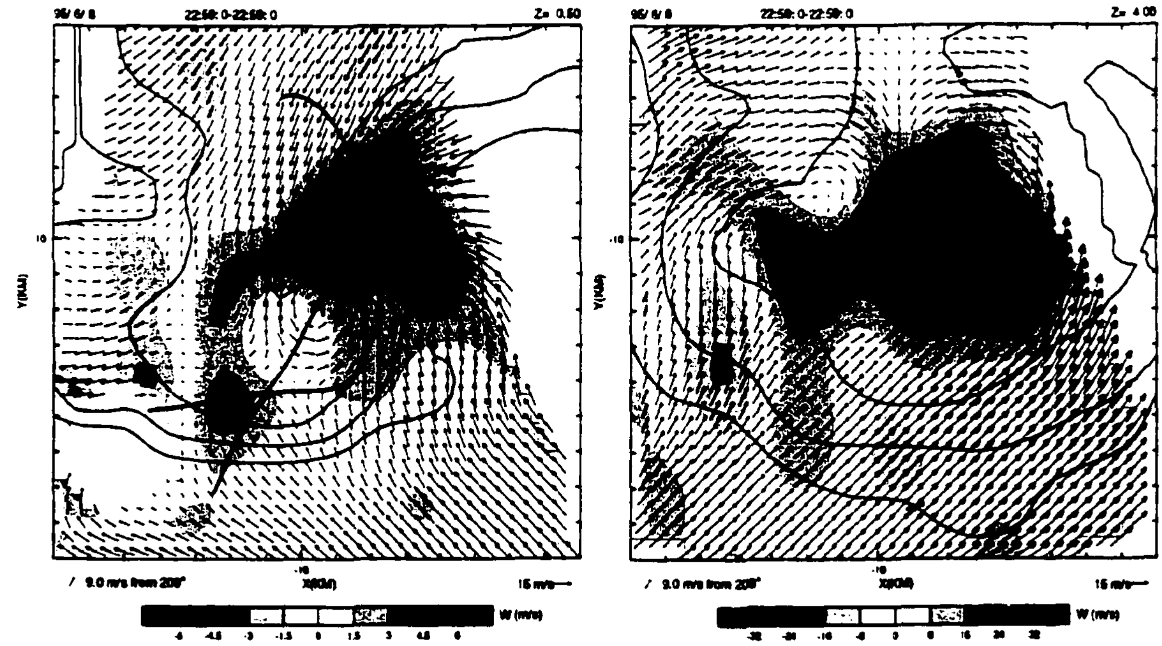

e) 2259 UTC

(Figure 3.2.6)

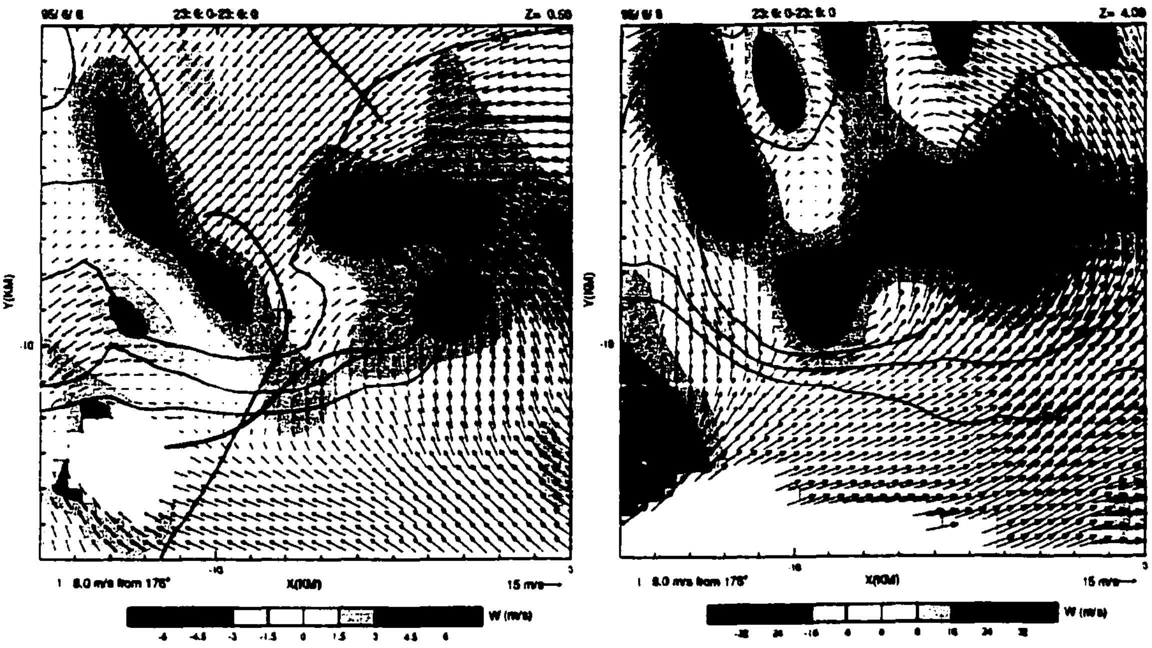

f) 2306 UTC

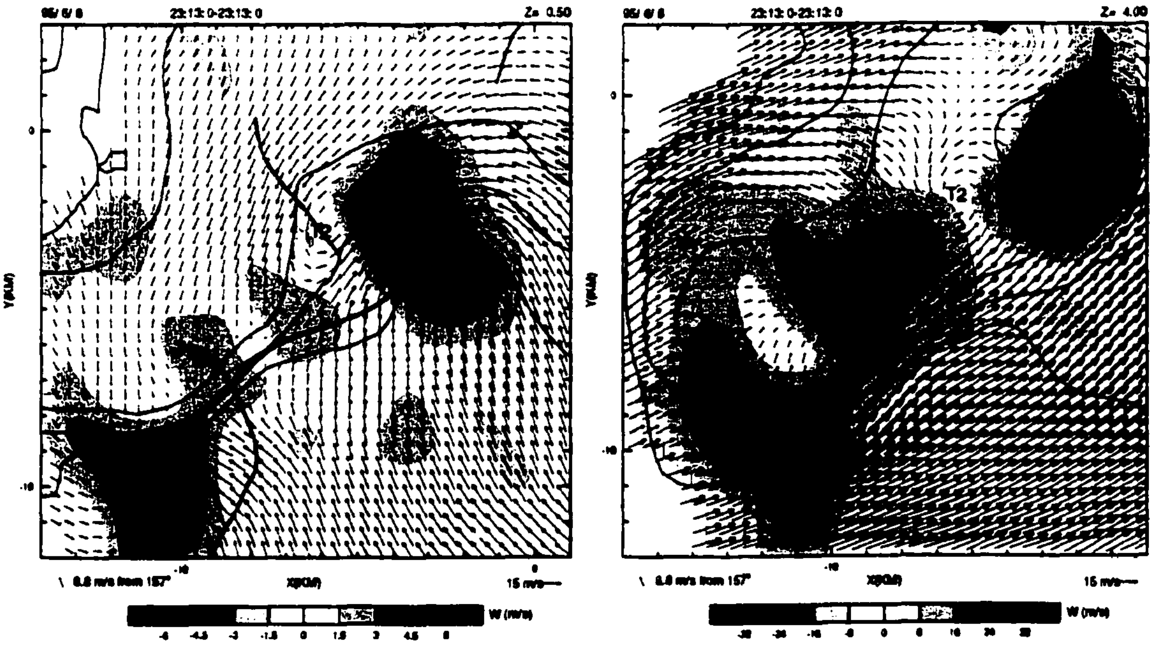

g) 2313 UTC

(Figure 3.2.6)

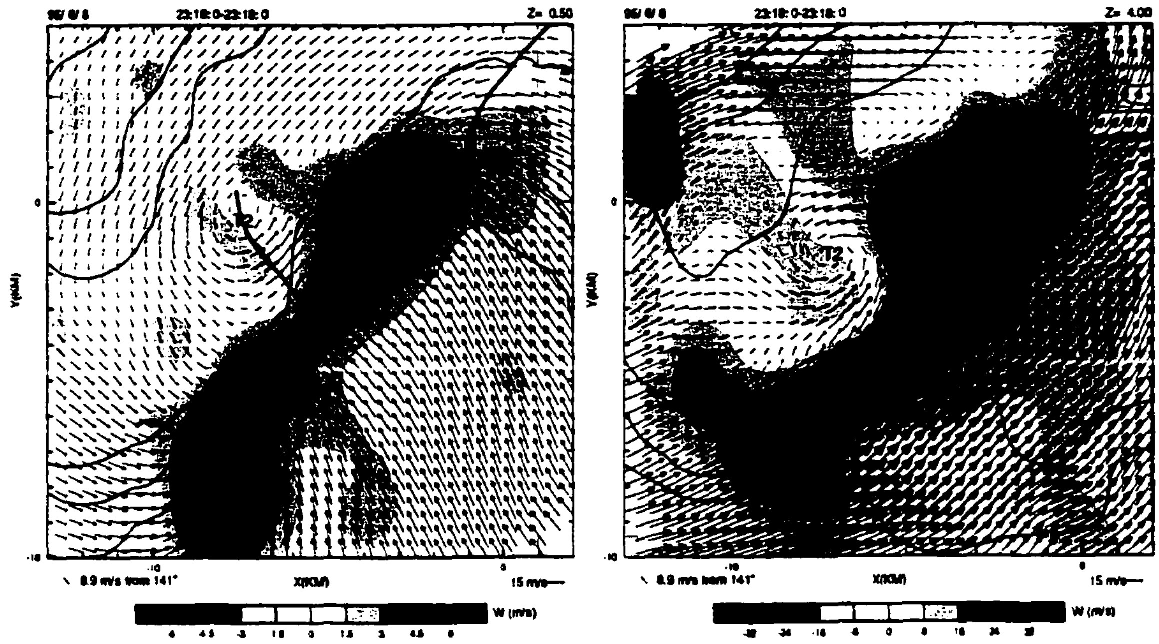

h) 2318 UTC

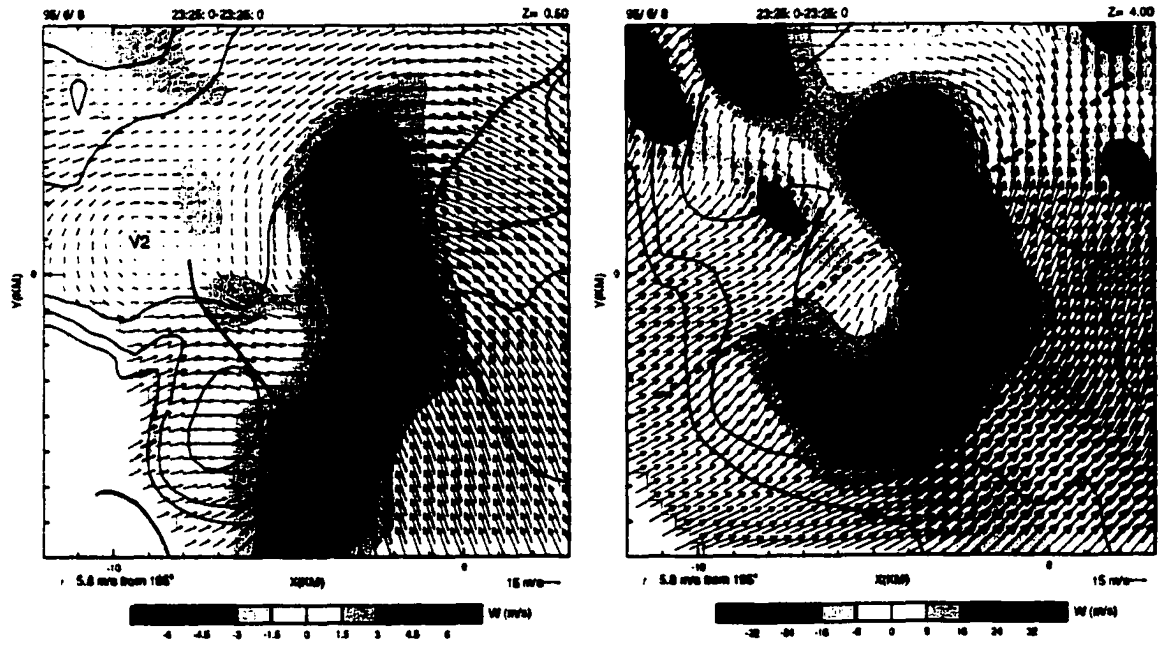

i) 2325 UTC

(Figure 3.2.6)

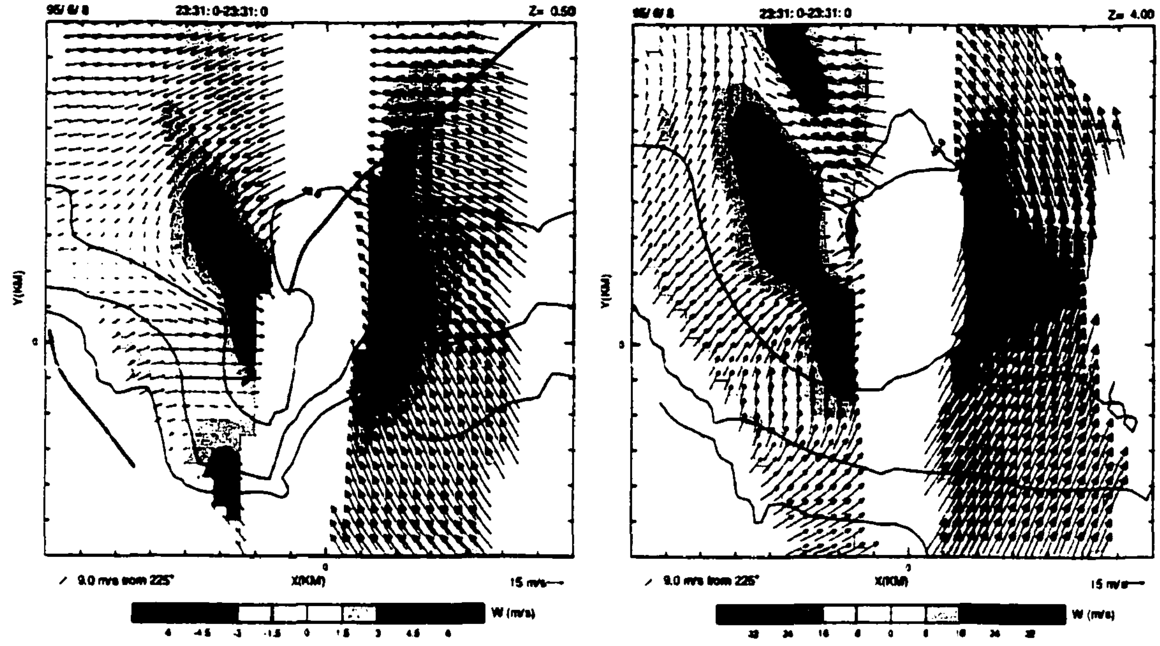

j) 2331 UTC

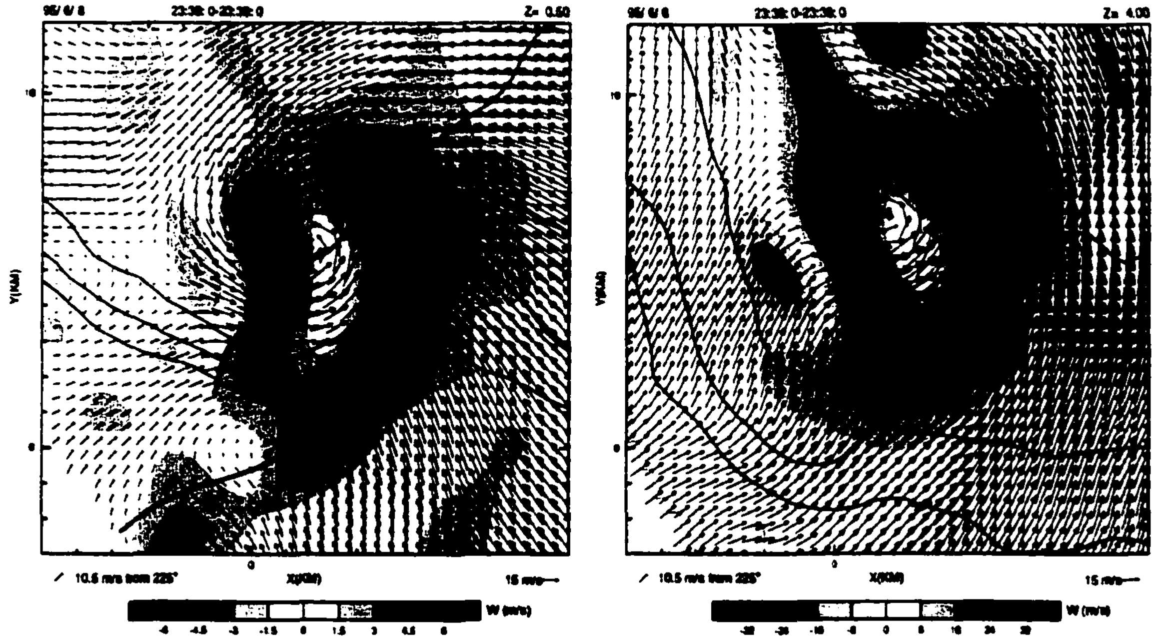

k) 2338 UTC

(Figure 3.2.6)

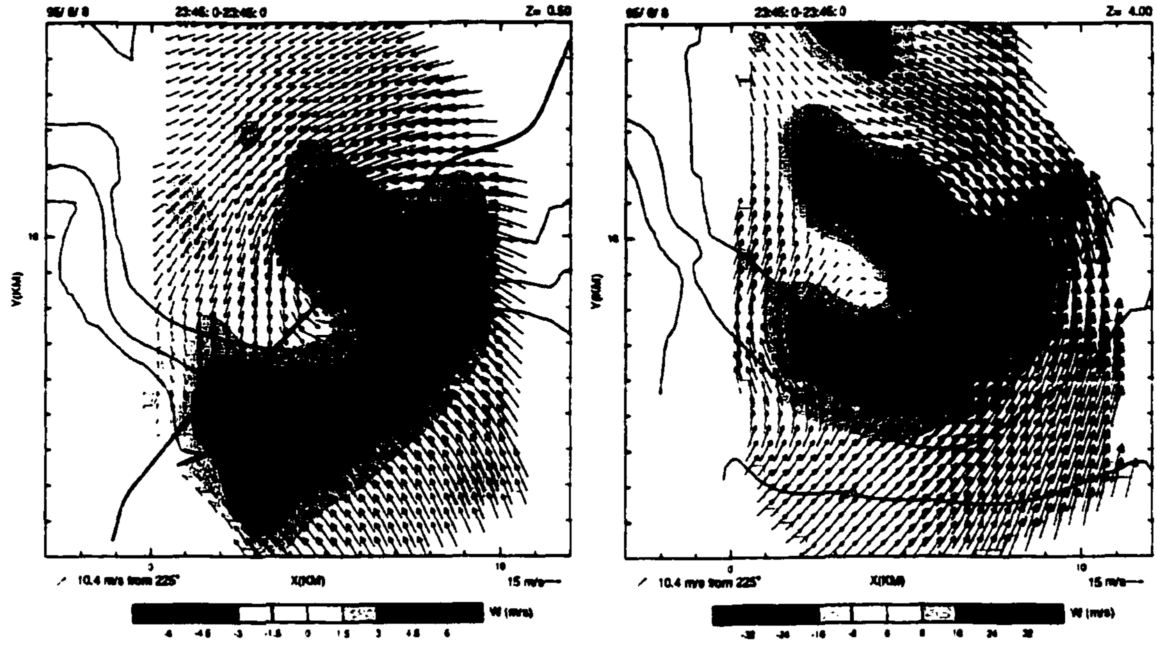

l) 2345 UTC

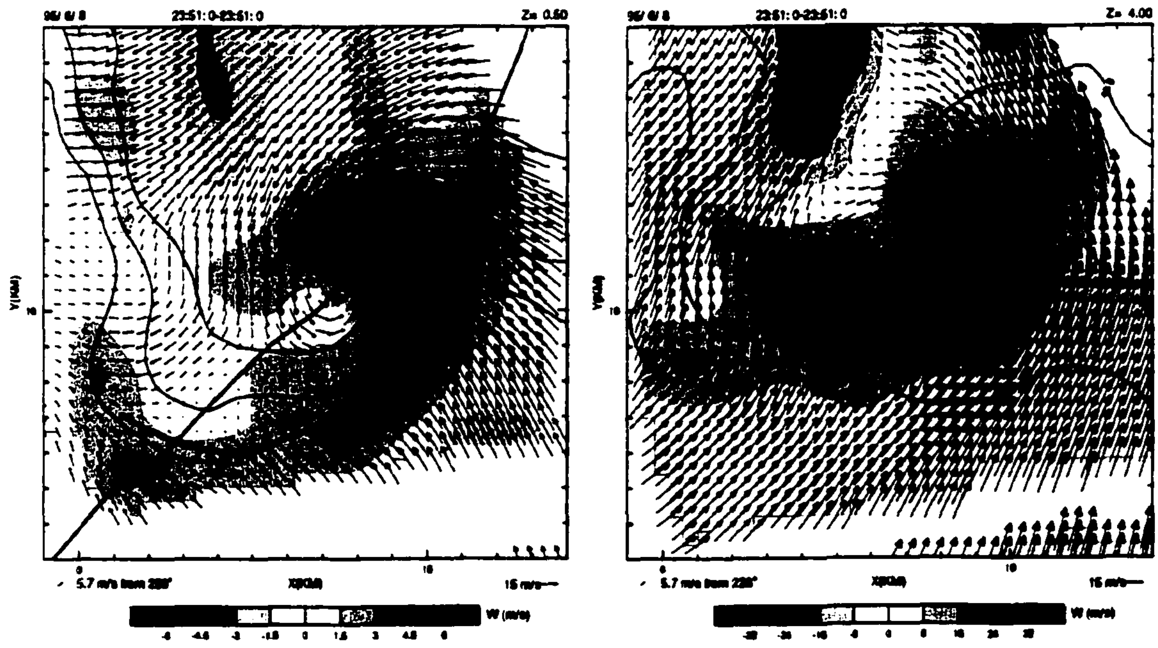

m) 2351 UTC

(Figure 3.2.6)

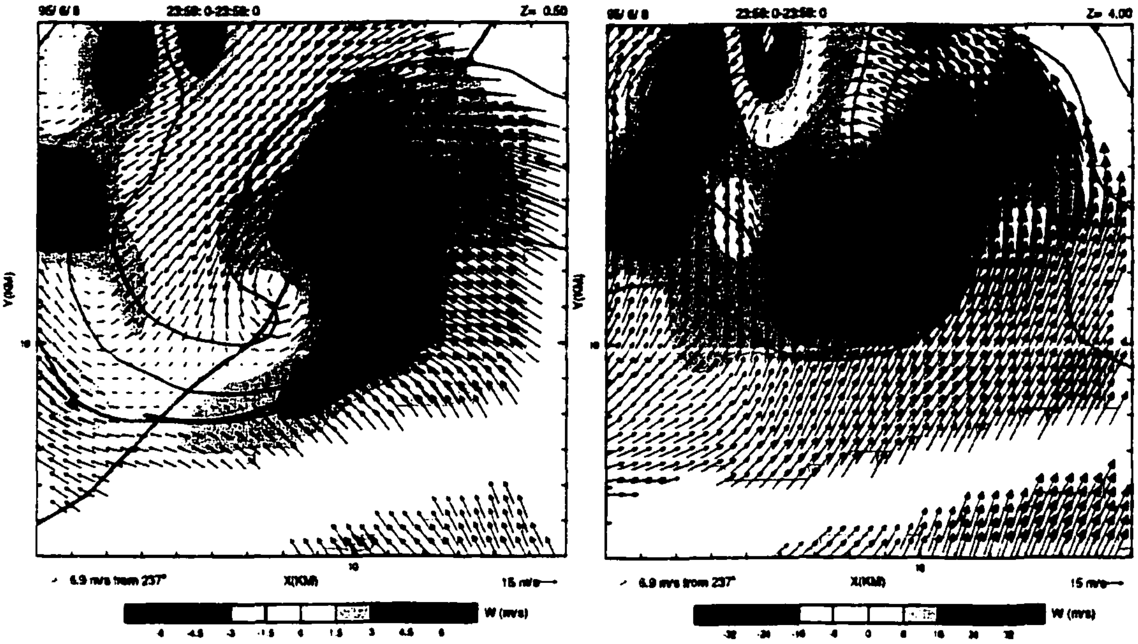

n) 2356 UTC

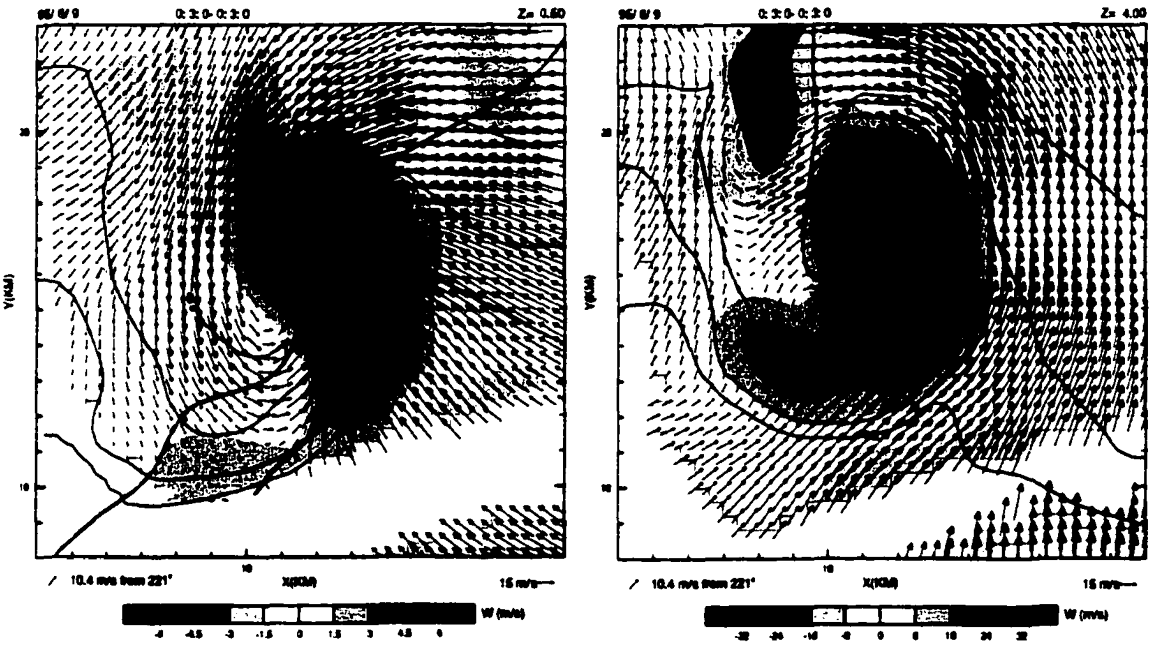

o) 0003 UTC

(Figure 3.2.6)

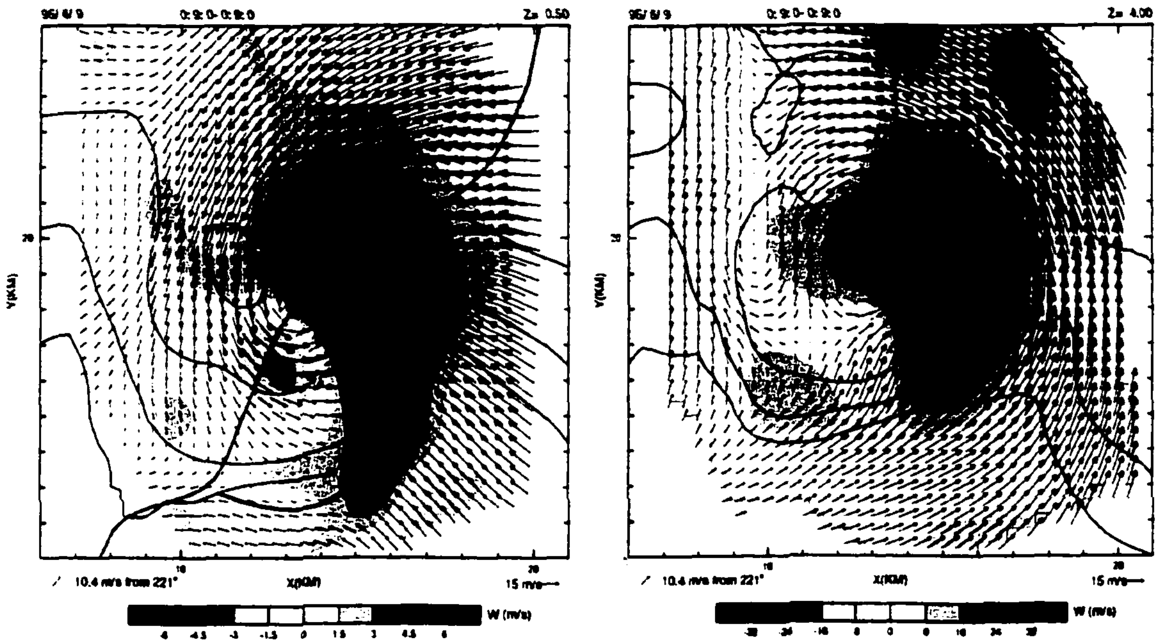

p) 0009 UTC

(Figure 3.2.6)

Figure 3.2.7. As in Fig. 3.2.6, except in vertical cross sections.

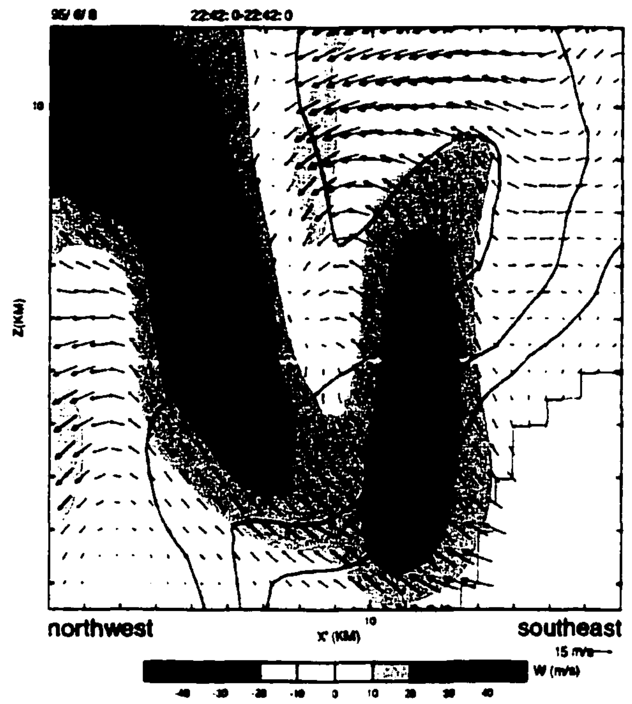

a) 2242 UTC. The location of the cross section is marked with a dashed line in Fig. 3.2.6.b.

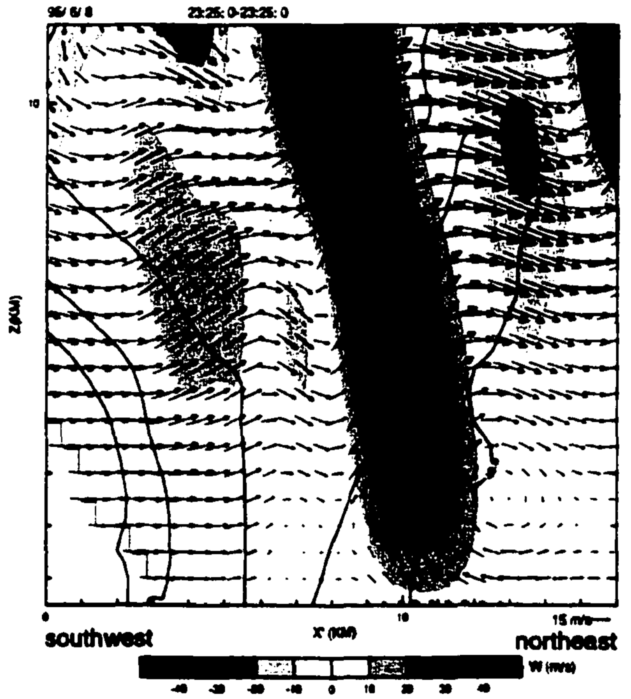

b) 2325 UTC. The location of the cross section is marked with a dashed line in Fig. 3.2.6.i.

Figure 3.2.8. Horizontal vorticity (vectors), vertical vorticity (shading at intervals of 0.005 s^{-1}), and vertical velocity (contours) at z=0.5 km AGL. Storm-relative streamlines (beginning heights in km) followed back 300 s from the vorticity maxima are shown in some of the figures in dark green. The gridded velocities were hole-filled before the calculation of the streamlines.

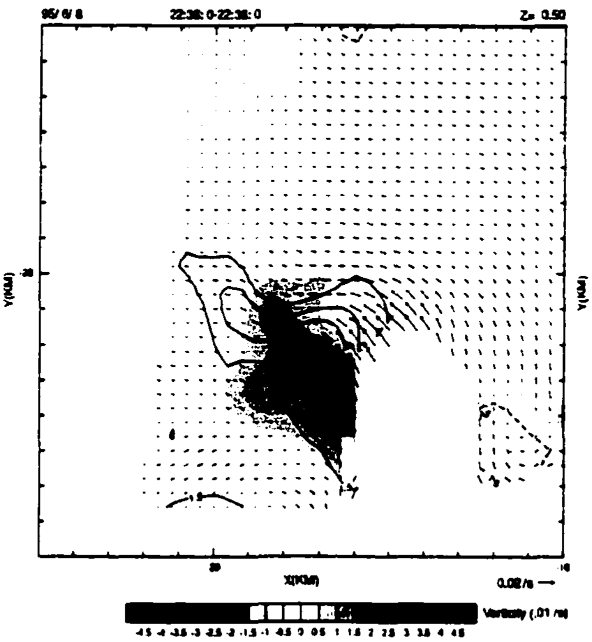

a) 2236 UTC.

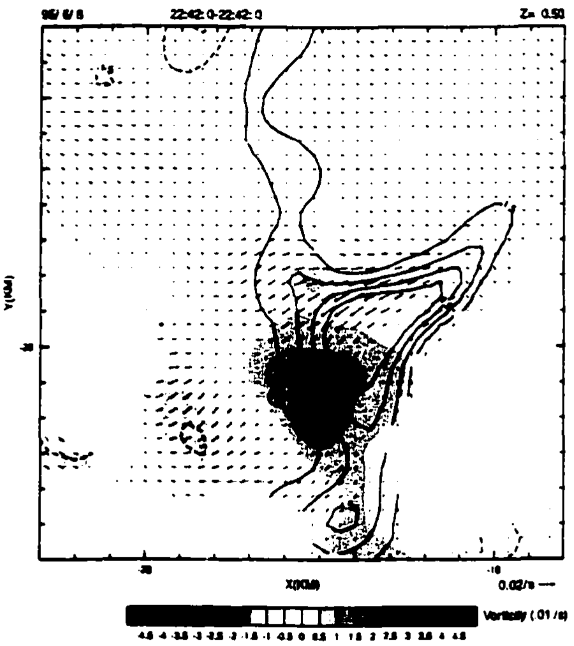

b) 2242 UTC.

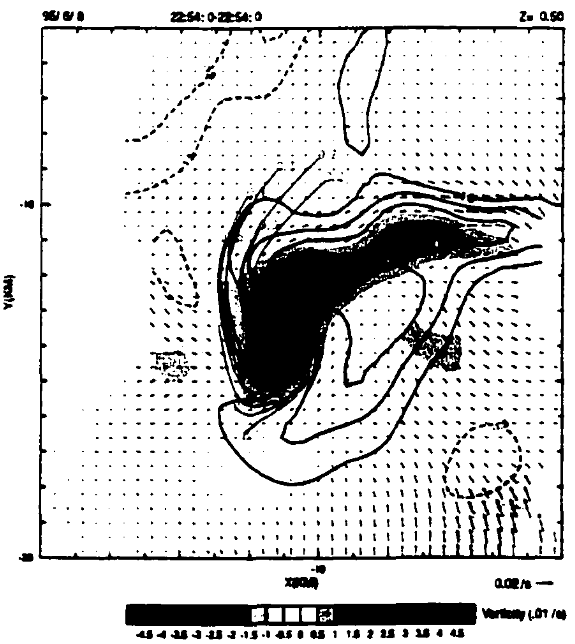

c) 2254 UTC.

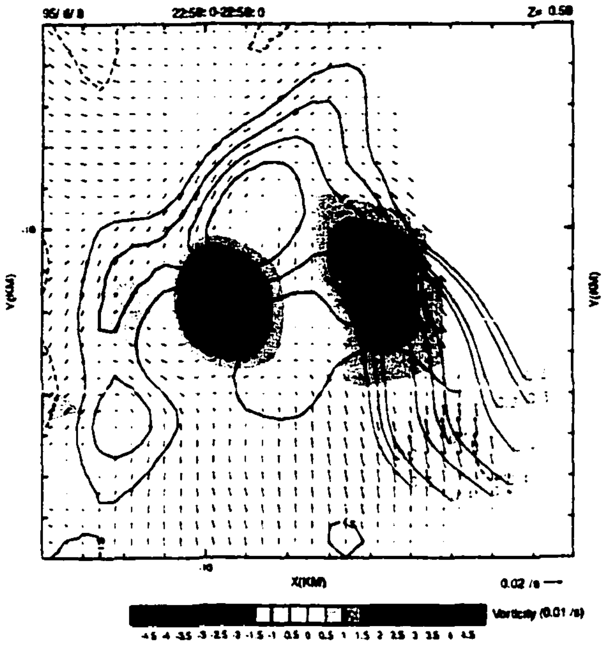

d) 2259 UTC.

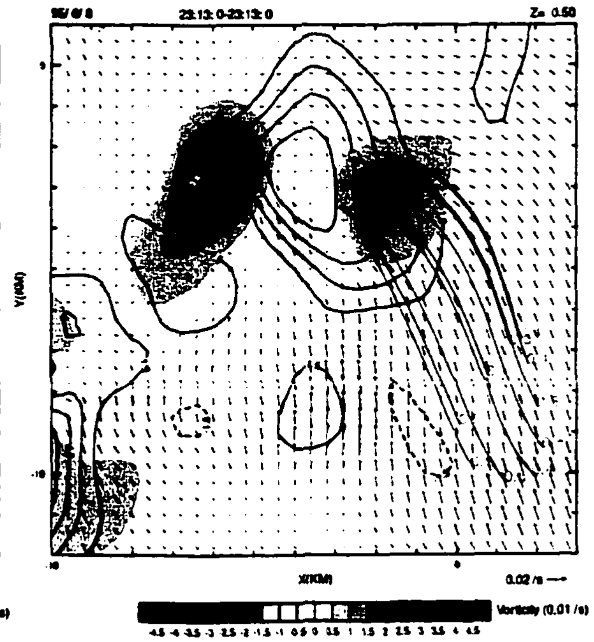

e) 2313 UTC.

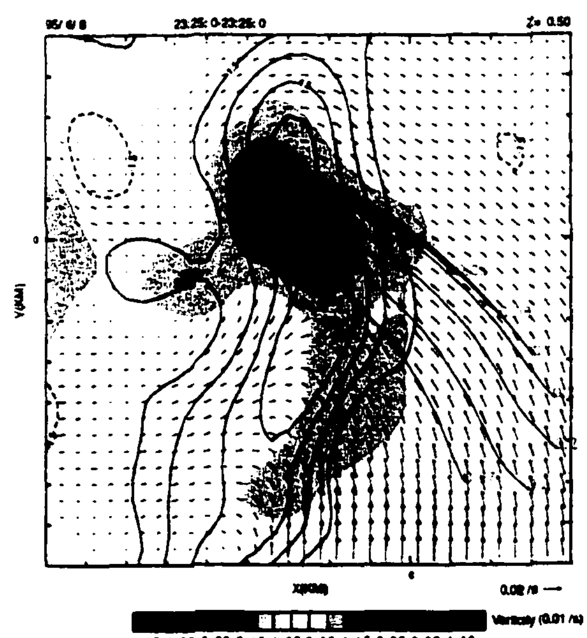

f) 2325 UTC.

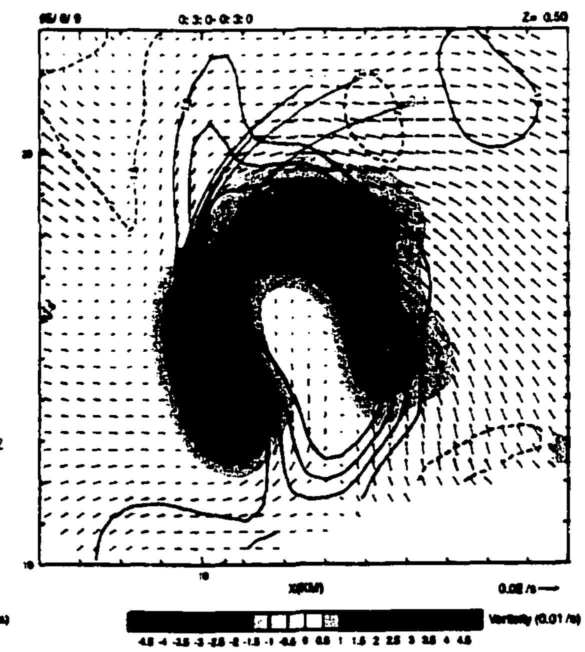

g) 0003 UTC.

Figure 3.2.9. Updraft characteristics in the pseudo-dual-Doppler analyses of the main storm updraft, as a function of time and height. The intervals when the tornado condensation funnels were observed are noted.

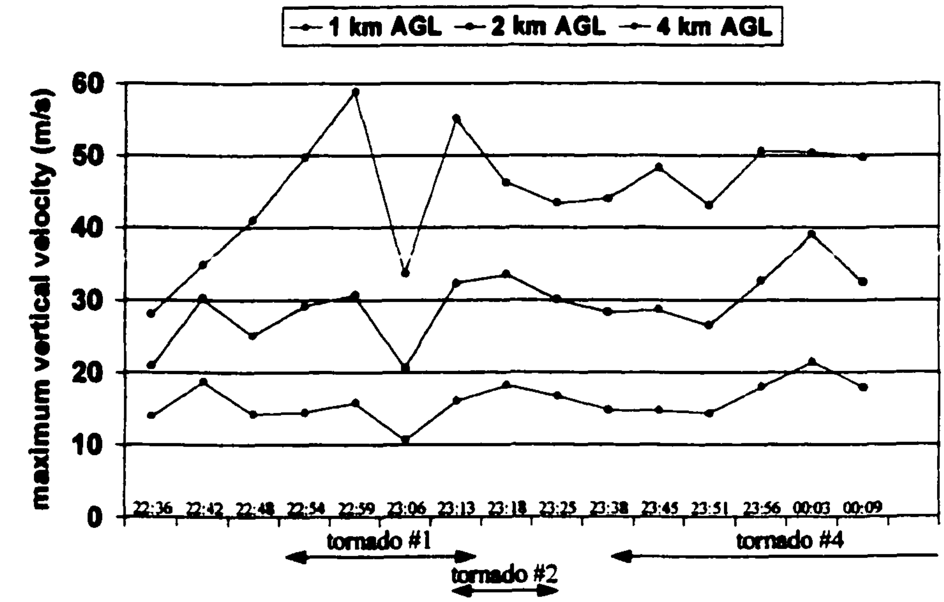

a) Maximum vertical velocity within the updraft.

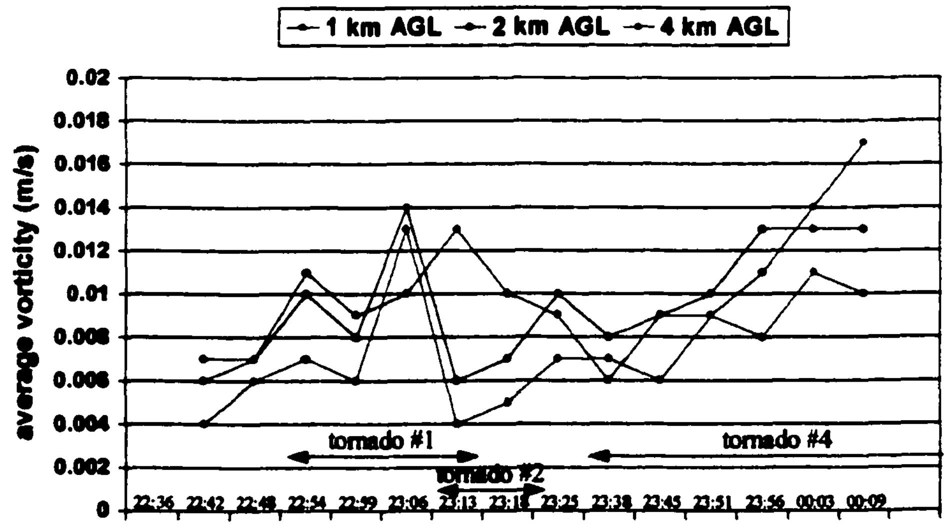

b) Average vertical vorticity within the updraft. The updraft regions at 1.0, 2.0, and 4.0 km AGL are defined as those regions enclosed by the 6.0, 12.0, and 16.0 m s^{-1} vertical velocity contours, respectively

Figure 3.2.10. Storm-relative wind (vectors), vertical velocity (contours), and retrieved dynamic vertical perturbation pressure gradient ($\partial p_{dn} / \partial z$) (shading) at 2254 UTC at z=1.0 km AGL. Red (blue) shading indicates upward (downward) acceleration.

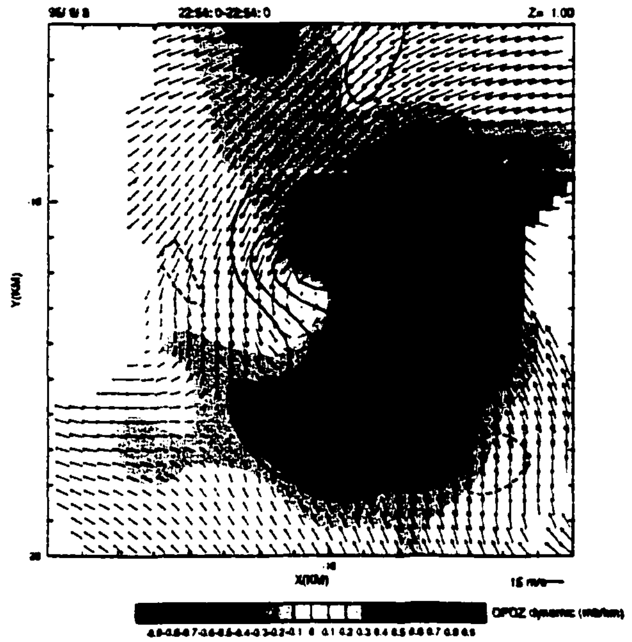

Figure 3.2.11. Average vertical vorticity (in 0.01 s^{-1}) as a function of height (left, in km) and radius (bottom, in km) in the vortex wind syntheses. Vorticity was computed as circulation divided by area for a circle around the vortex center. The vortex center was that location which yielded the maximum circulation for a circle of radius 1.0 km.

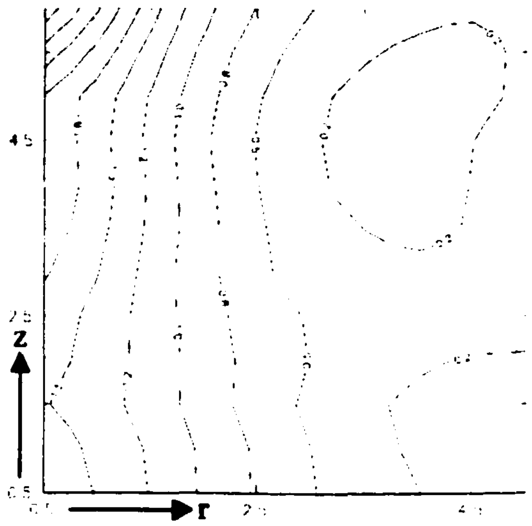

a) Pre-tornadic parent vortex of tornado #1 at 2242 UTC.

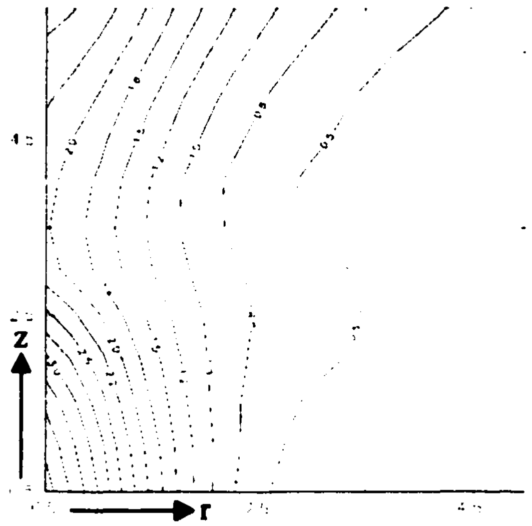

b) Tornado #1 at 2259 UTC.

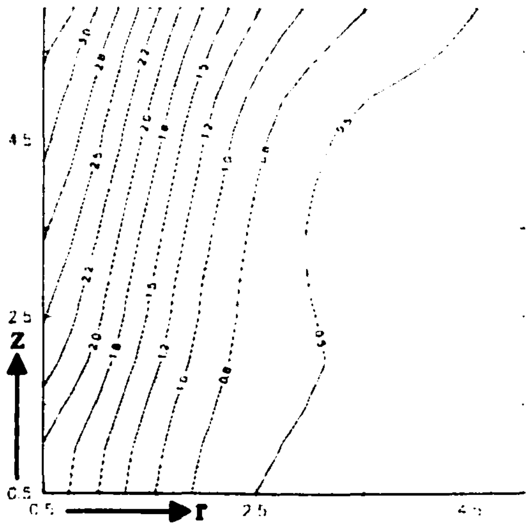

c) Weakening tornado #1 at 2306 UTC.

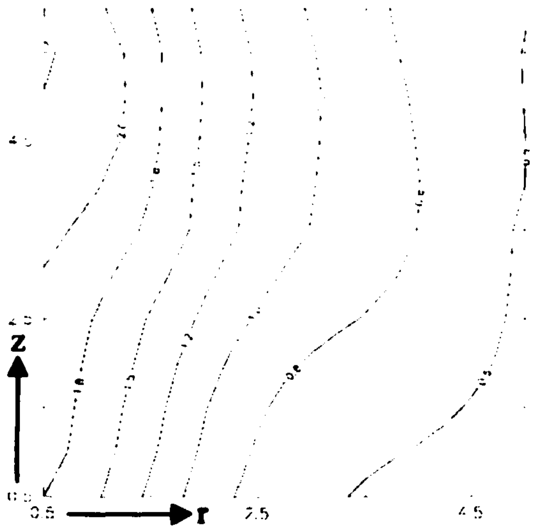

d) Pre-tornadic parent vortex of tornado #2 at 2259 UTC.

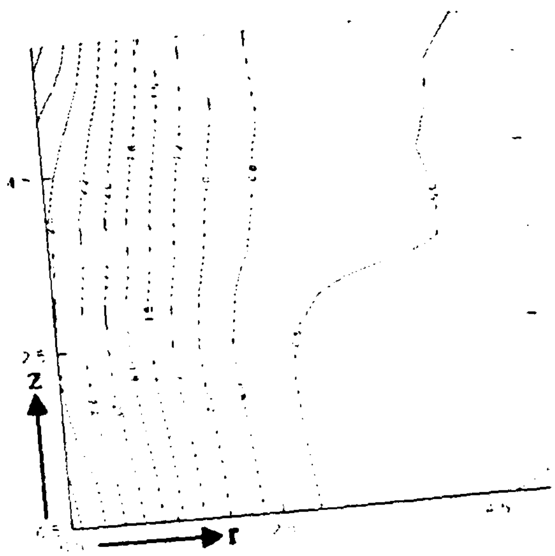

e) Tornado #2 at 2313 UTC.

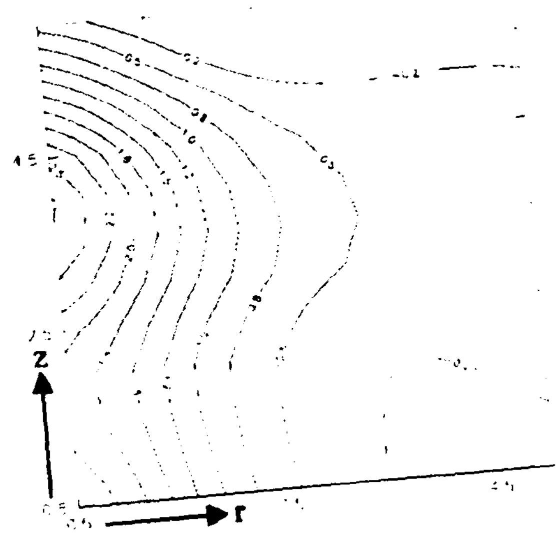

f) Weakening tornado #2 at 2318 UTC.

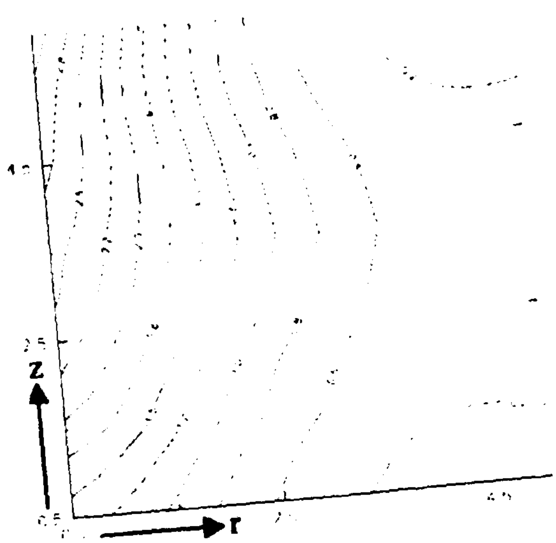

g) Pre-tornadic parent vortex of tornado #4 at 2318 UTC.

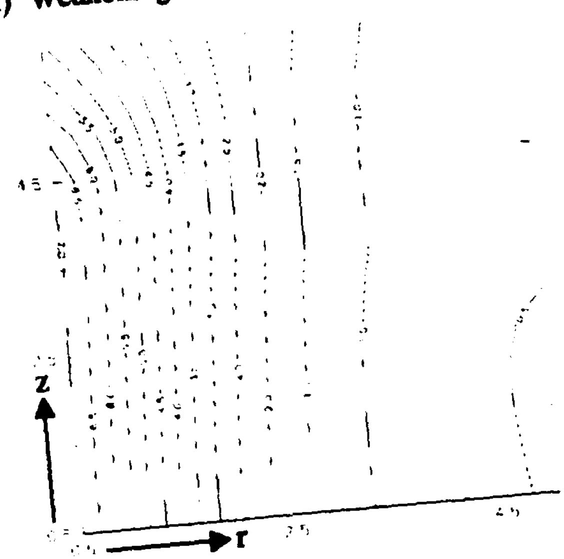

h) Tornado #4 at 2338 UTC.

(Figure 3.2.11)

Figure 3.2.12. Horizontal vorticity (vectors) and vertical velocity.

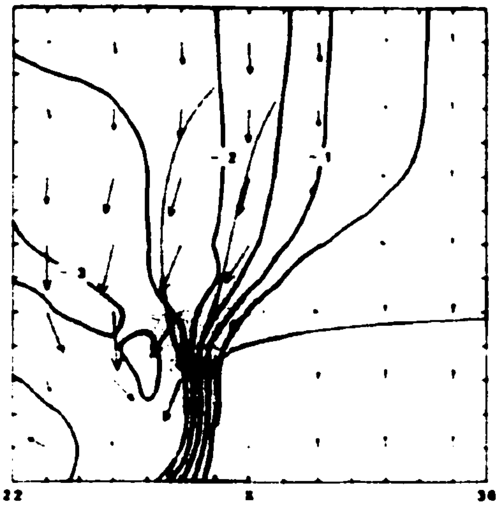

a) Numerical simulation of a supercell (from Rotunno and Klemp 1985, courtesy of the American Meteorological Society) at z=250 m. The updraft is shaded at w increments of 1 m s^{-1}. Buoyancy contours (interval of 0.05 m s^{-2}) are also shown. The maximum magnitude of horizontal vorticity in this image is approximately 0.025 s^{-1}.

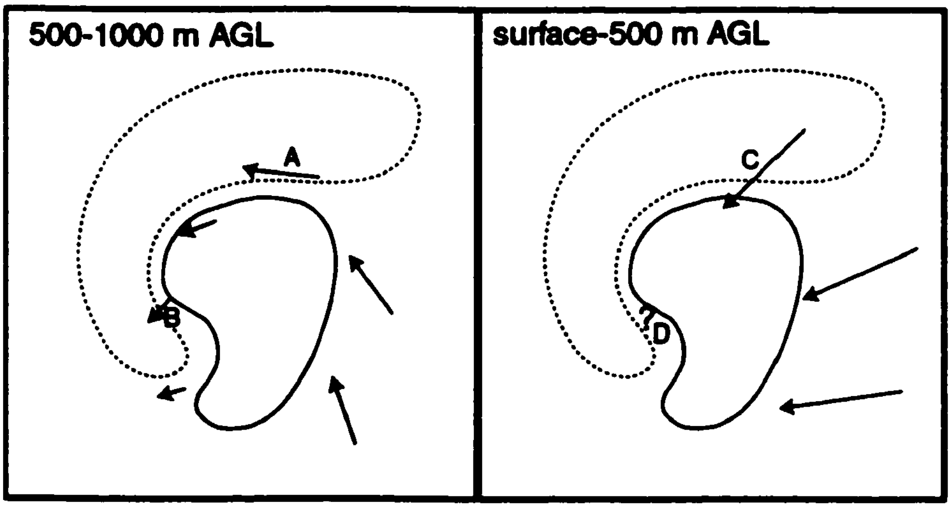

b) Example of the low-level structure in the McLean storm. The solid and dashed curves indicate the locations of the updraft and downdraft, respectively. The right panel is based on a comparison of mobile mesonet observations at the surface to ELDORA pseudo-dual-Doppler winds at 500 m AGL; the left panel is based entirely on ELDORA data. The maximum magnitude of horizontal vorticity is approximately 0.04 s^{-1} (in the right panel). The horizontal vorticity characteristics near "D" are unknown.

Figure 3.2.13. Composite images (courtesy of Paul Markowski) of mobile mesonet observations, reflectivity from the P-3 lower fuselage radar, and reflectivity from the Doppler on Wheels (inset). The positions of the mobile mesonet observations are based on time-to-space conversion. In these observations, temperature (tenths of °C, with decimal removed) is in the upper left, dewpoint (tenths of °C, with decimal removed) is at the lower left, and equivalent potential temperature (K) is at the upper right. Winds are storm-relative, and full wind barbs represent 10 kt (≈5 m s^{-1}). For these images, storm motion is 10.0 m s^{-1} from 220°. The location of tornado #4 is marked with a "T".

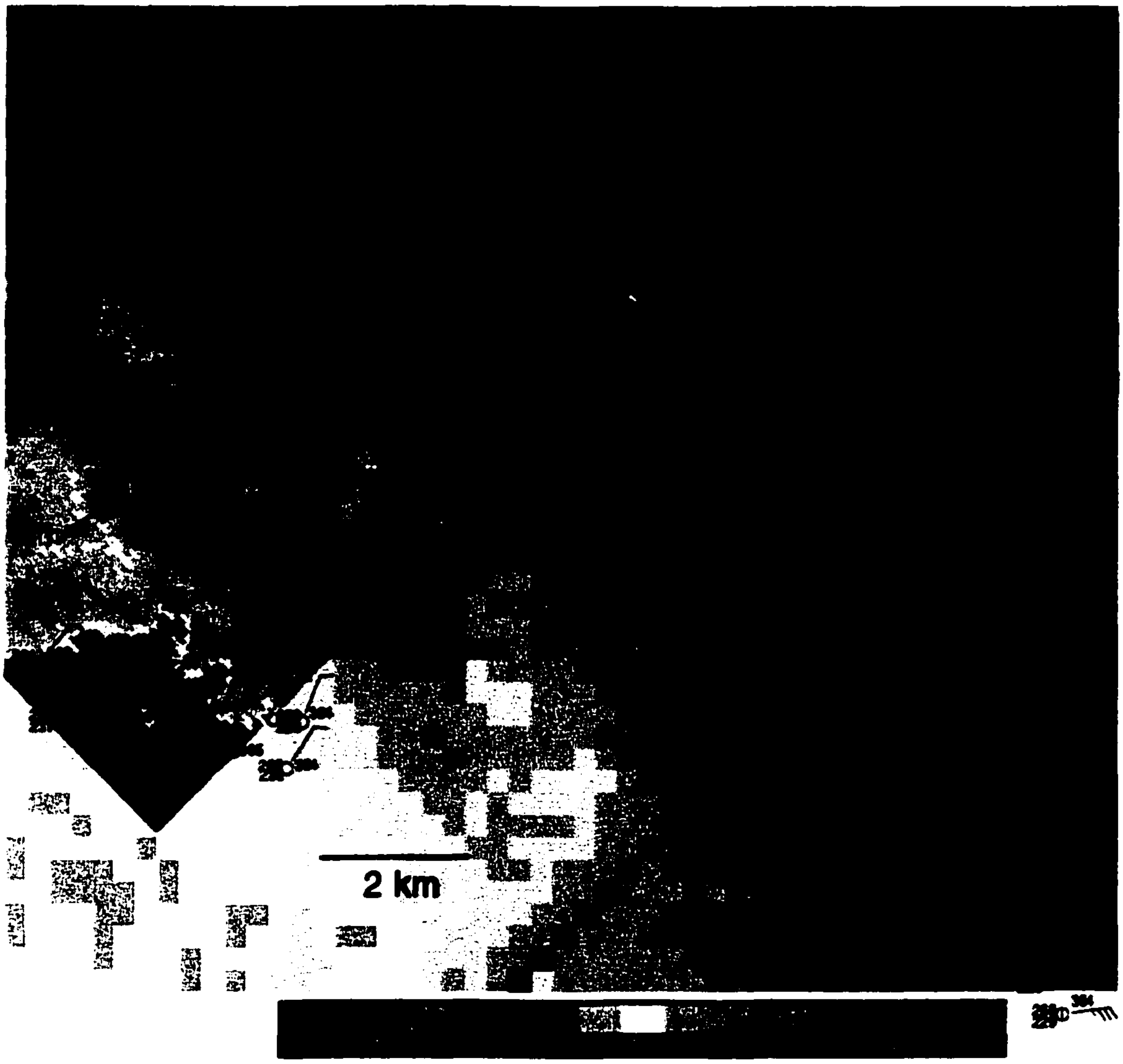

a) 0017 UTC 9 June 1995.

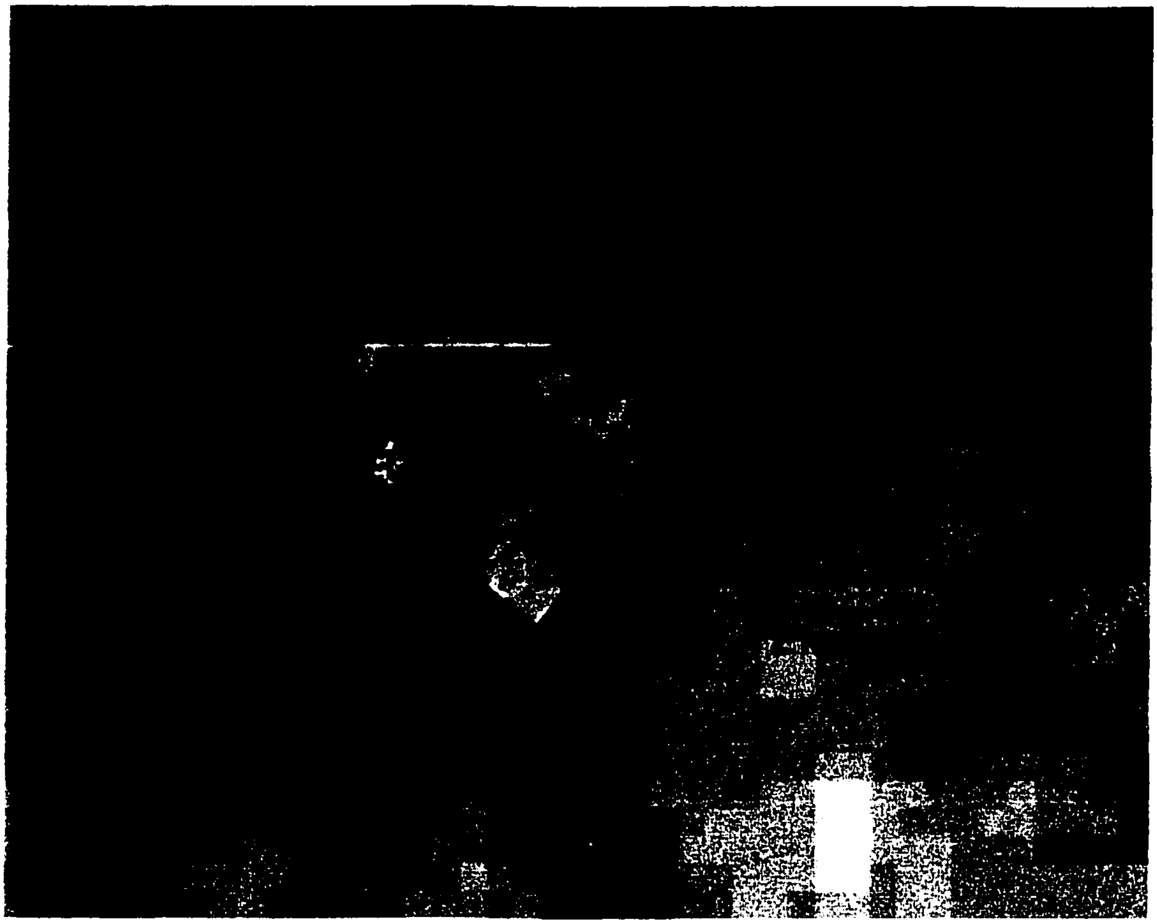

b) 0022 UTC 9 June 1995.

Figure 3.2.14. Magnitude of terms in the vertical vorticity equation in the dual-Doppler analyses of the McLean storm at z=0.5 km AGL. Horizontal storm-relative winds (vectors) and vertical velocity (contours) are also plotted.

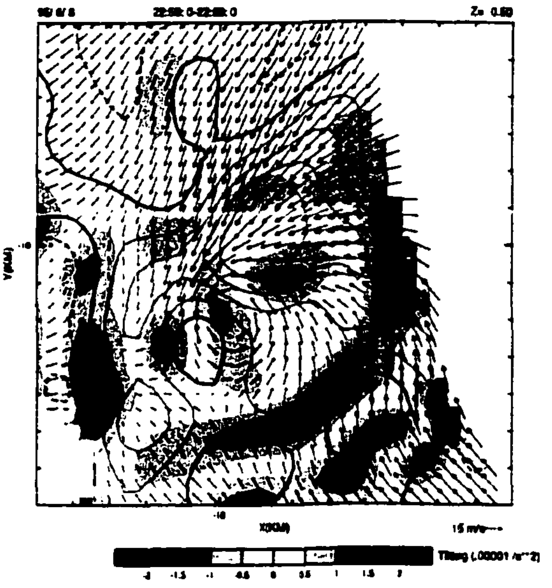

a) Tilting (shading at intervals of 5×10^{-6} s^{-2}) at 2259 UTC.

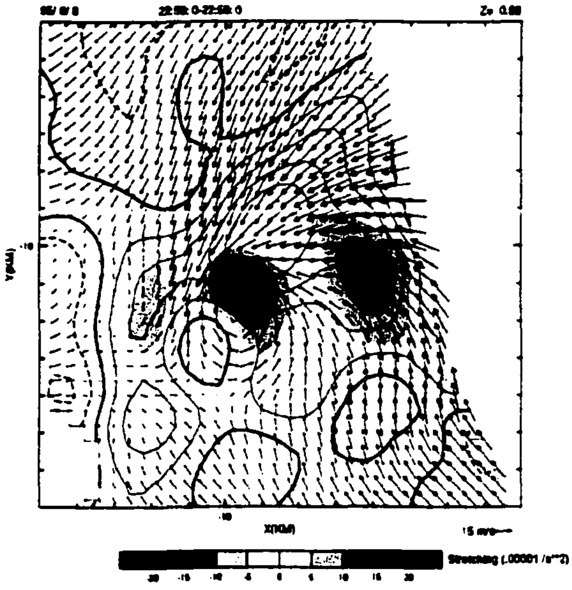

b) Stretching (shading at intervals of 5×10^{-5} s^{-2}) at 2259 UTC.

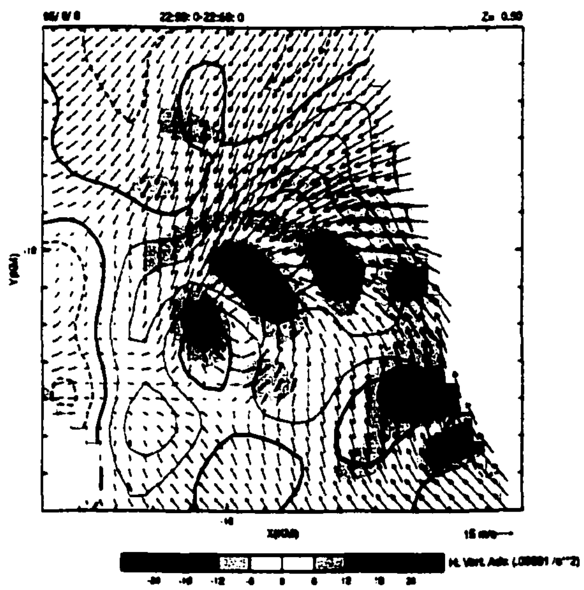

c) Advection of vorticity by the updraft-relative horizontal wind (shading at intervals of 6×10^{-5} s^{-2}) at 2259 UTC.

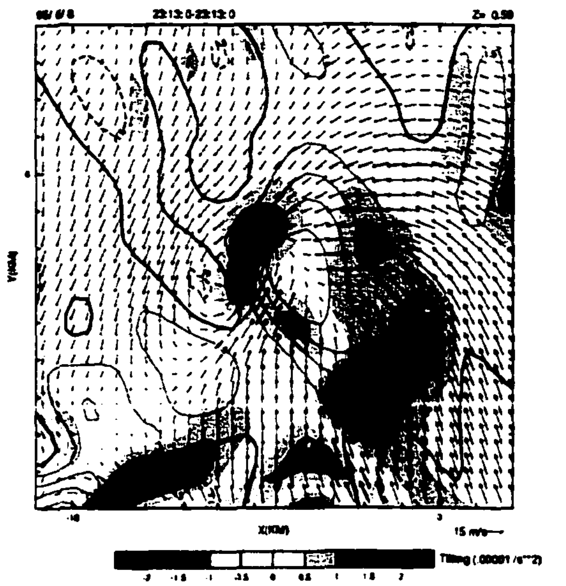

d) Tilting (shading at intervals of $5\times10^{-6}\ s^{-2}$) at 2313 UTC.

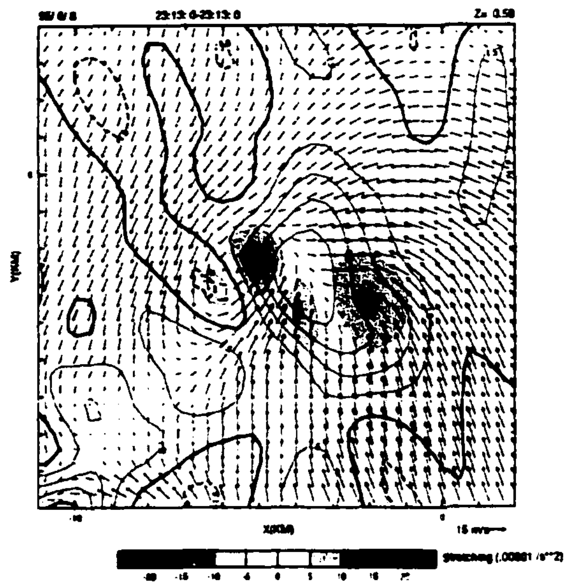

e) Stretching (shading at intervals of $5\times10^{-5}\ s^{-2}$) at 2313 UTC.

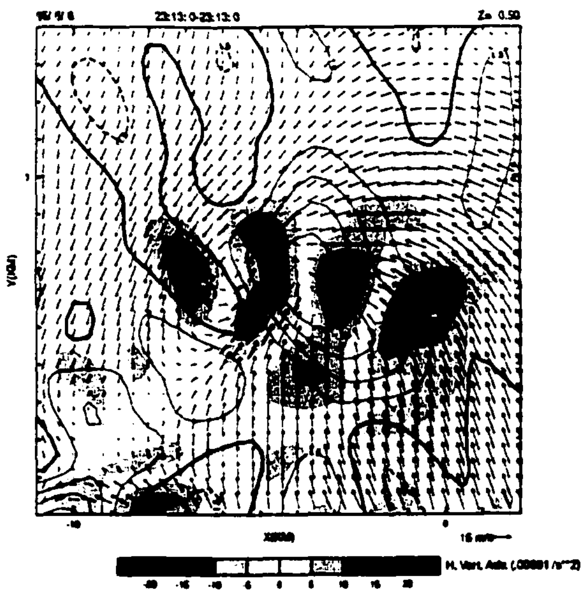

f) Advection of vorticity by the updraft-relative horizontal wind (shading at intervals of $5\times10^{-5}\ s^{-2}$) at 2313 UTC.

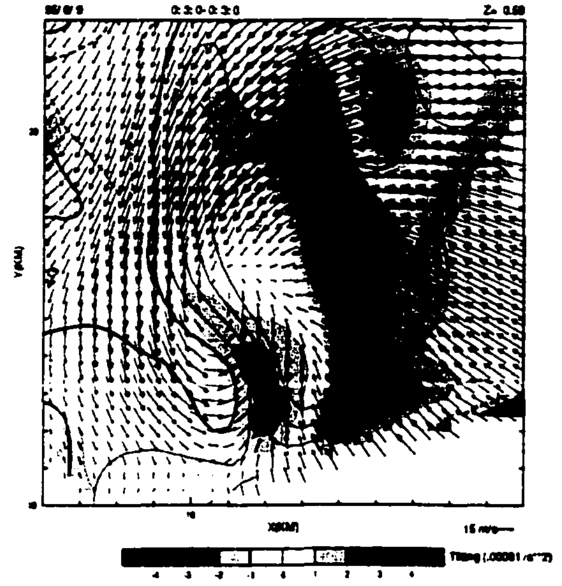

g) Tilting (shading at intervals of $1\times10^{-5}\ s^{-2}$) at 0003 UTC.

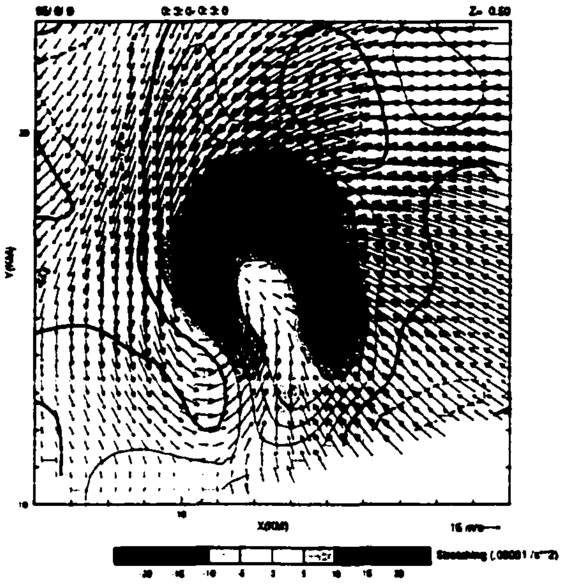

h) Stretching (shading at intervals of $5\times10^{-5}\ s^{-2}$) at 0003 UTC.

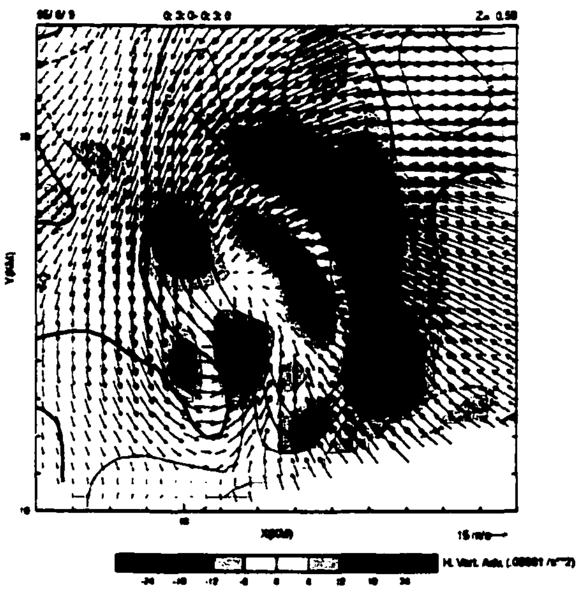

i) Advection of vorticity by the updraft-relative horizontal wind (shading at intervals of $6\times10^{-5}\ s^{-2}$) at 0003 UTC.

Figure 3.2.15. As in Fig. 3.2.6, except with ground-relative horizontal winds.

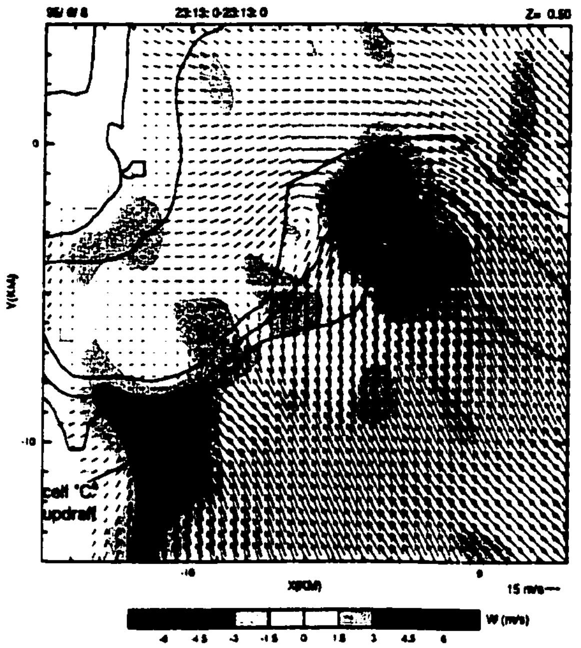

a) 2313 UTC.

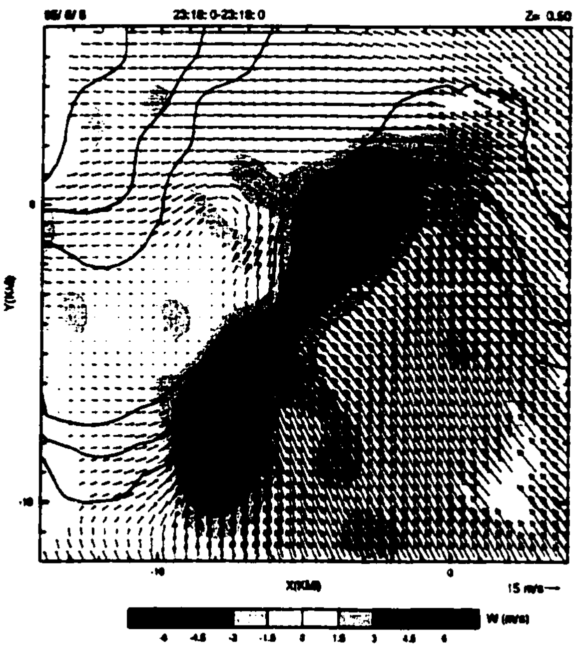

b) 2318 UTC.

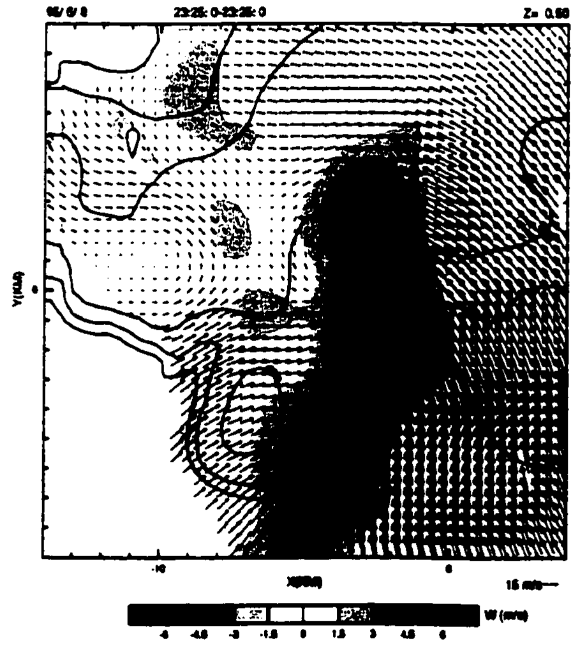

c) 2325 UTC.

d) 2338 UTC.

Figure 3.2.16. Circulation (km^2 s^{-1}) at 500 m AGL as a function of radius (km) from the center of the analyzed vorticity maxima. The calculations are centered on T1 at 2259 (Fig. 3.2.6.e), T2 at 2313 (Fig. 3.2.6.g), V4 at 2325 (Fig. 3.2.6.i), and T4 at 2338, 2356, and 0009 UTC (Fig. 3.2.6.k., 3.2.6.n, and 3.2.6.p).

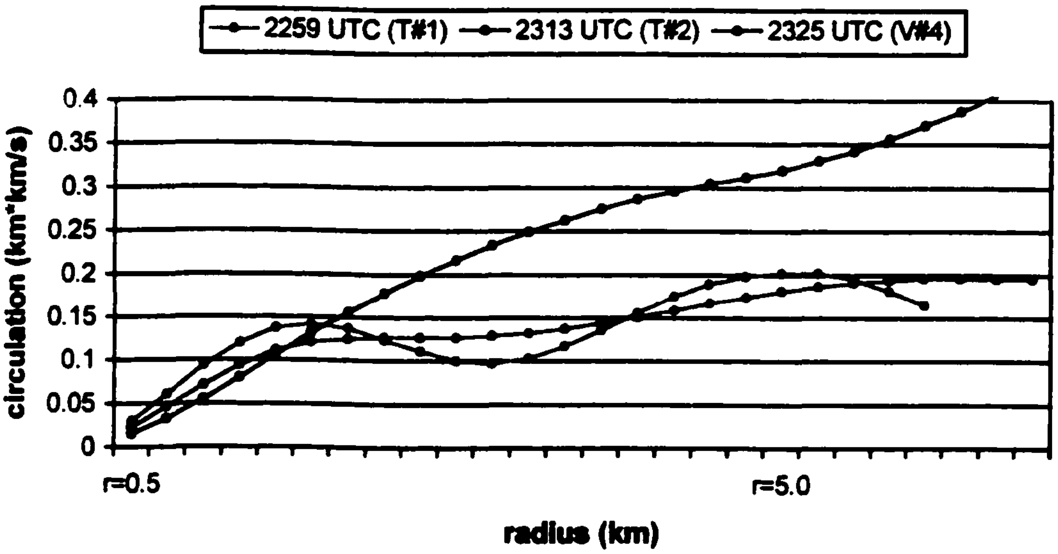

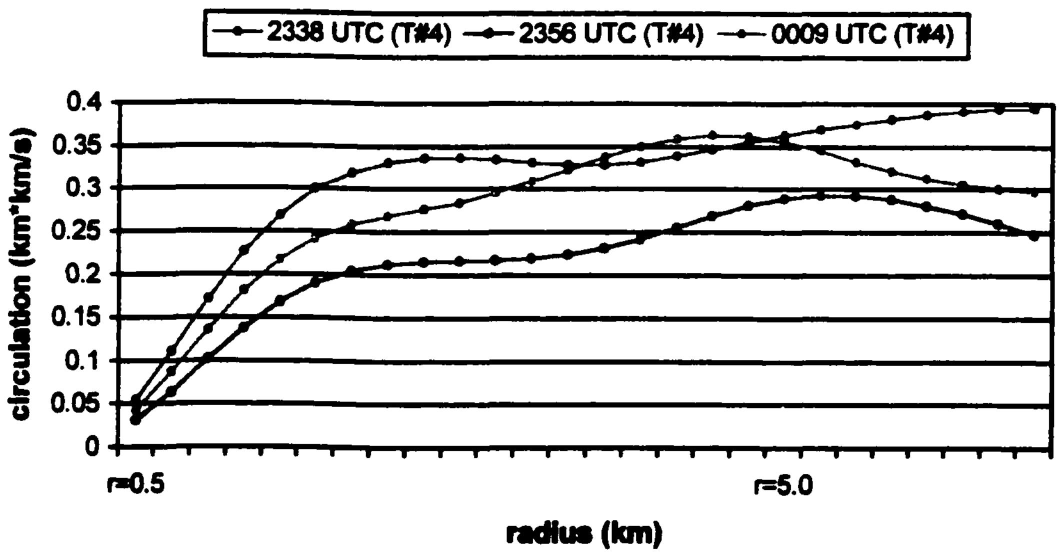

Figure 3.2.17. As in Fig. 3.2.10 (retrieved dynamic vertical perturbation pressure gradient, except at 2338 UTC at z=2.0 km AGL. Red (blue) shading indicates upward (downward) acceleration.

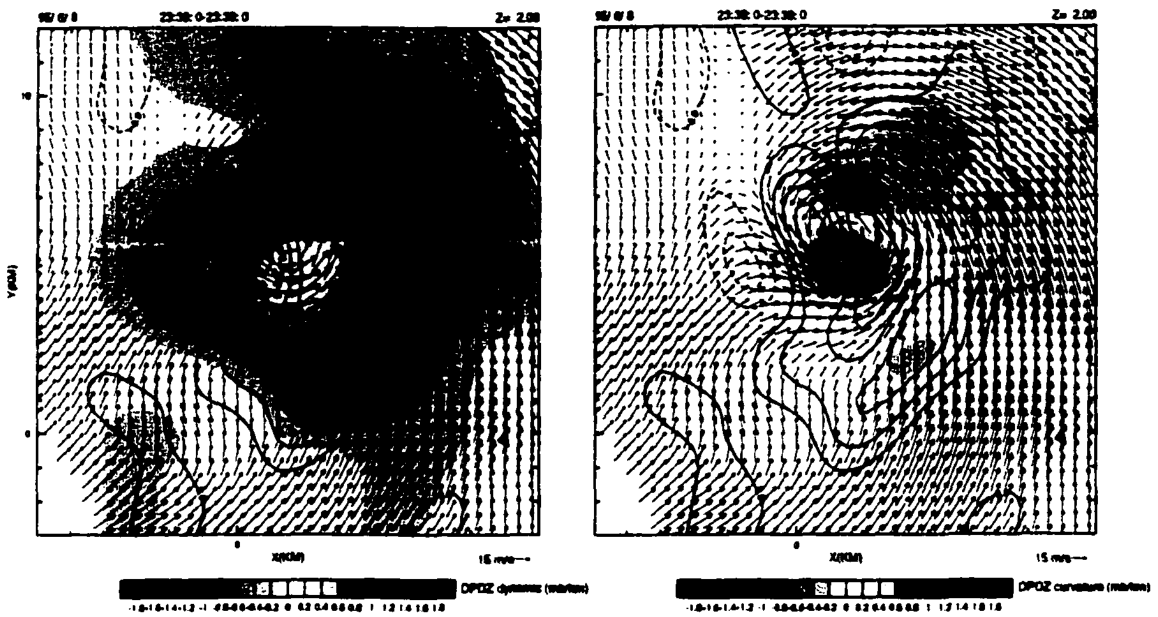

a) Total dynamic vertical pressure gradient $(\partial p_{dn} / \partial z)$.

b) Contribution from the horizontal curvature term $(\partial p_c / \partial z)$.

Figure 3.3.1. Conceptual model of a mesocyclone containing two long-lived tornado parent vortices (from Snow and Agee 1975).

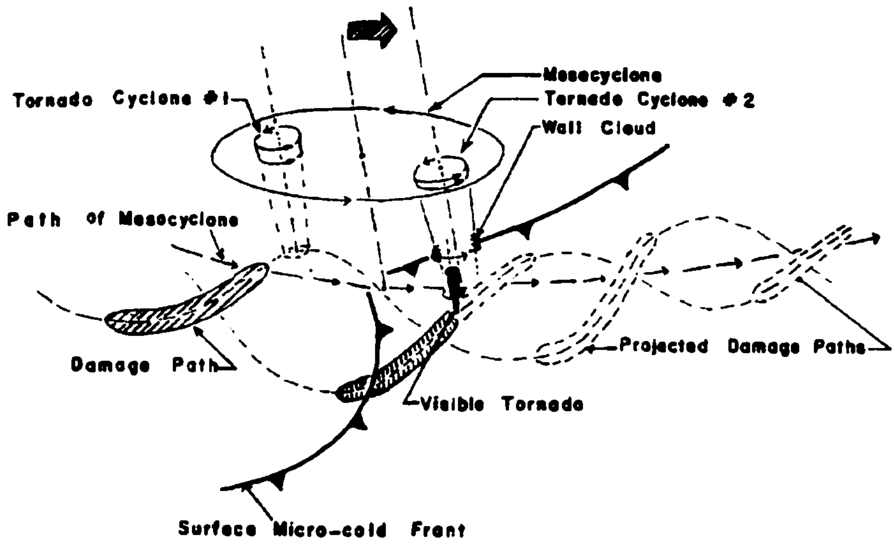

Figure 3.3.2. Photograph (copyright by Steve Gaddy) of tornadoes near Tahoka, Texas at 0056 UTC 11 April 1997. The view is toward the north. The third, fifth, and sixth tornadoes that the storm produced are numbered.

Figure 3.3.3. Conceptual model of cyclic mesocyclone core evolution (from Burgess et al. 1982). Thick lines represent forward-flank and rear-flank wind discontinuities, and tornado tracks are shaded. The inset square in the lower right shows the resulting tracks of the tornado family.

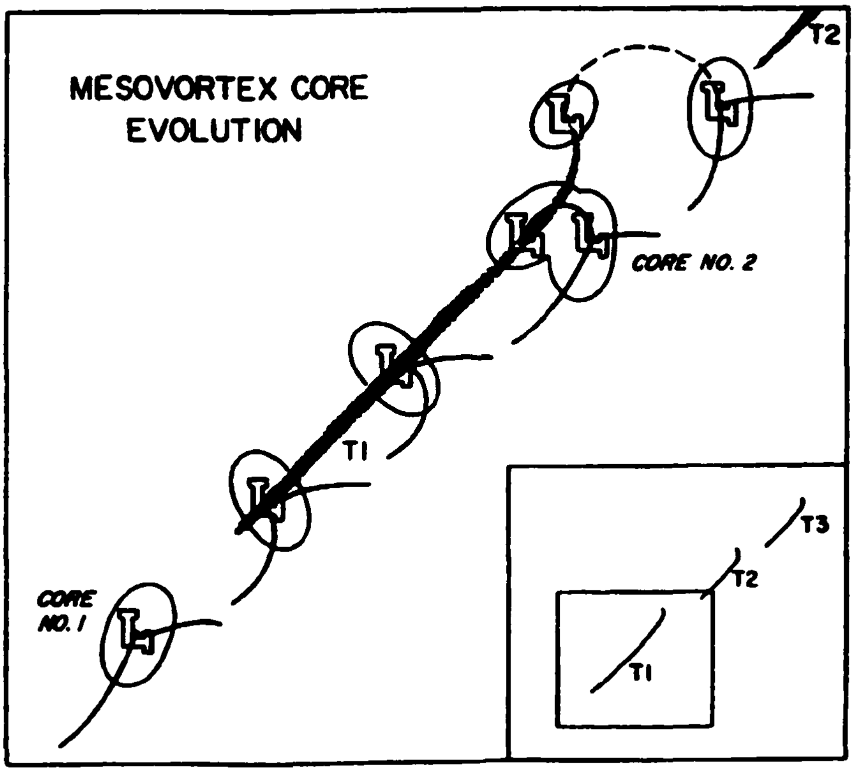

Figure 3.3.4. Vertical velocity (contours, with negative values dashed) in a numerical simulation of cyclic vortex formation (from Adlerman et al. 1999, courtesy of the American Meteorological Society). The cold front notation marks the edge of the surface cold pool (-1 K potential temperature perturbation). The dark outline is an isoline of 1 g kg^{-1} mixing ratio of rainwater. Heavy dashed lines enclose regions where the vertical vorticity is greater than 0.01 s^{-1}.

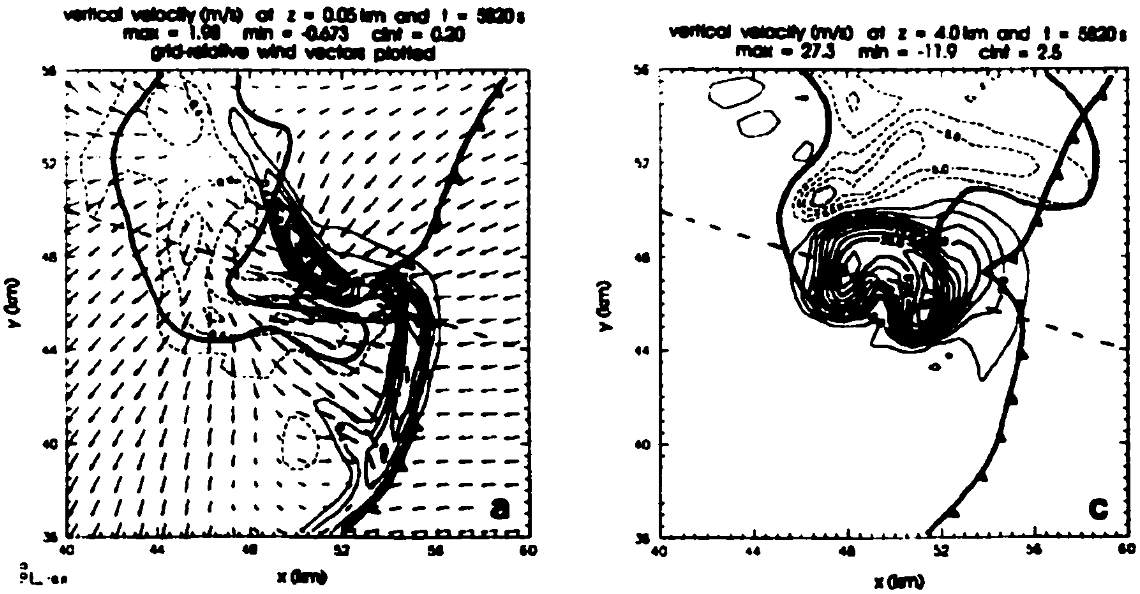

a) Horizontal cross sections at 50 m AGL (left, with horizontal wind vectors shown) and 4 km AGL (right) at t=5280 s.

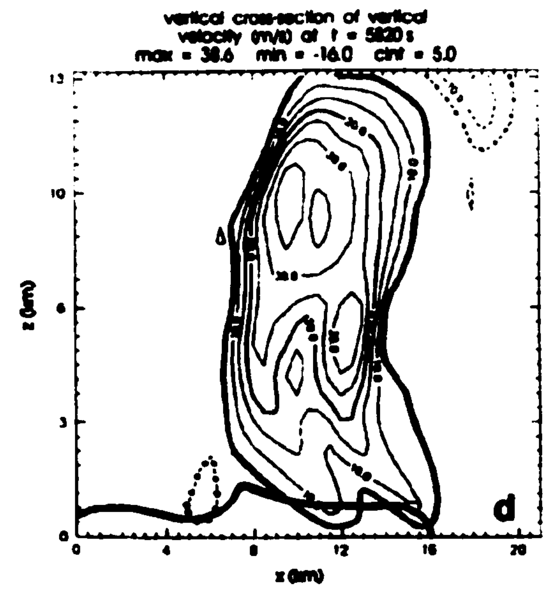

b) Vertical cross section at t=5280 s. The location of the slice is indicated by the dashed line in a).

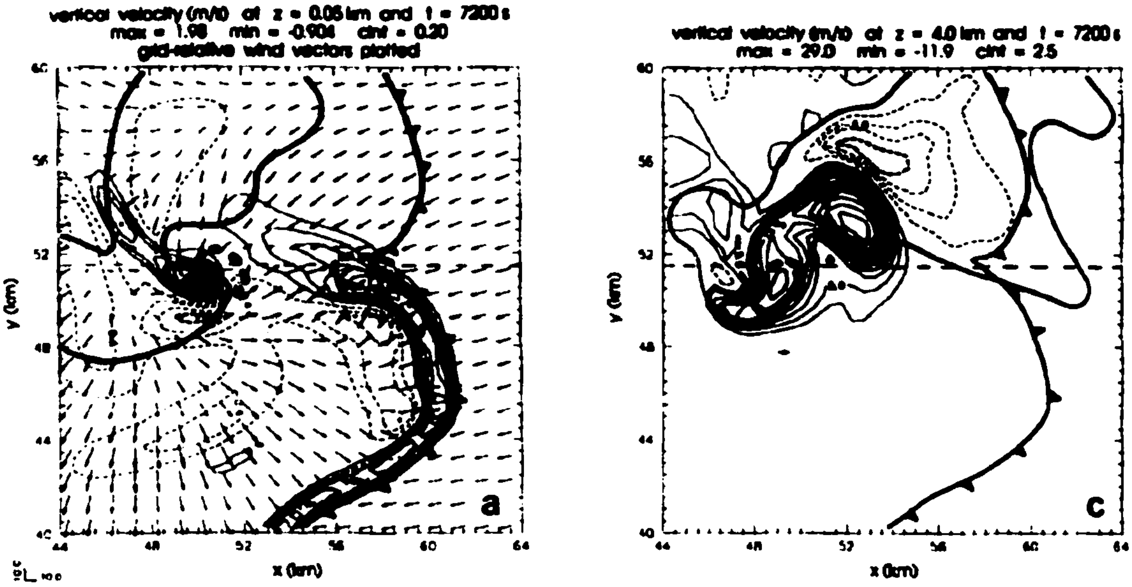

c) As in a), except at t=7200 s.

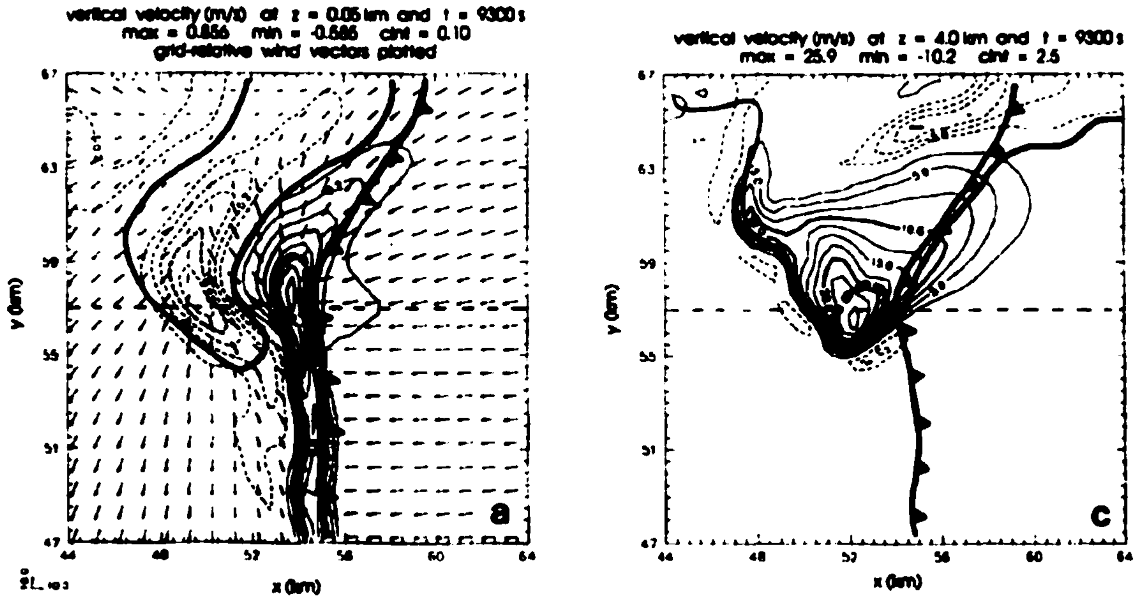

d) As in a), except at t=9300 s.

Figure 3.3.5. Images of a cyclonic-anticyclonic tornado pair in the Grand Island, Nebraska storm on 3 June 1980 (from Fujita and Wakimoto 1982). The left panel is from the Grand Island WSR-57 display, and the right panel depicts the low-level wind flow.

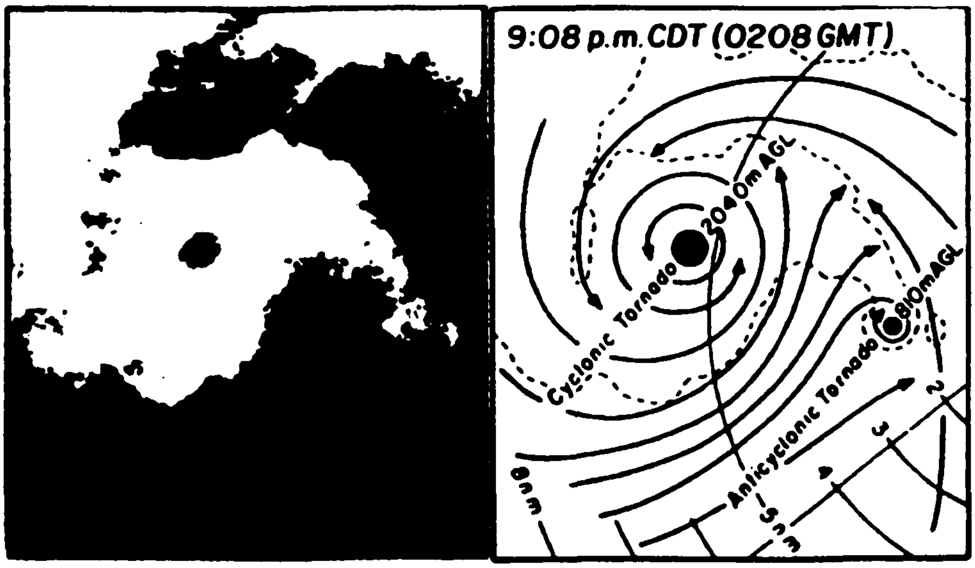

Figure 3.3.6. Schematic of cyclic tornado formation in the McLean storm. The irregular shape indicates the location of the main low-level updraft. A filled triangle indicates the location of a tornado. In stage 1, a new vortex (weak at low levels and strong aloft) forms on the east side of an updraft with an existing tornado. In stage 2, the low-level flow carries both the tornado and strengthening new vortex westward. In stage 3, the old tornado dissipates while the new tornado forms. In stage 4, another vortex forms on the east side of the updraft.

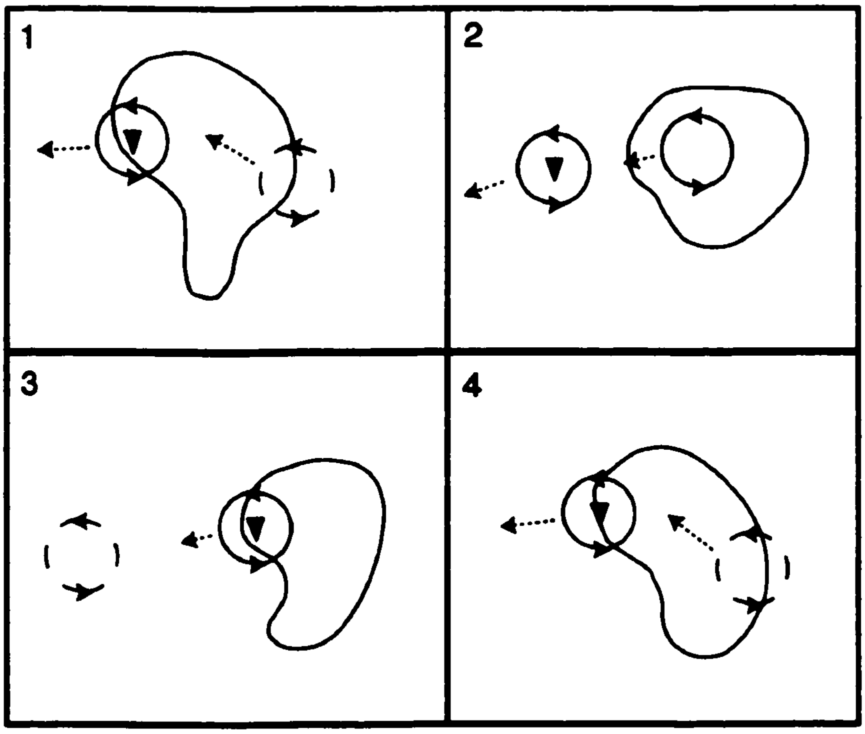

Figure 3.3.7. As in Fig. 3.2.10 (retrieved dynamic vertical perturbation pressure gradient), except at 2259 UTC at z=2.0 km AGL. Red (blue) shading indicates upward (downward) acceleration.

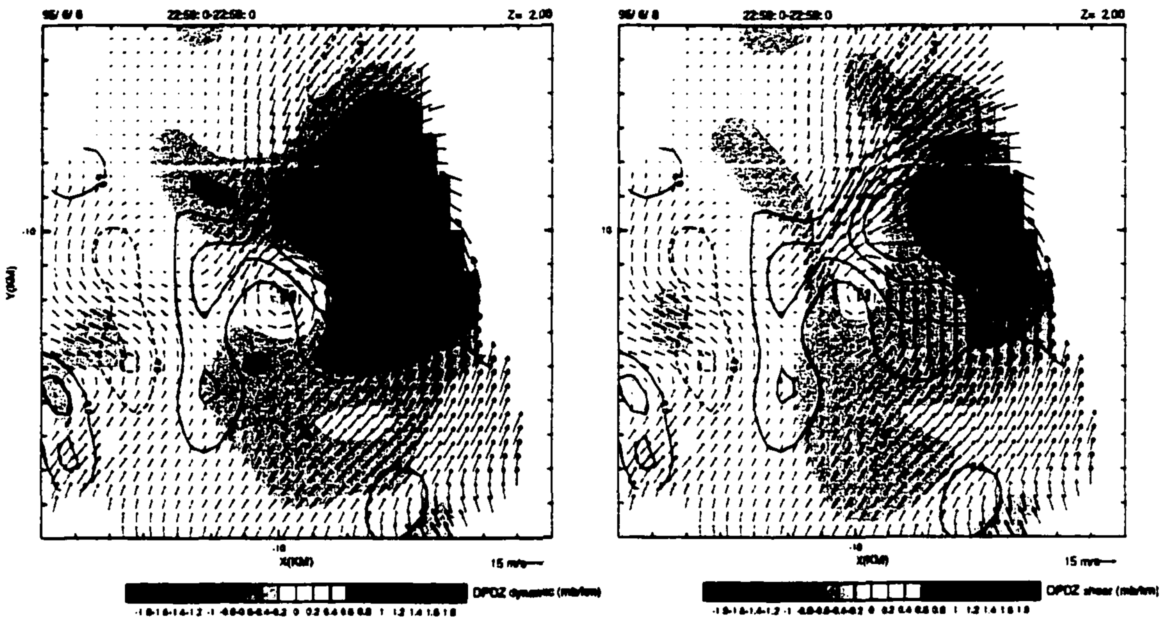

a) Total dynamic vertical pressure gradient $(\partial p_{dn} / \partial z)$.

b) Contribution from the shear term $(\partial p_s / \partial z)$.

Figure 3.3.8. As in Fig. 3.3.7 except at 2313 UTC.

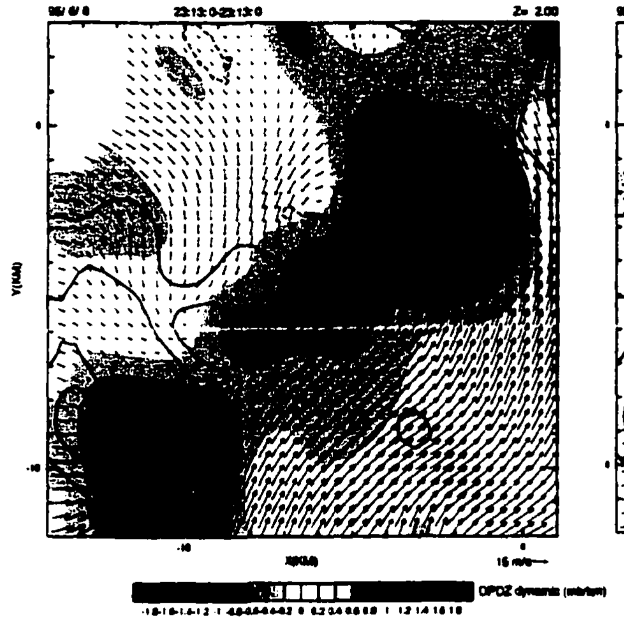

a) Total dynamic vertical pressure gradient $(\partial p_{dn} / \partial z)$.

b) Contribution from the shear term $(\partial p_s / \partial z)$.

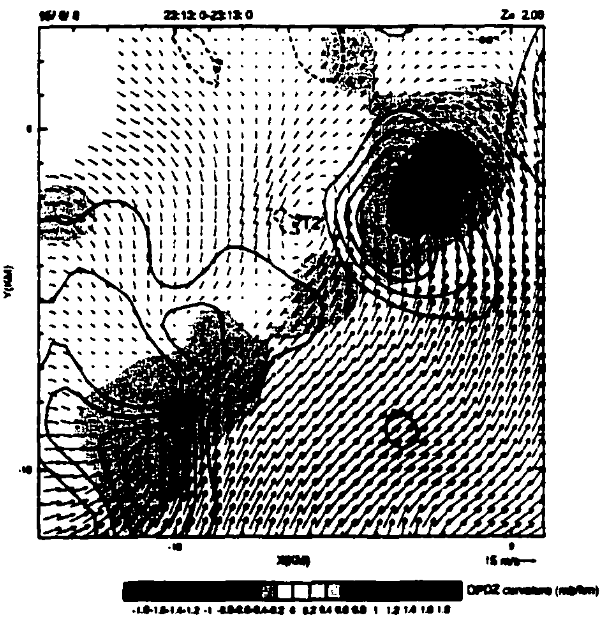

c) Contribution from the horizontal curvature term $(\partial p_c / \partial z)$.

Figure 3.3.9. As in Fig. 3.3.7 except at 2351 UTC.

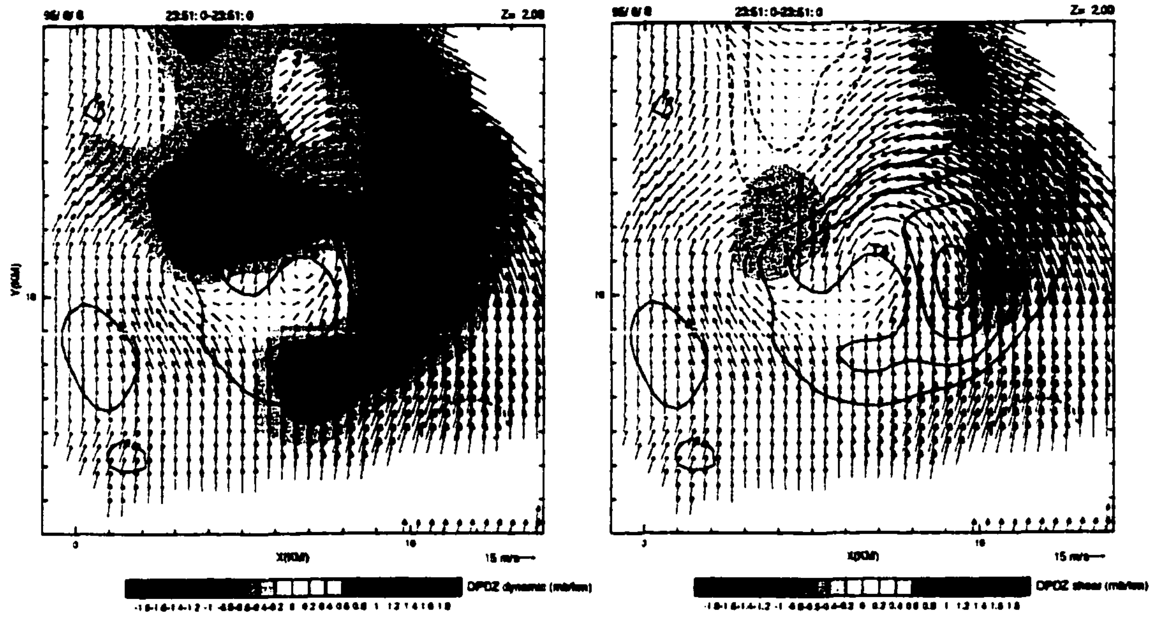

a) Total dynamic vertical pressure gradient $(\partial p_{dn} / \partial z)$.

b) Contribution from the shear term $(\partial p_s / \partial z)$.

Figure 3.3.10. Comparison of the eastward motion (m s^{-1}) of the updraft with the motion of the vorticity maxima as a function of time (UTC). The lavender circles indicate the u-component of motion of the updraft center at 4 km AGL. The red, blue, and green circles indicate the observed values of u of the vorticity maxima corresponding to tornadoes #1, #2, and #4, respectively, at 500 m AGL. The time intervals when the vortices were tornadic are noted. The triangles indicate the local mean values of u at z=500 m within circles of diameter 5 km around the vorticity maxima.

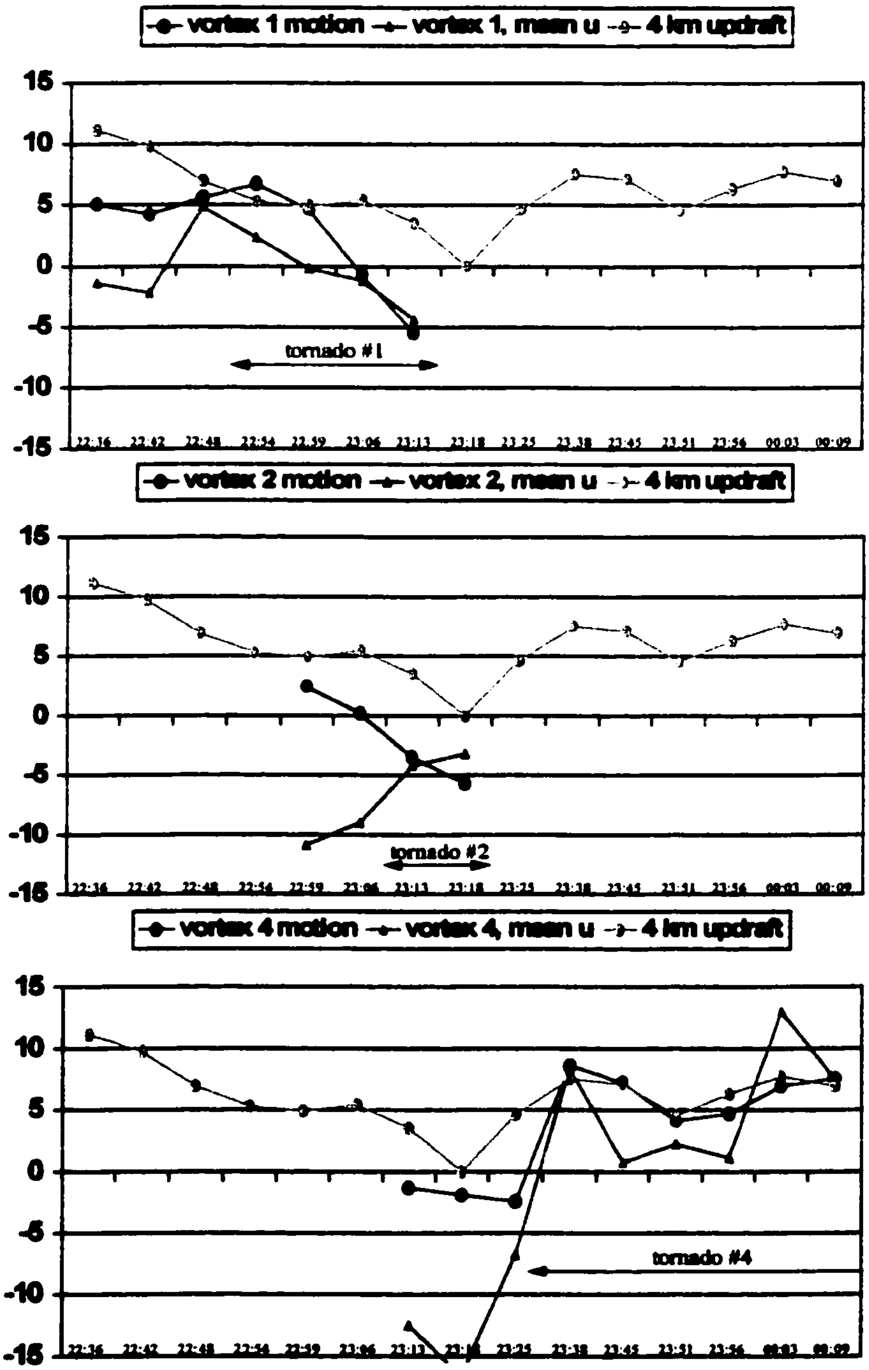

Figure 4.1. Characterization of supercell behavior according to inflow and outflow strength.

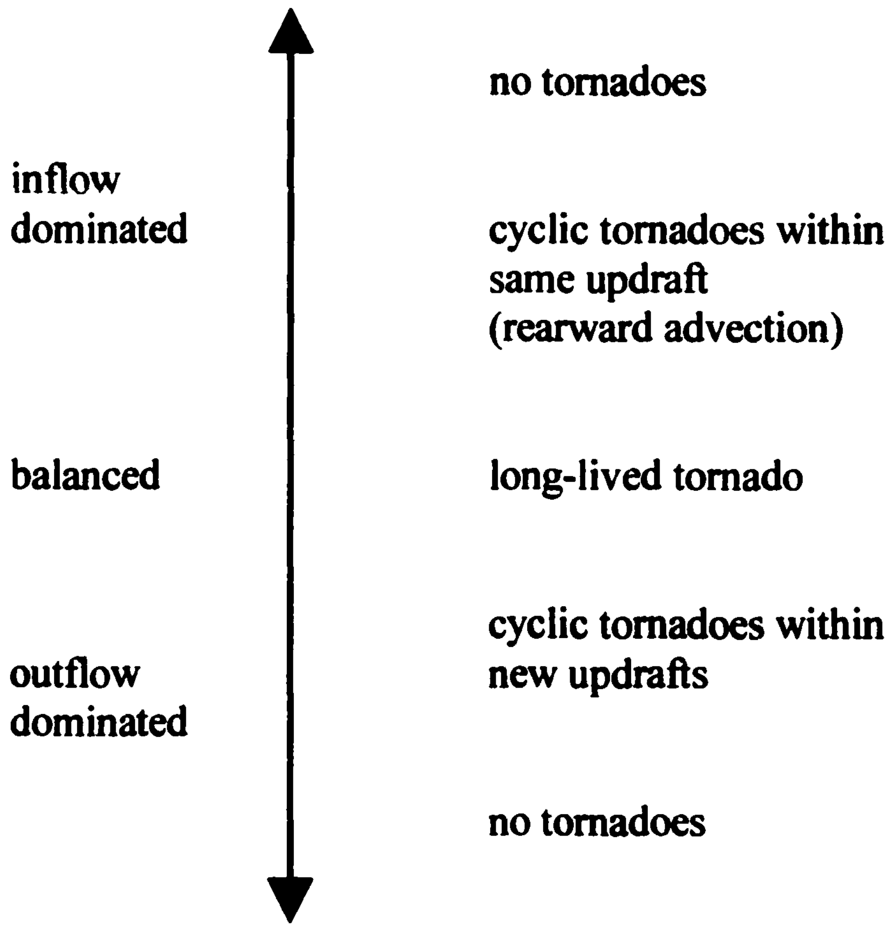

Figure 4.2. Increase of low-level outflow at the rear of a supercell. The gray shading indicates the location of the precipitation core, and the arrows depict relevant low-level flow. In example "a", an increase in westerly momentum beneath the main storm is associated with outflow from a nearby cell. In example "b", air parcels to the east of the main storm's mesohigh are accelerated toward the east.

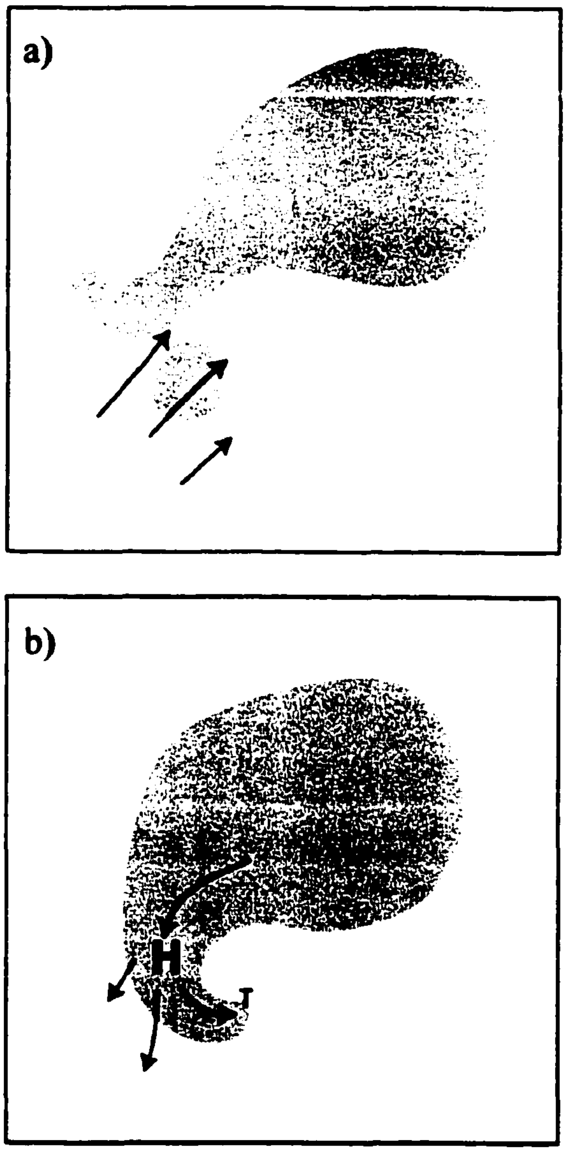

Figure A.1. As in Fig. 3.2.6 at 2259 UTC at z=0.5 km.

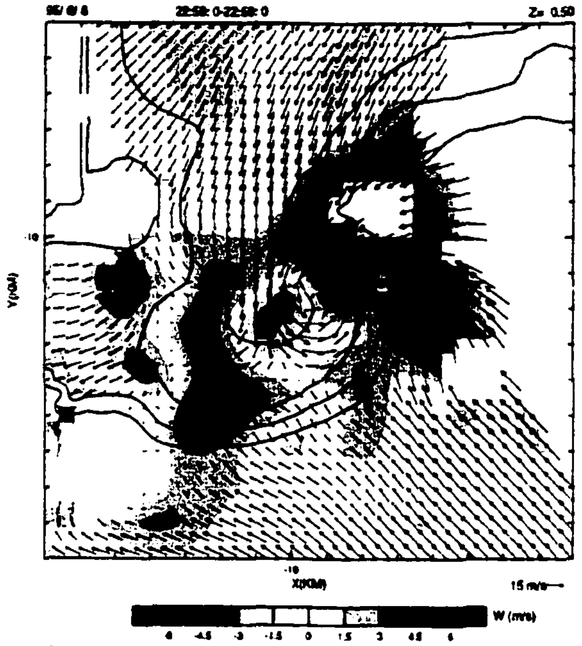

a) Objective analysis with a Cressman radius of influence of 0.6 km.

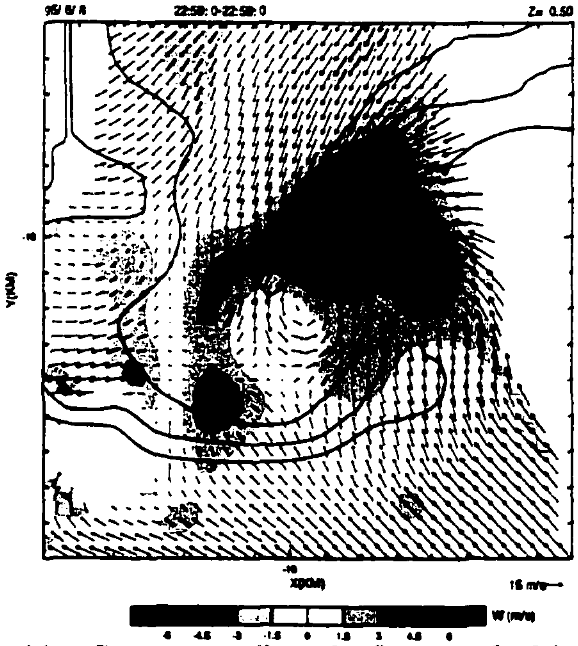

b) Objective analysis with a Cressman radius of influence of 1.2 km.

Figure B.1. Vertical cross section through a Cartesian grid. The dot indicates the location of the radar baseline, and the cross section is normal to the baseline. Azimuthal coordinate curves of a cylindrical coordinate system are also shown. A traditional iterative dual-Doppler analysis with upward integration in Cartesian coordinates is stable if the azimuthal coordinate curve approaches the point from an adjacent grid box (e.g., point 1) and unstable if it does not (e.g., point 2).

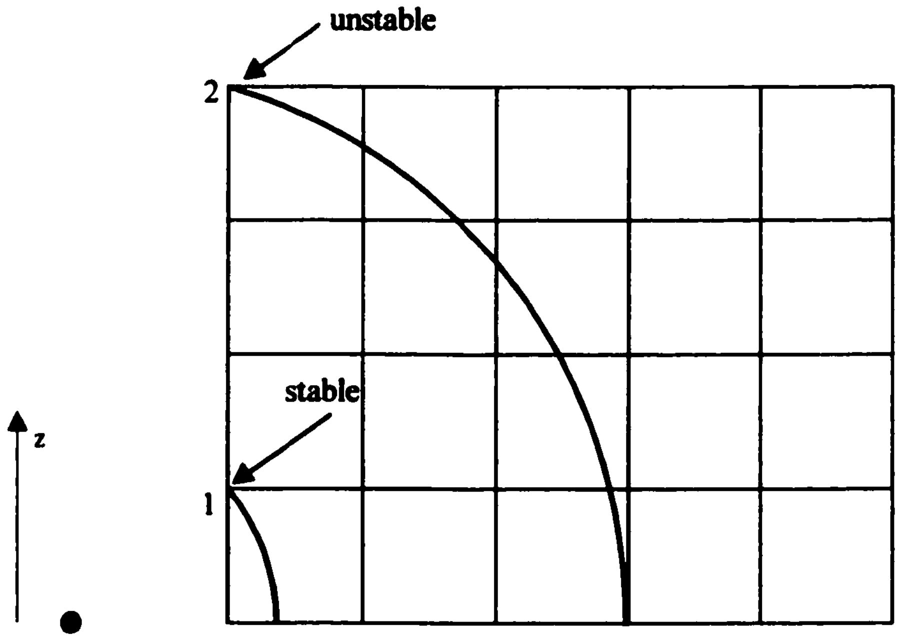

Figure C.1. Scanning geometry when fore and aft scans are directly above the flight track. If the vertical air velocity at the observed point is zero, then the scatterer along-track horizontal velocity (v_h) and vertical fall speed (w_t) can be determined directly from the observations.

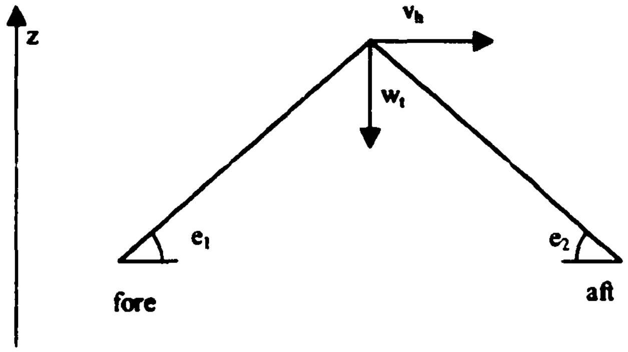

Figure C.2. Reflectivity (dBZ) vs. precipitation fall speed (m s^{-1}) in the McLean storm computed from ELDORA observations directly above the flight track. The values of w_t have been normalized to a common air density of 1.2 kg m^{-3}.

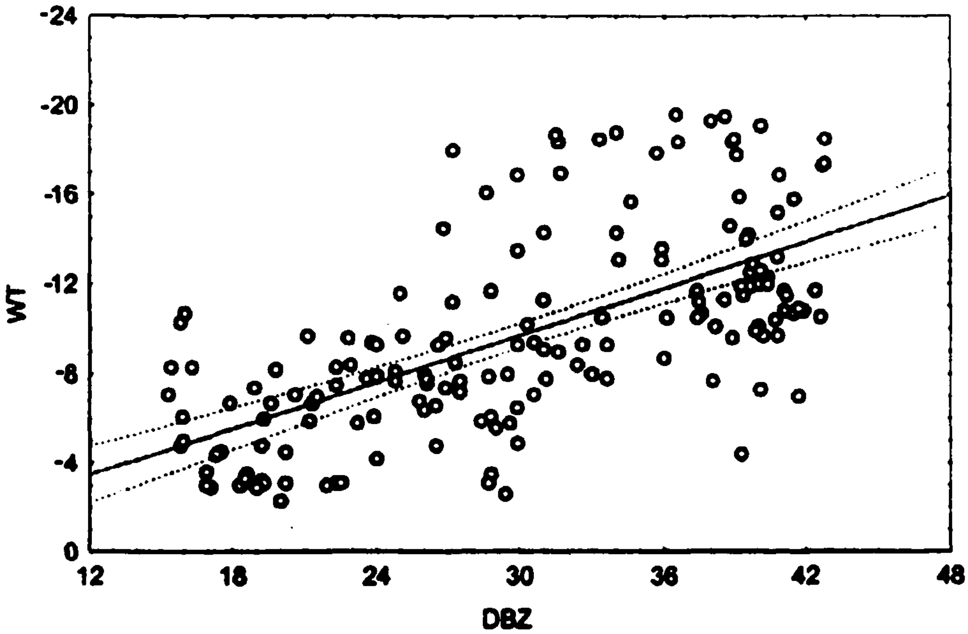

Figure E.1. Precipitation tangential velocity as a function of radius and time for 1.0 mm raindrops within a Rankine vortex. Curves are plotted for every 10 s of the simulation. The core of the Rankine vortex has a radius of 250 m and maximum tangential velocity of 50 m s^{-1}.

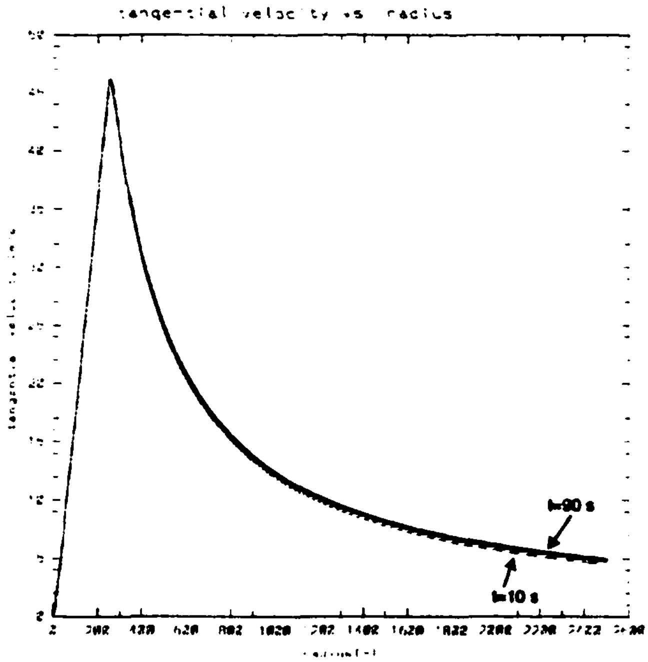

Figure E.2. As in Fig. E.1, except for precipitation radial velocity.

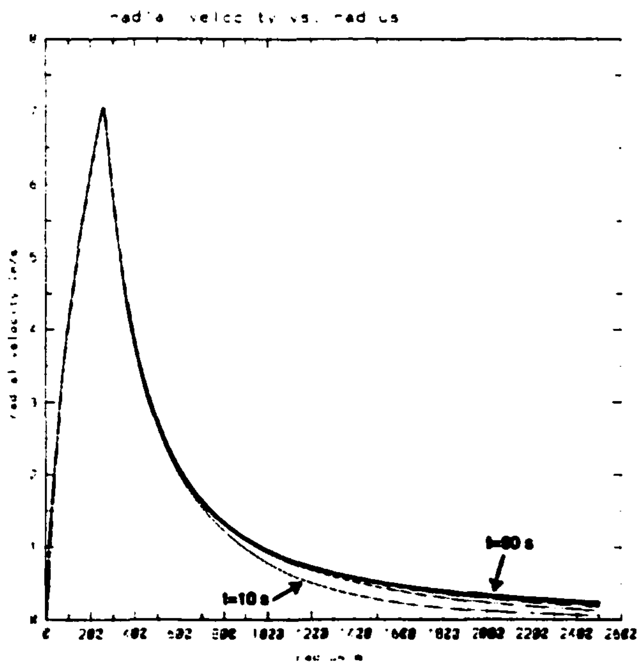

Figure E.3. As in Fig. E.1, except for precipitation number density (dimensionless).